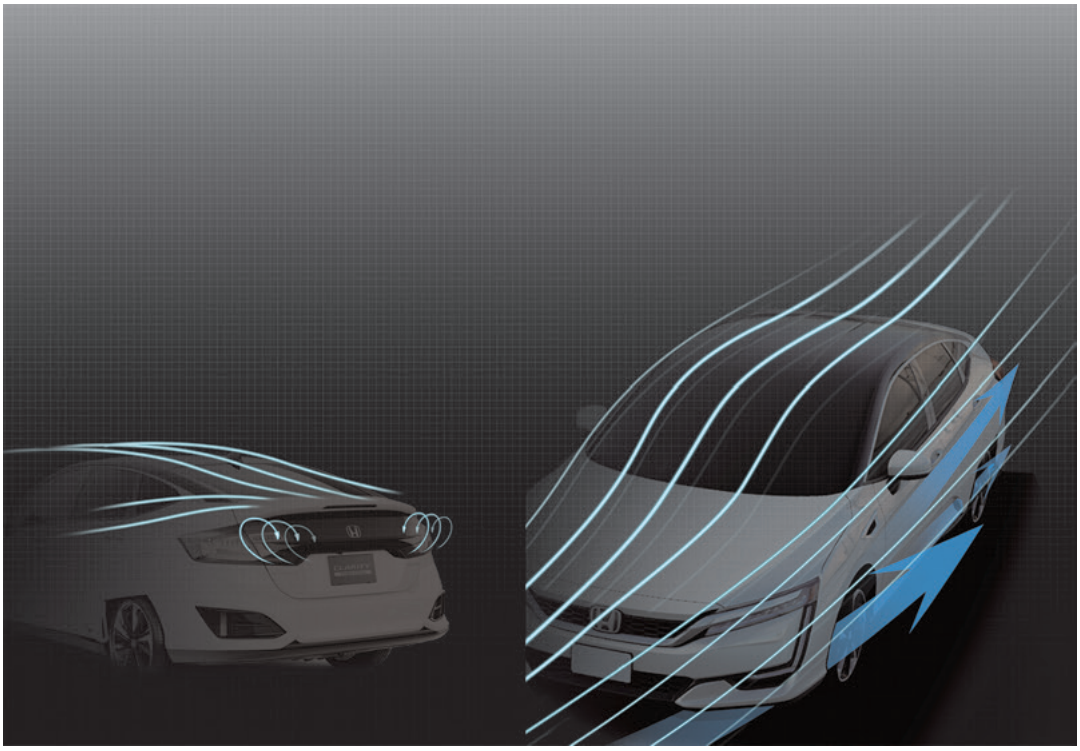
Honda R&D

Technical Review



April 2016
Vol.28 No.1



Comment on the Cover

To make the wind your ally is no easy matter.

Sometimes it lends you power, and sometimes becomes a barrier.

Though they may not appear so, car contours are always designed around the need to achieve harmony with the wind.

Developers consistently strive to realize new technologies that will make this invisible power work for them.

The cover of this issue of Honda R&D Technical Review has been designed using a motif from such a development process.



Motorcycle R&D Center
Ryo ITO



Motorcycle R&D Center
Shota NAKAHIRA

Technical Review

April
2016

Honda R&D

CONTENTS

Development of New Fuel Cell Vehicle CLARITY FUEL CELL
. . . . . .Kenichiro KIMURA・Teruaki KAWASAKI・Takayuki OHMURA
Yoshihiro ATSUMI・Kiyoshi SHIMIZU 1

Development of In-tank Solenoid Valve Compatible with 70 MPa High-pressure Hydrogen Storage
and Supply System for FCV . . . . . Saneto ASANO・Koichi KATO
Hiroyasu OZAKI・Makoto WADA 9

Development of CCM Water Content Distribution Measurement System for Fuel Cell Stack
. . . . . Masahiko SATO・Hiroto CHIBA・Masajiro INOUE 16

Numerical Prediction of Water Content Distribution of Catalyst Coated Membrane of Fuel Cell Stack using Simulation
. . . . . Kenji NAGUMO・Masajiro INOUE 26

Real-time Measurement of Water Content of CCM in On-board Fuel Cell Stack System
. . . . . Toru IWANARI・Kazuyoshi MIYAJIMA
Koichiro FURUSAWA・Masajiro INOUE 34

Empirical Model for Polymer Electrolyte Fuel Cell Electrocatalyst Degradation Using Platinum Stress
. . . . . .Masakuni YAMAMOTO・Hiroshi MATSUMORI 41

Life Prediction Model Estimating Chemical Degradation of Polymer Electrolyte Membrane for Fuel Cells
. . . . . Atsushi HIRAIDE 50

Life Prediction Technology of Fuel Cell Polymer Electrolyte Membrane under Mechanical Degradation
. . . . . .Masashi SUGISHITA・Suguru OHMORI 59

A Pore-Scale Multiphysics Method to Study PEMFC Catalyst Layers
. . . . . Koji MORIYAMA・Jinfen KANG・Seung Hyun KIM 68

Three Dimensional Large Scale Numerical Simulation of PEMFC with Low-Pt Loading
. . . . . .Koji MORIYAMA・Wenbin GU
Liang HAO・Chao-Yang WANG 78

Development of 70 MPa Differential-pressure Water Electrolysis Stack
. . . . . Hiroyuki ISHIKAWA・Eiji HARYU
Nobuyuki KAWASAKI・Hayato DAIMON 86

Design of Next-generation Environmental Vehicle CLARITY FUEL CELL, realizing Harmony
between Vehicles and Society . . . . . Fumihiro YAGUCHI・Kei KOBAYASHI
Ken SAHARA・Saki TOMITA 94

Styling Design of the Forza125 . . . . . Taro NISHIMOTO 106

Styling Design of New Tact, 50 cc Standard Scooter. . . . . Mamoru OTSUBO 119

Development of RC213V-S . . . . . Hiroshi UNUKI・Ryuji TSUCHIYA・Hodaka MUKOUHARA
Naoki MURASAWA・Satoru OKOSHI 127

New In-Line 4-Cylinder Gasoline Direct Injection Turbocharged Downsizing Engine
. . . . . Koji NAKANO・Yusuke WADA
Mitsutaka JONO・Shigeru NARIHIRO 139

6-Speed Manual Transmission for Honda S660
. . . . . Masaaki IWASAKI・Takuya HOSOKAWA・Dohta YAMAMOTO 147

Accurate Capacity Estimation and Forecast of Li-ion Battery for BEV Using Telematics
. . . . . Koichiro TAKEMASA・Takuya MIYASHITA・Kenji AKAMATSU
Satoshi HADA・Masao JOKO 153

Development of Vehicle System Supporting Vehicle-Grid Integration
. . . . . Hakaru SADANO・Yutaka MARUYAMA・Satoru SHINZAKI
Hiroyuki KANAZAWA・Jun KUDO・Takeshi FUJINO 160

Nonlinear Finite Element Method Solver for Design of Automotive Cable Layout
. . . . . Takuya SHUDO 168

Introduction of Heat Exchanger Production Technique for Stirling Engine Using Additive Manufacturing
. . . . . Masahiko ASANUMA・Tsuneo ENDO・Hitoshi SAKAI 174

Stir-casting Process and Mechanical Properties of Forged Mg-Zn-Y Alloys for Piston
. . . . . Yuichi IENAGA 183

Prediction of Fracture of Cylinder Block Main Bearing by Fretting Fatigue and Development of Verification Method
. . . . . Yoshimichi ISHIHARA・Takeru HAMAKAWA・Kenji SATOH
. . . . . Takeyuki YAMASAKI・Chao SHI・Hisashi HASHIMOTO
. . . . . Hiroaki HANEDA・Shinichi TAKAHASHI 191

Development of New Fuel Cell Vehicle CLARITY FUEL CELL

Kenichiro KIMURA* Teruaki KAWASAKI* Takayuki OHMURA*
Yoshihiro ATSUMI* Kiyoshi SHIMIZU*

ABSTRACT

The newly developed fuel cell vehicle, the CLARITY FUEL CELL, has evolved to provide new era appeal together with the same usability as a vehicle with an internal combustion engine. The fuel cell powertrain is mounted under the front hood, realizing the world's first fuel cell vehicle to be commercially available in a five-passenger sedan package. The key technologies in this achievement are the greater compactness and shock-resistant construction of the fuel cell stack, the adoption of an electric turbo air compressor and fuel cell voltage control unit, and the compact drive unit. Optimal placement of the hydrogen tank and increased pressure capacity extend the driving range (reference value) to approximately 750 km, and achieve a hydrogen refueling time of about three minutes. Driving performance is also heightened by pursuing reductions in vehicle body weight and enhancement in its aerodynamic performance, through increased power of the motor, and so on. These efforts have realized a level of usability on a par with vehicles running on internal combustion engines. In further innovation, this model features external power supply functionality, a new linking technology that gives a foretaste of the vehicle of tomorrow.

1. Introduction

Hydrogen is receiving attention as a technology that addresses both the issue of global warming caused by CO_2 and the depletion of resources, which are energy issues faced by motor vehicles today. It can be manufactured from a variety of energy sources, and it can be transported and stored. Hydrogen is therefore a promising energy carrier for the next generation.

With its aim to realize the joy of free mobility and a prosperous sustainable society, Honda started basic research on fuel cells in the 1980s. In 1999, Honda unveiled the FCX V1 and V2 test vehicles[1] and has engaged in development for the popularization of fuel cell vehicles (FCV). The FCX developed in 2002 was the first such vehicle in the world to receive certification in the United States, and Honda began lease sales in Japan and the United States[1]. In 2003, the world's first fuel cell stack capable of starting in temperatures below freezing (Honda FC Stack) was developed in-house[2, 3]. In 2008, the FCX CLARITY[4] was launched on the market as the world's first FCV to have an innovative sedan-type package and a whole new dimension of driving feel. Honda has led the field of other manufacturers in presenting vehicles with the new value and appeal that are distinctive attributes of the FCV.

In developing new vehicle models that serve to expand the popularization of the FCV, it was necessary to further evolve the FCV to provide both usability on a par with internal combustion engine vehicles and the appeal of a new era that is not present in conventional vehicles. This involved providing the data acquired to that point and the views of customers as feedback to the process.

2. Development Concept and Goals

The CLARITY FUEL CELL (Fig. 1) development concept was formulated as "Red Carpet to the New Era." The meaning of this concept is that, in order to replace internal combustion engine vehicles for the purpose of widely popularizing the FCV, such universal values as performance and usability would be left unchanged while adding new appeal that never previously existed. In this way, development would yield a vehicle that becomes a special one-of-a-kind vehicle for those customers who take the step forward into the new era.

Based on this concept, the development goals for the

* Automobile R&D Center

CLARITY FUEL CELL were defined as follows:

(1) Realize the world's first five-passenger FCV sedan package
Downsizing the fuel cell powertrain and installing it under the front hood realized a five-passenger cabin with a spacious feeling.

(2) Reduce the weight of the vehicle body and make comprehensive reductions in running resistance
High-strength materials were used to reduce the vehicle body weight while also seeking a body shape for aerodynamic performance together with reduction in running resistance by the configuration of aerodynamic parts.

(3) Achieve a balance of environmental performance and vehicle performance
Realize vehicle performance equal to or better than that of an internal combustion engine vehicle while providing the ultimate environmental performance of zero emissions.

(4) Linking technology that gives a foretaste of the vehicle of tomorrow
Provide external power supply functionality as standard equipment, and aim to make vehicles and society connect.



Fig. 1 Honda CLARITY FUEL CELL

3. Achieve the World's First Five-Passenger FCV Sedan Package

3.1. Fuel Cell Powertrain Installation Under the Front Hood

Following the "man maximum, machine minimum" philosophy, the CLARITY FUEL CELL was intended to provide the comfortable occupancy space of a sedan. Measures were therefore taken to downsize the fuel cell powertrain, and it was successfully installed for the first time in the world under the front hood of a commercially available sedan. This increased the space efficiency of the vehicle and realized an FCV sedan package that comfortably seats five adults. At the same time, this opened the way to future deployment in multiple vehicle types when the time comes for expanded popularization of the FCV.

This compact fuel cell powertrain was realized by the following four key technologies, which are shown in Fig. 2.

(1) Fuel cell (FC) stack downsized and made more shock-resistant
(2) Electric turbo air compressor adopted
(3) Fuel cell voltage control unit (FCVCU) adopted
(4) Drive unit downsized

3.1.1. FC stack downsized and shock resistance enhanced

As shown in Fig. 3, the current density of the new model FC stack was increased by a factor of 1.5, reducing the number of cells by approximately 30%, in order to downsize the stack. The cell structure, as shown in Fig. 4, inherits the unique Honda wave flow channel and cooling construction for every two cells while achieving a 1-mm thickness for each cell. The gas diffusion performance of the membrane electrode assemblies (MEA) was also enhanced and the height and width of the gas flow channels in the separators were reduced. As shown in Fig. 5, the FC stack realized the world's highest level of power output density at 3.1 kW/L and achieved a 33% reduction in size compared to former stacks.

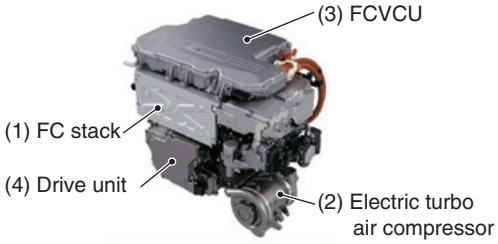


Fig. 2 Downsized fuel cell powertrain

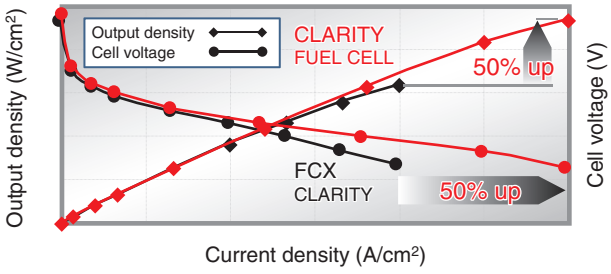


Fig. 3 Enhancement of FC current density

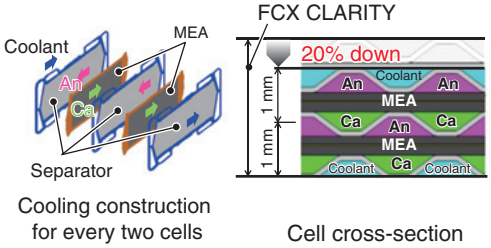


Fig. 4 FC structure

Figure 6 shows a cross-section of the stack to illustrate how its shock resistance has been increased by a factor of four by refining the cell retaining structure. This was done in order to assure safety in the event of a frontal collision.

Figure 7 shows the MEA construction with a resin frame around the outer periphery to which it is joined. The use of the resin frame reduces the amount of material in the MEA, while squaring off the MEA shape enabled continuous coating of catalyst and related material. This had the effect of reducing the amount of remnant material that is wasted. In combination, these measures reduced by approximately 40% the amount of expensive materials used, while contributing to the increased productivity of the fuel cell stacks and reducing their cost.

3.1.2. Electric turbo air compressor adopted

Figure 8 shows an external view of the newly developed air compressor that supplies air to the fuel cell stack.

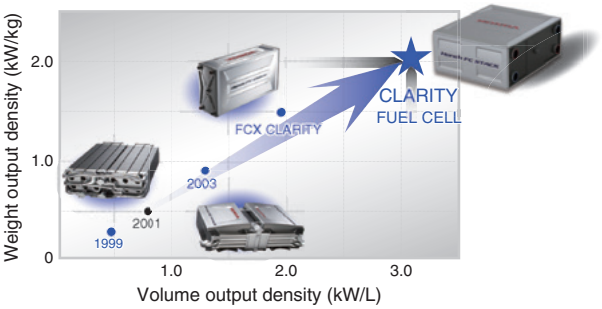


Fig. 5 Evolution of power density of FC stack

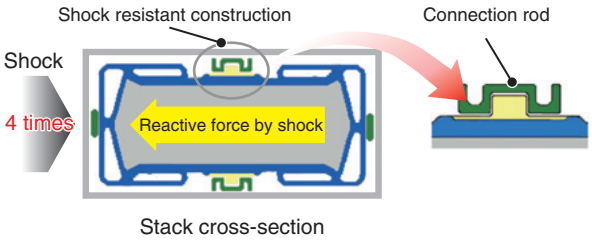


Fig. 6 Shock resistant construction of FC stack

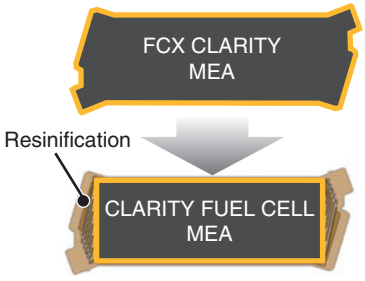


Fig. 7 Resin frame around MEA

An electric turbo air compressor with excellent flow rate characteristics, capacity, and cost was adopted. It is also very quiet, which contributes to cabin comfort even when the vehicle is accelerating or cruising at high speed. It is a coaxial two-stage motorized turbo-type compressor, which increased the pressure of the air supply by a factor of 1.7 over the conventional type and contributed to the downsizing of the fuel cell stack.

3.1.3. Fuel cell voltage control unit (FCVCU) adopted

The FCVCU was adopted because it is necessary to raise the voltage of the power supplied to the traction motor in order to reduce the number of cells stacked in a fuel cell and to increase the power output from the traction motor. A full-SiC Intelligent Power Module, the first such in the world to be used in a mass-production vehicle, was applied in the FCVCU, and its high-frequency switching at approximately 30 kHz was a step toward the downsizing of capacitor, inductor, and other such components. The adoption of a coupled inductor and the optimal layout of component parts also achieved approximately 40% downsizing of volume relative to previous types.

3.1.4. Drive unit downsized

In previous models, the power control unit (PCU) was mounted on top of the traction motor. In order to install the fuel cell stack under the front hood, the PCU was placed at the front of the traction motor and integrated with it. As shown in Fig. 9, this reduced its height relative to the FCX CLARITY by approximately 34%, thereby ensuring the space for mounting the fuel cell stack.

By means of these key technologies, the fuel cell



Fig. 8 Electric turbo air compressor

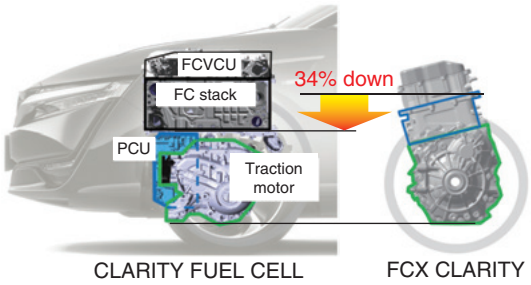


Fig. 9 PCU integrated with traction motor

powertrain was successfully reduced to the size of a conventional V6 engine, as shown in Fig. 10.

3.2. Optimal Placement of the Hydrogen Tanks

Figure 11 shows the vehicle package with the hydrogen tanks installed. The hydrogen tanks are installed below the floor under the rear seat and above the rear axle (between the back of the rear seat and the forward side of the trunk). This layout realized a sedan package that provides seating for five occupants and trunk space (capable of holding three golf bags) appropriate to the vehicle class. Table 1 shows a comparison with the basic dimensions of the 2013 model Accord and the 2015 model LEGEND.

Figure 12 shows the hydrogen tank as installed. It is

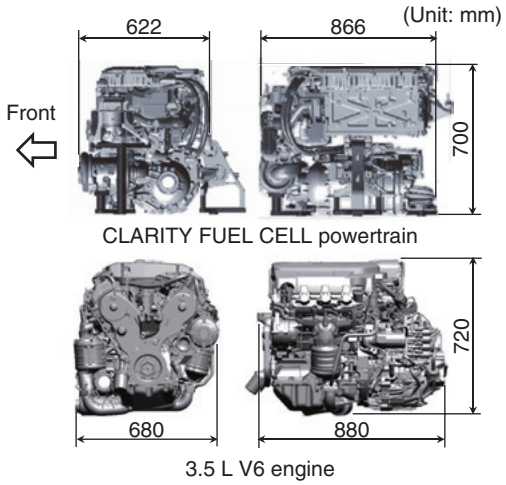


Fig. 10 FC powertrain equivalent to V6 engine in size

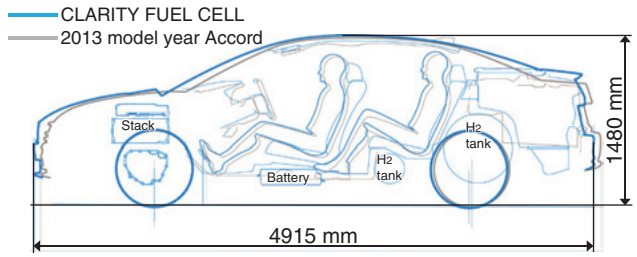


Fig. 11 Package (Japan model)

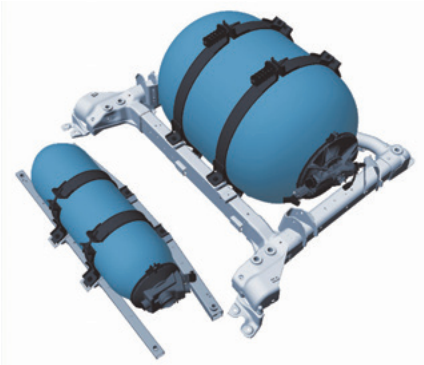


Fig. 12 Image of H_2 tank installation

Table 1 Basic dimension

Model / Specification	CLARITY FUEL CELL	2013 model year Accord PHEV	2015 model year LEGEND
Weight (kg)	1890	1740	1980
Length (mm)	4915	4915	4995
Width (mm)	1875	1850	1890
Height (mm)	1480	1465	1480
Wheel base (mm)	2750	2775	2850
Seating capacity	5	5	5

a Type 3[(5)] tank with an aluminum liner. It complies with global technical regulation GTR No. 13 and is capable of storing approximately 5 kg[*1] of highly compressed hydrogen gas at 70 MPa.

4. Reduction of Vehicle Body Weight and Comprehensive Reduction of Running Resistance

4.1. Reduction of Vehicle Body Weight by Use of High-Strength Materials

Figure 13 shows the technology used to reduce the weight of parts making up the vehicle body. Figure 14 shows the usage rate of reduced-weight materials. Parts in which the material was replaced by aluminum alloy

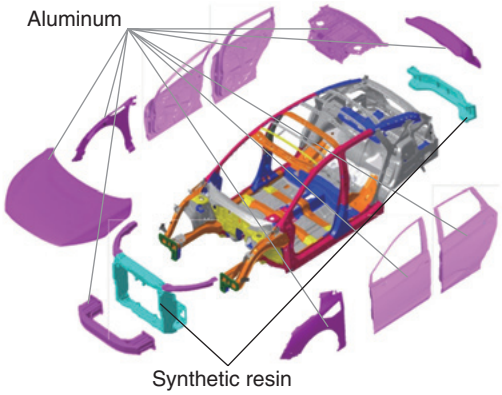


Fig. 13 Weight saving parts

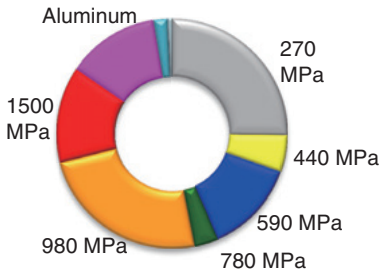


Fig. 14 Usage rate of lightweight materials

include the front bumper beam, front hood (skin and frame), fenders, front and rear door components (sash, skin, panels), trunk components (skin and frame), and rear parcel shelf. Parts in which the material was replaced by resin include the front bulkhead and rear bumper beam. The usage rate for ultra-high tensile strength steel sheet was also raised, and this realized approximately 15% of the weight reduction relative to former vehicles. Figure 15 shows a comparison by body weight.

4.2. Seeking Body Shape Informed by Awareness of Aerodynamic Performance

Figure 16 shows a conceptual image of the air flow along the top and sides of the vehicle body. This flow of air along the top of the vehicle body and the flow along the side converge at the rear of the vehicle body. Figure 17 shows the appearance of the air flow where it lifts up and toward the rear of the vehicle body. In the figure on the right in Fig. 17, the induced drag generated by the longitudinal vortex is reduced when the difference between the flow velocity at the upper surface and the side surfaces has been reduced by comparison with the figure on the left. In order to realize this body shape, a cabin silhouette that is advantageous in terms of aerodynamic performance was adopted, and in order to achieve a balance with cabin space, a distinctive sedan structure with the trunk lid placed at a higher level (a high-deck sedan structure) was adopted. The body shape was decided through the use of a wind tunnel with a rolling road[6] from the initial stage of development, and repeated wind tunnel tests were conducted.

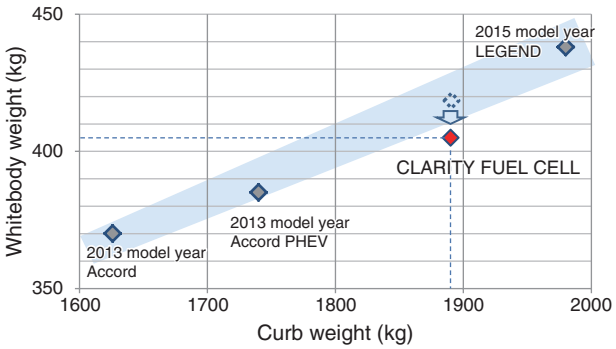


Fig. 15 Whitebody weight Ration



Fig. 16 Image of aerodynamic body shape image

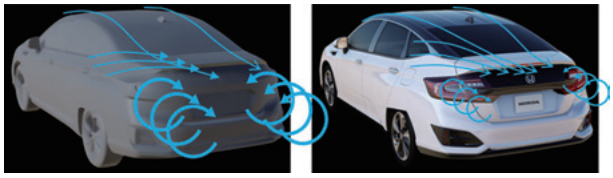


Fig. 17 Induced drag generated by longitudinal vortex

Table 2 Aerodynamic parts effect

Parts	⊿CD (%)
Rear spoiler	-1.0
Rear under cover	-1.0
Rear air curtain	-0.5
Rear combi washboard	-1.0
Tire cover	-1.0
Tank under cover	-1.5
Main floor under cover	-2.5
Front air curtain	-1.5
Motor under cover	-3.0
Total	-13.0

4.3. Device Configuration for Heightened Aerodynamic Performance

As shown in Fig. 18, all types of aerodynamic device were configured in order to reduce the aerodynamic drag. Air curtains on the sides of the front and rear tires for streamlining, tire covers over the tops of the rear tires, and flat covers under the floor to promote smooth air flow under the vehicle body yielded the effect of reducing the coefficient of drag by approximately 13%. Table 2

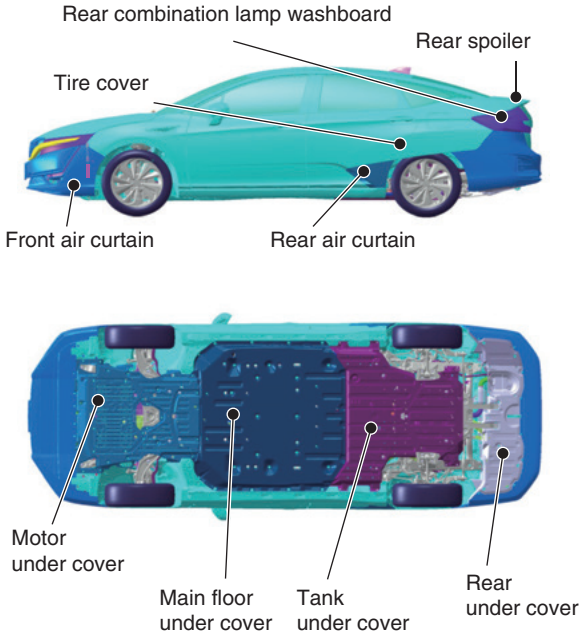


Fig. 18 Aerodynamic parts

shows the effects of individual devices on reduction of the coefficient of drag.

5. Achieving a Balance of Environmental Performance and Vehicle Performance

The CLARITY FUEL CELL was developed to have the ultimate environmental performance, known as zero emissions, while also aiming for vehicle performance equal to or greater than that of an internal combustion engine vehicle.

5.1. Achieved Driving Range (Reference Value) of Approximately 750 km[*2]

Equipped with a hydrogen tank with a pressure rating increased to 70 MPa, together with increased powertrain efficiency and reduced running energy, achieved a driving range (reference value) of approximately 750 km[*2] (when driving in JC08 mode, measured by Honda). This places it at the highest level in the world for a zero emissions vehicle.[*4] When refilled at a hydrogen station on the new standard expected to enter operation in fiscal year 2016 or later, the increased amount of hydrogen filling the tank is expected to give the vehicle a range of approximately 800 km.[*3] Moreover, the hydrogen refueling time taken to fill the tank once is expected to be about three minutes,[*5] which in combination with other factors means that the FCV achieves usability equal to that of an internal combustion engine vehicle.

5.2. Increased Motor Power and Driving Mode Switchable Between Normal and Sport Driving Yield Attractive Performance

By means of optimal voltage control by the FCVCU, the traction motor achieves power output of 130 kW. This is a 30% increase over former models, and it is gained while maintaining the same size as before. A switch that allows switching between normal and sport driving modes was also adopted. When sport mode is selected, more agile and direct acceleration is produced by the faster power response time for torque versus accelerator pedal opening during acceleration, as shown in Fig. 19. The responsiveness of power regeneration by the motor has also been enhanced, so that releasing the accelerator pedal will produce an effect corresponding to the engine brake in an internal combustion engine vehicle. These settings provide still more of the attraction of agile driving.

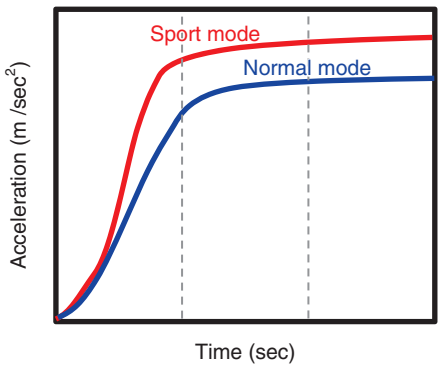


Fig. 19 Acceleration performance

5.3. Adoption of Dedicated Chassis Yields Driving with Quality Feeling

Figure 20 shows the front and rear suspension and the subframe construction. A strut-type front suspension and five-link rear suspension were adopted. For the front subframe, a hollow aluminum die cast process was used in a world first that achieved high rigidity with a weight reduction of approximately 46% relative to conventional manufacturing methods. All aluminum materials were also used in the rear subframe, yielding a weight reduction of approximately 27% while including frames for installing the hydrogen tanks.

Installation of a hydrogen tank below the rear seat lowered the vehicle's center of gravity by approximately 10 mm and reduced the static stability factor (SSF) by 5% relative to the Accord PHEV. As a result, rolling is less likely to occur due to steering while driving and the flat ride feeling is enhanced. Sensitive frequency response dampers (SFRD)[(7)] were adopted for the suspension, realizing smoother ride comfort. Dual pinion-assist electric power steering (EPS) was adopted for the steering gearbox (Fig. 21), and aluminum alloy was used for the tie rod ends, reducing the weight by 20% relative to conventional configurations. Electric servo brakes (ESB)[(8)] and an electric parking brake (EPB) were adopted for the brake system. Active noise control (ANC)[(9)] was also adopted to reduce road noise and increase cabin comfort.

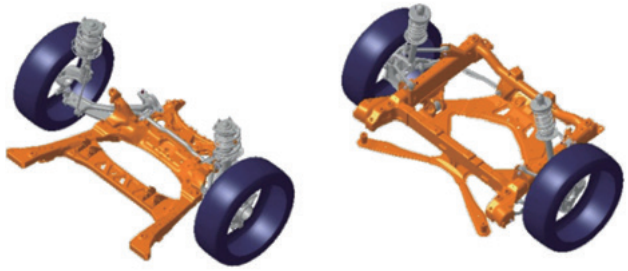


Fig. 20 Front suspension (left) and rear suspension (right)

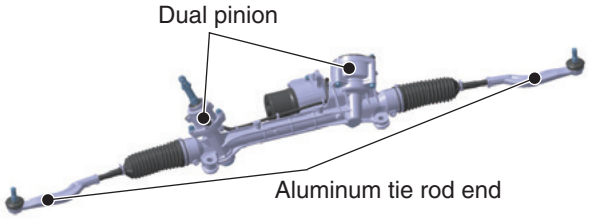


Fig. 21 Dual pinion assist EPS

6. Linking Technology that Gives a Foretaste of the Vehicle of Tomorrow

6.1. Honda's Vision for a Hydrogen Energy Society

Looking ahead to the coming hydrogen society, Honda has also engaged in hydrogen-related development other than the FCV. This effort is based on the three concepts of "generate hydrogen, use hydrogen, get connected with hydrogen" (Fig. 22).

From the perspective of generating hydrogen, Honda has developed the Smart Hydrogen Station (SHS) and is conducting proving tests. The SHS is intended to supply hydrogen energy in a distributed manner using renewable energy from such sources as photovoltaic energy and wind power to manufacture the hydrogen.

In terms of connecting with hydrogen, the FCV serves as a moving electric power source. The aim is to connect the vehicle with the local community by using it to supply electricity for use outdoors or in emergencies. The POWER EXPORTER 9000 is an external electric power source that features the high reliability cultivated through Honda's development of electric generators together with high-quality AC power output. It can provide an external supply of a maximum of 9 kVA from the CLARITY FUEL CELL. Figure 23 shows an external view of the unit connected to a vehicle. A dedicated socket with lid for supplying electricity has been provided out of consideration for usability.

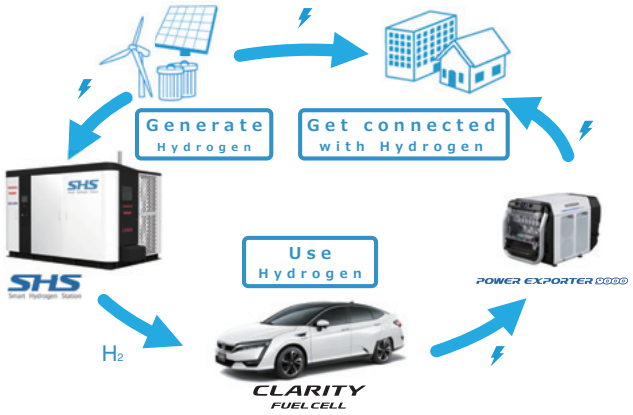


Fig. 22 Honda's vision of a hydrogen-powered future society



Fig. 23 POWER EXPORTER 9000

7. Conclusion

The CLARITY FUEL CELL was developed for the purpose of becoming a special vehicle for those customers who are taking a step forward into a new era. It is a vehicle for a new age, and it possesses both usability on a par with internal combustion engine vehicles and a new appeal that cannot be found in conventional vehicles.

The market for the FCV is still developing, and it will be important to continue with ongoing initiatives to expand the market in coordination with hydrogen infrastructure. Honda will strive to enhance the performance, reduce the cost, and take other such measures to further heighten the appeal of the FCV. Honda aims to realize the joy of free mobility and a prosperous sustainable society, and, as in the CLARITY's name, Honda's initiatives are bright and clear.

*1 Value measured by Honda in filling operations at a station supplying hydrogen under 70-MPa pressure in accordance with the criteria in SAE standard J2601.
*2 Value measured by Honda while driving in JC08 mode. This is a value measured by Honda based on filling operations at a station supplying hydrogen under 70-MPa pressure in accordance with the criteria in SAE standard J2601. If the vehicle is refilled at a hydrogen station with different specifications, the amount of hydrogen filling the hydrogen tank will differ, as will the range. Range can also vary greatly according to the environment of use (air temperature, congestion, etc.) and how the vehicle is driven (sudden starts, using air conditioner, etc.).
*3 Value measured by Honda under the same conditions as in *2, when the vehicle is filled at a hydrogen station on the new standard expected to enter operation in fiscal year 2016 or later.
*4 As of March 2016, according to a Honda study.
*5 Value measured by Honda in filling operations at a station supplying hydrogen under 70-MPa pressure in accordance with the criteria in SAE standard J2601. (Filling time may vary with the filling pressure and outside air temperature.)

References

(1) Kawasaki, S., Ogura, M., Ono, T., Kami, Y.: Development of the Honda FCX Fuel Cell Vehicle, Honda R&D Technical Review, Vol. 15, No. 1, p. 1-6
(2) Kawasaki, S., Uchibori, K., Murakami, Y., Shimizu, K., Fujimoto, S.: Development of New Honda FCX with Next-generation Fuel Cell Stack, Honda R&D Technical Review, Vol. 18, No. 1, p. 45-50
(3) Ogawa, T., Kimura, K., Uchibori, K., Fujimoto, S., Shimizu, K.: Development of New Power Train for Honda FCX Fuel Cell Vehicle, Honda R&D Technical Review, Vol. 15, No. 1, p. 7-12

(4) Matsunaga, M., Fukushima, T., Ojima, K., Kimura, K., Ogawa, T.: Fuel Cell Powertrain for FCX Clarity, Honda R&D Technical Review, Vol. 21, No. 1, p. 7-15
(5) Kanezaki, T., Mano, S., Miyagawa, K., Hayashi, N., Ogawa, T.: Life Design and Evaluation Method of Type 3 High-Pressure Hydrogen Tank for Fuel Cell Electric Vehicle, Honda R&D Technical Review, Vol. 26, No. 1, p. 150-159
(6) Koremoto, K., Kawamura, N., Aoki, M., Kuratani, N., Nakamura, S., Yoshioka, H.: Full-scale Wind Tunnel Equipped with Single-belt Rolling Road System, Honda R&D Technical Review, Vol. 23, No. 1, p. 18-22
(7) http://www.showa1.com/jp/technology/automobile/sfrd.html/2015/12/02
(8) Ohkubo, N., Nishioka, T., Akamine, K., Hatano, K.: Development of Electric Servo Brake System, Honda R&D Technical Review, Vol. 25, No. 1, p. 48-52
(9) Kawano, M., Tsushima, H., Akimoto, Y., Take, K., Harada, N., Nagaoka, S., Eguchi, Y.: Development of 2013 Model Year U.S. Accord, Honda R&D Technical Review, Vol. 25, No. 1, p. 13-22

■ Author ■


Kenichiro KIMURA


Teruaki KAWASAKI


Takayuki OHMURA


Yoshihiro ATSUMI


Kiyoshi SHIMIZU

Development of In-tank Solenoid Valve Compatible with 70 MPa High-pressure Hydrogen Storage and Supply System for FCV

Saneto ASANO* Koichi KATO*
Hiroyasu OZAKI* Makoto WADA*

ABSTRACT

In order to increase fuel cell vehicle mileage per filling, technologies have been developed to reduce the weight of the in-tank solenoid valve and boost hydrogen seal performance, both issues in increasing the pressure of a hydrogen storage and supply system.

It was necessary for the in-tank solenoid valve for use at 70 MPa to display twice the pressure resistance of the previous model (for 35 MPa use). However, realizing the necessary increase in pressure resistance would increase the size and weight of the valve. The in-tank solenoid valve is provided with a check valve on the hydrogen filling side and a shut-off valve on the hydrogen supply side; these valves connect to the high-pressure hydrogen tank and supply and shut off hydrogen. As a means of reducing weight in the developed in-tank solenoid valve, the functions of these valves were integrated, making it possible to share the flow channels for hydrogen filling and hydrogen supply. The temperature sensor was built into the tank, and aluminum alloy was employed as the material for the valve body. These measures reduced the weight of the developed in-tank solenoid valve by 41% against the previous 35 MPa model.

For the hydrogen seal, a structure that helps to ensure that the seal material is not damaged at a pressure of 70 MPa was adopted, and a high-strength seal material was employed. These measures made it possible to realize a high level of pressure resistance in the hydrogen seal.

1. Introduction

As part of efforts to address global warming and energy issues, fuel cell vehicles (FCV), which employ hydrogen as fuel, are considered to possess outstanding potential as environmentally conscious vehicles. Mileage per filling is an important element of FCV performance. It is necessary to increase hydrogen storage capacity in order to increase mileage per filling.

The high-pressure hydrogen storage and supply system employed in Honda's 2009 model FCV (35 MPa system) used 35 MPa as the pressure for hydrogen storage in the high-pressure fuel tank[(1)]. In the 2016 model, the hydrogen storage pressure in the high-pressure hydrogen storage and supply system (70 MPa system) has been increased to 70 MPa as an effective means of increasing mileage per filling. However, in order to produce a 70 MPa in-tank solenoid valve to take over the function of the previous 35 MPa technology, it would be necessary to increase thickness to help ensure body strength, and this would result in increased size and weight. In addition, because a pressure of 70 MPa would damage the previous 35 MPa hydrogen seal configuration, it would not be possible to ensure seal performance. Given this, the research discussed in this paper set out to address the issues presented by increased hydrogen storage pressure and develop a valve weight reduction technology and a hydrogen seal technology, making it possible to increase mileage per filling.

2. Development Goals

The following two main aims were set for the development of the 70 MPa system:

(1) Reduction of weight of high pressure-resistant in-tank solenoid valve
(2) Increase in pressure resistance of hydrogen seal

* Automobile R&D Center

3. System Configuration

Figure 1 shows the high-pressure hydrogen tanks employed in the 2016 model FCV In order to reconcile the space necessary for fitting the hydrogen tanks with passenger space, two tanks of differing external diameters were employed. The tanks were positioned under the rear seat and behind the rear seat.

Figure 2 shows a transparent view of the 70 MPa system. After passing through the receptacle [Fig. 2(a)] and the check valve [Fig. 2(b)], the hydrogen supplied by the hydrogen station diverges, and passes through the in-tank solenoid valve [Fig. 2(c)] before filling the two high-pressure hydrogen tanks [Fig. 2(d)]. The hydrogen stored in high-pressure hydrogen tanks passes through the in-tank solenoid valve and its pressure is reduced by the regulator [Fig. 2(e)] before being supplied to the fuel cell stack.

Figure 3 shows the amount of hydrogen stored per exterior volume (the hydrogen volume storage density) for the 35 and 70 MPa high-pressure hydrogen tanks. Increasing the hydrogen storage pressure from 35 to 70 MPa increases the hydrogen volume storage density by 30%.

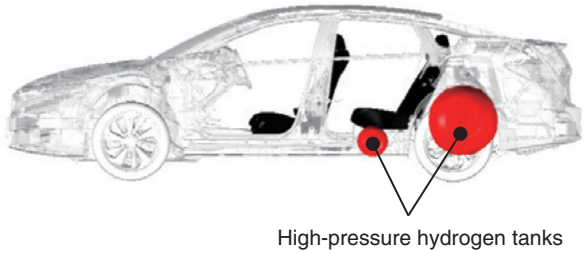


Fig. 1 High-pressure hydrogen tank installation layout

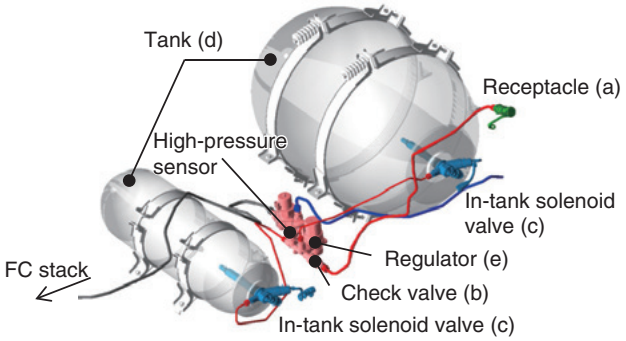


Fig. 2 Hydrogen storage and supply system for 2016 model year FCV

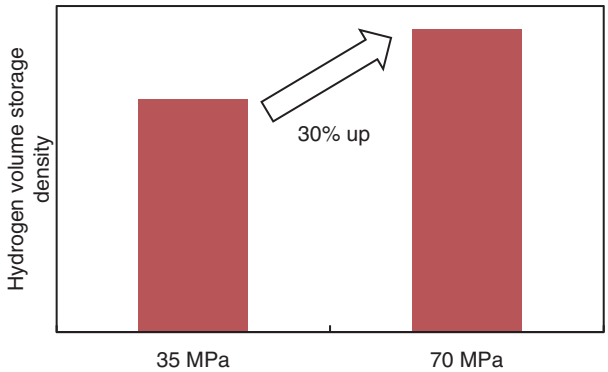


Fig. 3 Hydrogen volume storage density

4. Reduction of Weight of In-tank Solenoid Valve

4.1. Integration of Functions of Check Valve and Shut-off Valve

Figure 4 shows the configurations of the 35 and 70 MPa systems. In the 35 MPa system [Fig. 4(a)], separate gas flow channels were used for filling the tank with hydrogen and supplying hydrogen; this was appropriate for a configuration using a single high-pressure hydrogen tank. However, the development of a multiple-tank system based on the same concept [Fig. 4(b)] would necessitate the use of multiple gas flow channels for filling and supply, increasing the overall size of the system. For the 70 MPa system [Fig. 4(c)], the weight of the system was therefore reduced through the development of an in-tank solenoid valve that integrated the functions of the check valve and the shut-off valve and used a common flow channel for

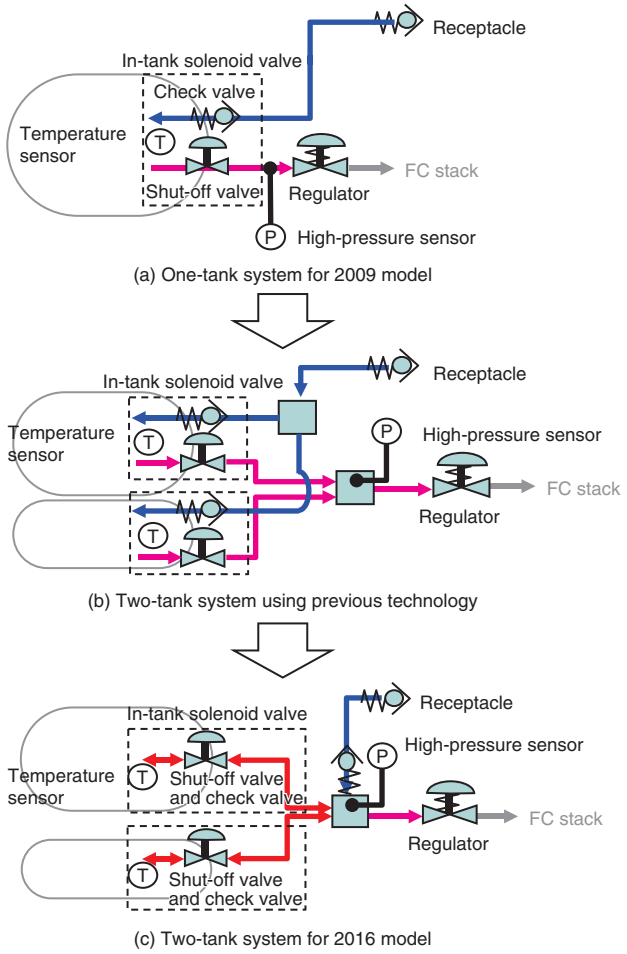


Fig. 4 Configuration of high-pressure hydrogen storage and supply system

filling and supply.

Figure 5 shows the structure of the in-tank solenoid valve and the hydrogen seal specifications for the 2009 model [Fig. 4(a)] and the 2016 model [Fig. 4(c)]. The use of a single gas flow channel for filling and supply in the 2016 model in-tank solenoid valve, which integrates the previous check valve and shut-off valve, reduced the number of parts by 6%.

4.2. Temperature Sensor Built Into Tank

The in-tank solenoid valve was provided with a temperature sensor to make it possible to monitor the temperature of the hydrogen in the high-pressure hydrogen tank during vehicle filling and operation. Figure 6 shows the layout and structure of the temperature sensors used in the 2009 and 2016 models. The thermistor elements used in the temperature sensor are transition metal oxides, mainly of Mn, Co, and Ni. When they come into contact with hydrogen, they are reduced and their properties change. Because of this, the thermistor elements employed in the temperature sensor used in the 2009 model were covered by a stainless steel (SUS) case and isolated from the hydrogen by O-ring seals (body and temperature sensor). However, in order to make the sensor compatible with a pressure of 70 MPa using a conventional O-ring seal configuration, it would be necessary to increase the thickness of the SUS case to help ensure strength, and this would increase the diameter of the opening of the in-tank solenoid valve in which the temperature sensor is fitted. In order to make the in-tank solenoid valve compatible with a pressure of 70 MPa at the same time as reducing its weight, the temperature sensor for the 2016 model was built into the tank.

The temperature sensor employed in the 2016 model does not employ an O-ring seal (body and temperature sensor) configuration of the type shown in Fig. 6 in order to isolate it from hydrogen. The temperature sensor is isolated from the hydrogen through the application of a hermetic seal technology, making it possible to build the sensor into the tank and realize a lower-diameter opening in the in-tank solenoid valve. A hermetic seal is realized by positioning glass and a lead wire in a metal tube; during slow cooling of the glass following melting, the difference between the rate of thermal expansion of the lead wire, glass, and metal tube induces compressive

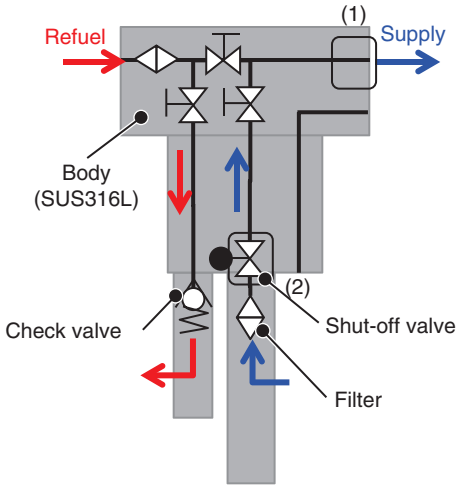
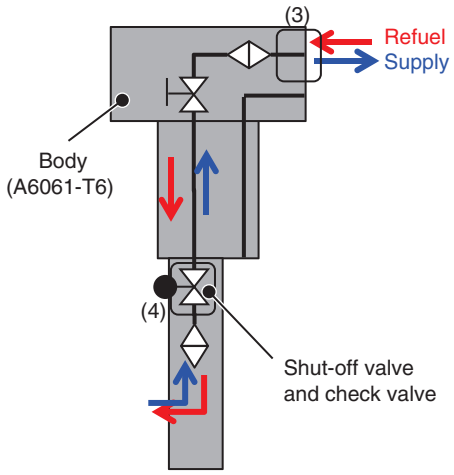
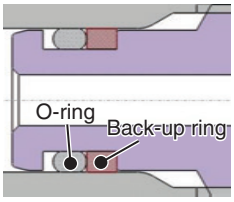
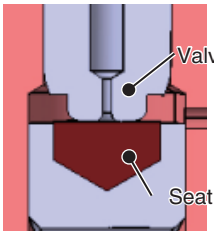
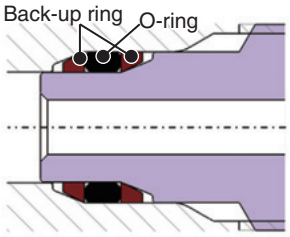
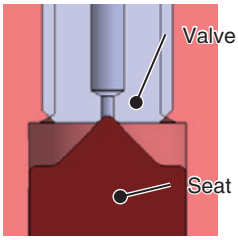
	2009 model	2016 model
Nominal working pressure	35 MPa	70 MPa
Weight	1.85 kg	1.09 kg
Structure		
Seal Structure	(1) O-ring seal 	(2) Valve seat 
	(3) O-ring seal 	(4) Valve seat 

Fig. 5 Structure and specifications of in-tank solenoid valve

stress in the glass, increasing the sticking force between the lead wire and the glass and forming a seal.

4.3. Use of Aluminum Alloy as Body Material

In order to reduce the weight of the in-tank solenoid valve, aluminum alloy was employed as the body material, replacing the SUS used in the 2009 model. Because non-ferrous materials such as aluminum alloys do not have fatigue limits, fatigue life design taking the degree and frequency of pressure fluctuations expected in an actual vehicle into consideration was applied in order to realize high pressure resistance in the body.

In addition, because aluminum alloys are more prone than SUS to corrosion in contact with alkaline chemicals, a non-electrolytic Ni plating treatment was applied to the surface of the alloy to help ensure chemical resistance. Global Technical Regulation (GTR) No. 13[(2)] specifies tests simulating a vehicle environment (Table 1) to verify the external appearance, airtightness, and pressure resistance of the valve following immersion in an aqueous sodium hydroxide solution and other solutions as tests for verification of the chemical resistance of in-tank solenoid valves. The results of these tests showed no corrosion on the valve body.

The application of the three measures discussed above (the integration of the functions of the check valve and the shut-off valve, the building of the temperature sensor into the tank, and the use of aluminum alloy as the sensor body material) reduced the weight of the sensor by 41% against the previous model while realizing compatibility with a pressure of 70 MPa.

Table 1 Tests stipulated by GTR No. 13

Component	Test items
Shut-off valve and check valve	Hydrostatic strength test Leak test Extreme temperature and pressure cycling test Salt corrosion resistance test Vehicle environment test Atmospheric exposure test Electrical test Vibration test Pre-cooled hydrogen exposure test
TPRD	Pressure cycling test Accelerated life test Temperature cycling test Salt corrosion resistance test Vehicle environment test Drop and vibration test Leak test Bench top activation test Flow rate test

5. 70 MPa Hydrogen Seal Technology

5.1. Development of O-ring Seal for 70 MPa Use

5.1.1. Concept of seal

When a seal is created using an O-ring at a joint (an O-ring seal), if the O-ring does not possess sufficient rigidity when subjected to pressure, the pressure can cause the O-ring to protrude into the gap between the body and the connector, damaging the O-ring and reducing the tightness

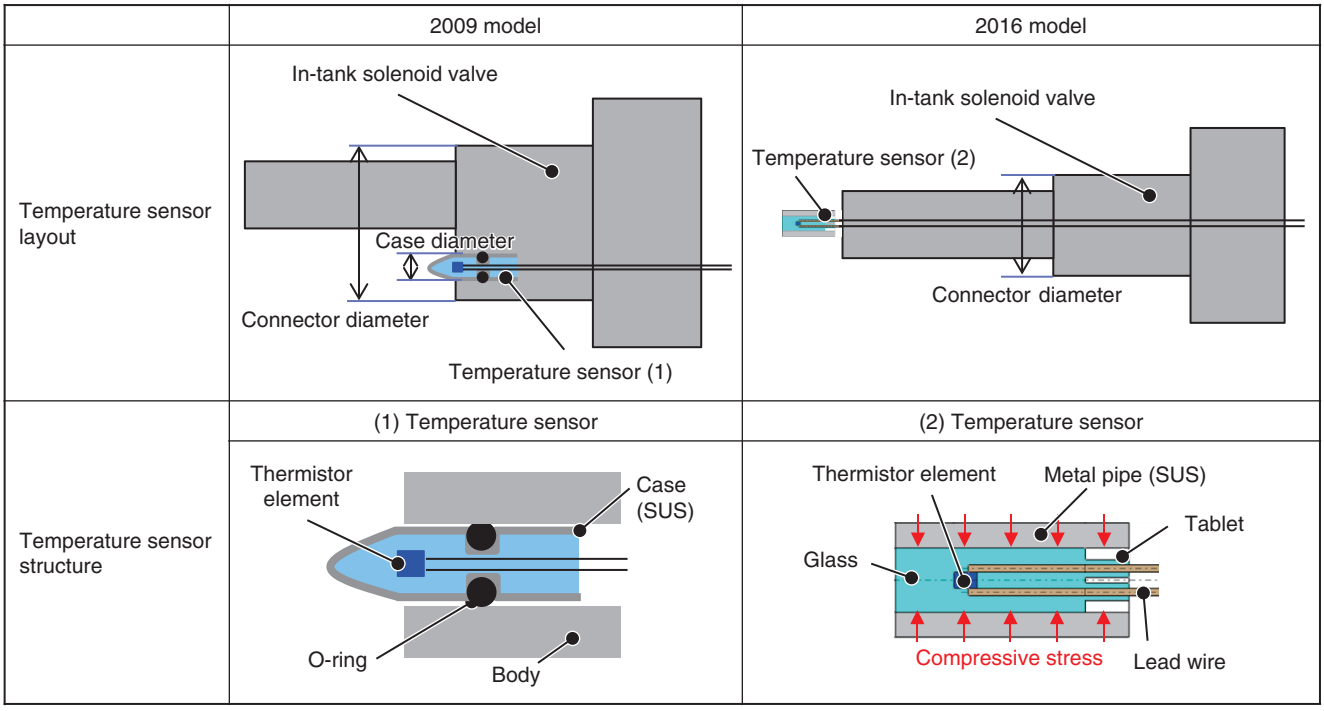


Fig. 6 Layout and structure of temperature sensor

of the seal (Fig. 7). It is essential, therefore, to design the O-ring to help ensure that it does not exceed the allowable gap (the run-over limit) at the pressure being used.

Figure 7 shows the 35 MPa O-ring seal structure employed in the 2009 model. In order to fill the gap into which the O-ring might protrude under pressure, a rubber back-up ring was positioned on the air side of the O-ring. This back-up ring filled the 0.09 mm gap. Figure 8 shows the allowable gap for the back-up ring under pressure (the run-over limit)[3]. The horizontal axis shows the diameter gap, and the vertical axis shows pressure. The red line shows the back-up ring run-over limit. When the red line is passed (upper right), the back-up ring protrudes into the gap. At a pressure of 35 MPa, the gap does not exceed the protrusion limit. At 70 MPa, however, the gap exceeds the run-over limit, and the back-up ring protrudes into the gap and is damaged. This indicated that the O-ring seal structure employed in the 2009 model was not suited to hydrogen storage at 70 MPa.

Research was therefore conducted in order to develop an O-ring seal structure for 70 MPa use.

5.1.2. Seal structure

Figure 9 shows the developed O-ring structure for use at 70 MPa. In the 2016 model, the material for the back-up ring was changed from rubber to resin to help ensure strength, and a tapered shape was employed to make it possible for the ring to deform under pressure and fill the gap[4].

Figure 10 shows CAE results showing the back-up ring deforming under pressure and filling the gap. From its initial state, the gap is gradually filled [in the order (a), (b), and (c) in Fig. 10] as pressure increases, until the gap becomes zero at the predetermined pressure in (c). Figure 11 shows the relationship between the O-ring run-over limit and the gap. The red line shows the O-ring run-over limit, and the blue line shows the relationship between the gap between the back-up ring (which is deformed by pressure) and the body

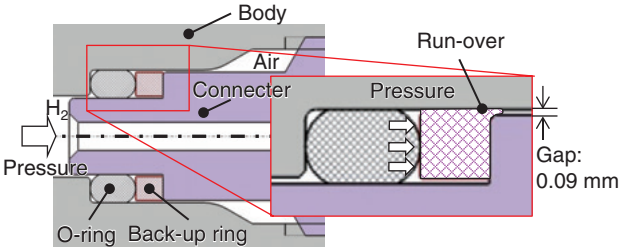


Fig. 7 O-ring seal structure for 35 MPa

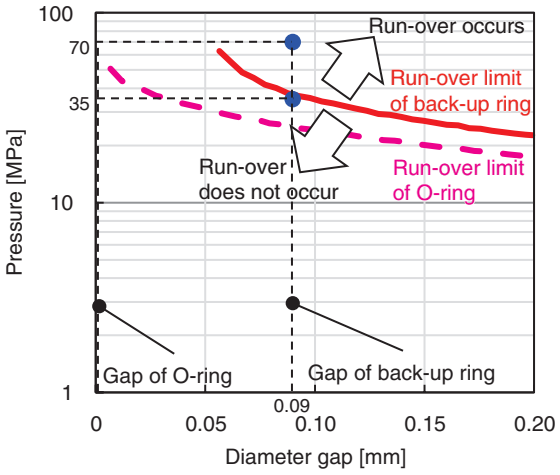


Fig. 8 Relationship of run-over and gap of back-up ring

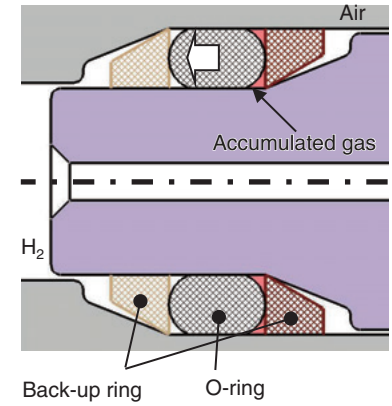


Fig. 9 O-ring seal structure for 70 MPa

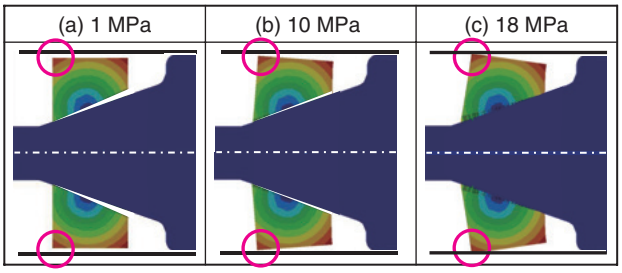


Fig. 10 CAE Results for run-over gap under pressure

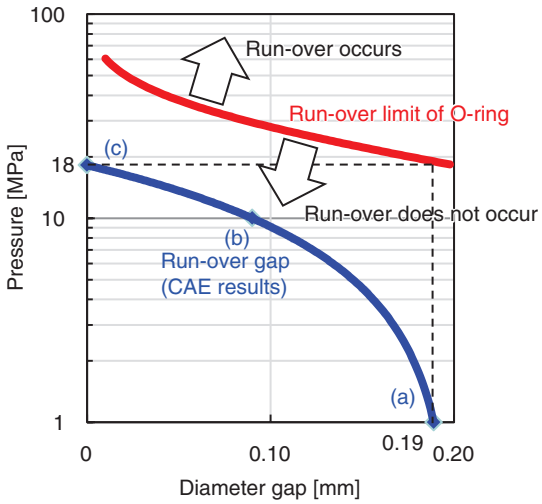


Fig. 11 Relationship between run-over and O-ring gap

and pressure. At a pressure of 18 MPa, the allowable gap for the O-ring is 0.19 mm and below. Because the gap at this time becomes zero (<0.19 mm) due to the deformation of the tapered back-up ring, the O-ring is not damaged by run-over into the gap. The gap calculated by CAE (the blue line) is lower than the run-over limit for the O-ring (the red line), and the O-ring is therefore undamaged.

Because the rubber O-ring is more hydrogen-permeable than the resin back-up ring, gas passes through the O-ring and accumulates between the O-ring and the back-up ring. When pressure decreases, this creates the possibility that the O-ring will be pushed to the hydrogen side and damaged by run-over into the gap. In addition, when the O-ring is exposed to a 70 MPa hydrogen environment for an extended period, the hydrogen penetrates inside the O-ring, resulting in swelling when pressure decreases. Taking this factor into consideration as well, a tapered back-up ring of the same type as used on the air side was also used on the hydrogen side of the O-ring.

5.2. Development of 70 MPa Valve Seat

5.2.1. Concept of seal

In addition to an O-ring seal, a valve seat structure of the type shown in Fig. 5 (2) and (4) is a necessary element of an in-tank solenoid valve that supplies and shuts off hydrogen. It is necessary for this valve seat to operate under conditions of pressure difference between upstream and downstream. In the 2009 model, the valve seat was manufactured from rubber, and a configuration in which a protruding valve pressed against a flat valve seat was adopted. However, if the 35 MPa valve seat employed in the 2009 model were operated under conditions of a 70 MPa pressure difference, the tensile stress generated in the rubber seat by the pressure would exceed the tensile strength of the seat material, with the result that the seat would enter the downstream flow channel and be damaged, and it would no longer be possible to ensure seal performance (Fig. 12).

A study of the seal material and seal structure to be employed for the 70 MPa valve seat was therefore conducted based on this consideration.

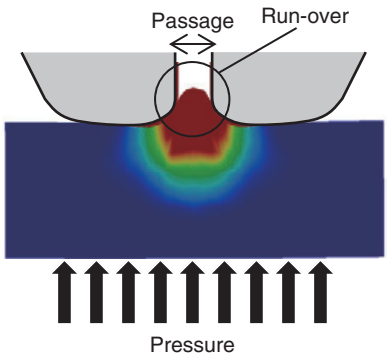


Fig. 12 Seat damage by run-over

5.2.2. Seal material

It was necessary to change the seal material to resin, which possesses a high level of mechanical strength, in order to adapt the seal to use at a hydrogen storage pressure of 70 MPa. However, when force increases, resins generally display elasticity, a property that causes them to rebound like a spring, and viscosity, a property that causes them to flow like a fluid. Because of this, when resins are soaked for long periods under high temperatures and high pressures, they undergo creep deformation and permanent deformation occurs. Figure 13 shows an image of creep deformation of a valve seat. When permanent deformation of the valve seat progresses, the deformation results in an increase in the contact area between the resin and the metal. As a result, the surface pressure of the valve seat declines, and leaks from the seal can occur.

Because of this, a polyamide-imide possessing a high level of mechanical strength and good creep resistance was selected as the resin material for the valve seat for use at a hydrogen storage pressure of 70 MPa. The use of the polyamide-imide material for the resin valve seat made it possible to realize durability in relation to operation under a pressure differential and heat aging. However, if the polyamide-imide material did not compress under comparatively high force, it would not be possible to fill the minute concavities and convexities on the surface of the valve, and seal performance could not be ensured. A study was therefore conducted to determine a structure making it possible to realize the valve seat surface pressure necessary for hydrogen seal performance.

5.2.3. Seal structure

Figure 14 shows the developed resin valve seat structure for use at 70 MPa.

Because force would act in the direction of alignment when the valve was closed and in contact with the valve seat in the case of a tapered resin seat structure, an appropriate relationship between the positions of the valve and the valve seat would be maintained. In addition, a tapered shape would disperse the load on the seat due to surface pressure, reducing stress on the seat.

Figure 15 shows the results of CAE analysis of the surface pressure generated on the valve seat under pressure. A 45° taper was selected for the resin valve seat structure because the stress generated in the valve seat when the

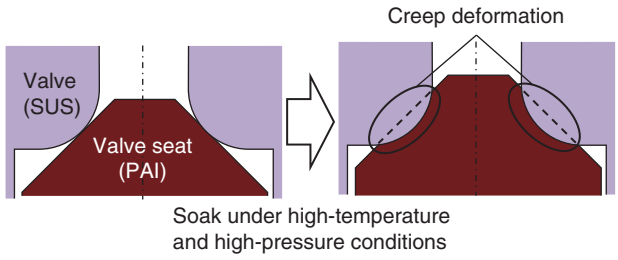


Fig. 13 Creep deformation of valve seat

pressure differential was high remained below the allowable surface pressure for the seat, and the necessary surface pressure for hydrogen seal performance was realized when the pressure differential was low.

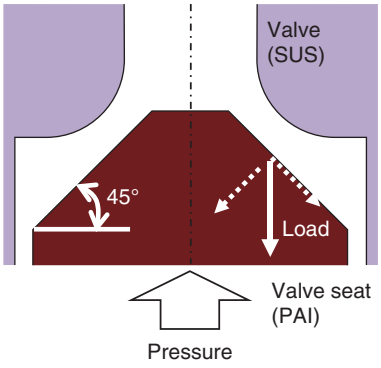


Fig. 14 Valve seat structure for 70 MPa

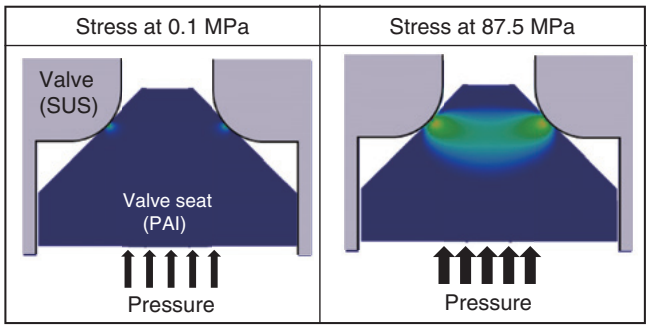


Fig. 15 CAE results for surface pressure

6. Conclusion

The weight of an in-tank solenoid valve was reduced and hydrogen seal performance was enhanced in order to realize the high pressure resistance necessary for a 70 MPa system.

(1) In order to reduce the weight of the in-tank solenoid valve, the check valve and the shut-off valve were integrated, and a shared gas flow channel inside the valve was employed for hydrogen filling and supply, reducing the number of parts by 6%. In addition, aluminum alloy was employed as the valve body material rather than SUS, and the temperature sensor was built into the tank, making it possible to reduce the diameter of the valve opening. Despite the fact that the developed valve was suitable for use at a pressure of 70 MPa, it was 41% lighter in weight than the previous model.

(2) For the hydrogen seal, a structure was adopted in which tapered back-up rings were positioned on the hydrogen and air sides of the O-ring in a 70 MPa O-ring seal structure. A resin valve seat structure with a 45º taper able to operate under a pressure differential of 70 MPa was also employed. These measures made it possible to realize a high level of pressure resistance in the hydrogen seal. As a result, it was possible to realize a 30% increase in the hydrogen volume storage density of the tanks against the 35 MPa model.

References

(1) Matsunaga, M., Fukushima, T., Ojima, K., Kimura, K., Ogawa, T.: Fuel Cell Powertrain for FCX Clarity, Honda R&D Technical Review, Vol. 21, No. 1, p.7-15
(2) Global technical regulation (GTR) No. 13: Global technical regulation on hydrogen and fuel cell vehicles, (2013)
(3) JFPS 1003 : yuatsu shirinda yo pakkin no shiyo sentei hoshin, (1999) (in Japanese)
(4) Japan Patent 3543617, (1999)

Author


Saneto ASANO


Koichi KATO


Hiroyasu OZAKI


Makoto WADA

Development of CCM Water Content Distribution Measurement System for Fuel Cell Stack

Masahiko SATO* Hiroto CHIBA* Masajiro INOUE*

ABSTRACT

A system was developed that uses impedance measurement of membrane electrode assemblies to quantify water content distribution in the polymer electrolyte membrane. That distribution influences fuel cell degradation factors including membrane damage in polymer electrolyte membranes and functional deterioration of electrode catalysts.

The impedance measurement sensors in this system are fabricated using flexible printed circuit technology to form thin shunt resistors for current measurement. This allows sensors to be produced in the same form as the membrane electrode assemblies.

With the development of these sensors, it became possible to measure the water content distribution in polymer electrolyte membranes in a fuel cell stack in real time while it is generating electricity. Those measurement results have been put to use in the 2016 model year for control of the water content of electrolyte membranes in actual fuel cell vehicles.

1. Introduction

The environmental effects of CO_2, NOx and other pollutants in automotive exhaust gases and the future depletion of fossil fuels make the development of clean, high-fuel-efficiency vehicles an urgent task. Seeking to realize a sustainable society based on energy circulation, Honda is engaged in research and development efforts in relation to fuel cell vehicles (FCV), which use hydrogen rather than fossil fuels, and fuel cell technologies[(1)].

Figure 1 shows an image of the structure of a fuel cell and its internal chemical reactions. The fuel cell (simply termed "cell" below) is made up of a membrane electrode assembly (MEA) and separators that form gas channels. A fuel cell stack (termed "stack" below) is created by layering multiple cells together.

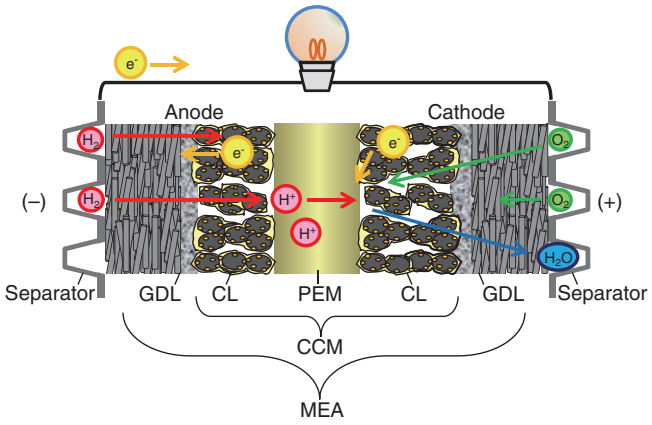


Fig. 1 Schematic image of fuel cell

The MEA is made up of a polymer electrolyte membrane (PEM), a catalyst layer (CL), and a gas diffusion layer (GDL). The PEM making up the CL are also called catalyst-coated membranes (CCM).

In the cell, a hydrogen oxidation reaction occurs at the anode electrode as shown by Eq. (1), and an oxygen reduction reaction occurs at the cathode electrode as shown by Eq. (2). These chemical reactions between hydrogen and oxygen produce electricity and water.

$$\text{Anode electrode (An):}\quad H_2 \rightarrow 2H^+ + 2e^- \qquad (1)$$

$$\text{Cathode electrode (Ca):}\quad 1/2O_2 + 2H^+ + 2e^- \rightarrow H_2O \qquad (2)$$

In addition to seeking increased compactness and weight reductions, and realizing high-efficiency-generation performance with higher output, it is also necessary for the stacks fitted in FCV to display durability in relation to the fluctuations in current load to which cells used in automotive environments are subjected. To help ensure durability in cells, it is necessary to maintain the surface area of the electrode catalysts, which contributes significantly to the output of the cell, and to maintain the thickness of the PEM, which functions both to separate the oxygen and the hydrogen that serves as fuel, and to electrically insulate the anode and the cathode.

The ability to maintain the surface area of the electrode

* Automobile R&D Center

catalysts and the thickness of the PEM is closely related to the in-plane water content of the CCM in the cell. Generally, when the water content is high, the electrode catalysts become coagulated due to dissolution, agglomeration, and redeposition, and the decline in the catalyst surface area accelerates. It has also been reported that when the water content is low, impurities and hydrogen peroxide accumulate in the PEM, promoting chemical degradation and reducing the thickness of the PEM[(2)].

In order to increase the durability of automotive fuel cells, it is therefore necessary to identify the in-plane distribution of the water content of the CCM and control it to within the proper range.

2. Purpose of Development

Obtaining a clear grasp of the CCM water content distribution is not only important in terms of enhancing performance and limiting degradation. It also has an important position in stack development because it provides useful information for setting operating conditions as well as for creating and analyzing durability modes.

The development of the stack for the 2016 model FCV therefore sought to realize increased stack durability through the development of multi-segment impedance sensors to identify the in-plane distribution of water content of the CCM in the cells and the calculation of the optimum in-plane water content distribution using simulations.

This paper will describe the development of the sensor that quantifies CCM water content distribution and the construction of a system employing that sensor.

3. Issues in Conventional Water Content Measurement

Methods for measuring CCM water content distribution include nuclear magnetic resonance (NMR) and neutron radiography[(3)-(6)]. Honda has long used neutron radiography as an analytical method for clarifying the condition of water accumulation in a fuel cell[(7)]. This measurement method involves irradiating the fuel cell with neutrons from a planar direction. The neutrons are converted into light by a scintillator, and the attenuation of the neutrons by the water is detected by a CCD camera as attenuation of that light. The light is converted into electrical signals and image processing is used to quantify the water content. As shown in Fig. 2, however, this method of measurement using neutron transmission includes the water accumulated in separator channels as well as water in the gas diffusion layer in that measurement. Therefore visual observation of CCM water content distribution was not readily achievable.

The fuel cell stack for the 2016 model is configured for power generating conditions that tend not to result in water accumulation in the separator channels.

There is an issue when the water content and distribution in a CCM with a thickness of several tens of micrometers are measured using neutron radiography, because the lower water content causes the errors in image processing to increase, thereby reducing accuracy.

Figure 3 shows the results of measurement by neutron radiography during low-load electric generation. The blue portions in Fig. 3(a) indicate the presence of larger amounts of water. Figure 3(b) shows a graph of quantified in-plane water distribution as obtained by calculating the thickness of water from the density of images produced by measurement. The vertical axis of the graph shows the water content as a percentage, where the maximum CCM water content is 100%.

The results from quantification of the water content distribution in the cell by neutron radiography show instances of water content exceeding 100%. This happens because there is water present in the channels and gas diffusion layer, and it indicates that the water content in a CCM with a thickness of several tens of micrometers, which is extremely thin, cannot readily be measured with accuracy. Given this background, there was a call for development of

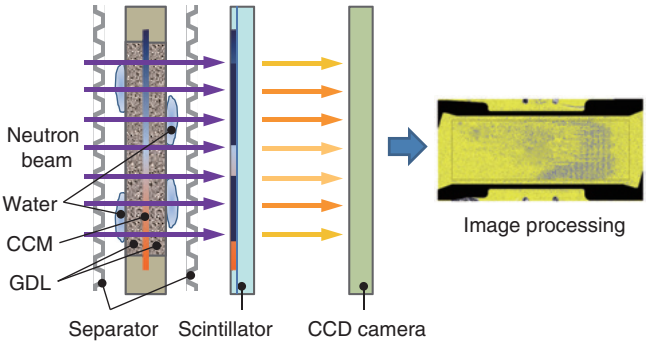


Fig. 2 Schematic image of detected water using Neutron RG

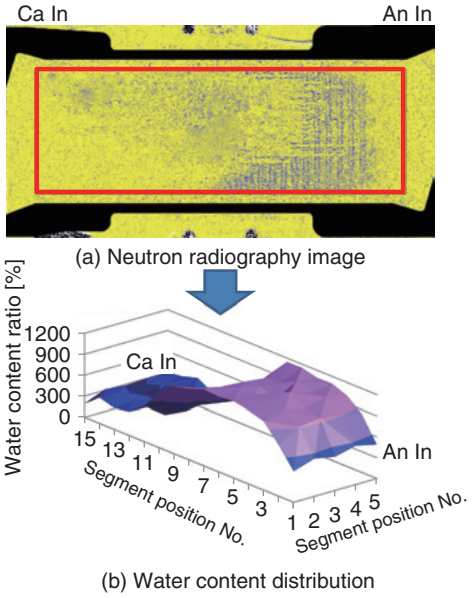


Fig. 3 Neutron Radiography and quantification result

a measurement system capable of accurately measuring the water content of the CCM alone.

4. Selection of Measurement Method

The construction of a system for controlling CCM water content in an actual vehicle, including during vehicle acceleration and deceleration, necessitated a method of instrumentation that would make it possible to obtain measurements without influencing the in-plane temperature distribution, humidity distribution, gas flow distribution, and other such factors during electric generation in a fuel cell system mounted in an actual vehicle. Selection of a measurement method involved examination from six perspectives in addition to the capability to measure CCM water content. The perspectives were production loading; ability to reproduce the humidity distribution, temperature distribution, and other such factors in the electric generation environment in the fuel cell; spatial resolution; time resolution; and capability to perform real-time measurement. The results of examination are shown in Table 1.

Measurement by X-ray and NMR offers high levels of resolution but requires bulky, elaborate equipment, which means that observations cannot readily be made with the system mounted in an actual vehicle. The impedance measurement method, on the other hand, works with a compact measurement system and by incorporating sensors in the system can perform measurement when mounted in an actual vehicle. This means it is capable of performing measurement in an actual electric generation environment.

Based on the results of the above examination, the impedance method was selected for mounting in actual vehicles to make measurements of changes in water content during actual vehicle operation, including acceleration and deceleration, and development carried out.

Table 1 Various measurement methods of water content inside fuel cell

	Imped-ance	Neutron RG	X-ray RG	X-ray CT	NMR
Indistinguishability for water content of PEM	○	△	△	○	○
Production loading	◎	×	×	×	×
Environment reproducibility	◎	△	×	×	×
Spatial resolution	△	○	◎	◎	○
Time resolution	◎	△	△	×	△
Real time measurement	○	△	△	×	×

◎ : Excellent, ○ : Good, △ : Fair, × : Poor

5. Development of the In-plane Water Content Distribution Measurement System

5.1. Fuel Cell Stack Construction

A distinctive feature of the fuel cell stack manufactured by Honda is the cell structure, adopted since the 2009 model FCX Clarity, which provides for cooling alternate cells[(1)]. This reduced by one-half the number of cooling layers previously needed in each fuel cell. The number of separators needed for two MEAs in this structure was reduced from four to three, aiding in making the stack more compact and achieving lighter weight.

The cell structure for cooling alternate cells is in a laminar arrangement with two MEAs and three separators making up a single unit. Figure 4(a) shows a cross-section of the conventional fuel cell structure, and Fig. 4(b) shows the structure with the developed sensors deployed.

5.2. Sensor Development

Figure 5 shows an overview of the sensor portion of the Water Content Distribution Measurement System developed to perform impedance measurement at the MEA surface in the fuel cell. The sensor was named the IDMS, from the initial letters of Impedance Distribution Measurement Sensor.

The sensor is intended for incorporation in a fuel cell stack and was therefore designed with the same shape as the MEA. As a result, it becomes possible to obtain CCM water content measurements without any need to prepare special separators or seals for the purpose because the sensor can be inserted into the fuel cell stack in place of one of the MEAs that make up the stack.

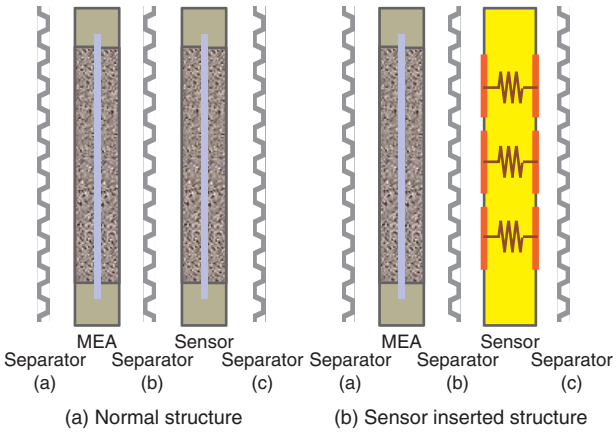


Fig. 4 Cell unit configuration of fuel cell stack

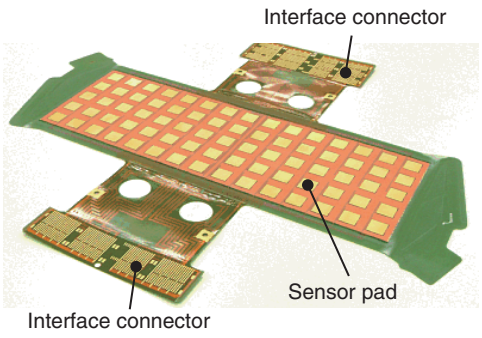


Fig. 5 Impedance distribution measurement sensor

The surface on either side of the sensor has multiple square sensor pads arranged on it. These sensor pads are used to make impedance measurements of the MEA. The sensor pads are designed so that each one handles the measurement of an equal area of the corresponding part of the power generating portion of the MEA that is on the other side of the separator placed between the sensor pad array and the MEA. The area of their contact with separator channels is also equal and their specifications limit measurement error factors resulting from differences in contact resistance.

Figure 6 shows the principle of measurement in this system.

The measurement of water content by means of impedance makes use of the change in ionic conductivity of the PEM due to differences in the water content of the CCM. Measurement superimposes an alternating current over the fuel cell stack as a whole. The membrane resistance is calculated from the current and voltage measurement figures from the sensors, and this is converted into membrane water content.

The superimposed alternating current is detected by shunt resistors inside the sensors. The IR drop that occurs (V_1) when a current flows through a resistor is measured and the current flowing in each sensor pad is derived from Eq. (3), below.

$$i_n = \frac{V_n}{R_n} \tag{3}$$

i_n : Terminal passing current [A]
V_n : Shunt resistor voltage [V]
R_n : Shunt resistance [Ω]

The voltage (V_2) is also measured between the sensor pad and separator (a).

The measured current and voltage value data is acquired with a PXIe-6358 (manufactured by National Instruments Corporation). Arithmetic processing is carried out by LabVIEW to calculate the impedance.

Impedance conversion is carried out in LabVIEW using Eq. (4), below.

$$Z_n = \frac{\Delta V_n}{\Delta R_n} \tag{4}$$

Z_n : Impedance [Ω]
ΔV_n : AC voltage modulation [V]
ΔI_n : AC current modulation [A]

The conversion of impedance measurement values into membrane water content is described in section 5.4.

5.3. Examination of Specifications

During sensor development, the focus was placed on resolution and measurement accuracy of in-plane CCM water content distribution. The design was examined in relation to the following headings.

5.3.1. Number of in-plane segments

The sensors are manufactured using flexible printed circuit (FPC) technology that allows complex wiring to be made thin. The flexible printed circuits have an adhesive layer formed on an insulating film that is from 12 to 50 μm thick. On top of that is affixed a conductive foil that is about 12 to 50 μm thick. Compared to the usual rigid substrate made of glass epoxy, this is thinner, more workable, and can be fabricated in more complex shapes.

Wiring inside the sensors is structured from five layers of wiring sheets that are formed by etching. Connections between layers are made through holes created by laser and plated inside to form conductive through-holes. Electric wiring in this three-dimensional structure is used to connect each sensor pad to an interface connector that connects to the measuring instrument (Fig. 7). Wiring with the same length and same resistance is used for the signal lines from each sensor pad in order to enhance measurement accuracy.

The upper limit and lower limit for the number of sensor pad segments needed in order to measure the water content distribution were examined from the perspectives of the feasibility of manufacturing the sensor and the accuracy of measurements obtained by the sensor.

Figure 8 shows the relationship between the current flowing in each sensor pad and the number of sensor pad segments, on the assumption that current flows equally in-

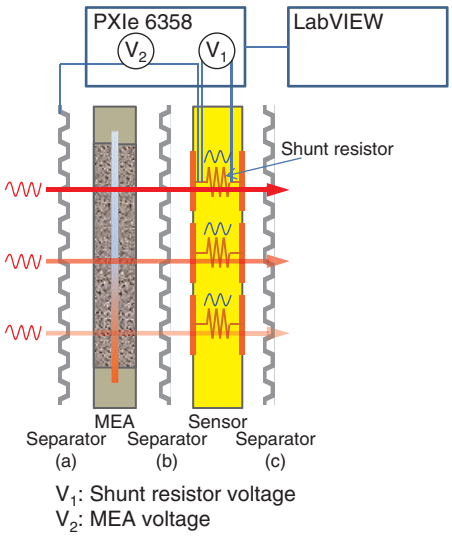


Fig. 6 Principle of CCM resistance measurement

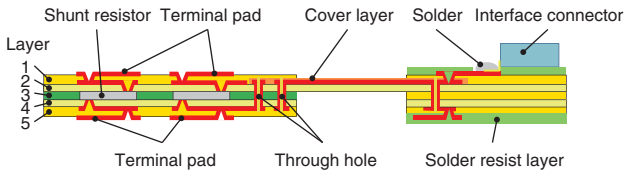


Fig. 7 Schematic image of FPC

plane within the electricity-generating electrodes of the fuel cell stack.

With the same amount of generated electric current in the stack, a larger number of sensor pad segments or partitions means that a smaller current flows through each pad [Fig. 9(a)]. Conversely, when there is a smaller number of sensor pad segments, the current flowing through each one will be larger [Fig. 9(b)].

When the interior wiring layers of the sensor are designed to ordinary parameters for conductor thickness, wiring width, and plating thickness, the upper limit for the current that can flow through each sensor pad is estimated to be about 7 A. Considering the variation in current density distribution when the stack is generating at maximum power, a safety factor of about 20% is added to the current transmitted through each sensor pad. The lower limit for the number of sensor pad segments is then about 60 segments.

The upper limit for the number of sensor pad segments greatly influences the wiring layout of the flexible printed circuit described earlier. Increasing the number of sensor pads complicates the wiring layout leading from the sensor pads at the center portion of the cell surface to the interface connector, so that the number of substrate layers needs to be increased. Considering that sensors are fabricated in the shape of the MEA, an increase in the number of substrate layers and subsequent thickness of the sensors makes the mounting layout infeasible. The upper limit on the number of sensor pad segments will therefore generally be about 100 segments.

The results from the above examination of the number of sensor pad segments together with the aspect ratio of the electricity-generating portions of the MEA electrodes led to a sensor pad layout of 75 segments in five longitudinal columns and 15 lateral rows.

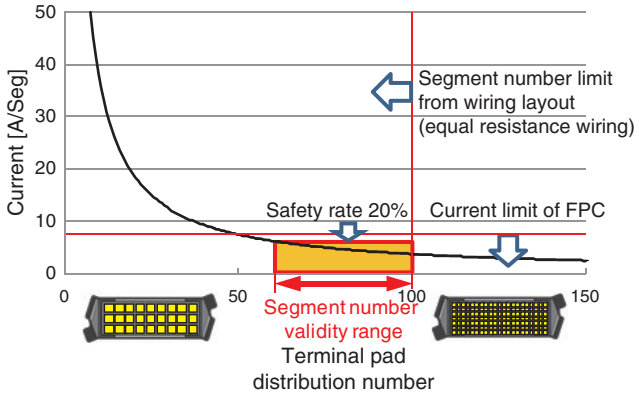
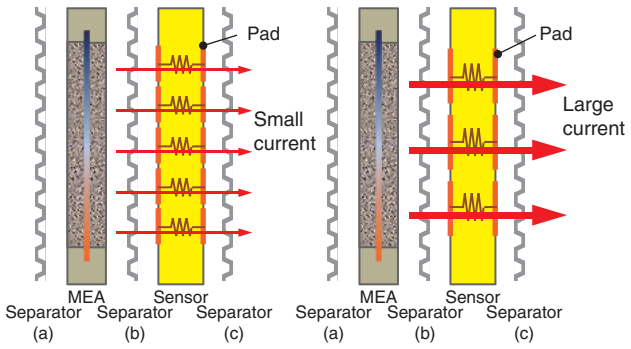


Fig. 8 Through current value of each sensor pad at various distribution numbers



(a) Large number of partitions (b) Small number of partitions

Fig. 9 Image of electric current quantity

5.3.2. Sensor pad pitch

The electric current trapping rate was taken as the index for sensor measurement accuracy. The sensor pad size and shunt resistor magnitude were decided accordingly.

The electric current trapping rate indicates the percentage of an electric current that can be acquired by the corresponding sensor pad located opposite to the terminal outputting the current that will pass through the corresponding portion of the MEA and separator.

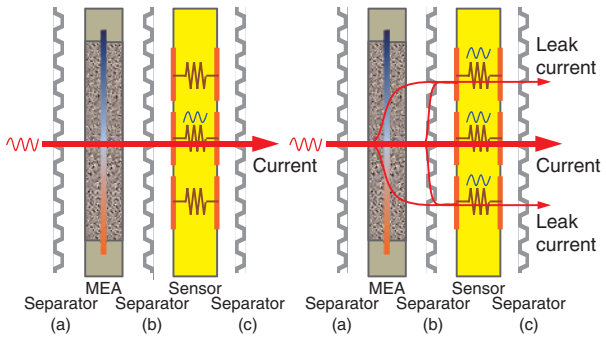
A conceptual image of the electric current trapping rate is shown in Figs. 10 and 11.

In a sensor with a high electric current trapping rate, the sensor pad-detected current in the current-impressing part is larger [Fig. 10(a) and Fig. 11(a)]. In a sensor with a lower trapping rate, however, the current values will be higher in parts of the sensor pad other than the current-impressing part, so that the sensor pad-detected current in the current-impressing part will be lower [Fig. 10(b) and Fig. 11(b)].

This indicates that a leak current flowing in a planar direction in a separator, a gas diffusion layer, or other such plane object is lowering the measurement accuracy.

The electric current trapping rate can also vary with the sensor pad arrangement and shunt resistor value. For this development, the pitch between sensor pads and the shunt resistor values were treated as parameters in working from the model in Fig. 12 to calculate the leak current from the contact resistance and specific resistance of each component. The electric current trapping rate of the sensor was then derived.

Figure 13 shows the results from calculation of

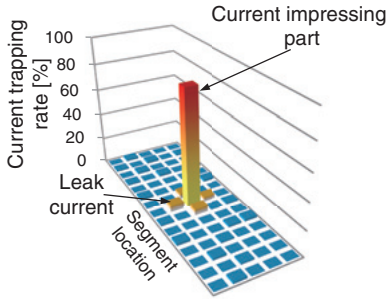


(a) High current trapping rate (b) Low current trapping rate

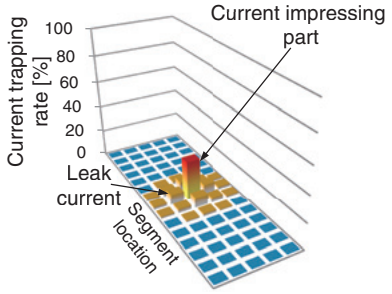
Fig. 10 Image of current trapping rate

variations in electric current trapping rate according to the pitch between sensor pads and the different ratings of shunt resistors used. Increasing the pitch between sensor pads can raise the electric current trapping rate. This happens because of the increase in distance between the separators that carry current to the sensor pad, thus increasing the resistance so that the flow of the leak current is impeded (Figs. 13 and 14). However, increasing the pitch between sensor pads means that the sensor pad size is reduced. This reduces the contact area with separators, reducing the current path, so that the distribution can no longer be measured accurately.

The total sensor pad area needed to assure a necessary minimum current path was determined from the amount of current flowing when the stack is generating maximum power and from the contact resistance between sensors and separators. The size of each sensor pad was calculated from the necessary minimum total sensor pad area, and pitch between pads was set at 8 mm.

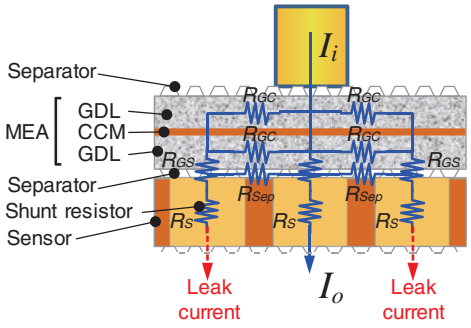


(a) High current trapping rate



(b) Low current trapping rate

Fig. 11 Measuring result of current trapping rate (Image)



$$\text{Current trapping rate} = \frac{I_o}{I_i} \times 100\ (\%)$$

I_i : Input current
I_o : Output current
R_{GC} : GDL/CAT resistance
R_{GS} : GDL-separator contact resistance
R_{Sep} : Separator resistance
R_S : Shunt resistor

Fig. 12 Model of current trapping rate

5.3.3. Shunt resistor rating

Manganin (Cu-Mn-Ni alloy) was used for the resistive element in the shunt resistor. This is a material that experiences only slight change in resistance with changes in temperature. The wiring used for current flow in the sensor was completely isolated from the wiring used for voltage measurement, and the specifications were arranged so that the influence of wiring resistance could be excluded from measurement.

Reducing the shunt resistance value can raise the electric current trapping rate. This is because the ratio of the resistance in the stacking direction to the resistance in the separator surface direction becomes smaller, and the flow of

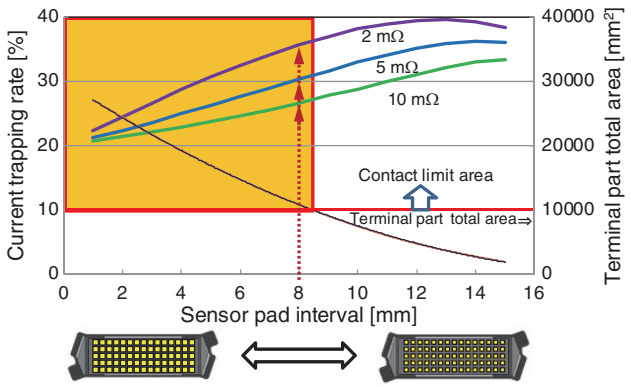
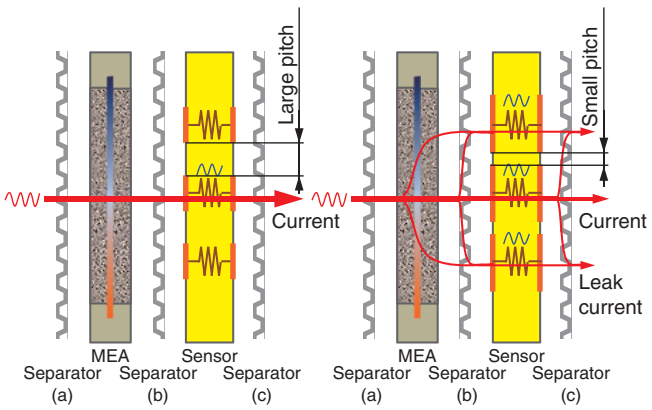


Fig. 13 Electric current trapping rated at various sensor pad intervals (75 segments)



(a) Large partition pitch (b) Small partition pitch

Fig. 14 Image of leak current at various segment pitches

current in the stacking direction is less impeded (Fig. 15).

However, although reducing the resistance value can raise the electric current trapping rate, this also means that requirements for the dimensional accuracy of the shunt resistors become more demanding.

The resistance of 5 mΩ was adopted. This was a figure that allowed confirmation of the forming accuracy of shunt resistors manufactured by etching while also ultimately achieving the target of 3% or less variation between the shunt resistors arranged in each sensor pad.

Given the above examination of the number of sensor pad segments, the sensor pad arrangement and area, the shunt resistance values, and the flexible printed circuit production technology, it was ultimately decided to manufacture 5 mΩ shunt resistors to be positioned at intervals of 8 mm.

5.4. Verification of Sensor Function

5.4.1. Evaluation fuel cell

Verification of IDMS function was carried out as shown in Fig. 16(a), by deploying the sensors in a full stack mounted in a 2016 model vehicle. The object of measurement by the sensors was the MEA of the fuel cell at the end of the stack. The sensors were installed in a position where they were adjacent to the end fuel cell, and measurements were made. The generation equipment used was 150 kW-class generation equipment employed for stand-alone evaluation testing of a full stack.

Sensor measurement accuracy was confirmed using a 2016 model mini-cell [Fig. 16(b)], which was being used to acquire MEA water content characteristics in a humid environment. The mini-cell has an electrode surface area of 12.5 cm^2 and is designed to have uniform in-plane temperature distribution, gas flow distribution, and humidity distribution, with the same channel geometry in the separators as those that make up the 2016 model stack. Cell temperature is controlled by an externally affixed heater. It was assembled to provide the same electrode contact pressure as the 2016 model.

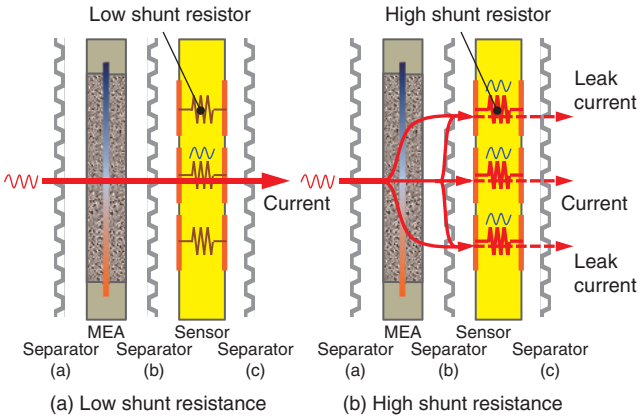


Fig. 15 Image of leak current at different shunt resistance

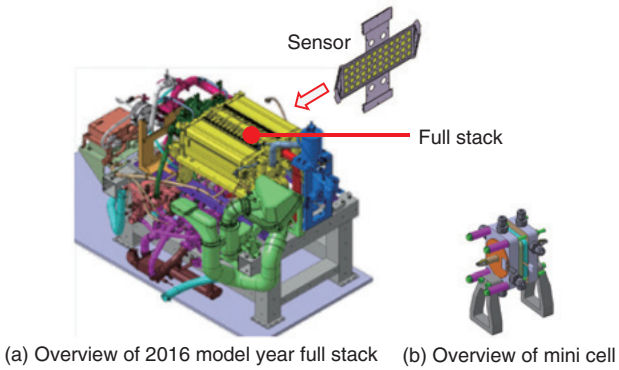


Fig. 16 Schematic image of full stack incorporating IDMS and mini cell for correlation test

5.4.2. Confirmation of resistance measurement results

In order to confirm the resistance measurement values obtained with the IDMS, resistance values were acquired in a temperature environment of 70°C with the humidity environment varied. The results were compared with the measurement results obtained under the same conditions from the mini-cell.

Variances in measurement accuracy due to differences in sensor electrode position were confirmed by taking the impedance measurement values obtained at 25 locations such as gas ports and the central portion on the IDMS 75-sensor pad array, where impedance measurement values tend to differ even under the same conditions, and comparing them with the impedance measurement values in the mini-cell (electrode surface area of 12.5 cm^2). The same gases as during electric generation were used for input, with hydrogen gas on the anode side and air on the cathode side. The time maintained at each humidity level was set at two hours, a period during which the relative humidity would become stable throughout the entire MEA. The relative humidity was changed in increments of 10% from lower to higher humidity. Figure 17 shows the results for impedance measurement at each humidity level. When IDMS impedance values were compared with the mini-

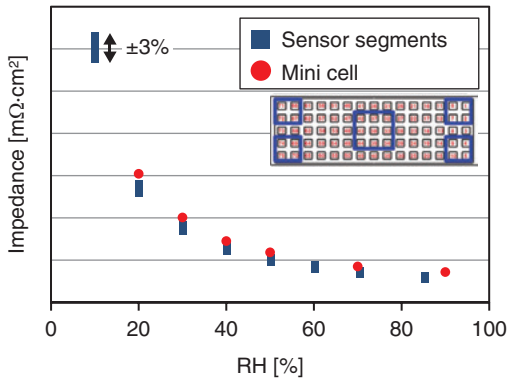


Fig. 17 Impedance CCM measurement value at various RH levels

cell values, it was found that values were uniformly lower by 10% or so across the full range of humidity. This is likely to be because contact resistance within the cell has increased because the mini-cell has fewer cell layers and the fastening load therefore tends to decrease. Differences of approximately ±3% also exist between the segments, and this is thought to occur due to in-plane surface pressure distribution in the full stack as well as in-plane distribution of the humidity environment at the surface.

In order to correct for the influence of these surface pressure and humidity environment distribution factors, the relationship between humidity and impedance was obtained for each segment. This enabled accurate calculation of the water content, which will be described later.

5.4.3. Conversion of measured resistance values to water content

Figure 18 shows the sequence followed in converting the resistance values obtained at each electrode to water content.

First, the distribution of resistance values obtained by impedance measurement is converted to the humidity environment indicated by those resistance values [Fig. 18(a)]. The standard curve obtained from sensor measurements of resistance against changes in humidity was used in making this conversion. Next, the humidity environment was converted into the MEA water content [Fig. 18(b)]. The conversion to water content was carried out using the humidity and MEA water content standard curve.

5.4.4. Measurement of sensor resistance values against changes in humidity

With the IDMS installed on the full stack, the humidity of the input gas was varied and the change in MEA resistance in each segment was measured at the temperature for the electricity generation condition that is to be measured. Figure 19 shows the standard curve obtained (the same 25 segments as in Fig. 17). This standard curve was used, as shown in Fig. 18(a), to convert the resistance value of each segment into the humidity that indicates that resistance value.

5.4.5. Measurement of MEA mass against changing environmental humidity

The CCM water content at the humidity levels described above was measured using a water sorption/desorption analyzer (the IGA-SORP manufactured by Hiden Analytical).

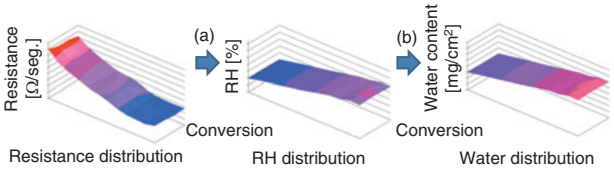


Fig. 18 Conversion of resistance to water distribution

The measurement procedure is shown in Fig. 20.

CCM pieces 20 × 20 mm in size (4 cm^2) were used as samples. The samples were placed in a stainless steel mesh sample holder [(1) in the figure] and inserted in the IGA-SORP (constant temperature) [(2) in the figure) and dried under a flow of nitrogen gas [(3) in the figure] for two hours. After measuring the mass when the sample was dry, continuous measurements of mass were made under controlled temperature and humidity [(4) in the figure]. The CCM mass obtained after holding for 30 minutes at each humidity condition was used to calculate the water content under each humidity environment. Figure 21 shows a graph of the water content calculated from each humidity level

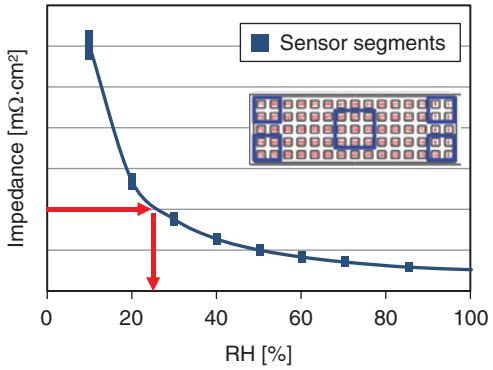


Fig. 19 Impedance CCM measurement value at various RH levels

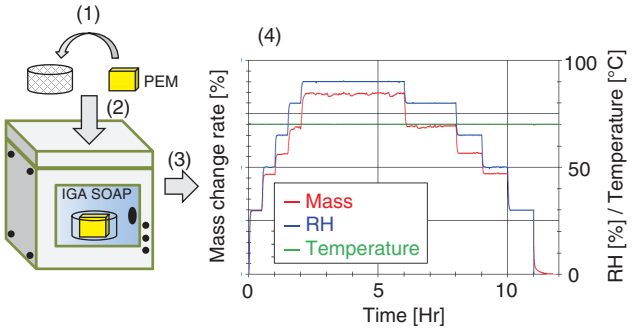


Fig. 20 Test procedure of adsorption and desorption measurement

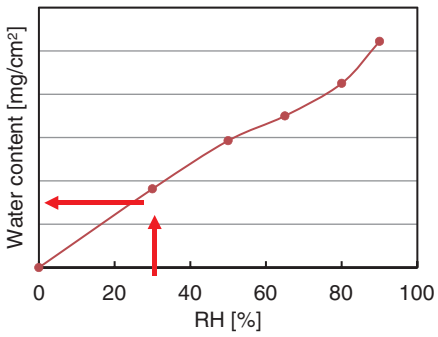


Fig. 21 Water content measurement of CCM at various RH levels

and CCM mass. The graph in Fig. 21 was used to convert the humidity distribution into water content distribution [Fig. 18(b)], yielding the MEA water content distribution during electric generation.

6. Results from Application to Fuel Cell Stacks

6.1. Real-Time Measurement of Water Content

Figure 22 shows the changes in water content and load during electric generation in the stack evaluation operating mode used during development. The sensors are incorporated into the fuel cell stack of a system mounted in an actual vehicle. The CCM water content shows the change over time at the anode inlet side, the central portion, and the cathode inlet side. Under high load, the water content reaches the highest level in the central portion. Meanwhile, it also became clear that the water content on the anode input side shows only slight change.

This measurement system is capable of making impedance measurements in each area at 0.5-second intervals. The time resolution is finer than with neutron radiography, which involves individual 8-second picture acquisition times. As a result, changes in CCM water content during acceleration and deceleration can now be confirmed in detail. The spatial resolution is also sufficient with 75 segments, and the measurements are accurate enough for discussion of upper and lower limits of in-plane water content distribution in the CCM. With development of the IDMS, therefore, CCM water content in an operating fuel cell stack can now be measured in real time and in detail.

6.2. Measurement of Water Content Distribution

The results from IDMS measurement of water content distribution during electric generation under low load [Fig. 23(b)] were compared with those from quantification by neutron radiography [Fig. 23(a)]. Neutron radiography was only capable of measurement that included water in the separator channels and gas diffusion layer. With measurement using IDMS, however, the distribution of CCM water content could be measured.

The measurement of CCM water content distribution using IDMS has enabled prediction and actual verification of acceleration modes of mechanical degradation caused by repeated contraction of the CCM when dry and expansion when moist[8] and enhancement of the predictive accuracy of simulation[9]. Measurement of CCM water content in a system mounted in an actual vehicle also resulted in the creation of water content control during system operation[10], which was applied in actual vehicles.

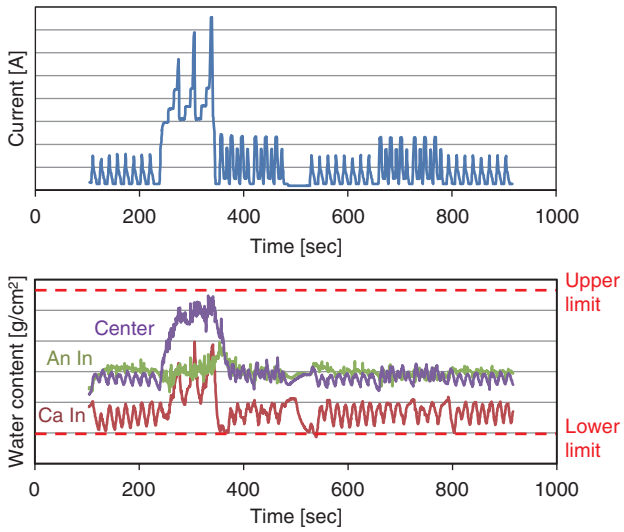


Fig. 22 Change of water content during generation

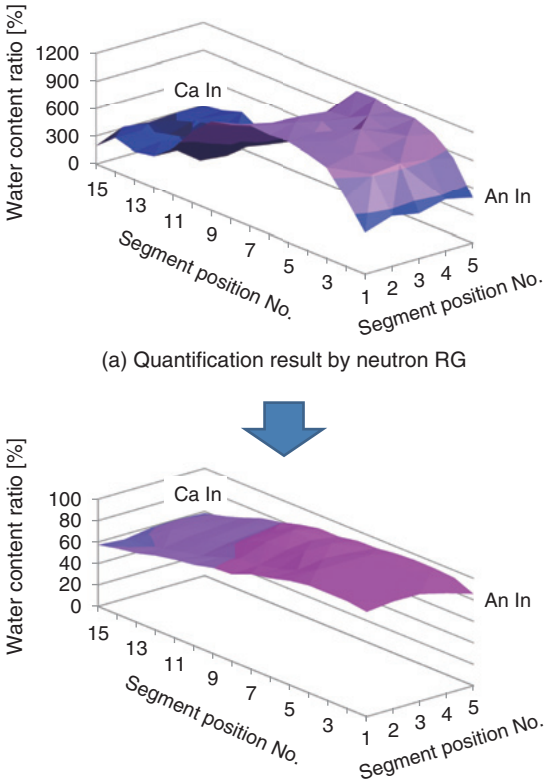


Fig. 23 CCM water content distribution at low generation condition

7. Conclusion

(1) An impedance measurement sensor with MEA shape enabling incorporation in systems mounted in actual vehicles was developed. The sensor was made capable of measuring CCM water content distribution in real time in an actual vehicle operating environment.

(2) Examination of the number of sensor pads and their placement interval enabled accurate, high-resolution measurement of CCM water content distribution in a fuel cell stack.

References

(1) Saito, N., Kikuchi, H., Nakao, Y.: New Fuel Cell Stack for FCX Clarity, Honda R&D Technical Review, Vol. 21, No. 1, p. 16-23

(2) Nishikawa, H.: Nenryodenchi no Gijutsu -Kotaikoubunshigata no Kadai to Taisaku-, Tokyo Denki University Press, p. 84-113, (2010) (in Japanese)

(3) Wang, H., Yuan, X-Z., Li, H.: PEM FUEL CELL DIAGNOSTIC TOOLS, CRC Press, 260p., (2012)

(4) Hickner, M. A., Siegel, N. P., Chen, K. S., Hussey, D. S., Jacobson, D. L.: Observations of Transient Flooding in a Proton Exchange Membrane Fuel Cell Using Time-Resolved Neutron Radiography, Journal of The Electrochemical Society, Vol. 157, Issue 1, B32-B38, (2010)

(5) Eller, J., Rosén, T., Marone, F., Stampanoni, M., Wokaun, A., Büchi, F. N.: Progress in In Situ X-Ray Tomographic Microscopy of Liquid Water in Gas Diffusion Layers of PEFC, Journal of The Electrochemical Society, 158 (8), B963-B970, (2011)

(6) Teranishi, K., Tsushima, S., Hirai, S.: Analysis of Water Transport in PEFCs by Magnetic Resonance Imaging Measurement, Journal of The Electrochemical Society, 153 (4), A664-A668, (2006)

(7) Chiba, H., Iwasawa, C.: Optimization of Fuel Cell Generation Environment by Water Observation using Neutron Radiography, Honda R&D Technical Review, Vol. 25, No. 1, p. 122-131

(8) Sugishita, M., Ohmori, S.: Life Prediction Technology of Fuel Cell Polymer Electrolyte Membrane under Mechanical Degradation, Honda R&D Technical Review, Vol. 28, No. 1, p. 59-67

(9) Nagumo, K., Inoue, M.: Numerical Prediction of Water Content Distribution of Catalyst Coated Membrane of Fuel Cell Stack using Simulation, Honda R&D Technical Review, Vol. 28, No. 1, p. 26-33

(10) Iwanari, T., Miyajima, K., Furusawa, K., Inoue, M.: Real-time Measurement of Water Content of CCM in On-board Fuel Cell Stack System, Honda R&D Technical Review, Vol. 28, No. 1, p. 34-40

Author



Masahiko SATO



Hiroto CHIBA



Masajiro INOUE

Numerical Prediction of Water Content Distribution of Catalyst Coated Membrane of Fuel Cell Stack using Simulation

Kenji NAGUMO* Masajiro INOUE*

ABSTRACT

The distribution of the water content of catalyst-coated membranes (CCM) is a factor that affects the durability of polymer electrolyte fuel cells. Because the in-plane distribution of the water content of the CCM in fuel cell stacks changes with changes in fuel cell operating conditions such as the coolant inlet temperature and the cathode electrode gas inlet flow rate, the setting of appropriate operating conditions is important in helping to ensure fuel cell durability.

The research discussed in this paper therefore developed a simulation making it possible to accurately predict operating conditions in a short period, and studied the effect of operating conditions on the in-plane distribution of the water content of the CCM. The results of this study indicated that the in-plane distribution of water content could be controlled via three operating condition parameters: the coolant inlet temperature, the cathode gas inlet pressure, and the cathode gas inlet flow rate.

Using the developed simulation and the results of the study of the effect of operating conditions on the in-plane distribution of the water content of the CCM made it possible to maintain the in-plane distribution within the upper and lower limit values and reduced variation in the distribution. It was also possible to apply accurate operating conditions in the 2016 FCV fuel cell stack in a period of several days.

1. Introduction

The environmental effects of CO_2, NOx and other pollutants in automotive exhaust gases and the future depletion of fossil fuels make the development of clean, high-fuel-efficiency vehicles an urgent task. Seeking to realize a sustainable society based on energy circulation, Honda is engaged in research and development efforts in relation to fuel cell vehicles (FCV), which use hydrogen rather than fossil fuels, and fuel cell technologies[1].

Figure 1 shows an image of the structure of a fuel cell and its internal chemical reactions. The fuel cell (simply termed "cell" below) is made up of a membrane electrode assembly (MEA) and separators that form gas channels. A fuel cell stack (termed "stack" below) is created by layering multiple cells together.

The MEA is made up of a polymer electrolyte membrane (PEM), a catalyst layer (CL), and a gas diffusion layer (GDL). The PEM making up the CL are also called catalyst-coated membranes (CCM).

In the cell, a hydrogen oxidation reaction occurs at the anode electrode as shown by Eq. (1), and an oxygen reduction reaction occurs at the cathode electrode as shown by Eq. (2). These chemical reactions between hydrogen and oxygen produce electricity and water.

$$\text{Anode electrode (An): } H_2 \rightarrow 2H^+ + 2e^- \quad (1)$$

$$\text{Cathode electrode (Ca): } 1/2O_2 + 2H^+ + 2e^- \rightarrow H_2O \quad (2)$$

In addition to seeking increased compactness and weight reductions, and realizing high-efficiency-generation performance with higher output, it is also necessary for the stacks fitted in FCV to display durability in relation

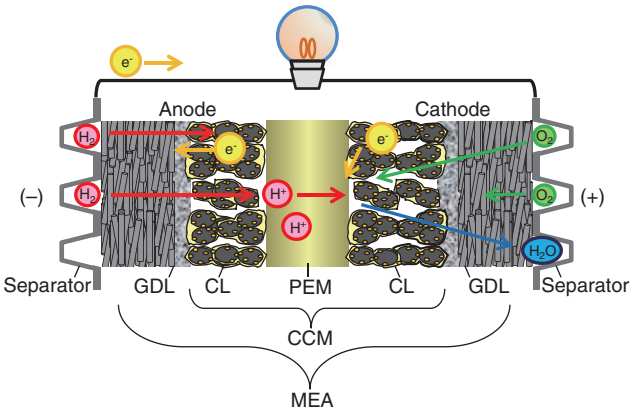


Fig. 1 Schematic image of fuel cell

* Automobile R&D Center

to the fluctuations in current load to which cells used in automotive environments are subjected. To help ensure durability in cells, it is necessary to maintain the surface area of the electrode catalysts, which contributes significantly to the output of the cell, and to maintain the thickness of the PEM, which functions both to separate the oxygen and the hydrogen that serves as fuel, and to electrically insulate the anode and the cathode.

The ability to maintain the surface area of the electrode catalysts and the thickness of the PEM is closely related to the in-plane water content of the CCM in the cell. Generally, when the water content is high, the electrode catalysts become coagulated due to dissolution, agglomeration, and redeposition, and the decline in the catalyst surface area accelerates. It has also been reported that when the water content is low, impurities and hydrogen peroxide accumulate in the PEM, promoting chemical degradation and reducing the thickness of the PEM[(2)].

In order to increase the durability of automotive fuel cells, it is therefore necessary to identify the in-plane distribution of the water content of the CCM and control it to within the proper range.

2. Development Goals

The development of the stack for the 2016 model FCV therefore sought to realize increased stack durability through the development of multi-segment impedance sensors[(3)] to identify the in-plane distribution of water content of the CCM in the cells and the calculation of the optimum in-plane water content distribution using simulations.

This paper will discuss prediction of the in-plane distribution of the water content of CCM in fuel cell stacks through the use of simulations.

As indicated above, the in-plane distribution of the water content of the CCM affects the durability of the cells, and the in-plane distribution of water content is itself significantly affected by the operating conditions of the cells. This means that it is important to set appropriate operating conditions in order to realize increased cell durability.

Six operating condition parameters are relevant in this process: the coolant inlet temperature and flow rate, and the inlet flow rate and pressure of the An and Ca gases.

Up to the present, the in-plane water content of the CCM in the cells has been measured using neutron radiography or weight measurement methods. However, in addition to the fact that a large number of combinations of parameters are possible, measurements also take time[(3), (4)], and it has been challenging to determine parameters with an adequate level of accuracy in a short period.

In order to address this issue, the research discussed in this paper first developed a simulation that would produce results displaying a good level of accuracy in a short period, and used the simulation in conducting advance studies of the effect of the various operating condition parameters on the in-plane distribution of the water content of the CCM. The goal of the development of the simulation was to make it possible to accurately predict operating conditions that would maintain the in-plane water content of the CCM within the appropriate range in a short period using both the developed simulation and the results of the advance studies.

3. Development of Simulation

3.1. Simulation of In-plane Distribution of Water Content of CCM in Cells

In order to develop a method of simulation of the in-plane water content of CCM in cells, original Honda functional modifications were made to a commercially available polymer electrolyte fuel cell simulation software[(5)].

3.2. Cell and Stack Configuration and Operating Conditions

Figure 2 shows a schematic image of the cells employed in the 2016 model FCV. The main structures applied in the simulation are the wave flow channel separators, the cooling structures serving every two cells[(1)], the stack transverse mounting structure, the structures generating counter flows of An and Ca gases and co-flows of Ca gas and coolant, and the independent gas flow control structure for the An and Ca via the resin frame structure around the MEA[(6)].

These cells are organized into multiple layers to form stacks, and this was applied in the setting of conditions in the simulation (the setting of the periodic boundary conditions).

In the simulations of operating conditions, the current value was held constant, and the effect of the other parameters was determined. The value that has the greatest effect on the durability and reliability of the cells was employed as the current value.

3.3. Simulation Results and Characteristics

Figures 3(a) and (b) show the respective results of in-plane simulation of an A cell and a B cell. In the figures, “Ca in” represents the air inlet, “Ca out” represents the air outlet, “An in” represents the hydrogen inlet, “An out” represents the hydrogen outlet, “Coolant in” represents the coolant inlet, and “Coolant out” represents the coolant outlet.

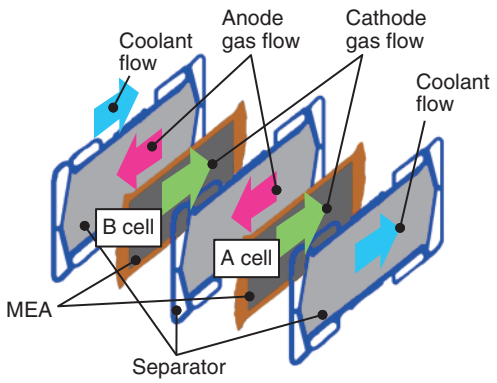


Fig. 2 Schematic image of cell structure

With regard to the characteristics of the cells, the in-plane water content of the CCM is lowest on the Ca gas inlet side, and increases towards the Ca gas outlet side. This is because the water produced on the Ca side flows towards the Ca outlet and accumulates there. However, the position in the cell that displays the highest value for the in-plane water content of the CCM is not the Ca gas outlet (P1 in the figure), but rather a position slightly further towards the Ca gas inlet side (P2 in the figure).

Figure 4 shows a schematic image that explains the characteristics of the in-plane distribution of the water content of the CCM. Two factors determine the in-plane water content of the CCM: the diffusion of water via the CCM due to the difference in water vapor partial pressure between the Ca and the An [(1) in the figure], and the amount of water carried away from the CCM by gas [(2) in the figure].

It is considered that the in-plane water content of the CCM does not reach its maximum at the position of the Ca gas outlet (P1 in Fig. 3) because the amount of water carried away from the CCM by An gas [(2) in Fig. 4] exceeds the amount of water that diffuses via the CCM [(1) in Fig. 4].

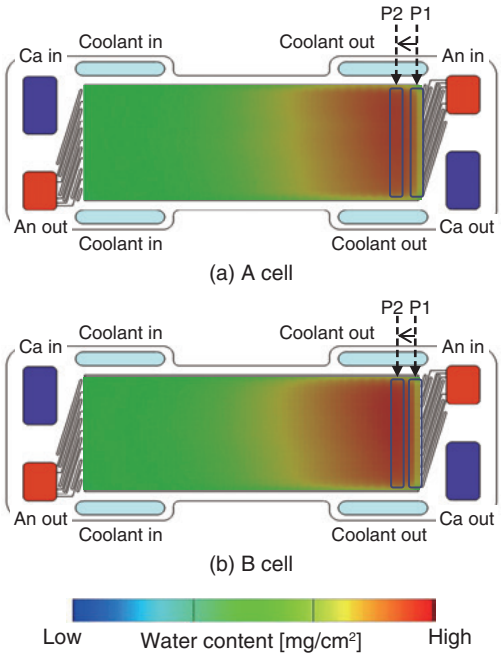


Fig. 3 Simulation results for water content distribution

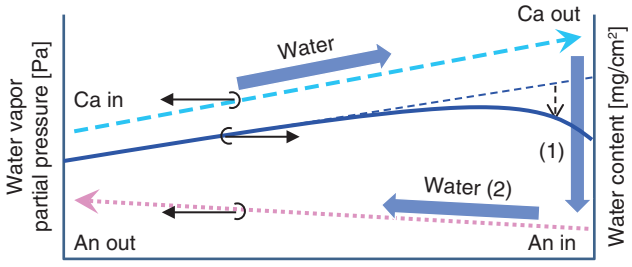


Fig. 4 Schematic image of movement of water in CCM

3.4. Comparison of Simulation and Test Results for Distribution of CCM Water Content

For the development of the stack employed in the 2016 model FCV, a newly developed sensor system[3] was used in the measurement of the in-plane distribution of the CCM water content. Figure 5 shows a schematic image of the system. This system divides the cell in the in-plane direction into 75 segments to measure the in-plane distribution of water content. In order to compare the results of measurements using this system with simulation results, the simulation data was also divided into 75 segments, and an averaging procedure was applied to the data in each segment.

Figures 6(a) and (b) compare respective simulation results and measurement results for the A cell and the B cell. The comparison was conducted for the central group of segments, as shown in Fig. 5.

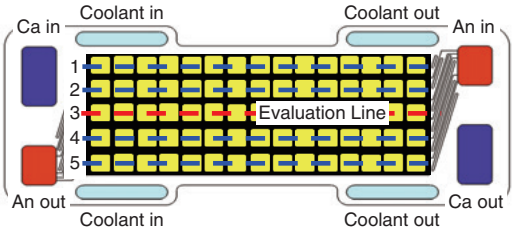


Fig. 5 Schematic image of 75-segment impedance measurement system

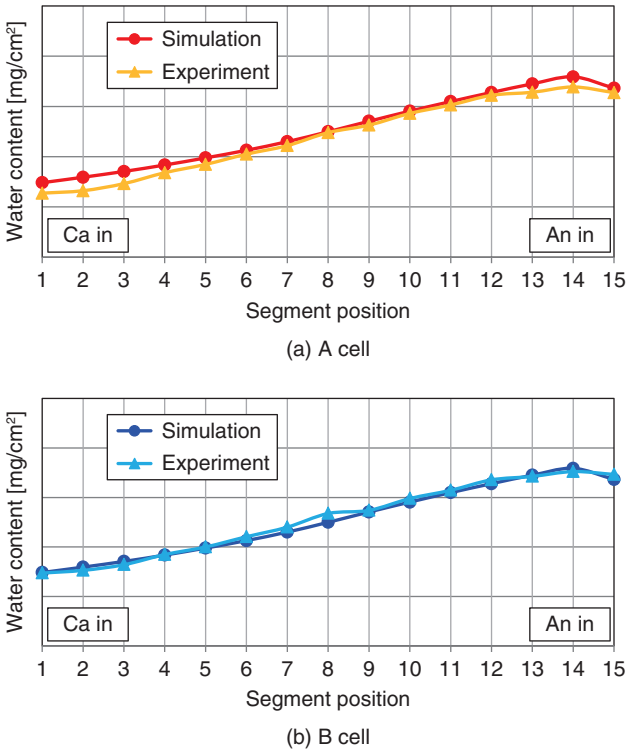


Fig. 6 Results of comparison of simulation and experiment

The stack employs cooling structures serving every two cells, and the measurement and simulation results correspond well in indicating no difference in the water content of the CCM in the A and B cells. In addition, the average predictive accuracy for the 75 segments was within 5.0%.

4. Study of Degree of Effect of Operating Condition Parameters

The operating condition parameters (the inlet temperature and flow rate of the coolant, the An gas inlet flow rate, the Ca gas inlet flow rate, the An gas inlet pressure, and the Ca gas inlet pressure) were varied, and the effect on the in-plane distribution of the water content of the CCM in the cells was studied. The respective operating conditions were changed ±10%, encompassing the range in which the fuel cell system was able to continue to operate in relation to the operating conditions applied in Section 3.2.

Because both the A and B cells displayed identical changes in response to the changes in operating conditions, only the A cell results will be discussed below.

4.1. Effect of Coolant Inlet Temperature

Figure 7 shows simulation results with change in the coolant inlet temperature.

Change in the coolant inlet temperature does not produce any change in the tendency of the in-plane distribution of water content in the CCM, but does produce a significant change in the absolute value of the water content. When the coolant inlet temperature is increased, the temperature in the cell increases, and the in-plane water content of the CCM decreases; when the coolant inlet temperature is reduced, the temperature in the cell decreases, and the in-plane water content of the CCM increases.

4.2. Effect of Coolant Inlet Flow Rate

Figure 8 shows simulation results with change in the coolant inlet flow rate.

Change in the coolant inlet flow rate produces almost no change in the in-plane distribution of the water content of the CCM. However, a consideration of detailed values indicates that when the coolant inlet flow rate is increased, a higher quantity of the heat produced by the CCM is carried away by the coolant. As a result, the temperature in the cell close to the coolant outlet (Segment position 14 in the figure) increases in the in-plane direction as the coolant temperature increases, and the water content of the CCM in the cell decreases. By contrast, when the coolant inlet flow rate is decreased, the coolant is less able to carry away the heat produced by the CCM. Because of this, the coolant temperature decreases, and the in-plane water content of the CCM increases close to the coolant outlet (Segment position 14 in the figure).

4.3. Effect of An Gas Inlet Flow Rate

Figure 9 shows simulation results with change in the An gas inlet flow rate.

Change in the An gas inlet flow rate produces almost no change in the distribution of the in-plane water content of the CCM. However, a consideration of detailed values indicates that when the An gas inlet flow rate is increased, the amount of water carried away from the CCM by the An gas on the An inlet side (Segment position 15 in the figure) increases, and the in-plane water content of the CCM decreases; however, because the amount of water carried

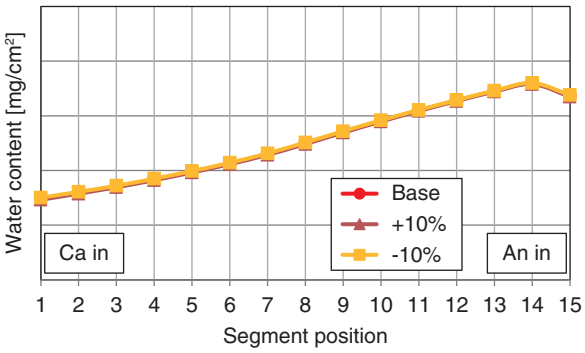


Fig. 8 Simulation results with change in coolant inlet flow rate

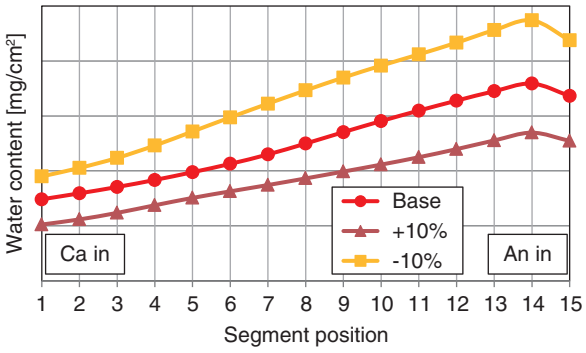


Fig. 7 Simulation results with change in coolant inlet temperature

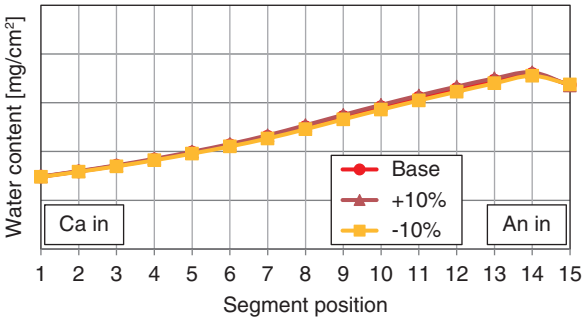


Fig. 9 Simulation results with change in An gas inlet flow rate

away by the An gas decreases downstream of the An gas (Segment positions 1 to 14 in the figure), the in-plane water content of the CCM increases. When the An gas inlet flow rate is reduced, the amount of water carried away from the CCM by the An gas decreases, and the in-plane water content of the CCM on the An inlet side (Segment position 15 in the figure) increases, but because the amount of water carried away by the An gas increases in the downstream section of the An gas flow path (Segment positions 1 to 14 in the figure), the in-plane water content of the CCM decreases.

4.4. Effect of Ca Gas Inlet Flow Rate

Figure 10 shows simulation results with changes in the Ca gas inlet flow rate.

Change in the Ca gas inlet flow rate produces little change in the in-plane water content of the CCM at the Ca gas inlet (Segment position 1 in the figure). However, when the Ca gas inlet flow rate is increased, the maximum in-plane water content of the CCM in the cells (Segment position 14 in the figure) decreases, and when the Ca gas inlet flow rate is reduced, the maximum in-plane water content of the CCM (Segment position 14 in the figure) increases. This is due to the fact that the amount of water carried away increases when the Ca gas inlet flow rate increases, and decreases when the Ca gas inlet flow rate decreases.

4.5. Effect of An Gas Inlet Pressure

Figure 11 shows simulation results with changes in An gas inlet pressure.

Change in the An gas inlet pressure produces almost no effect. However, a consideration of detailed values indicates that, based on the principle of the movement of water in the CCM (Fig. 4), when the An gas inlet pressure increases, the water vapor partial pressure of the An gas increases, and the difference between the Ca and An gas water vapor partial pressures decreases. As a result, the amount of movement of water produced at the Ca to the An decreases, and the in-plane water content of the CCM at all the segment positions decreases. Because the An gas water vapor partial pressure decreases when the An gas inlet pressure is reduced, the difference between the Ca and An water vapor partial pressures increases, and the amount of movement of water produced at the Ca to the An increases. As a result, the in-plane water content of the CCM in all segment positions also increases.

4.6. Effect of Ca Gas Inlet Pressure

Figure 12 shows simulation results with changes in Ca gas inlet pressure.

The results show that change in this parameter significantly changes the in-plane distribution of the water content of the CCM. As in the case of the principle of movement of water in the CCM discussed in Section 4.5., when the Ca gas inlet pressure increases, the difference between the An and Ca gas water vapor partial pressure increases, and the amount of movement of water produced at the Ca to the An increases, increasing the in-plane water content of the CCM. Because the Ca gas water vapor partial pressure decreases when the Ca gas inlet pressure is reduced, the difference between the An and Ca gas water vapor partial pressures decreases, and the amount of movement of water produced at the Ca to the An decreases, resulting in a decrease in the in-plane water content of the CCM.

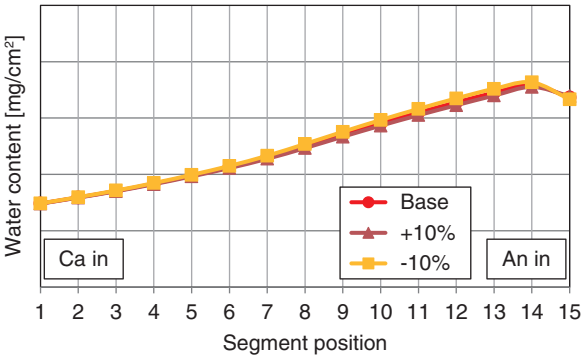


Fig. 11 Simulation results with change in An gas inlet pressure

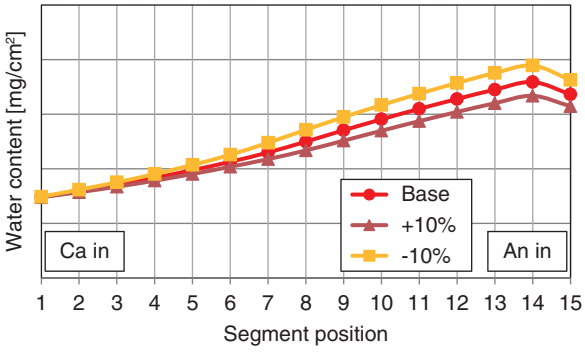


Fig. 10 Simulation results with change in Ca gas inlet flow rate

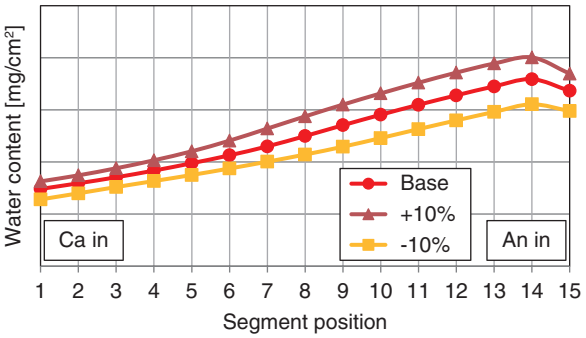


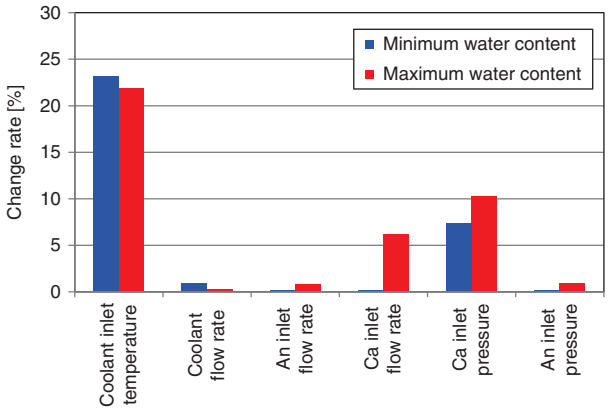
Fig. 12 Simulation results with change in Ca gas inlet pressure

4.7. Sensitivity to Operating Condition Parameters

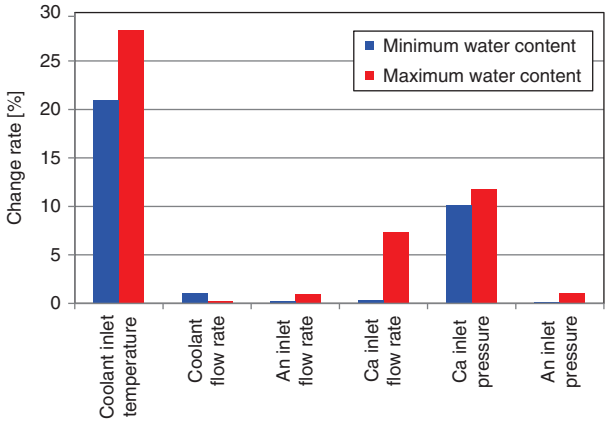
As indicated in the Introduction, it is important to maintain the in-plane distribution of the water content of the CCM in the cells within the appropriate range. Based on the results shown in Figs. 7 to 12, Fig. 13(a) shows the rate of change in maximum and minimum in-plane water content of the CCM when each parameter is increased by 10%, while Fig. 13(b) shows the rate of change for 10% reductions in the parameters.

The graphs in both Fig. 13(a) and (b) show that the rate of change is greatest in relation to the coolant inlet temperature. The maximum and minimum in-plane water content each change by more than 20% in response to change in this parameter. The next greatest rate of change was in response to the Ca gas inlet pressure, with the minimum in-plane water content of the CCM changing by between around 5 to 10% and the maximum in-plane water content of the CCM changing by around 10% in response to change in this parameter. The third greatest rate of change was in response to the Ca gas inlet flow rate. While there was minimal change in the minimum in-plane water content of the CCM in relation to this parameter, the maximum in-plane water content of the CCM displayed a rate of change of around 5%.

These results as a whole indicated that it would be possible to control the minimum in-plane water content of the CCM in the cells by means of the coolant inlet temperature or the Ca gas inlet pressure. The results further indicated that it would be possible to control the maximum in-plane water content in the CCM by using the coolant inlet temperature or the Ca gas inlet pressure as the main parameter and the Ca gas inlet flow rate as a secondary parameter. By this means, it would be possible to control the in-plane distribution of water content in the CCM.



(a) With 10% increase (in each parameter)



(b) With 10% decrease (in each parameter)

Fig. 13 Rate of change of maximum and minimum water content for individual operating condition

5. Application in Stack

Figure 14 shows the results for in-plane distribution of CCM water content when the results of the studies discussed above were applied to operating conditions for the 2016 model FCV stack. “Upper limit” and “Lower limit” in the figure respectively show the upper limit and lower limit values for in-plane CCM water content necessary for maintaining the durability of the stack.

In the in-plane water content distribution in the CCM for conventional operating conditions (shown as the circles in the figure), the upper limit value was exceeded, meaning that it would not be possible to ensure the durability of the stack.

By contrast, in the case of the operating conditions determined by simulation with consideration of in-plane water content distribution in the CCM (shown as the squares in the figure), increasing the coolant inlet temperature has reduced the overall in-plane water content of the CCM, and increasing the Ca gas inlet flow rate has reduced the maximum in-plane water content of the CCM, making it possible to maintain water content within the upper and lower limit values.

The diamonds in the figure show results for the in-plane distribution of CCM water content in a cell in a stack

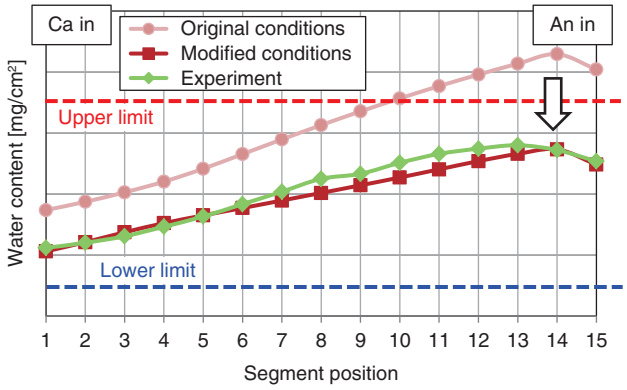


Fig. 14 Original and enhanced water content distribution

measured in measurement tests. A comparison of simulation results (the squares in the figure) and figures from stack measurement (the diamonds in the figure) show that the figures display a good match, reconfirming the judgment that the simulation realized an adequate level of accuracy.

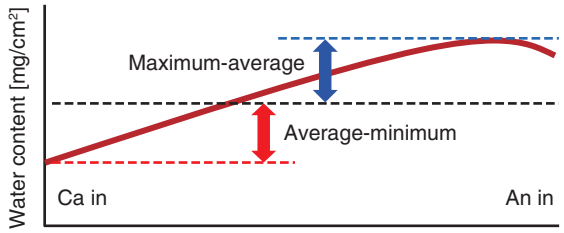
Figure 15(a) shows a schematic image of indexes that express the in-plane distribution of CCM water content in the cells.

Two indexes have been established: the difference between the maximum value and the average value for in-plane CCM water content ("Maximum-average" in the figure), and the difference between the average value and the minimum value for in-plane CCM water content ("Average-minimum" in the figure). In both cases, the in-plane distribution of CCM water content is more desirable the lower the figure.

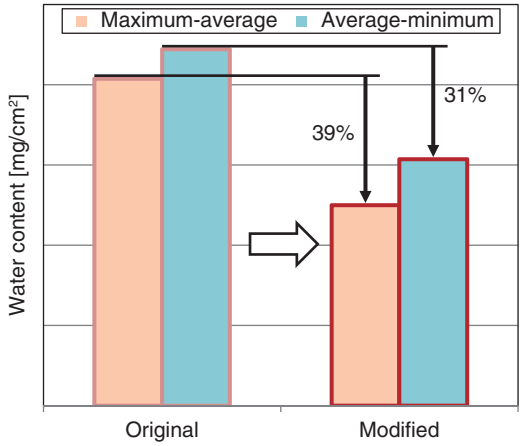
Figure 15(b) shows the in-plane distribution of CCM water content in terms of these indexes before and after the modification of the operating conditions.

Following the modification of the operating conditions, the difference between the maximum value and the average value for in-plane CCM water content ("Maximum-average" in the figure) was reduced by 39%, and the difference between the average value and the minimum value for in-plane CCM water content ("Average-minimum" in the figure) was reduced by 31%. It was possible to reduce variations in the distribution of water content in the CCM at the same time as maintaining the in-plane distribution within the upper and lower limits[4].

In addition, the use of the developed simulation made it possible to determine operating conditions in several days that would previously have necessitated several weeks using tests.



(a) Schematic image of maximum-average and average-minimum



(b) Maximum-average and average-minimum water content change for original and modified operating conditions

Fig. 15 Enhancement of water content distribution

6. Conclusion

A simulation of the in-plane distribution of the water content of CCM in cells was developed. The following results were obtained from the use of the simulation.

(1) A simulation was conducted for the stack configuration employed in the 2016 model FCV, and the results of measurements using a sensor system and simulation results for the in-plane distribution of the water content of the CCM were compared. The results indicated that the simulation achieved a predictive accuracy of within 5.0%.

(2) An advance study of the effect of operating condition parameters on the in-plane distribution of the water content of the CCM was conducted. The results of this study indicated that the minimum in-plane water content of the CCM could be controlled by means of the coolant inlet temperature or the Ca gas inlet pressure. The study also showed that the maximum in-plane water content of the CCM could be controlled by employing the coolant inlet temperature or the Ca gas inlet pressure as the main parameter and the Ca gas inlet flow rate as a secondary parameter. In this way, it would be possible to control the in-plane distribution of the water content of the CCM.

(3) Using the developed simulation and a coolant inlet temperature, Ca gas inlet pressure, and Ca gas inlet flow rate helping to enable control of the in-plane distribution of water content in the CCM made it possible to maintain the in-plane distribution within the upper and lower limit values and reduced variation in the distribution. It was also possible to apply accurate operating conditions in the stack in a period of several days.

References

(1) Saito, N., Kikuchi, H., Nakao, Y.: New Fuel Cell Stack for FCX Clarity, Honda R&D Technical Review, Vol. 21, No. 1, p. 16-23

(2) Nishikawa, N.: Nenryodenchi no Gijyutsu -Kotaikoubunshigata no Kadai to Taisaku-, Tokyo Denki University Press, p. 84-113, (2010) (in Japanese)

(3) Sato, M., Chiba, H., Inoue, M.: Development of CCM Water Content Distribution Measurement System for Fuel Cell Stack, Honda R&D Technical Review, Vol. 28, No. 1, p. 16-25

(4) Iwanari, T., Miyajima, K., Furusawa, K., Inoue, M.: Real-time Measurement of Water Content of CCM in On-board Fuel Cell Stack System, Honda R&D Technical Review, Vol. 28, No. 1, p. 34-40
(5) Yoneda, M., Tago, Y., Suzuki, K., Takimoto, M., Ejiri, E.: Macroscopic Modeling and Simulation for Polymer Electrolyte Membrane Fuel Cells, ECS Transactions, 11-1, p. 1105-1114, (2006)
(6) Kimura, K., Kawasaki, T., Atsumi, Y., Ohmura, T., Shimizu, K.: Development of New Fuel Cell Vehicle CLARITY FUEL CELL, Honda R&D Technical Review, Vol. 28, No.1, p. 1-8

■ Author ■


Kenji NAGUMO


Masajiro INOUE

Real-time Measurement of Water Content of CCM in On-board Fuel Cell Stack System

Toru IWANARI* Kazuyoshi MIYAJIMA*
Koichiro FURUSAWA* Masajiro INOUE*

ABSTRACT

In order to increase the durability of fuel cell stacks, the in-plane water content of the catalyst-coated membranes (CCM) in the cells is controlled within the proper range using stack impedance.

Setting out to elucidate the status of the in-plane water content of the CCM, the research discussed in this paper employed a water content distribution measurement system to conduct real-time measurements of the in-plane water content of the cells in a fuel cell stack forming part of an on-board generation system. The use of the system makes it possible to determine the in-plane water content of the CCM during both constant current generation and transient current generation. The results of this study verified the effectiveness of the in-plane CCM water content control employed in the 2016 model FCV. In addition, optimization of the control of in-plane water content of the CCM has also had an effect in further increasing the durability of the fuel cell stacks.

1. Introduction

The environmental effects of CO_2, NOx and other pollutants in automotive exhaust gases and the future depletion of fossil fuels make the development of clean, high-fuel-efficiency vehicles an urgent task. Seeking to realize a sustainable society based on energy circulation, Honda is engaged in research and development efforts in relation to fuel cell vehicles (FCV), which use hydrogen rather than fossil fuels, and fuel cell technologies[(1)].

Figure 1 shows an image of the structure of a fuel cell and its internal chemical reactions. The fuel cell (simply termed "cell" below) is made up of a membrane electrode assembly (MEA) and separators that form gas channels. A fuel cell stack (termed "stack" below) is created by layering multiple cells together.

The MEA is made up of a polymer electrolyte membrane (PEM), a catalyst layer (CL), and a gas diffusion layer (GDL). The PEM making up the CL are also called catalyst-coated membranes (CCM).

In the cell, a hydrogen oxidation reaction occurs at the anode electrode as shown by Eq. (1), and an oxygen reduction reaction occurs at the cathode electrode as shown by Eq. (2). These chemical reactions between hydrogen and oxygen produce electricity and water.

$$\text{Anode electrode (An): } H_2 \rightarrow 2H^+ + 2e^- \quad (1)$$

$$\text{Cathode electrode (Ca): } 1/2O_2 + 2H^+ + 2e^- \rightarrow H_2O \quad (2)$$

In addition to seeking increased compactness and weight reductions, and realizing high-efficiency-generation performance with higher output, it is also necessary for the stacks fitted in FCV to display durability in relation to the fluctuations in current load to which cells used in automotive environments are subjected. To help

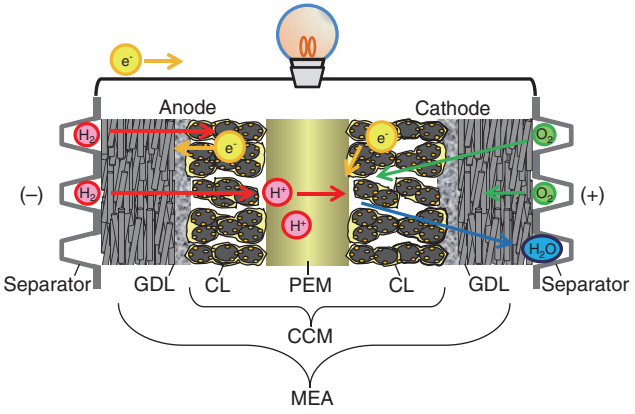


Fig. 1 Schematic image of fuel cell

* Automobile R&D Center

ensure durability in cells, it is necessary to maintain the surface area of the electrode catalysts, which contributes significantly to the output of the cell, and to maintain the thickness of the PEM, which functions both to separate the oxygen and the hydrogen that serves as fuel, and to electrically insulate the anode and the cathode.

The ability to maintain the surface area of the electrode catalysts and the thickness of the PEM is closely related to the in-plane water content of the CCM in the cell. Generally, when the water content is high, the electrode catalysts become coagulated due to dissolution, agglomeration, and redeposition, and the decline in the catalyst surface area accelerates. It has also been reported that when the water content is low, impurities and hydrogen peroxide accumulate in the PEM, promoting chemical degradation and reducing the thickness of the PEM[(2)].

In order to increase the durability of automotive fuel cells, it is therefore necessary to identify the in-plane distribution of the water content of the CCM and control it to within the proper range.

2. Development Goals

The development of the stack for the 2016 model FCV therefore sought to realize increased stack durability through the development of multi-segment impedance sensors[(3)] to identify the in-plane distribution of water content of the CCM in the cells and the calculation of the optimum in-plane water content distribution using simulations[(4)].

The research discussed in this paper set out to use the developed impedance distribution measurement system (IDMS) in order to conduct real-time test bench measurements of the in-plane distribution of water content of the CCM of the cells in a stack used in an actual on-board generation system, and to verify that the in-plane water content was within the proper range. The outcomes of the research would be reflected in the control method employed in actual on-board generation systems.

3. Necessity for Measurements

The in-plane distribution of water content of the CCM in the cells displays a range of variation due to instantaneous changes in operating conditions, including the flow rate and pressure of the gases supplied to the stack, the temperature of the stack, and the current being generated. However, in order to increase the durability of the cells, it is essential to constantly maintain the in-plane water content of the CCM to a range within upper and lower limits. Upper and lower limit values for in-plane water content of the CCM were set based on the results of CCM durability tests using miniature cells, as shown in Fig. 2.

In the actual on-board generation system, the in-plane water content of the CCM in the cells is controlled within upper and lower limits using the measured stack impedance, based on the relationship between in-plane water content and stack impedance shown in Fig. 3.

While a variety of factors affect the in-plane water content of the CCM, in the on-board generation system used in the 2016 model FCV, the method applied to control water content is control of the level of humidity of the air supplied to the stack. A humidifier bypass control valve connected in parallel to a humidifier adjusts the quantity of airflow through the humidifier, controlling the in-plane water content of the CCM in the cells (Fig. 4).

The range for control of stack impedance ("Target impedance" in Fig. 3) is affected by the uneven in-plane distribution of water content of the CCM ("Distribution of water content" in Fig. 3) and measurement error. The optimization of the uneven in-plane distribution of water content of the CCM by means of simulation of constant current generation contributed to expanding the range for control of stack impedance.

However, despite the fact that the uneven in-plane distribution of water content of the CCM was taken into consideration in setting the range for control of stack impedance, it was predicted using a simulation of constant

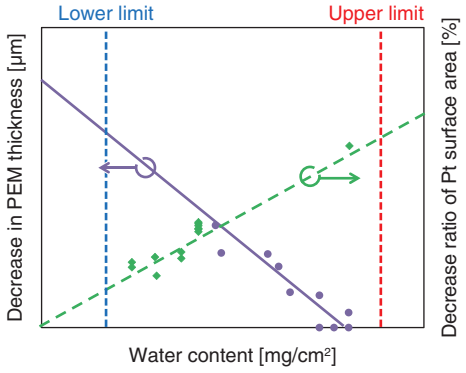


Fig. 2 Upper and lower limits for water content to maintain PEM thickness and Pt surface area

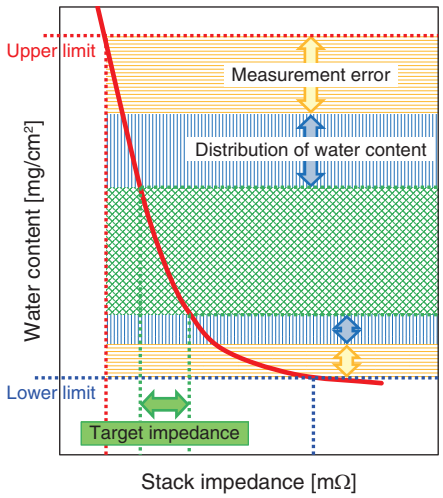


Fig. 3 Relationship between stack impedance and water content

current generation. Because of this, it was necessary to verify whether the in-plane water content of the CCM was maintained within the scope of the upper and lower limit values during transient current generation in an actual on-board generation system.

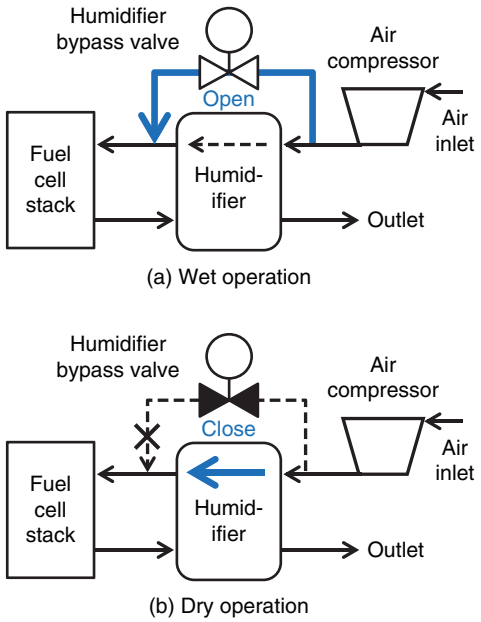


Fig. 4 Schematic image of humidity control of supplied air

4. Issues of Conventional Measurement Method

Conventionally, the dry weight method (Fig. 5) or the nuclear magnetic resonance (NMR)[5] method have been used to measure the in-plane distribution of water content of the CCM.

The dry weight method takes the difference in weight between objects when they contain water and when they do not as the weight of the water. When employing this measurement method, the cells are operated for a set period of time under the conditions for which it is desired to take measurements of the in-plane water content of the CCM, following which they are dismantled. The CCM is then cut into a set number of segments, which are placed in bags from which their water content cannot evaporate, and then weighed. Following this, they are dried, and weighed once again. The difference in weight between the two measurements is considered to be the in-plane water content of the CCM. Given the potential for evaporation of the water content during the dismantling of the cells and the cutting of the CCM, it is necessary to perform the operations quickly in a high-humidity environment. In addition, because the in-plane water content of the CCM can only be measured under fixed generating conditions, the facts that it is necessary to take repeated measurements for each operating condition, and that it is not possible to conduct measurements under transient conditions, have represented issues for the method.

In the NMR method, a test specimen is placed in a magnetic field, and is bombarded by a high-frequency magnetic field in order to excite nuclear spin resonance. The NMR signal produced by the test specimen is received and its atomic state is measured, enabling measurement of the local amount of water in the CCM in real time. Because this method necessitates exposing the stack and the actual on-board generation system to a strong magnetic field, the large size of the measurement apparatus and the potential for malfunctioning of the system have represented issues.

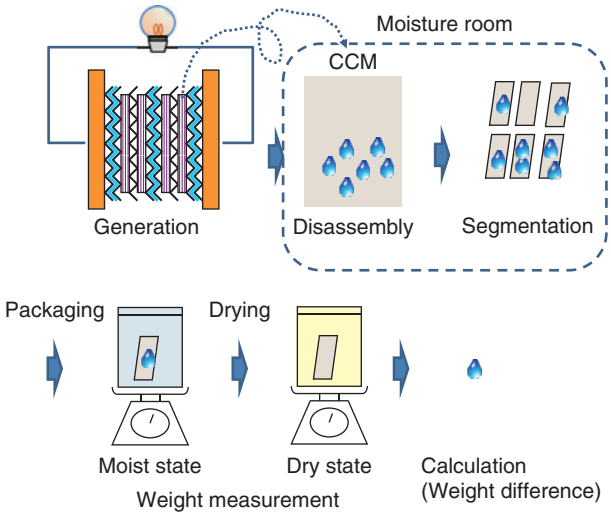


Fig. 5 Dry weight method for measurement of water content of CCM

5. Method of Addressing Issues

An IDMS for the test bench measurement of the distribution of water content of the cells through measurement of impedance in the stacks used in actual on-board generation systems was introduced in order to measure water content of the CCM, as shown in Fig. 6. The current superimposed for measurement is measured as a current signal (V_2) by means of the shunt resistor of a terminal pad with split sensors [shown in Fig. 6(b)]. At the same time, the cell voltage signal (V_1) is measured [Fig. 6(c)]. This makes it possible to calculate impedance, and thus to calculate in-plane water content of the CCM. It can then be verified whether the in-plane water content of the CCM remains within the upper and lower limit values during constant current generation and transient current generation. Because these measurements are conducted in a high-voltage and high-frequency environment, adequate consideration is given to insulation of devices and measures to respond to noise.

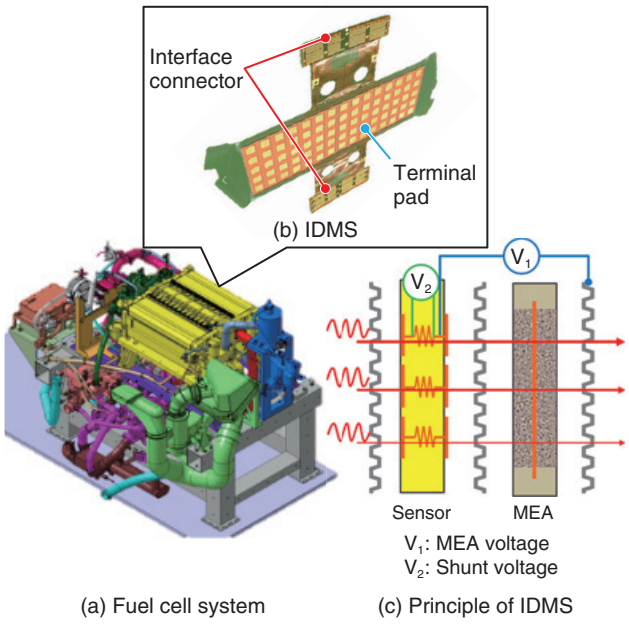


Fig. 6 Fuel cell system with IDMS for bench use

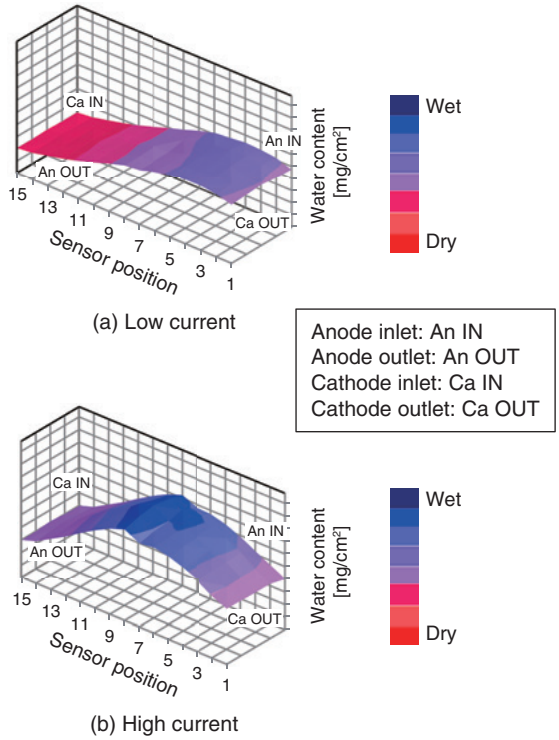


Fig. 7 Water content distribution under conditions of constant current generation

6. Results of Bench Test

6.1. Constant-speed Running Mode

The first verification measurements focused on whether the in-plane water content of the CCM remained within the upper and lower limit values in constant-speed running mode (constant current generation).

Figure 7 shows results for the in-plane distribution of water content of the CCM for different current ranges. In the low-current range, as shown in Fig. 7(a), because the water produced on the cathode side flows towards the outlet (Ca OUT), the amount of in-plane water in the CCM increases the closer the CCM are to the outlet. Because of this, it is possible for the amount of in-plane water in the CCM on the cathode inlet side (Ca IN) to drop below the lower limit value. It is considered that the slight decline in the amount of in-plane water in the CCM on the cathode outlet side (Ca OUT), as shown in Fig. 8, is due to water flowing to the opposite anode side via the CCM. By contrast, in the high-current range, the highest amount of in-plane water in the CCM shifts from the cathode outlet side (Ca OUT) to the cathode inlet side (Ca IN). It is considered that this is because, with the increase in current, the area of generation shifts to the cathode inlet side (Ca IN), which has a high concentration of oxygen. Because generation produces a high amount of water, it is possible that the in-plane water content of the CCM in the central area of the cell could increase above the upper limit value.

Figure 9 shows results for the in-plane water content of the CCM for different current ranges. The results make it possible to confirm that the stack impedance value is appropriately controlled within the upper and lower limit

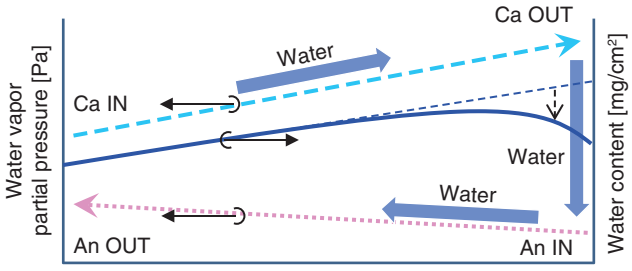


Fig. 8 Schematic image of movement of water in CCM

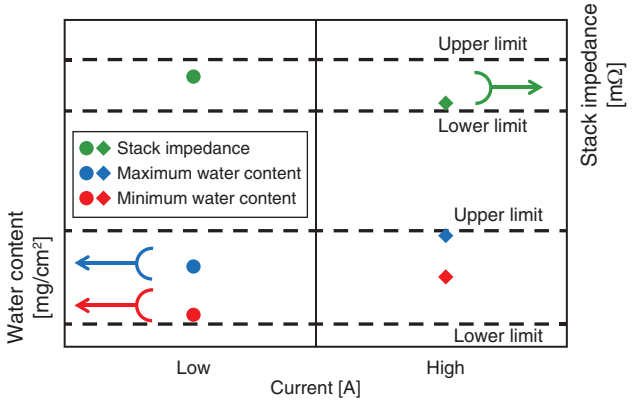


Fig. 9 Results for water content under conditions of constant current generation

values. It was also confirmed that the in-plane water content of the CCM remained within the upper and lower limit values in the cases of the lower limit value on the cathode inlet side in the low-current range and the upper limit value for the CCM in the central area of the cell in the high-current range.

6.2. Stack Evaluation Running Mode

Figure 10 shows a schematic image of stack evaluation modes (transient current generation) and stack impedance values employed during development. Using the water content distribution measurement system, it was possible to measure the in-plane distribution of water content of the CCM in real time during running mode.

The in-plane water content of the CCM varies considerably during running mode, increasing (the impedance value declines) during acceleration, and decreasing (the impedance value increases) during deceleration and idling. The study therefore focused on whether or not the in-plane water content of the CCM remained within the upper and lower limit values in all areas of the cell. The results of verification for each operating mode will be discussed below.

6.2.1. During acceleration and deceleration

Figure 11 shows time series data for the maximum and minimum values for in-plane water content of the CCM during acceleration and deceleration. Figure 12(a) shows results for the measurement of the in-plane distribution of water content of the CCM in the direction of the length of the cell, where the in-plane water content reaches its maximum during acceleration. The blue and red circles within the figure show maximum and minimum values for the in-plane water content of the CCM in the width direction of the cell. As in the case of the high-current range during constant-speed running operation [Fig. 7(b)], during acceleration the in-plane water content of the CCM reaches its maximum value in the center of the cell in the direction of gas flow but remains below the upper limit value.

Figure 12(b) shows the results of measurements of the in-plane water content of the CCM during deceleration, when water content reaches its minimum. In the transition from acceleration to deceleration, the in-plane water content of the CCM at the cathode inlet declines to close to the lower limit value. In the high-current range, as shown in Fig. 12(a), the in-plane water content of the CCM is high because the amount of water produced by generation is high, but during deceleration, the amount of water produced

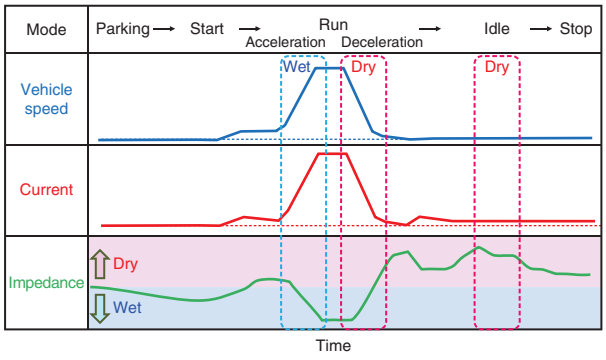


Fig. 10 Schematic image of evaluation running mode for fuel cell vehicle

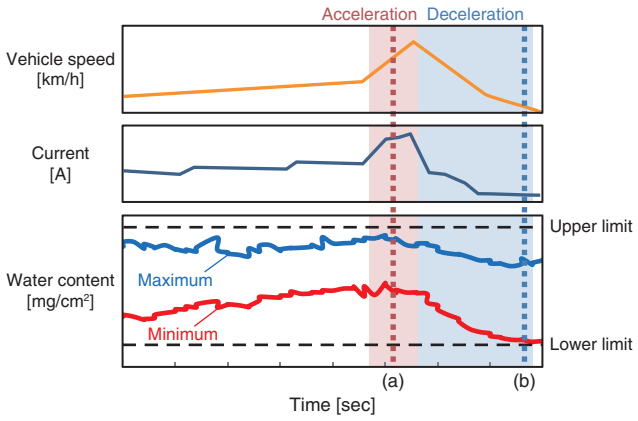


Fig. 11 Time-series results for water content in acceleration mode and deceleration mode

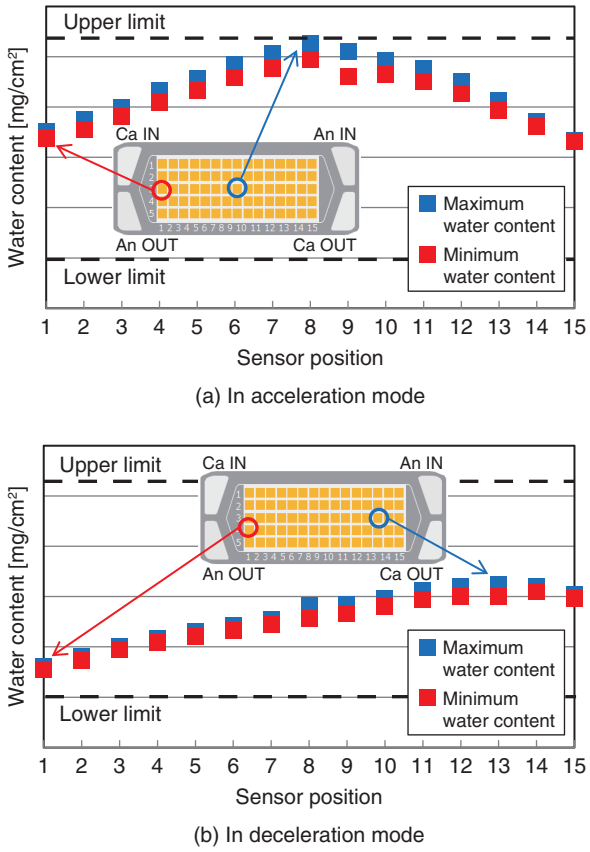


Fig. 12 Results for water content distribution in acceleration mode and deceleration mode

by generation declines in response to the current. In addition, because the high-current generation immediately preceding deceleration increases the temperature of the stack, the amount of saturation vapor in the gases increases, and more water is discharged outside the stack. In addition, during deceleration the quantity of airflow becomes excessive because of a lag in the response of air supply control. It is considered that the synergistic effect of these factors reduces the in-plane water content of the CCM close to the cathode inlet. It was verified, however, that the in-plane water content of the CCM during deceleration remained within the upper and lower limit values.

6.2.2. During idling

Figures 13 and 14 show the results of measurement of the in-plane water content of the CCM during idling. As the results show, the in-plane water content of the CCM at the cathode inlet declines with time, until it drops below the lower limit value. Despite the fact that stack impedance is controlled within the desired range, during idling the amount of water produced by generation is low, and dry air is supplied to the stack, with the result that the decline in the in-plane water content of the CCM close to the cathode inlet is greater than initially projected.

In response, in addition to adjusting the total quantity of air supplied to the stack, the ratio of supplied air passing through the humidifier was increased during idling, when very little water is produced by generation, increasing the water content of the CCM close to the cathode inlet.

It was verified that this change in control was effective, with the results shown in Fig. 15 demonstrating that the water content of the CCM at the cathode inlet no longer declines below the lower limit value during idling.

Real-time measurement of the in-plane distribution of water content of the CCM in cells employed in actual on-board generation systems has made it possible to verify that the water content is controlled within upper and lower limit values even in stack evaluation running mode.

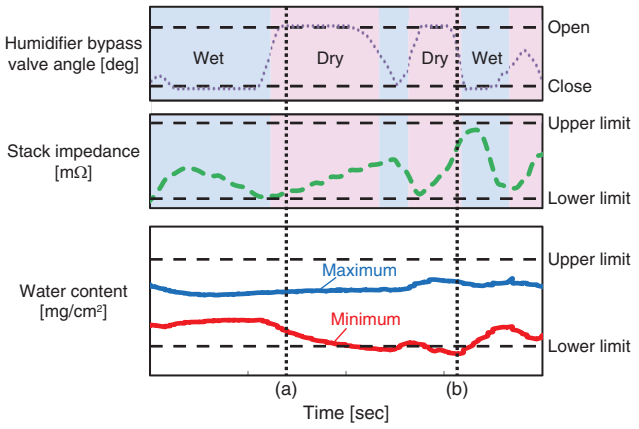


Fig. 13 Time-series results for water content in idling mode

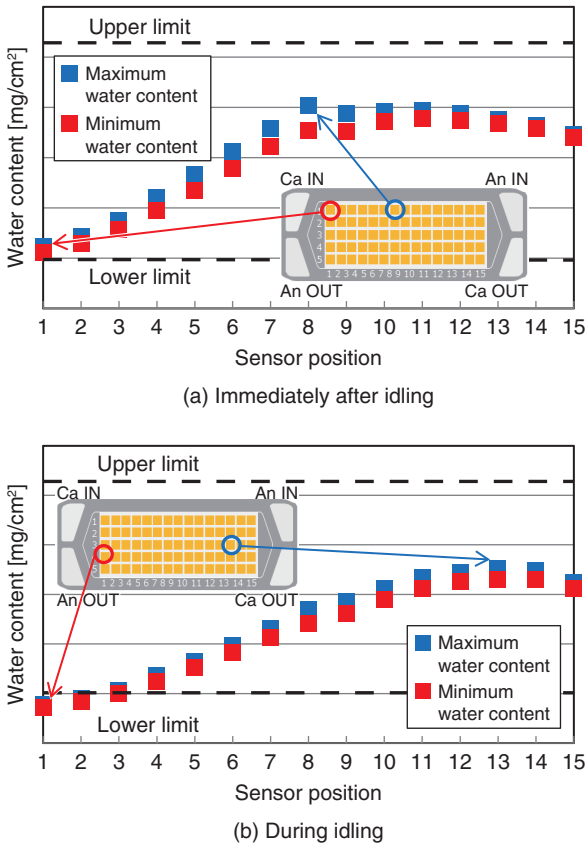


Fig. 14 Results for water content distribution in idling mode

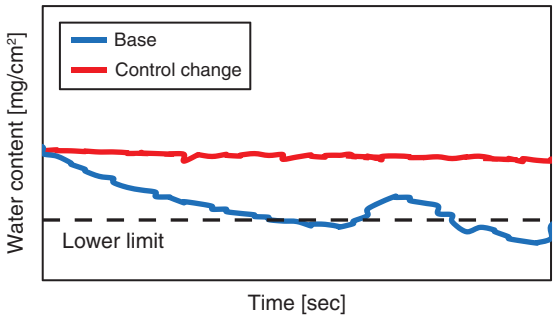


Fig. 15 Effect of change in control on water content at cathode inlet

7. Conclusion

Verification of the control of the in-plane water content of the CCM in cells employed in the 2016 model FCV generation system produced the following results:

(1) It was verified that during constant current generation, stack impedance control maintained the in-plane water content of the CCM within the upper and lower limit values.

(2) It was verified that the in-plane water content of the CCM was maintained within the upper and lower limit values during acceleration and deceleration, when transient current generation is occurring.
(3) The causes of a reduction in the in-plane water content of the CCM below the lower limit value during idling were identified, and measures introduced in response were verified to be effective.

These results demonstrate the effectiveness of control of the in-plane water content of the CCM in cells using stack impedance. In addition, the optimization of control has also had an effect in increasing the durability of the fuel cell stack.

References

(1) Saito, N., Kikuchi, H., Nakao, Y.: New Fuel Cell Stack for FCX Clarity, Honda R&D Technical Review, Vol. 21, No. 1, p. 16-23
(2) Nishikawa, N.: Nenryodenchi no Gijyutsu -Kotaikoubunshigata no Kadai to Taisaku-, Tokyo Denki University Press, p. 84-113, (2010) (in Japanese)
(3) Sato, M., Chiba, H., Inoue, M.: Development of CCM Water Content Distribution Measurement System for Fuel Cell Stack, Honda R&D Technical Review, Vol. 28, No. 1, p. 16-25
(4) Nagumo, K., Inoue, M.: Numerical Prediction of Water Content Distribution of Catalyst Coated Membrane of Fuel Cell Stack using Simulation, Honda R&D Technical Review, Vol. 28, No. 1, p. 26-33
(5) Yokouchi, Y., Ogawa, K., Haishi, T., Ito, K.: Current and water-content measurements in PEFC generating electric power using NMR sensors. Spatial distribution and time-dependence change in current and water-content, The 47th National Heat Transfer Symposium, A213, (2010)

Author


Toru IWANARI


Kazuyoshi MIYAJIMA


Koichiro FURUSAWA


Masajiro INOUE

Empirical Model for Polymer Electrolyte Fuel Cell Electrocatalyst Degradation Using Platinum Stress

Masakuni YAMAMOTO* Hiroshi MATSUMORI*

ABSTRACT

A method of predicting polymer electrolyte fuel cell performance loss due to electrocatalyst degradation was developed in order to reduce the performance loss caused by fuel cell startup and stop and by acceleration and deceleration during driving.

An electrochemical method was used to define a platinum stress index to express the influence on platinum (Pt) catalyst degradation from potential cycles in a fuel cell stack. It was found that Pt stress shows an exponential relationship with the rate of loss of catalyst activity, and an empirical prediction model for Pt catalyst degradation was developed.

When the developed model based on Pt stress was used to predict performance loss in a stack during startup and stop, the results showed that a prediction accuracy of approximately 90% was achieved and confirmed that the model could be applied as a catalyst degradation prediction model.

Operating conditions derived from the prediction model were incorporated into fuel cell system development. The results showed that the rate of performance loss during startup and stop was reduced by approximately 57 points compared to the conventional rate, thereby confirming the usefulness of the model.

1. Introduction

A fuel cell vehicle (FCV) that uses hydrogen for fuel has driving performance on a par with gasoline vehicles and also has high environmental performance with its clean emissions and high efficiency.

The motors also provide smooth driving and quiet operation. The FCV is therefore attracting attention as a method for reducing the environmental impact of the automobile.

Widespread popular adoption of the FCV will necessitate higher fuel cell (FC) stack performance and durability as well as lower cost. In previous development, one issue in FC durability has been performance loss, and performance loss is known to be greater at startup and stop and when the vehicle is driving (Fig. 1).

One factor in the acceleration of performance loss at startup and stop that has been proposed is the mechanism whereby the electrocatalyst of Pt nanoparticles supported on carbon black is ionized due to repeated operation of the cathode high potential during startup and stop, so that the Pt is dissolved and diffused in the polymer electrolyte membrane, after which the Pt is deposited due to reduction of Pt ions by crossover of hydrogen through the anode side [(1)-(3)]. The catalyst in a single cell was actually observed using a scanning transmission electron microscope (STEM) after assumed startup and stop testing. Figure 2(a) shows the Pt nanoparticles dispersed on carbon black before the testing, whereas Fig. 2 (b) shows these are dissolved and deposited in the polymer electrolyte membrane (Fig. 2(b) area outlined in red). STEM observations shown in Fig. 2 match with the previously hypothesized mechanism.

The degradation of electrocatalyst is the main factor in performance loss, and establishment of a technique to inhibit this degradation is an urgent issue for enhancement of FC durability. It is important, therefore, to have an index representing the relationship of Pt catalyst degradation to

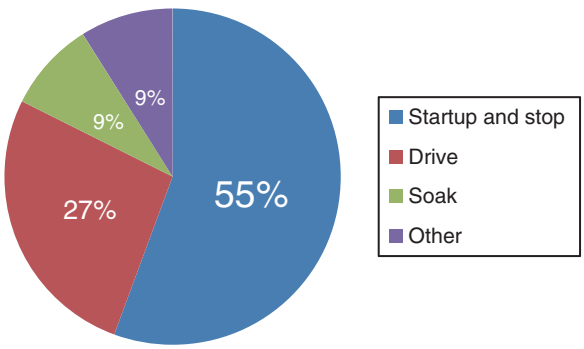


Fig. 1 Breakdown of performance loss in conventional FC stack

* Automobile R&D Center

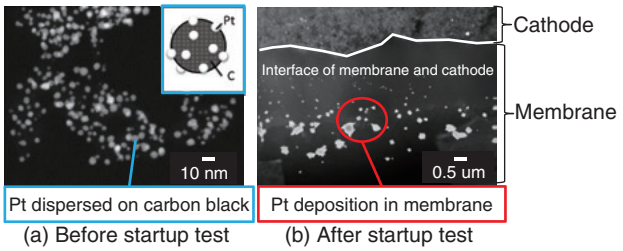


Fig. 2 STEM image of Pt catalyst on carbon black support (Pt/C) before (a) and after startup test at 1000 cycles (b)

FC system control, but there are virtually no instances of the relationship between control and Pt catalyst being clearly represented in the form of an index.

2. Development Goals

This paper will describe the development of a new index that represents the relationship between FC system control and Pt catalyst degradation, and the development of an empirical model, based on that index, for predicting Pt catalyst degradation.

It will also describe cases relating to the development of FC system control in order to mitigate catalyst degradation during startup and stop according to the prediction.

Issues involved in the development of an index representing the relationship between FC system control and Pt catalyst degradation and in development of a catalyst degradation prediction model include the following:

Issue 1: A method for quantifying and indexing the influence that potential cycle in the FC have on catalyst degradation; and

Issue 2: Setting the quantitative correlation between the index and FC stack performance loss.

First of all, resolving Issue 1 will require research on a method for detecting the changes that occur in Pt catalyst with respect to potential cycles.

Cell voltage in FC is expressed as the difference between the potential at the cathode and at the anode, and the anode potential (reversible hydrogen electrode, RHE) is the reference for the cathode potential (cathode potential [V vs. RHE] in Fig. 3).

Since hydrogen oxidation reaction (HOR) of the fuel occurs at the anode, the RHE in the case of pure hydrogen will generally show as around 0 V. Figure 3 shows an example of a typical pattern of the cathode potential cycle when the RHE is taken as the reference and the current that loads on the stack (the FC current in Fig. 3)[3]. By feeding hydrogen as fuel into the anode and air as an oxidizing agent into the cathode, the cathode will be in a high potential state (the "Start" portion in Fig. 3), just as in the case of open circuit voltage (OCV) in an ordinary battery. Low power operation with the FC in an idle state causes a slight loss in the cathode potential (the "Idle" portion in Fig. 3). The subsequent patterns of the cathode potential cycle of the stack become complicated, with the sudden drop in the potential due to high power loaded (the "High load" portion in Fig. 3), the cathode potential cycles resulting from acceleration and deceleration during driving (the "Acceleration or deceleration" portion in Fig. 3), and the state of reduced cathode potential due to cathode oxygen concentration control when stopping (the "Stop" portion in Fig. 3).

Cyclic voltammetry (CV) was taken up as an electrochemical method for understanding changes that occur in the Pt catalyst with respect to these voltage cycles.

CV can provide information about Pt catalyst reactions with regard to potential in terms of the current caused by electrochemical reaction. Figure 4 shows a typical current-potential curve obtained by CV using carbon-supported Pt catalyst. The insets in Fig. 4 show a schematic representation of reactions on the Pt catalyst surface. At around 0.5 V, a current charged/discharged by

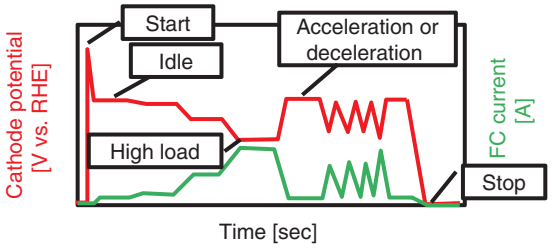


Fig. 3 Typical pattern of cathode potential cycle in FCV

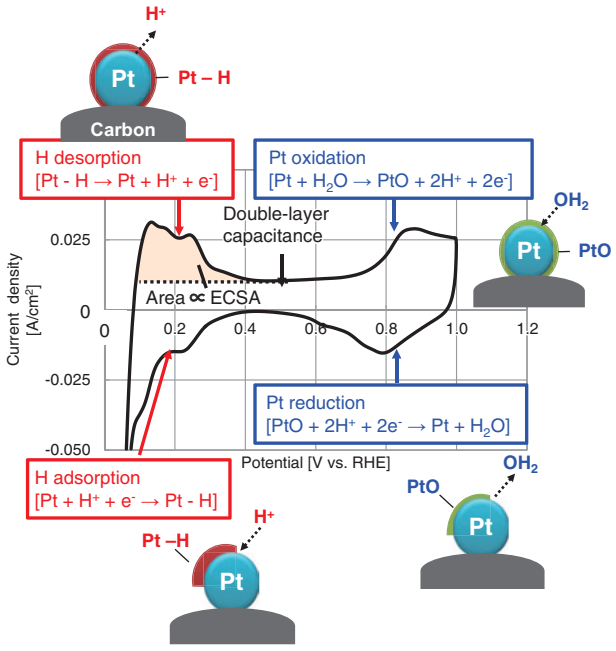


Fig. 4 General CV depicting features observed on the surface of Pt catalyst

electrochemical double-layer capacitance is observed in the FC, and from 0.6 to 1.0 V, formation of a Pt oxide layer is caused by an adsorption reaction of Pt and molecular water (Pt oxidation). The Pt oxide is reduced to bare Pt surface by scanning potentials from 1.0 to 0.6 V.

At an potential lower than 0.5 V (from 0 to around 0.45 V), however, hydrogen adsorption desorption (HAD) occurs on the Pt catalyst. The charge of HAD (q_{HAD}) and the electrochemical surface area (ECSA) of the catalyst are in the relation of proportionality shown in Eq. (1). Therefore, the effective Pt catalyst surface area can be obtained from q_{HAD}.

$$\text{ECSA } [\text{cm}^2] = \frac{q_{HAD}[\text{uC}]}{210\ [\text{uC/cm}^2]} \quad (1)$$

In Eq. (1), 210 uC/cm^2 is the commonly used conversion ratio of q_{HAD} and electrochemically effective surface area of Pt catalyst.

Given the above characteristics, CV was adopted as the method for quantifying the influence that potential cycle in FC has on catalyst degradation.

Next, in order to resolve Issue 2, the index determined by CV had to be tied to FC performance. We therefore focused on the relationship between FC performance loss and catalyst degradation.

FC performance is commonly evaluated using the polarization curve (Pol. curve) shown in Fig. 5[4]. The factors in the voltage loss can largely be placed in three main categories, which include:

(1) Ohmic loss (iR_{loss}) in the FC system;
(2) Overvoltage (η_{ORR}) relating to the oxygen reduction reaction (ORR) in the cathode; and
(3) Overvoltage (η_{tx}) relating to oxygen transport to the cathode catalyst.

The cell voltage in the FC stack is expressed as the difference between the voltage losses in (1) to (3) and the voltage loss due to anode HOR (HOR_{loss} in Fig. 5).

Of the three, factor (2) accounts for the greatest part of the voltage loss. Since factor (2) depends on the kinetics of ORR, it has a determining influence on catalyst activity, and ECSA loss in the Pt catalyst contributes greatly to it.

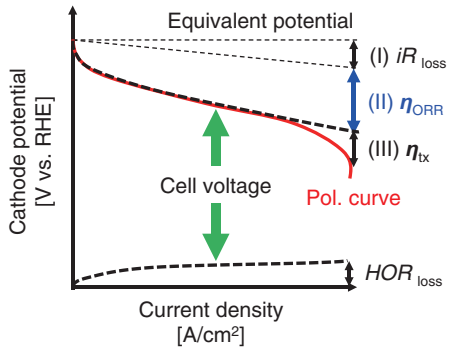


Fig. 5 Diagram of relationship between FC polarization curve and voltage loss

ORR occurs because molecular oxygen is adsorbed in and desorbed from the surface of the Pt catalyst in the FC, as with catalysts in general. In order to increase the ORR rate, therefore, the ECSA becomes an important physical property because it indicates the active sites of Pt catalyst reaction. The quantity η_{ORR} that is derived from the equation for the catalytic reaction rate is theoretically expressed by Tafel's equation in Eq. (2), and it is known to have a logarithmic relationship with the ECSA[5].

$$\eta_{ORR} = \frac{2.303 \times RT}{\alpha F} \times \log\left(\frac{\text{ECS A} \times i_0}{i}\right) \quad (2)$$

R is the ideal gas constant, T is the absolute temperature, α is the cathode transfer coefficient, F is Faraday's constant, i is the reaction current density, and ECSA×i_0 corresponds to the effective exchange current density of the catalyst.

It was reasoned that the development of a catalyst degradation model capable of predicting ECSA loss from the relationships in Fig. 5 and Eq. (2) would enable estimation of performance loss. To that end, the mechanism of presumed ECSA degradation was hypothesized in order to correlate the index describing catalyst degradation due to potential cycles in the FC with the ECSA, which is a catalyst property.

As indicated in Chapter 1, previous reports indicated that the coagulation of Pt nanoparticles caused by dissolution and deposition of Pt were the determining factor in ECSA loss[1]. The view was therefore taken that the basic mechanism was loss of catalyst activity due to the potential cycle.

In order to address the potential cycles caused by startup and stop in FC and by acceleration and deceleration during driving, shown in Fig. 3, potential cycle was further subdivided into the three elements of the attained potential, the hold time at one, and scan rate.

Quantification of the influence on Pt catalyst was examined in terms of these three elements.

3. Quantification of the Influence of Potential Cycle on Catalyst Degradation

3.1. Experimental

In order to quantify the influence of potential cycle on Pt catalyst, CV measurement was carried out using a single cell.

The membrane electrode assembly (MEA) used for evaluation was fabricated by hot pressing commercially available catalyst layer decals onto polymer electrolyte membranes (catalyst coating membrane, CCM) and sandwiched by gas diffusion layers (GDL). The MEA is placed into a single cell, which has a 50 cm^2 active area (Fig. 6).

The single cell operating conditions are summarized in Table 1.

The basic conditions for cell operation were set with reference to previous reports[6]. The cell temperature was

Table 1 Operating conditions of single cell

Operating condition	Anode (RE/CE)	Cathode (WE)
Atmosphere (flow rate) [NLM]	H_2 (0.3)	N_2 (2)
Pressure [kPa]	230	200
Temperature [°C]	70	
RH [%]	50	73

controlled by thermocouple to maintain a level of 70°C, and the relative humidity (RH) at the anode and cathode was adjusted using a humidifier. Humidified pure hydrogen gas was fed into the anode flow field at 0.3 NLM, while an inert gas (N_2) was fed into the cathode flow field at 2 NLM, and total gas pressures were maintained at the anode of 230 kPa and at the cathode of 200 kPa.

The cathode was set as the working electrode (WE) and the anode as the reference and counter electrode (RE and CE). WE potential with respect to the RHE was controlled using a potentio-galvanostat (PGS) in order to measure the reaction current on the Pt catalyst. Figure 6 shows a schematic diagram of the measurement system.

The CV measurements were performed by setting from the potential elements (attained potential and hold time at one) at 50 mV s^{-1} sweep rate.

3.2. Quantification of the Influence of Upper Level Potential Due to Startup and Stop Operation and Its Hold Time

First, the influence of the upper level potential (ULP) assumed by a high cathode potential during startup was confirmed. As an example of verification, Fig. 7 shows the cathode potential cycling profile and current-potential curves with ULP set at 0.9 V and 1.0 V.

As shown in Fig. 4, the total current for HAD observed at the potentials from 0 to 0.45 V showed low dependence on ULP.

By contrast, it was verified that Pt reduction current obtained at the potential from 0.6 to 1.0 V was strongly dependent on ULP.

The higher the ULP, the greater the increase in the reduction current of the PtO layer formed by the rise in cathode potential, and this means that the electrochemical oxidation of Pt progressed due to molecular oxygen. It was found that ULP is the main factor that accelerates Pt catalyst oxidation, as reported in a previous study[7].

Next, the ULP was fixed and CV measurements were made by the profile of cathode potential cycles with changed hold times (Fig. 8) in order to clarify the influence of Pt catalyst oxidation in terms of ULP hold time. From the CV measurement results in Fig. 8, it was found that a difference appears in the current from reduction of the Pt

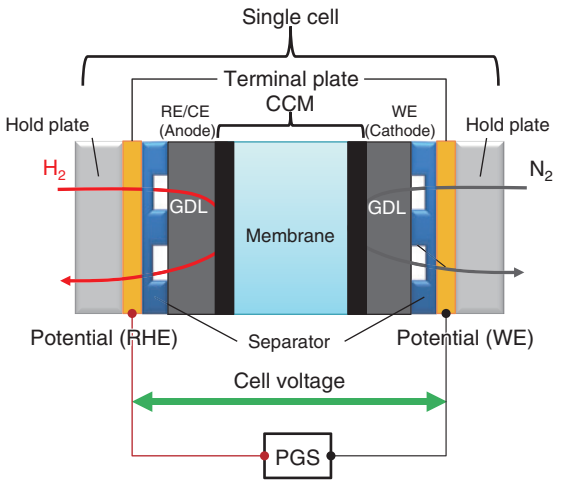


Fig. 6 Schematic drawing of electrochemical system using single cell

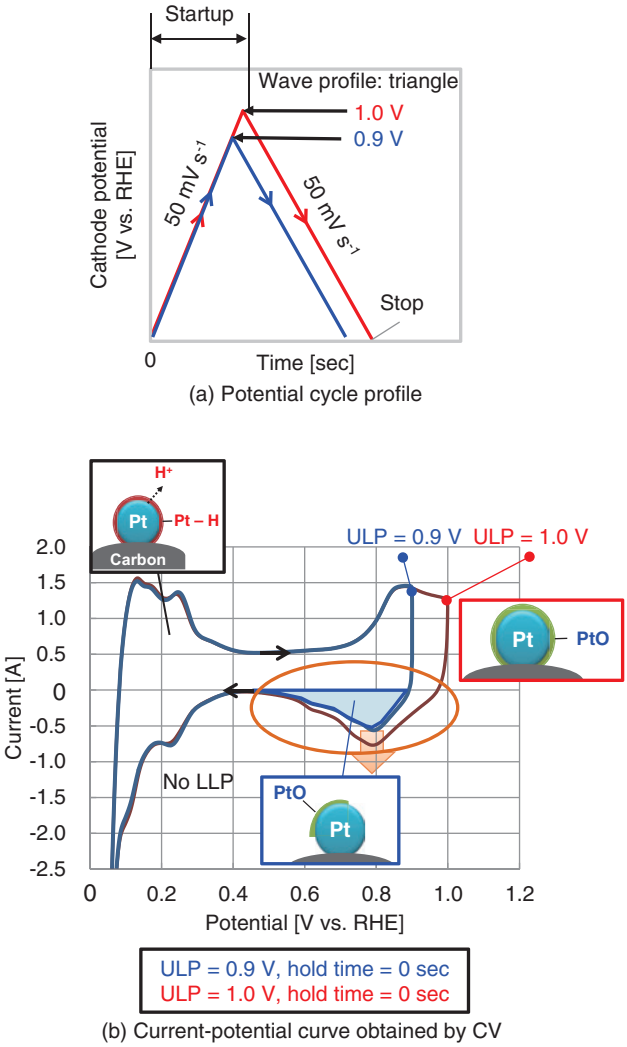


Fig. 7 Graph of WE potential trend, showing changed ULP levels using CV (a). CVs obtained at each ULP from 0.05 V up to 0.9 V (blue solid line), up to 1.0 V (red solid line) (b).

catalyst and molecular oxygen even when the ULP remains at the same 1.0 V as shown by the dotted curve in Fig. 8. Because the reduction current increases with respect to potential hold time, electrochemical oxidation of Pt surface was found to be dependent on these factors.

3.3. Quantification of the Influence of Lower Level Potential from Acceleration and Deceleration During Driving and Its Hold Time

Next, CV measurements were taken with the lower level potential during driving (LLP) due to potential cycles during acceleration set. The purpose was to quantify the influence of cathode potential cycles from acceleration and deceleration during driving. As an example of verification, Fig. 9 shows the cathode potential cycling profile and current-potential curve obtained by CV after ULP hold at 1.0 V for 100 sec and LLP hold at 0.8 V for 100 sec. The LLP in Fig. 9 assumes cathode potential drop due to the load applied during acceleration and deceleration. Comparison of results is shown in Fig. 8, which assumed startup and stop, and in Fig. 9, which simulates cathode potential cycles due to acceleration and deceleration during driving. The total reaction charge of the Pt oxidation reaction due to ULP on the assumption of startup in Fig. 8, whose potential profile has no LLP operation, could be obtained as the charge of the PtO layer reduction reaction (Q_1 in Fig. 8).

On the other hand, when LLP operation at 0.8 V occurs on the assumption of cathode potential cycles due to acceleration and deceleration during driving, the Q_1 from ULP is reduced from a to b in Fig. 9 due to the hold time at LLP. It is thought that the charge of the reduction of PtO due to ULP is decreased by LLP holding caused by the load of acceleration and deceleration.

From these verifications that CV was used to quantify the influence of potential cycles in the FC on Pt catalyst, examination of the CV results shows that the charge caused from the PtO layer (the Pt reduction reaction current in Fig. 4) demonstrates strong dependence, and can clearly be seen to increase and decrease according to the ULP, LLP and their hold times.

Based on the above results, Pt stress was defined as the index of catalyst degradation as shown in Eq. (3) below. The purpose of this is to differentiate the influence of

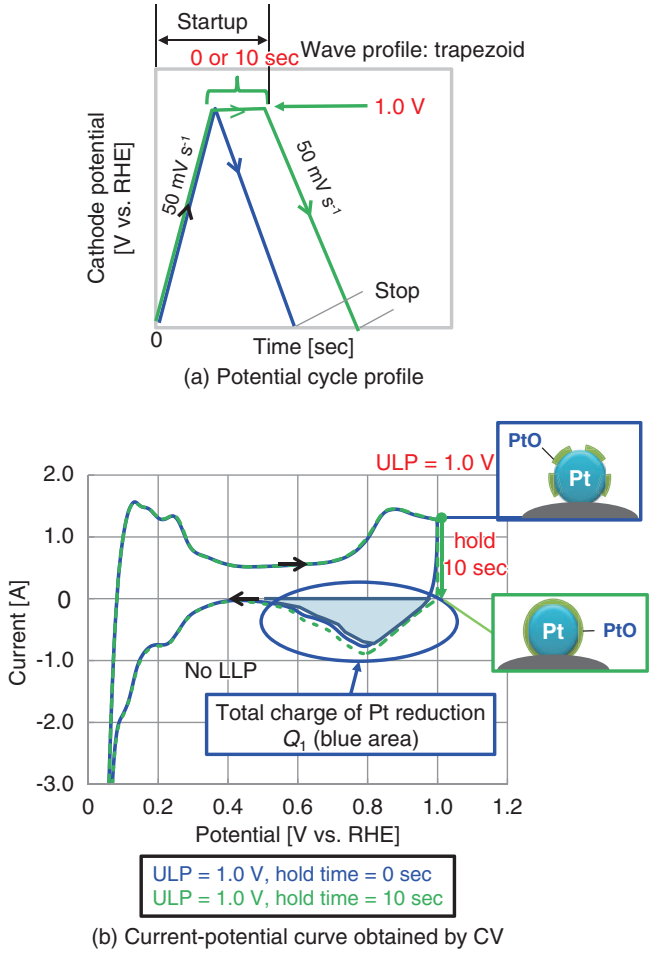


Fig. 8 Potential trend at cathode in CV (a). CVs obtained at same ULP from 0.05 V up to 1.0 V (blue solid line), and hold at 1.0 V for 10 sec (green dotted line) (b).

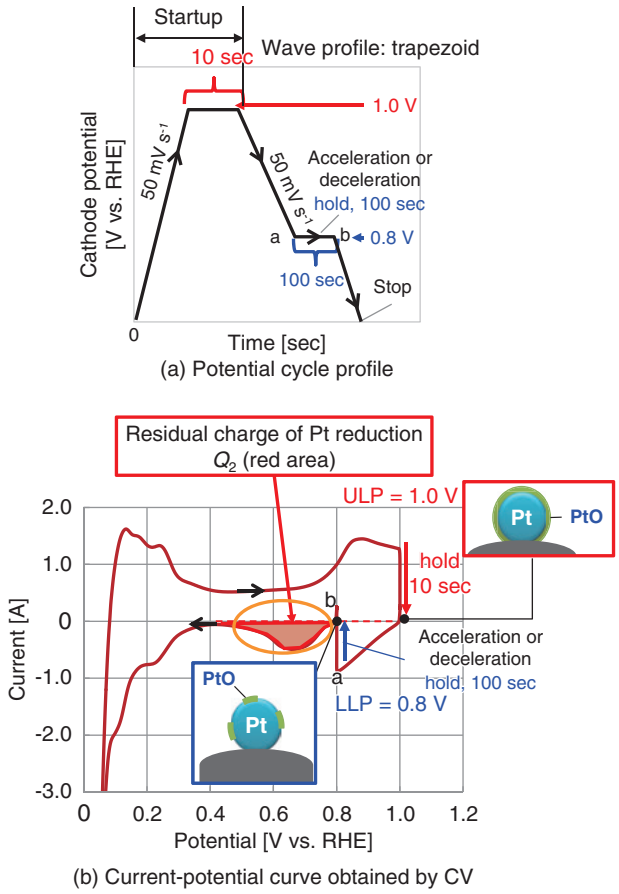


Fig. 9 Potential trend at cathode in CV (a). CV measured by 10 sec hold at ULP = 1.0 V, and 100 sec hold at LLP = 0.8 V (b)

cathode potential cycles resulting from startup and stop and from acceleration and deceleration during driving.

$$\text{Pt stress} \equiv \Delta Q = Q_1 - Q_2 \quad (3)$$

Q_1 is the total charge of the PtO layer when cathode high potential is assumed to occur during startup and stop. Q_2 is the residual charge of the PtO layer after reduction by load cycles during driving (Q_2 in Fig. 9). The Pt stress is determined from these charges that are based on electrochemical reactions. The influence of potential cycle resulting from mode of operation (ULP, LLP, and their hold times) is expressed by the variation of change (ΔQ). As distinct from results previously reports[7], it becomes possible to determine the influence of LLP that arises from load cycle by Pt stress defined as variation of ΔQ.

In light of the above, the use of Pt stress as an index enabled the influence that potential cycles in the FC operation have on catalyst degradation to be expressed quantitatively. In the following, Pt stress will be termed ΔQ.

In order to apply to potential cycles during FC operation of the kind shown in Fig. 3 with ΔQ as an index, the ULP, the LLP, and these hold times were varied while obtaining CV measurements, and the dependence of ΔQ on potential was mapped (Fig. 10). By using Fig. 10, it became possible to quantify the influence of potential cycles in actual vehicle of the kind as shown in Fig. 3.

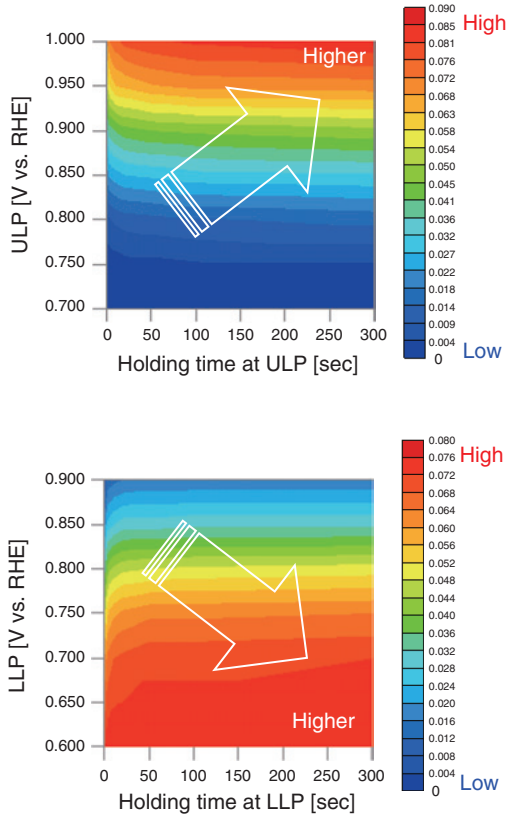


Fig. 10 Dependence of ΔQ on ULP, LLP and holding time at each potential. CVs obtained by the same conditions as Table 1

Table 2 List of accelerated stress test (AST) by potential cycling mode using single cell

Mode	Assumption	Cell temperature [°C]	RH [%]		Potential [V vs. RHE]			
			An.	Ca.	ULP	LLP	Wave profile	Holding time [sec]
Load cycle-I	Drive low RH	70	50	40	0.90	0.70	Rectangle	4
Load cycle-II	Drive middle RH	70	50	73	0.90	0.70	Rectangle	4
Load cycle-III	Drive high RH	70	50	100	0.90	0.70	Rectangle	4
Potential cycle-IV	Start up middle ULP	45	100	100	0.95	0.80	Trapezoid	4
Potential cycle-V	Start up high ULP-1	45	100	100	1.20	0.80	Trapezoid	4
Potential cycle-VI	Air Start up	45	100	100	1.40	0.80	Trapezoid	5
Potential cycle-VII	Fuel starvation	45	100	100	1.60	0.80	Trapezoid	5
Potential cycle-VIII	High load	70	50	73	0.95	0.65	Trapezoid	4
Potential cycle-IX	Middle load	70	50	73	0.90	0.70	Triangle	0

4. Setting the Correlation Between ΔQ and FC Stack Performance

The dependence between ΔQ and ECSA, which determines the voltage drop due to ORR, was confirmed in order to clarify the correlation between FC stack performance loss and ΔQ, quantified above through Chapter 3.

In order to confirm the dependence of ECSA on ΔQ, a single cell was used to conduct potential cycle testing, and the dependence between the rate of ECSA loss and ΔQ was verified. CV measurement was implemented under the same measurement conditions as described in Section 3.1. In the potential cycle test, ΔQ was varied by the conditions in Table 2, which simulates the potential cycles in actual vehicle. Modes IV to VII reflect cathode potential and temperature that assume startup and stop operation, and the rest of the modes were taken to assume acceleration and deceleration during driving.

Figure 11 shows the results from comparison of modes VIII and IX, which assume acceleration and deceleration during driving.

According to the ULP, LLP, and their hold times, the ΔQ per unit cycle can vary by a factor of approximately 2.5 even in the same acceleration and deceleration mode.

Potential cycle testing on the assumption of acceleration and deceleration in which ΔQ differs by a factor of approximately 2.5 was conducted for the designated number

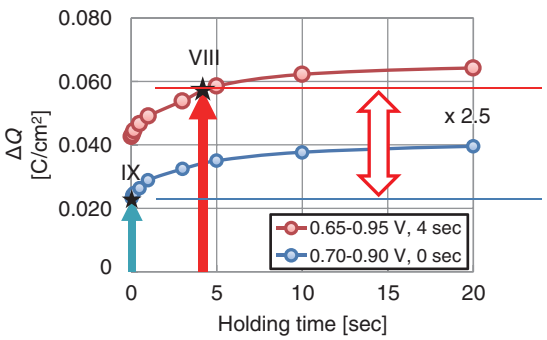


Fig. 11 Comparison of ΔQ under operating conditions of modes VIII and IX

of repetitions. Transitions in the rate of ECSA loss were confirmed.

Figure 12 shows the relationship between ΔQ and the rate of ECSA loss.

The rate of ECSA loss during potential cycles in which ΔQ varies by a factor of approximately 2.5 was found to change by two orders of magnitude or more. Similarly, when the levels of ΔQ were varied according to Table 2, the results were found to show an exponential relationship with the rate of ECSA loss. However, although the correlation accuracy (correlation coefficient; $R^2 = 0.975$) in Fig. 12 is high, there is a difference from the actual measurement value. It was thought that the difference from the correlation occurs because ECSA loss operated under the conditions set to assume startup and stop (IV to VII) in Table 2 include the influence of carbon corrosion as well as the expected Pt degradation.

The influence of carbon corrosion on ECSA loss has not yet been defined. However, the results in Fig. 12 enable management of the rate of ECSA loss in each operating mode by means of ΔQ. This made it possible to clarify the difference between the catalyst degradation that occurs in startup and stop operation and in driving operation, in both of which it results in large performance losses.

It also becomes possible to estimate the rate of ECSA loss by calculating ΔQ from the control elements (ULP, LLP, and their hold times) for an actual vehicle when the map in Fig. 10 is used.

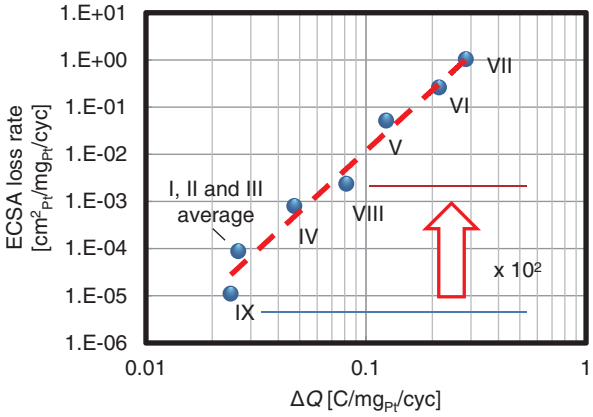


Fig. 12 Correlation of ΔQ and ECSA loss rate

5. FC System Control with Platinum Stress as Index

5.1. Verification of the Catalyst Degradation Prediction Model

In order to confirm the accuracy of the catalyst degradation prediction model that was developed as described up through the previous chapter, the performance loss was verified in tests assuming startup and stop operation with a short stack.

Figure 13 shows the average voltage profile for the stack in assumed startup and stop testing.

The stack starts up at around 0 V due to control of the gas environment at both electrodes; then, when the air as oxidizing agent feeds into the cathode during startup, stack voltage rises. The cathode of the stack is held at OCV for the designated times, and when the operation of the stack stops it returns to around 0 V due to the control of oxygen concentration. Consequently, the Pt catalyst undergoes repeated potential cycles from 0 V to 1 V.

Catalyst degradation in startup and stop simulation testing was predicted according to the flow chart in Fig. 14 in order to estimate ΔQ according to the potential cycle in Fig. 13.

ULP and ULP hold time during startup and stop are identified from the average voltage profile for the short stack shown in Fig. 13. (In Fig. 14, ULP = 1.0 V and holding time = 100 sec.) The ΔQ during startup and stop is calculated from these potential elements and the ΔQ map in Fig. 10. The calculated ΔQ is converted into numerical values per amount of Pt loading in the cathode, and the exponential relationship in Fig. 12 is used to estimate the rate of ECSA loss during startup and stop in the short stacks.

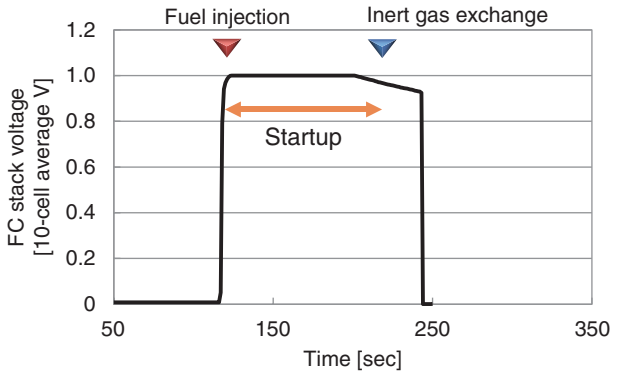


Fig. 13 Average voltage profile of FC stack at startup

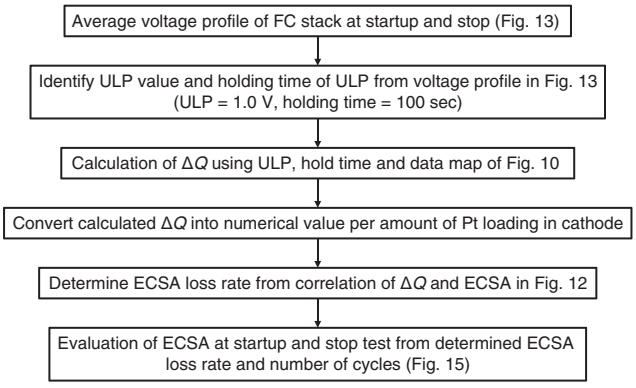


Fig. 14 Prediction flow of catalyst degradation in FC stack using empirical model based on ΔQ

The rate of ECSA loss estimated in Fig. 14 is multiplied by the number of cycles of the startup and stop simulation test, and the ECSA loss during startup and stop was predicted. Figure 15 shows the results from comparison of the estimated curve obtained by the catalyst degradation model (the dotted line in Fig. 15) with the actual ECSA values obtained from using the short stacks by CV measurement (the filled circle in Fig. 15).

Comparison of the ECSA loss rates in the final test cycle (end of test, EOT) showed that the model had prediction accuracy yielding approximately 90% conformity. These results demonstrate that the model developed with a single cell can be used to estimate catalyst degradation in the FC stack of an actual vehicle.

5.2. Verification of the Effectiveness of FC System Control with Pt Stress as an Index

Given the confirmation that the developed model is applicable to stacks, the empirical catalyst degradation model is complete. This model was used to examine operation modes that would inhibit catalyst degradation in order to reduce the performance loss during startup and stop that has been an issue with conventional stacks.

As shown in Fig. 13, cathode high potential cycle occurs at potentials from 0 V to 1 V during startup and stop. Reduction of ΔQ during startup and stop will be an important approach to inhibiting catalyst degradation. It was reasoned, therefore, that it would be necessary to have control that lowers ULP due to OCV during startup.

When the conventional FC stacks stop, the stack voltage falls instantly to 0 V, which causes ΔQ to increase. An attempt was made to address this by reducing the margin of voltage loss after the cathode potential is held at startup. In other words, control to hold LLP at a higher level was implemented in order to reduce ΔQ.

Given the direction shown by estimation using the model and the feasibility of FC system control, voltage control during startup and stop was introduced to the stack to realize these goals. As a result, ΔQ was successfully reduced. The use of voltage control cut such high cathode potential as the OCV during startup, reducing the influence on ΔQ, which is an index of Pt catalyst degradation caused by ULP. Control of the voltage drop when stopping was also implemented to optimize LLP.

Control measures reduced ΔQ by approximately 10% at startup and approximately 20% during stopping relative to conventional FC figures. Catalyst degradation was inhibited, reducing the rate of stack performance loss during startup and stop by approximately 57 points (Fig. 16).

Following the above research, control to reduce performance loss based on the newly developed Pt catalyst degradation prediction model was demonstrated in FC system development and its usefulness was confirmed.

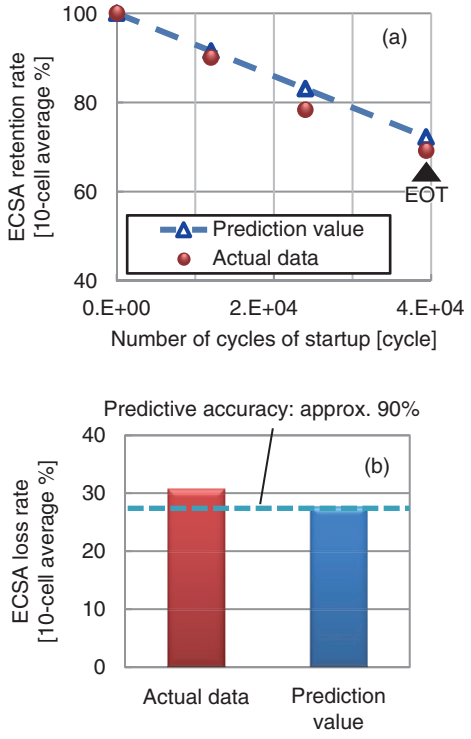


Fig. 15 Actual data of ECSA during startup cycle and prediction line (a). Comparison of actual data and predicted data at EOT (b)

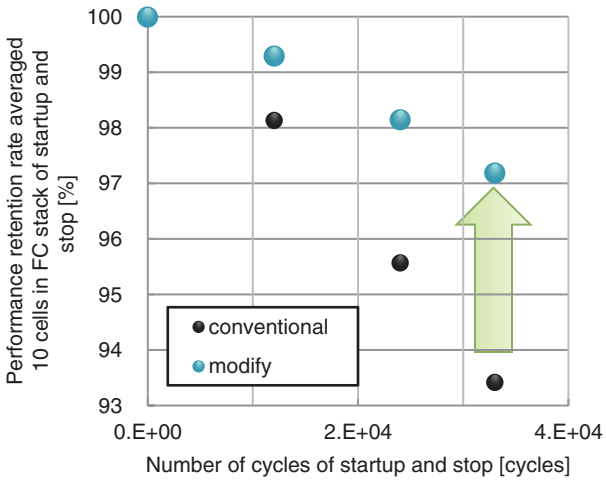


Fig. 16 Verification result of effect to performance loss in FC stack by modify mode at startup and stop

6. Conclusion

(1) Pt stress was newly developed as a quantification of the influence that potential cycles in the FC have on catalyst degradation. This enabled quantification of the extent of influence of each operating mode.

(2) The correlation of the rate of ECSA loss with Pt stress was newly discovered. By use of this correlation, Pt

stress could be calculated from operating conditions, making it possible to rapidly estimate ECSA loss trend.

(3) Use of the developed empirical catalyst degradation prediction model enabled estimation of catalyst degradation in the FC stack in an actual vehicle and confirmed that the model is highly accurate. The model links the catalyst with operating conditions, and therefore enables estimation of conditions that inhibit degradation from the catalyst perspective, and the fact that the model can be used in development of a method for FC system control has confirmed its usefulness.

Acknowledgements

The authors wish to take this opportunity to express profound gratitude to the late Mr. Fusao Nakagawa, who led the way in this research from the initial concept design to the creation of evaluation methods.

References

(1) Ferreira, P. J., la O', G. J., Shao-Horn, Y., Morgan, D., Makharia, R., Kocha, S., Gasteiger, H. A.: Instability of Pt/C Electrocatalysts in Proton Exchange Membrane Fuel Cells; Journal of The Electrochemical Society, 152 (11), A2256-A2271, (2005)

(2) Shao-Horn, Y., Ferreira, P. J., la O', G. J., Gasteiger, H. A., Makharia, R.: Coarsening of Pt Nanoparticles in Proton Exchange Membrane Fuel Cells Upon Potential Cycling, ECS Transactions, 1 (8), p. 185-195, (2006)

(3) Iiyama, A., Shinohara, K., Iguchi, S., Daimaru, A.: Membrane and catalyst performance targets for automotive fuel cells, Handbook of Fuel Cells, Vol. 6, Chapter 61, (2010)

(4) Ishihara, A., Ohta, K.: Denkikagakushisutemu no Tokusei, Genrikaratoraeru Denkikagaku, SHOKABO Co., Ltd., p. 123, (2006) (in Japanese)

(5) Jomori, S., Nonoyama, N., Yoshida, T.: Analysis and modeling of PEMFC degradation: Effect on oxygen transport, JSAE Annual Congress Proceedings, No. 60-12, p. 1-4, (2012) (in Japanese)

(6) Fuel Cell Commercialization Conference of Japan (FCCJ): Target and research and development issue of polymer electrolyte fuel cell, and proposal of evaluation method, p. 22, (2011)

(7) Subramanian, N. P., Greszler, T. A., Zhang, J., Gu, W., Makharia, R.: Pt-Oxide Coverage-Dependent Oxygen Reduction Reaction (ORR) Kinetics; Journal of The Electrochemical Society, 159 (5), B531-B540, (2012)

Author



Masakuni YAMAMOTO



Hiroshi MATSUMORI

Life Prediction Model Estimating Chemical Degradation of Polymer Electrolyte Membrane for Fuel Cells

Atsushi HIRAIDE*

ABSTRACT

A calculation method was developed that can predict the lifetime of polymer electrolyte membrane for fuel cells. The chemical degradation of polymer electrolyte membrane is caused by two reaction mechanisms, scission of polymer main chains and unzipping reaction. It was made clear by both experimental and theoretical approaches that the degradation behaviors can be closely approximated with exponential function. By defining the coefficient of the exponential function as the accelerating factor of membrane degradation, the size of the effect of factors accelerating or mitigating chemical degradation could be evaluated quantitatively, and the influence of multiple factors could be represented by a single variable. With the development of a method for predicting membrane lifetime, it became possible to estimate the durability of the polymer electrolyte membrane under the specific fuel cell control as envisioned in the actual operation of an FCV. As a result, polymer electrolyte membrane design values related to the trade-off between fuel cell performance, efficiency, cost, and durability could be optimized.

1. Introduction

A fuel cell is a power source that utilizes electrochemical reactions. The power generating part is termed the membrane electrode assembly (MEA) (Fig. 1). An MEA is composed of two electrodes — the anode and cathode — and a polymer electrolyte membrane (PEM) that is positioned between the electrodes. The hydrogen that is the fuel is decomposed into protons and electrons on the anode catalyst. PEM is an electrical insulant to transmit protons selectively between the two electrodes without conducting electrons. Protons that come from the anode are used for reaction on the cathode catalyst with oxygen that is taken from the atmosphere, and the water is then produced as the reaction product. Because the two electrodes are insulated by a PEM, electromotive force is generated between the electrodes. The electrons are parted from the protons to travel between the electrodes, causing a current to flow in the circuit. The number of electrons flowing in the circuit is equal to the number of protons moving through the PEM, so that the performance of the fuel cell is mainly determined by the activity of the catalyst on the two electrodes and by the proton conductivity of the PEM.

In order to produce high power output, a fuel cell installed in a fuel cell vehicle (FCV) has hundreds of MEAs

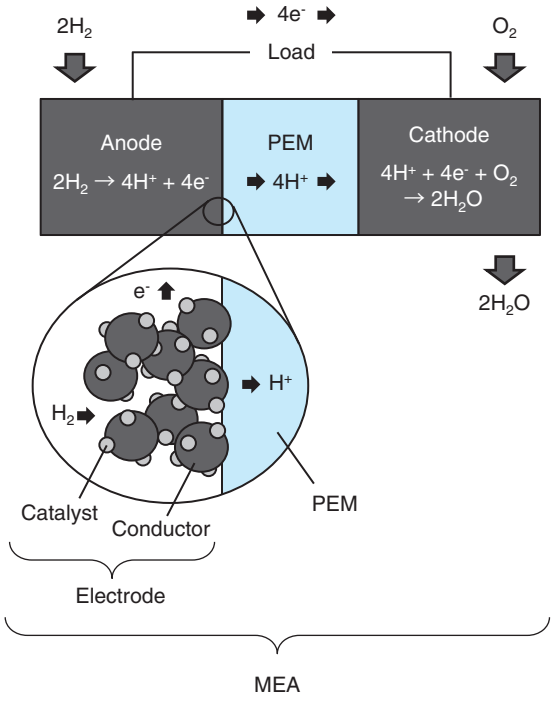


Fig. 1 Schematic cross section of typical fuel cell

* Automobile R&D Center

stacked in layers, thus it is referred to as a fuel cell stack. Development of fuel cell stacks for FCV use always seeks to achieve greater compactness by means of higher power density and greater driving range by means of enhanced energy efficiency. At the same time, stacks also require endurance reliability comparable to internal combustion engines and need to achieve cost reduction to enable widespread use by consumers (Fig. 2).

Characteristics of the fuel cell stack are related to design parameters of the PEM, including membrane thickness, ion exchange content, and the amount of additives. For performance of a fuel cell stack, higher ion exchange content and a thinner membrane are better for increased PEM proton conductivity. For durability, a thicker membrane and lower ion exchange content are preferable. In many cases, the additives used to assure PEM durability impede proton transportation, so that performance is sacrificed. For efficiency, a membrane that is too thick will resist proton transportation, while one that is too thin will allow hydrogen, which is the fuel, to permeate through to the cathode side. In either case, energy efficiency is reduced.

As this indicates, PEM design parameters are related to several fuel cell stack characteristics. Changing one PEM design parameter will cause interlinked changes in multiple fuel cell stack characteristics. Furthermore, these fuel cell stack characteristics involve trade-offs, so that PEM design necessitates optimization of the required fuel cell stack characteristics. Every time a PEM design is changed, it is necessary to evaluate the balance of performance, energy efficiency, and durability, so optimization of the PEM design is not readily achieved.

A particular issue that used to be faced in optimization of PEM design was the amount of time it took to estimate PEM durability. PEM degradation includes mechanical degradation due to fatigue caused by mechanical stress as well as chemical degradation in which molecules are

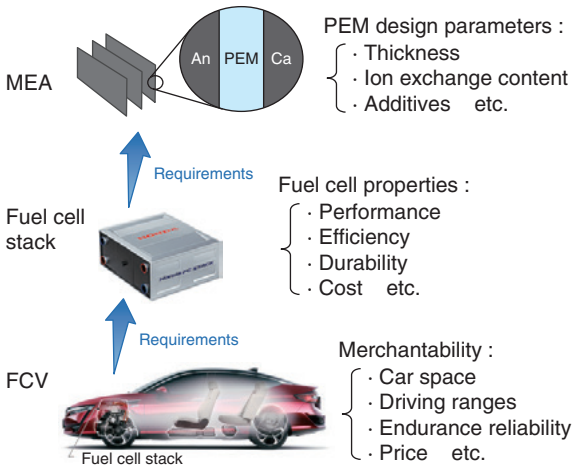


Fig. 2 Hierarchy of requirements from vehicle to materials

decomposed by chemical reactions[1]. Regarding mechanical degradation, there have been reports of design using computer-aided engineering (CAE) for material strength calculations. PEM durability is estimated based on the fatigue limits of polymeric material determined from the mechanical properties of the membrane[2, 3]. In other words, model-based approaches have been employed to estimate PEM durability in a shorter period of time by the use of CAE, in the case of mechanical degradation. As for chemical degradation, however, there have been issues with quantitative evaluation of the degradation rate because chemical degradation tends to occur locally or suddenly, so that former reports have been confined to clarification of reaction mechanisms[4] and development of highly durable materials[5]. The only method that has been available for estimating PEM durability or lifetime, therefore, has been to implement durability testing over extended periods of time, and this has been a factor in lengthening the process of fuel cell development.

2. Purpose of Development

In order to optimize the PEM design within a brief period in the development of fuel cells for FCV use, new technology capable of estimating the durability of a designed PEM without implementing durability testing needs to be developed.

A model-based development approach was employed in this report as a method for quantitative evaluation of chemical degradation. Quantitative evaluation of degradation speed and PEM durability enable the computational prediction of the PEM lifetime.

3. Modelization and Mathematical Description of Chemical Degradation

3.1. Ascertaining Degradation Behavior

The chemical degradation of PEM does not occur at a fixed rate[6]. Prediction of PEM lifetime therefore requires a grasp of how the rate of degradation changes. The reaction mechanism of chemical degradation was therefore modelized and the rate of degradation was formulated in the mathematical description as a function of operating time, thereby enabling prediction of the estimated PEM lifetime.

The 2016 model FCV adopts a perfluorosulfonic acid (PFSA) membrane with the goal of chemical stability. PFSA molecules feature a fluorocarbon backbone (-CF_2-) that is well known as Teflon®. The typical chemical structure of PFSA is shown in Fig. 3. The causative agent of chemical degradation of PFSA membrane is thought to be a radical species represented by hydroxyl radical, which is a side reaction product of fuel cell operation. Radicals are highly reactive reagents, and are known to be causative agents that generally attack and degrade polymeric material. It has been suggested that the following reaction formulas describe the main PFSA membrane degradation reactions[4].

$$R_f - CF_2COOH + \cdot OH \rightarrow R_f - CF_2 \cdot + CO_2 + H_2O \quad (1)$$

$$R_f - CF_2 \cdot + \cdot OH \rightarrow R_f - CF_2OH \rightarrow R_f - COF + H^+ + F^- \quad (2)$$

$$R_f - COF + H_2O \rightarrow R_f - COOH + H^+ + F^- \quad (3)$$

It is known that as chemical degradation causes the PFSA membrane to decompose, the membrane grows thinner. The reason is that the carbon (C) and fluorine (F) that are component substances of the PFSA membrane are released from the PEM in the form of CO_2 and fluoride ions.

An example of a report of PFSA membrane durability testing is shown in Fig. 4[5]. The vertical axis shows the amount of hydrogen crossover through the PEM in terms of the crossover current value. The permeation volume of the gas is in inverse proportion to the thickness of the membrane, so when the PEM degrades and grows thinner, the hydrogen permeation volume increases. However, the chemical degradation of a PEM generally occurs locally, so the increase in hydrogen permeation volume that accompanies reduction in membrane thickness is hardly observed at all. A sudden increase takes place at the stage of reaching pinhole failure of the PEM. Thus, there are no conspicuous signs that warn of impending PEM failure, and this is the issue for prediction of membrane lifetime.

The release of fluoride ions that occurs with chemical degradation of the PFSA membrane is termed fluoride release, and comparisons of the amounts or rates of fluoride release are sometimes made when evaluating PEM's stability against chemical degradation. However, the fluoride release rate does not remain constant in durability testing even when tested under steady-state conditions[6]. It had been thought, therefore, that PEM lifetime could not be predicted from the fluoride release rate. Another consideration was that evaluation of fluoride release involved measurement of the total quantity of fluoride ions and averaging it out over the electrode area, so that correct evaluation could not readily be carried out when local degradation existed.

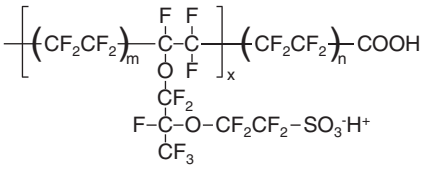


Fig. 3 Chemical structure of PFSA (Nafion®)

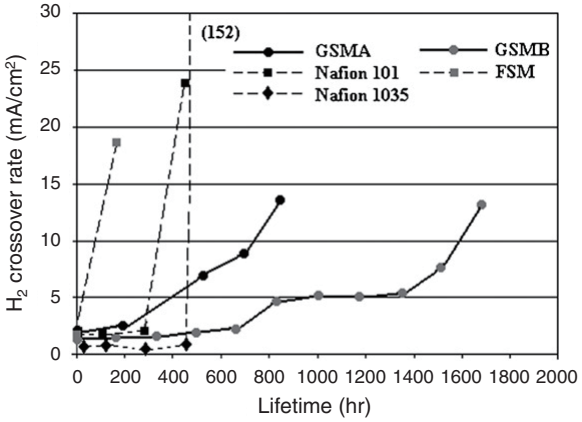


Fig. 4 Comparison of Nafion®, GORE-SELECT® membranes (GSM A, B) and their comparative non-reinforced membrane (FSM)

Previously, therefore, chemical degradation of PEM occurring locally interfered with the quantitative evaluation of the degradation speed. The present research examined methods for evaluating chemical degradation under conditions that would not cause local degradation in the PEM. Conceivable causes of local chemical degradation would be inhomogeneous environments, such as temperature and humidity inside the cell used for durability testing, as well as flow rate and pressure of reaction gas. This was addressed by devising a cell heater capacity and heater shape, and arranging the proper placement of thermal insulator in order to maintain an appropriate balance of heating and heat release in order to achieve homogeneous temperatures. For the reaction gas, the shape of gas flow channels and the gas flow rate were also determined properly so that gas would be homogeneously distributed throughout the cell interior.

Evaluation of chemical degradation was carried out by open circuit voltage (OCV) testing. By placing the fuel cell in a particular state in which it is supplied with fuel but is not generating electricity, the fuel cell tends to produce many radical species that are a side reaction product of fuel cell reaction, as shown in Fig. 1. Since the radical species promotes the PEM degradation reaction, this is a prevalent method of accelerated testing for evaluation of PEM durability against chemical degradation[6].

The results for fluoride release quantity during OCV testing are shown in Fig. 5. When the temperature or gas in the fuel cell are not homogeneously distributed (shown by box-shaped points in Fig. 5), the released fluoride quantity increases rapidly. This behavior matches with the former generally accepted view. The results of analysis confirmed that local degradation originating from the fuel cell structure was occurring. On the other hand, when the internal environment of the cell was made homogeneous, and when homogeneity and high reproducibility of chemical degradation of the PEM were achieved (shown by round points in Fig. 5), the fluoride release rate could be seen to increase smoothly.

The PEM thickness was measured after OCV testing, which clearly indicates that the size of the reduction in membrane thickness and the fluoride release quantity are correlated, as shown in Fig. 6. If calculation of fluoride release behavior were to become possible, therefore, the lifetime of PEM could be predicted by converting fluoride

release quantity into the reduction in membrane thickness using the relationship shown in Fig. 6.

3.2. Modelization of the Degradation Mechanism

A proposed mechanism of the chemical degradation of PFSA membrane is shown in Fig. 7[7]. There are thought to be two reaction mechanisms involved. One is scission of the main chains of polymer (shown by green scissor symbols in Fig. 7) and the other is an unzipping reaction in which the end groups of the main chains progressively degrade (refer to Eqs. (1) to (3) in the previous section; shown by blue arrows in Fig. 7). When scission of the main chain occurs, the location of the cleavage becomes two new end groups, which suggests that number of points of origin for the unzipping reaction increases exponentially. The reaction mechanism for chemical degradation of the PFSA membrane was therefore modelized and the fluoride release behavior calculated, and it was confirmed that the experimental results shown in Fig. 5 could be explained by these two reaction mechanisms of chemical degradation.

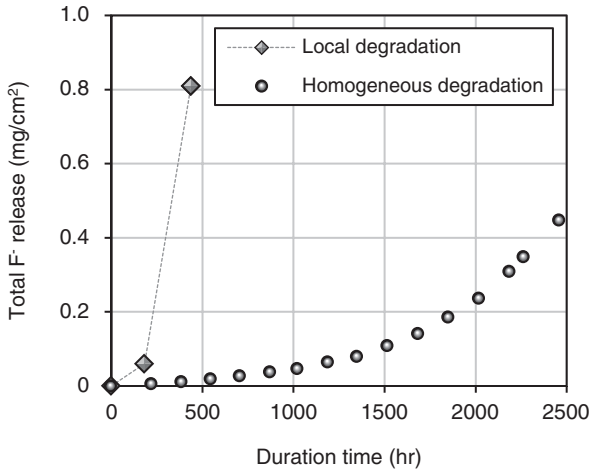


Fig. 5 Fluoride release behavior during stable condition durability test

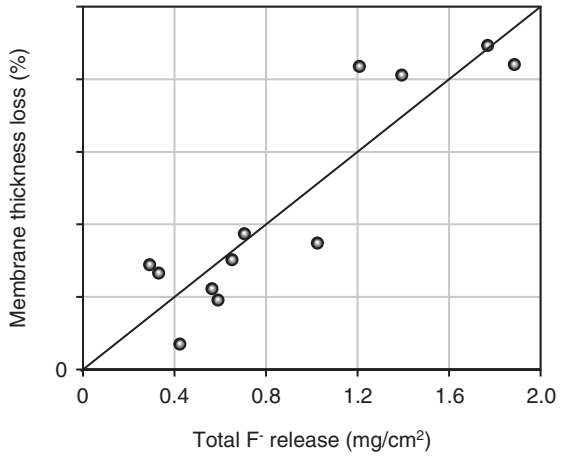


Fig. 6 Correlation between total amount of fluoride release and reduction of membrane thickness

In creating the model, the formation rate of the radical species per unit time that is a causative agent of chemical degradation was set as v_{Rad}. The number of -CF_2- bonds in the polymer main chain was set as N_{Main}, with the end group number set as N_{End}, and the initial values of these were set by the average molecular weight of the polymer. The probability that the radical species would encounter the main chain or the end group was determined with reference to the general diffusion model for polymers, and it was presumed to be in proportion to the ratio of N_{Main} and N_{End}. The main chain degradation probability R_{Main} was taken as the probability that when the radical species encountered the polymer main chain, scission of the main chain would occur. The probability R_{Main} was determined in consideration of the chemically stable structure of the fluorocarbon backbone (-CF_2-) of the PFSA polymer molecule. Since the main chain degradation number D_{Main} is in proportion to v_{Rad}, R_{Main}, and the abundance ratio of the main chain unit number N_{Main}, it can be described as follows:

$$D_{Main} = v_{Rad}\, R_{Main} \left(\frac{N_{Main}}{N_{Main} + N_{End}} \right) \tag{4}$$

In the same way, when the radical species encounter an end group of the main chain, the probability that degradation will occur due to the unzipping reaction is set as the end group degradation probability R_{End}. Since the end group degradation number D_{End} is in proportion to v_{Rad}, R_{End}, and the abundance ratio of chain end group number N_{End}, it can be described as follows:

$$D_{End} = v_{Rad}\, R_{End} \left(\frac{N_{End}}{N_{Main} + N_{End}} \right) \tag{5}$$

Next, since the N_{Main} is reduced by the scission of the main chain and degradation of end groups, this becomes:

$$N_{Main\ t+1} = N_{Main\ t} - (D_{Main\ t} + D_{End\ t}) \tag{6}$$

Since the N_{End} has two end groups created at each scission location, this becomes:

$$N_{End\ t+1} = N_{End\ t} + 2D_{Main\ t} \tag{7}$$

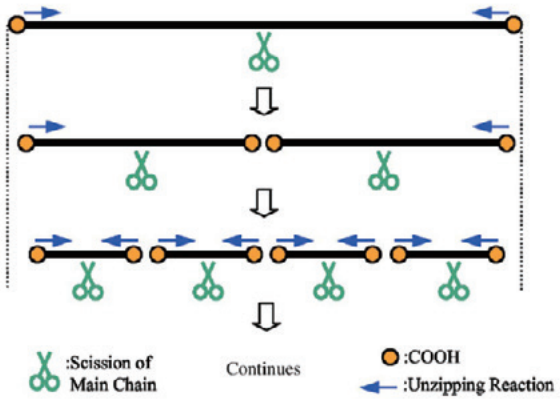


Fig. 7 Degradation mechanism of PFSA membrane

Given Eqs. (1) to (3), the degradation of one end group produces two fluoride ions. Therefore the fluoride release quantity F over time t can be described as follows:

$$F = \sum_{t} (c\, D_{\mathrm{Main}\,t} + 2D_{\mathrm{End}\,t}) \quad (8)$$

c is a constant that is determined by the chemical structure of the PFSA polymer molecule, an example of which is shown in Fig. 3. Figure 8(1) shows the results of the fluoride release quantity calculation. The experimental results shown in Fig. 5 are also shown in this figure (marked as "Experimental data" in Fig. 8), and the scale of the axes is adjusted to fit the experimental results. Modeling of the two reaction mechanisms of chemical degradation of PFSA membrane — main chain scission and the unzipping reaction — enabled confirmation that the calculated fluoride release quantity formed a smoothly increasing curve that is similar to the curve of the experimental results.

It was also confirmed that when either the degradation probability R_{Main} or R_{End} in the created model is defined as zero, in either case the fluoride release behavior becomes a straight line and does not match the experimental results (Fig. 8). Case (2) supposes occurrence only of the unzipping reaction, and case (3) supposes occurrence only of scission of the main chain. These calculation results from modeling of the chemical degradation reaction not only substantiate the notion that chemical degradation of the PFSA membrane consists of the two reaction mechanisms of main chain scission and unzipping reaction, but also corroborate the notion that the fluoride release rate increases continuously and the graph of fluoride release amount describes a smooth curve.

3.3. Mathematical Description of Fluoride Release Behavior

It was confirmed by both experimental and theoretical approaches that the fluoride release quantity shows

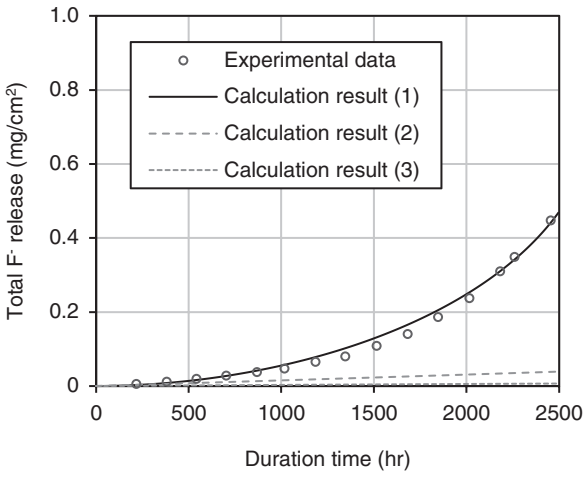


Fig. 8 Fluoride release behavior, calculated by PFSA membrane degradation model

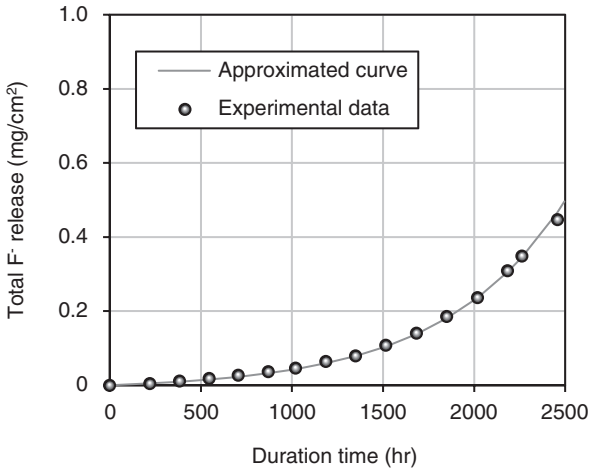


Fig. 9 Experimental data of fluoride release behavior, approximated by exponential function

smoothly increasing behavior. In order to describe the fluoride release quantity F as a function of OCV test time t, Eq. (9) was formulated as an experimental equation that closely matches the experimental results.

$$F(t) = a[\exp(b \cdot t) - 1] \quad (9)$$

Figure 9 shows the experimental result that was shown in Fig. 5, being fitted with Eq. (9). Coefficient a and coefficient b include information on the degradation speed and chemical stability of PEM.

4. Evaluation by the Accelerating Factor of Chemical Degradation

4.1. Acceleration of Degradation by Metal Ions

One of the factors that influence the PFSA membrane chemical degradation rate is contamination by metal ions. Among metal ions, ferrous ions in particular are known to act powerfully to accelerate PFSA membrane degradation. This is because ferrous ions have catalytic activity of the Fenton reaction that decomposes hydrogen peroxide. In fuel cells, there is a side reaction to the fuel cell reaction shown in Fig. 1, whereby there is a certain probability that hydrogen peroxide will be formed. Ferrous ions decompose the hydrogen peroxide by the Fenton reaction shown in Eq. (10), forming a highly reactive hydroxyl radical. Fe^{3+} reacts with hydrogen peroxide or other such active species and reduces to Fe^{2+}, and is thought to function repeatedly as a catalyst[7].

$$Fe^{2+} + H_2O_2 + H^+ \rightarrow Fe^{3+} + \cdot OH + H_2O \quad (10)$$

Ferrous ions were mixed into a PEM and carefully kept in a homogeneous concentration in order to confirm the relationship between the concentration of ferrous ions and their accelerating effect of chemical degradation. An OCV test was then carried out, with the result shown in

Fig. 10. As the concentration of ferrous ions increases to 0.2, 0.3, and 0.5 μg/cm^2, the slope of the fluoride release quantity curve grows steeper, confirming that the chemical degradation is being accelerated by the ferrous ions.

At the same time, Fig. 10 also shows the results of fitting the exponential function of Eq. (9) to fluoride release quantity during the OCV test. The data for a ferrous ion concentration of 0.0 μg/cm^2 (below the lower detection limit) is the same as shown in Fig. 9. The fitting results show that the fluoride release behavior can be represented by fixing coefficient b and varying only coefficient a. Coefficient a is therefore defined as the accelerating factor of chemical degradation. The accelerating factor can be obtained by fitting Eq. (9) with the experimental fluoride release data, and it can be used as an indicator of the severity of chemical degradation. At the same time, the accelerating factor is also an indicator of the size of the effect of factors that accelerate chemical degradation. Since the accelerating factor increases as the ferrous ion concentration in the PEM increases, the accelerating factor is a function of ferrous ion concentration.

4.2. Degradation Mitigation by Radical Quencher

In order to mitigate chemical degradation of PEM, adding a radical quencher is a well-known method to assure the durability of the PFSA membrane. A radical quencher is an additive that actively reacts with a radical species and renders it harmless. This function is frequently fulfilled by metal ions or organic molecules with conjugated systems. When metal ion X is used as a radical quencher, for example, the reaction can be described by Eq. (11)[8].

$$\cdot OH + X^{n+} + H^+ \rightarrow X^{(n+1)} + H_2O \qquad (11)$$

$X^{(n+1)+}$ ions oxidized by hydroxyl radical are reduced to X^{n+} ions by hydrogen or some other means so that they function repeatedly as a catalyst. The effect of radical quencher in mitigating the rate of chemical degradation can also be indicated by the accelerating factor. As in the case of ferrous ion, the accelerating factor is a function of the amount of radical quencher.

Moreover, when using a radical quencher as an additive, accelerating factor becomes a function of the two factors of ferrous ion concentration and amount of additive in the PEM. In order to decide the amount of additive required to assure sufficient durability of the PEM relative to the assumed amount of ferrous ion contamination during FCV operation, it is necessary to know the relationship between the quantities of these two factors and the value of accelerating factor. There is an interaction here between the acceleration effect of ferrous ions and the mitigation effect of the radical quencher. This means that a map of the value for accelerating factor that is determined by the two factors needs to be created experimentally by combination testing.

Figure 11 shows the map of accelerating factor obtained through testing. The ferrous ion contamination amount and radical quencher additive amount are placed on horizontal axes and the blue points are experimental data of the accelerating factor obtained by OCV testing. Based on these test results, the three-dimensional map was created to represent the accelerating factor as a function of the ferrous ion contamination amount and the radical quencher additive amount. The introduction of the concept of the accelerating factor in order to represent the degree of the fluoride release rate has made it possible to not only deal quantitatively with the effect of factors that accelerate or mitigate chemical degradation, but also to indicate the size of the effect of multiple factors by a single variable.

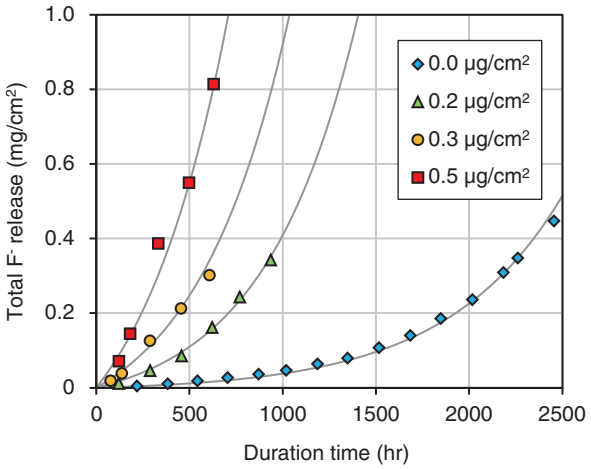


Fig. 10 Comparison of fluoride release behavior between membranes with different amounts of Fe ion contamination

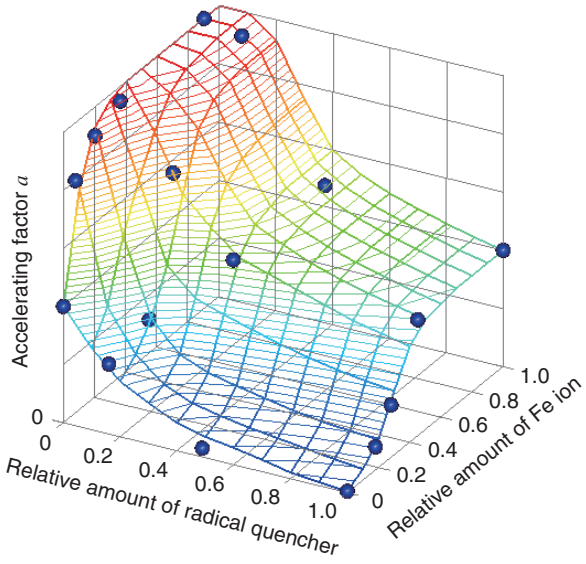


Fig. 11 3D visualized map of accelerating factor a

5. Technology for Predicting PEM Lifetime

5.1. Predicting Lifetime in a Non-Steady State

In Chapter 4, the OCV test aiming to evaluate the accelerating factor was carried out in a steady state. In order to fit the exponential function to the behavior of fluoride release quantity, it was necessary for the factors being studied, the environment in the cell, and other conditions to be kept constant during testing.

During FCV operation, however, the operating environment, the operating conditions, the amount of metal ion contamination, and other such factors that influence the rate of chemical degradation are constantly changing. Therefore the values of accelerating factor will be constantly changing. Consequently, the PEM lifetime prediction method considering actual FCV operation necessitates confirmation of whether the degradation behavior represented by the exponential function in Equation (9), which was set by OCV testing in a steady state, can also be applied in a non-steady state.

Figure 12 presents an example of non-steady state testing. As a model case, the accelerating factor was arranged to change by adding metal ion contamination in PEM, at a certain time of OCV testing. In this case, the behavior of the fluoride release cannot be represented by the single accelerating factor. Based on the experimental test results shown in Fig. 12, it is necessary to consider how to handle the mathematical formulas for non-steady states in which the accelerating factor changes during OCV testing. Figure 12 shows that the behavior of fluoride release according to test conditions (1) and (2) can be approximated by the two exponential functions in which the accelerating factor is expressed as a_1 and a_2. Accelerating factors a_1 and a_2 are inserted into Eq. (9), Eqs. (12) and (13) below are the result.

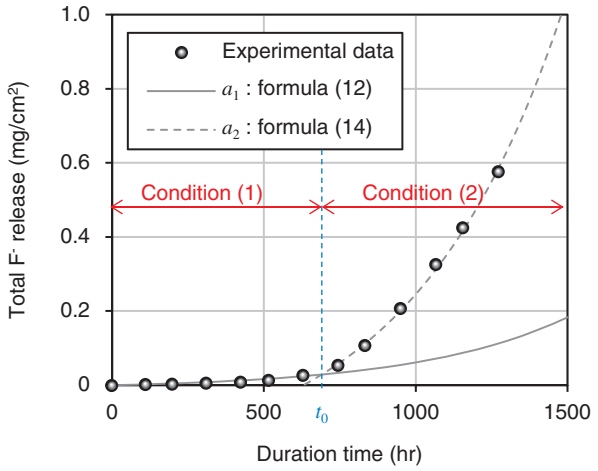


Fig. 12 Fluoride release behavior in case of non-steady state in which test condition was changed at 700 hr

$$F_1(t) = a_1[\exp(b\cdot t)-1] \quad (12)$$

$$F_2(t) = a_2[\exp(b\cdot t)-1] \quad (13)$$

Since Eqs. (12) and (13) both pass through the origin, Eq. (13) is fitted into Fig. 12 by shifting just the time difference Δt in the direction of the x axis. If this function is $F_2'(t)$, then:

$$F_2'(t) = a_2\{\exp[b\cdot(t-\Delta t)]-1\} \quad (14)$$

Next, consideration was given to expressing Δt by the accelerating factors a_1 and a_2. In Fig. 12, the time at which the testing conditions are changed so that the accelerating factor changes from a_1 to a_2 can be expressed as $t = t_0$. In that case, at t_0 it will be the case that $F_1(t_0) = F_2'(t_0) = F_2(t_0 - \Delta t)$, so that:

$$\begin{aligned} F_1(t_0) &= a_1[\exp(b\cdot t_0)-1] \\ &= a_2\{\exp[b\cdot(t_0-\Delta t)]-1\} = F_2'(t_0) \end{aligned} \quad (15)$$

Solving this equation (15) for Δt results in:

$$\Delta t = t_0 - \frac{\log\{\frac{a_1}{a_2}[\exp(b\cdot t_0)-1]+1\}}{b} \quad (16)$$

Thus, in the case that the accelerating factor changes during durability testing at ($t = t_0$), the exponential function (13) with new accelerating factor should be displaced toward the x axis for the size of the Δt determined in Eq. (16). Then the fluoride release behavior can be expressed by connecting the exponential functions while keeping the fluoride release quantity the same at time t_0.

In this way, it was confirmed from the test result shown in Fig. 12 that fluoride release behavior can be calculated as a function of the accelerating factor even in a non-steady state in which the value of accelerating factor changes over time. This indicates that lifetime of PEM can be predicted in the kind of non-steady state envisioning an actual FCV operating environment.

5.2. PEM Lifetime Design

A calculating method considering non-steady state was developed in order to predict PEM lifetime envisioning actual FCV operation. The results can be used to estimate excesses or deficiencies in PEM durability. Optimization of PEM design and fuel cell stack operation control was carried out according to the calculation result. This process is shown in Fig. 13. The PEM thickness is indicated by the black line, while the accelerating factor is indicated by the red line. The solid lines and the broken lines are in respectively corresponding relationships.

In order to predict PEM lifetime that envisions actual FCV operation, it is necessary to grasp the changes in accelerating factor that occur during FCV operation. The operating conditions, the amount of metal ion contamination, and other such factors that affect chemical degradation of the PEM are constantly undergoing change during FCV operation. For example, since the fuel cell

stack uses many parts that contain steel, the amount of ferrous ions that contaminate the PEM gradually increases during FCV operation. As described in section 4.2., the introduction of the accelerating factor makes it possible to represent the effects of multiple factors affecting the chemical degradation of the PEM by a single variable. The effects of these factors were confirmed using the results from bench testing that demonstrate the driving modes of an actual vehicle using a fuel cell stack with the same specifications as stacks installed in actual vehicles (the red broken line in Fig. 13).

Next, a calculation method that was developed to consider a non-steady state shown in section 5.1. was used to calculate the fluoride release quantity from the accelerating factor. Then the relationship between membrane thickness and fluoride release quantity shown in Fig. 6 was used to convert the fluoride release quantity into the amount of reduction in membrane thickness. This allowed calculations predicting a decrease in membrane thickness during FCV operation (the black broken line in Fig. 13). In the calculations, past user data was used for reference to devise an operating method sufficiently demanding in terms of chemical degradation of the PEM. The calculation results confirm that, with the initial design shown by the broken lines in Fig. 13, the accelerating factor starts increasing immediately after the FCV starts operating, and that the membrane thickness decreases at a rapid rate. These results show clearly that PEM durability is insufficient.

Because the method for predicting lifetime by calculation makes prolonged durability testing unnecessary, the durability and the lifetime of the PEM can be readily designed. Also, because it becomes possible to seek out parameters that will effectively increase PEM durability without degrading performance or energy efficiency, PEM design can be readily optimized.

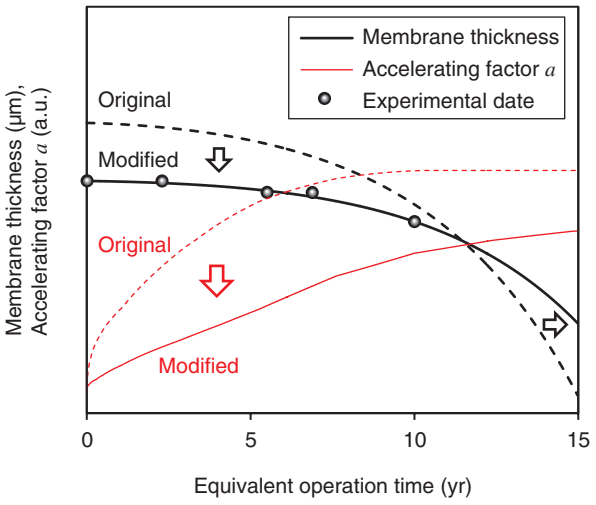


Fig. 13 Achievement of satisfying lifetime without reducing FC performance and efficiency.

As a result of this investigation of durability enhancement, the PEM design and fuel cell stack operation control were modified. The calculation results for the modified specifications are shown in Fig. 13 by the solid lines. Changes to PEM design included an increase in the amount of radical quencher added with consideration of the map in Fig. 11 obtained in section 4.2. This made it possible to hold down the increase in accelerating factor that occurred when ferrous ions contaminated the PEM. Changes made in fuel cell stack operation control also achieved control of the water content in the fuel cell stack[9]. This made it possible to help prevent the release of ferrous ions from metal parts and their contamination of the PEM as well as to limit the increase in the accelerating factor.

As a result of measures like these, the accelerating factor was found to increase at a lower rate than with the previous specifications, as shown by the solid red line in Fig. 13. It was also confirmed from the results for calculation of membrane thickness, as shown by the solid black line in the figure, that the rate of decrease in membrane thickness was suppressed. These results further confirm that sufficient durability is assured by the specifications incorporating the measures, and that there is an available margin for further reduction of the initial PEM thickness to improve fuel cell performance.

In Fig. 13, the experimental results of durability testing carried out with specifications incorporating the measures are also plotted. As was the case with the calculations, past user data was used for reference to devise an operating method sufficiently demanding in terms of chemical degradation of the PEM. The horizontal axis shows the equivalent years to actual vehicle operation. The test results match closely with the calculation results, confirming that the lifetime prediction method developed in the present research is highly predictive. This method has enabled quantitative evaluation of PEM durability. As a result, PEM lifetime can be predicted by calculation, without implementing durability testing over long periods of time, and the results can be provided as feedback for PEM design. This technology was applied to the 2016 model FCV, and the optimization of PEM design contributed to the balance of performance and durability achieved in the fuel cell stack.

6. Conclusion

In this report, a calculation methodology for predicting PEM lifetime was developed. The chemical degradation behavior of PFSA membrane is modelized as a function of operating time of fuel cells, which enable quantitative estimation of chemical degradation speed and durability of PEM.

(1) It was confirmed that chemical degradation of the PFSA membrane causes the fluoride release and its quantity increases smoothly due to the two reaction mechanisms of chemical degradation — the scission of polymer main

chain and the unzipping reaction. It was also confirmed by both experiment and modeling that those behaviors can be approximated by exponential functions.

(2) By defining the coefficient of the exponential function that approximates fluoride release behavior as the accelerating factor, it became possible to quantitatively estimate the effect of factors that accelerate or mitigate chemical degradation of the PEM. This also made it possible to represent the size of the effects of multiple factors by a single variable.

(3) It became possible to calculate fluoride release behavior as a function of the accelerating factor even in non-steady states in which the value of the accelerating factor changes with time. This enabled PEM lifetime prediction that envisions actual FCV operation.

References

(1) Borup, R., et al.: Scientific Aspects of Polymer Electrolyte Fuel Cell Durability and Degradation, Chem. Rev., 107, p. 3904-3951, (2007)

(2) Kai, Y., Kitayama, Y., Omiya, M., Uchiyama, T., Kato, M.: Crack Formation in Membrane Electrode Assembly Under Static and Cyclic Loadings, ASME J. Fuel Cell Sci. Technol., 10, p. 021007, (2013)

(3) Sugishita, M., Ohmori, S.: Life Prediction Technology of Fuel Cell Polymer Electrolyte Membrane under Mechanical Degradation, Honda R&D Technical Review, Vol. 28, No. 1, p. 59-67

(4) Curtin, D. E., Lousenberg, R. D., Henry, T. J., Tangeman, P. C., Tisack, M. E.: Advanced materials for improved PEMFC performance and life, J. Power Sources, 131, p. 41-48, (2004)

(5) Liu, W., Ruth, K., Rusch, G.: Membrane Durability in PEM Fuel Cells, J. New Mater. Electrochem. Syst., 4, p. 227-231, (2001)

(6) Coms, F. D.: The Chemistry of Fuel Cell Membrane Chemical Degradation, ECS Transactions, 16 (2), p. 235-255, (2008)

(7) Hommura, S., Kawahara, K., Shimohira, T., Teraoka, Y.: Development of a Method for Clarifying the Perfluorosulfonated Membrane Degradation Mechanism in a Fuel Cell Environment, J. Electrochem. Soc., 155 (1), p. A29-A33, (2008)

(8) Endoh, E.: Development of Highly Durable PFSA Membrane and MEA for PEMFC Under High Temperature and Low Humidity Conditions, ECS Trans., 16 (2), p. 1229-1240, (2008)

(9) Nagumo, K., Inoue, M.: Numerical Prediction of Water Content Distribution of Catalyst Coated Membrane of Fuel Cell Stack using Simulation, Honda R&D Technical Review, Vol. 28, No. 1, p. 26-33

■ Author ■



Atsushi HIRAIDE

Life Prediction Technology of Fuel Cell Polymer Electrolyte Membrane under Mechanical Degradation

Masashi SUGISHITA* Suguru OHMORI*

ABSTRACT

A method was developed for predicting electrolyte membrane life under mechanical degradation, by quantifying the mechanical stress generated on the fuel cell polymer electrolyte membrane and quantitatively understanding the impact on mechanical degradation. In an environment with repeated drying and wetting, mechanical degradation of the electrolyte membrane progresses at the cracks inside the catalyst layers that are bonded to the electrolyte membrane. This study focused on changes in the electrolyte membrane and catalyst layer properties in the temperature and humidity environment in which fuel cells operate as a factor that increases stress. The electrolyte membrane and catalyst layer properties were measured at the temperatures and humidity under which fuel cells operate, and the measured property values were reflected to a stress analysis model that uses the finite element method in an effort to increase the stress prediction accuracy. The cumulative fatigue damage law was applied to the relationship between the generated stress and stress frequency and the material limit line to quantify the impact of mechanical degradation on life as the life consumption rate, and it was confirmed that the life consumption rate is correlated with the thickness of the electrolyte membrane after durability tests. This enabled prediction of electrolyte membrane life according to mechanical stress. Durability tests that accelerate mechanical degradation were performed using a full-scale-size membrane electrode assembly, and the accuracy of the developed life prediction technology was verified. A high correlation was obtained, which confirmed that the developed life prediction technology can be applied to an on-board-size membrane electrode assembly.

1. Introduction

Fuel cells are power-generating devices that produce electricity by the electrochemical reaction between hydrogen and oxygen. The actual reactions are the oxidization reaction of hydrogen at the anode shown in reaction equation (1), and the oxygen reduction reaction at the cathode shown in reaction equation (2).

$$\text{Anode: } H_2 \rightarrow 2H^+ + 2e^- \quad (1)$$

$$\text{Cathode: } 1/2O_2 + 2H^+ + 2e^- \rightarrow H_2O \quad (2)$$

The electrochemical reactions in a fuel cell are as follows. First, hydrogen supplied to the anode is split into protons (H^+) and electrons on the catalyst, and the H^+ pass through the polymer electrolyte membrane (PEM) and move toward the cathode. The oxygen supplied to the cathode bonds with the electrons that pass around the outside from the anode and the H^+ that pass through the PEM to produce water. At this time the oxygen reduction reaction occurs on the cathode catalyst and produces electromotive force.

Figure 1 shows a schematic image of a fuel cell. The fuel cell structure consists of a membrane electrode assembly (MEA) that has a PEM sandwiched between catalyst layers (CL) and gas diffusion layers (GDL), and separators that form gas and coolant channels.

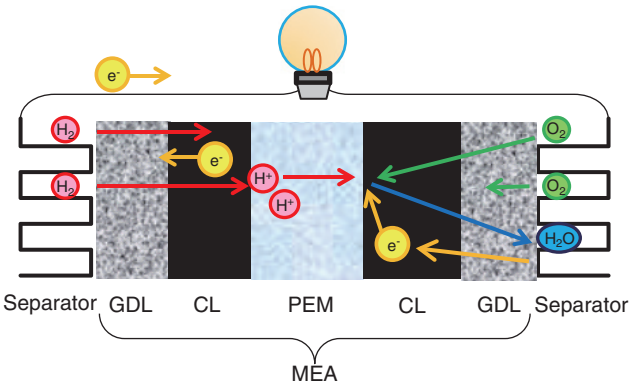


Fig. 1 Schematic image of fuel cell

* Automobile R&D Center

Fuel cell stacks for automotive applications call for a smaller size and higher power than those for home applications. In particular, reducing the PEM thickness enhances H^+ conductivity that increases the power, so a thin PEM with a thickness on the order of several tens of μm is generally used. In addition, development is under way to achieve even thinner membranes. However, securing durable reliability for PEM with thinner membranes is an issue. The fuel cell generating environment includes chemical degradation factors specific to polymers such as heat, generated water, and impurity ions[(1), (2)], and there are also various mechanical fatigue degradation factors as a result of repeated stress due to pressure differences, heating-cooling cycles, and dry-wet cycles. Among these factors, mechanical degradation of PEM is known to progress in environments where PEM experience excessive and repeated shrinking due to drying and swelling from wetting (dry-wet environment)[(2)-(6)]. This paper focused on mechanical degradation of PEM. The amount of water produced during fuel cell generation varies according to the power generation load, which means that the PEM water content also varies according to the power generation load. The PEM thickness and in-plane dimensions vary according to the water content, and much water is produced at a high power generation load, so in this condition the PEM water content increases and the PEM swells. In contrast, the PEM water content decreases and the PEM shrinks in the low power generation load condition or when power generation is stopped. Figure 2 shows a slice image of the electrode surface imaged using X-ray computed tomography. Figure 3 shows a cross-sectional image of electrode cracks. Minute electrode cracks on the order of several μm to several tens of μm in size that extend to the PEM surface form in the CL during fabrication. Figure 4 shows a cross-sectional image of PEM deformation at an electrode crack in a wet environment, and Fig. 5 shows a cross-sectional image of PEM deformation at an electrode crack in a dry environment. Mechanical degradation of PEM at electrode cracks has been reported to progress at a faster rate under this type of dry-wet environment[(2), (3), (5)].

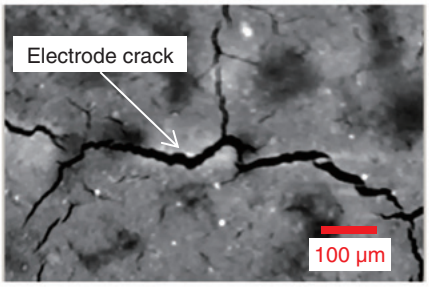


Fig. 2 Image of electrode surface using X-ray computed tomography

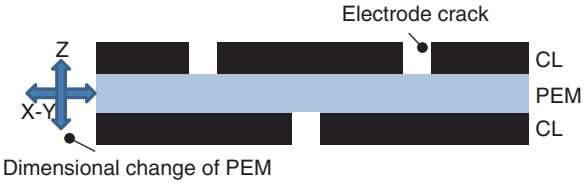


Fig. 3 Cross-sectional image of electrode crack

As part of continuing efforts to reduce degradation due to these phenomena, various methods have been reported for addressing the issue, such as methods of controlling PEM water content fluctuation, catalyst layer fabrication technology that reduces electrode cracks during fabrication, and enhancement of PEM fatigue durability[(3)]. However, it is unlikely that sufficient power generation performance and durable reliability can be achieved by using only a single method. Optimization of each aspect of technology to control PEM water content, catalyst layer fabrication technology, and material technology is called for. For this reason, it is important to understand PEM deformation behavior in a dry-wet environment, clarify the resulting stress applied to the PEM, and understand the impact of this stress on PEM life. However, no known life prediction technology has been established for understanding the impact of mechanical degradation on PEM life.

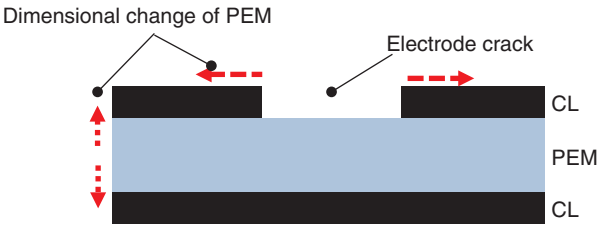


Fig. 4 Cross-sectional image of electrode crack at wet condition

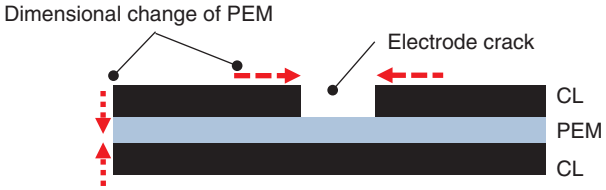


Fig. 5 Cross-sectional image of electrode crack at dry condition

2. Goal

PEM degradation at electrode cracks progresses in a dry-wet environment. Therefore, mechanical degradation of PEM is thought to progress as a result of stress concentration due to the influence of the change in the PEM water content during power generation, the resulting change in PEM dimensions, and the difference in the Young's modulus of the CL and PEM. A technique that uses the impedance

method to understand the change in the PEM water content during power generation has been proposed[7, 8]. However, the PEM is sandwiched by both electrodes as shown in Fig. 1, and it is challenging to directly understand the amount of PEM dimensional change when the water content fluctuates. In addition, the dimensional change of this part is on the order of several percent, so there are issues with using a strain gauge or other means to directly measure the stress generated on the PEM in an environment with water present during power generation. Therefore, the stress generated on the PEM is estimated from a stress analysis model using the finite element method (FEM)[4].

When constructing life prediction technology for PEM under mechanical degradation, the key factors are to clarify the generated stress and the impact of that stress on PEM life. Therefore, the goal of this study was to clarify these factors and to establish life prediction technology for PEM under mechanical degradation.

3. Establishment of Life Prediction Technology

It was thought that mechanical degradation of PEM at electrode cracks could be predicted from the generated stress and the impact of that stress on PEM life in the same manner as for typical resin materials. It was also considered that the stress generated in each water content environment could be derived using FEM from the difference in the Young's modulus of the CL and PEM and the PEM dimensional change rate in the environment in question, and that the impact on fatigue life could be estimated from the relationship between the material limit line and the generated stress and frequency in that environment. In addition, when stress is repeatedly applied to PEM, plastic deformation and cracking occur and the PEM thickness decreases[9]. Therefore, an attempt was made to predict PEM life under mechanical degradation by determining the relationship between the life and the membrane thickness.

3.1. Determination of PEM and CL Properties for Reflection to Stress Analysis

3.1.1. Determination of PEM and CL Young's modulus

The Young's modulus of the PEM and CL depend on the temperature and humidity, so the Stress-Strain (SS) curve under each environment was measured in a constant temperature and humidity chamber, and the Young's modulus was calculated from the SS curve. Table 1 shows the environmental conditions used for measurement. The shape of the sample used for measurement was a 10 mm × 50 mm rectangle, the distance between chucks was set to 20 mm, and the tensile speed was set to 50 mm/min. As it is not easy to measure the CL Young's modulus E_{CL} alone, this was calculated from the PEM Young's modulus E_{PEM}, the Young's modulus E_{CCM} of the catalyst-coated membrane (CCM) consisting of the CL coated on the PEM, and the CL volume fraction V_{CL} as shown in Eq. (1).

Table 1 Measurement conditions of Young's modulus

	PEM and CL (CCM)	
	Temperature (°C)	RH (%)
SS curve (Young's modulus)	-35	Dry
	23	50
	70	Dry
		95
	90	Dry
		95

Relative humidity: RH

Table 2 Measurement conditions of dimensional change rate

	Direction	PEM		CCM
Dimensional change rate	X-Y (in-plane)	23°C RH50%, 70°C RH95% , 70°C dry, -35°C		
	Z (thickness)	23°C	Wet to dry	
		70°C	Wet to dry	

$$E_{CL} = \frac{[E_{CCM} - (1 - V_{CL})E_{PEM}]}{V_{CL}} \quad (1)$$

3.1.2. Measurement of PEM dimensional change rate

The PEM water content fluctuates and the dimensions change according to the humidity, so the dimensional change rate was measured in a constant temperature and humidity chamber at each temperature and humidity condition shown in Table 2. In addition, the shape of the sample used to measure the dimensional change rate in the in-plane (X-Y) direction was a 10 mm × 50 mm rectangle. The distance between chucks was set to 20 mm, a displacement sensor was attached to the lower part of the measurement sample, and the dimensional change rate in the in-plane direction was measured in each environment. The shape of the sample used to measure the dimensional change rate in the thickness (Z) direction was a 3 mm × 3 mm square, and the dimensional change rate in the thickness direction was also measured in each environment.

3.2. Stress Analysis

The fuel cell internal environment, shape and other factors have various conditions, and direct visualization of the PEM deformation behavior under these conditions takes time. Accurate evaluation of life calls for quantification of stress, and stress analysis using FEM is an effective means of its achievement.

The cross-sectional structure of a fuel cell consisting of the separators, GDL, CL including crack structures, and the PEM was modeled, and stress analysis was performed in the condition with in-plane strain applied. NASTRAN was used as the FEM software, and the material property definitions were treated as material non-linear and anisotropic materials

in order to more accurately reproduce the PEM material properties. In addition, heating and pressurization processes are used when fabricating the MEA, so the interfaces between the GDL and CL and between the CL and PEM are defined as bonded interfaces. Figure 6 shows the model used to perform FEM analysis in this study. FEM analysis was performed in two steps, with input of a clamping load to the MEA via the separators as Step 1, and input of PEM and CL swelling and shrinking as Step 2. The results were used to calculate the stress produced on the PEM at electrode cracks when the PEM swells and shrinks.

3.3. Determination of Material Limit Line

The durability to fatigue resulting from PEM swelling and shrinking drops under high-temperature and high-humidity environments in the same manner as for typical resin materials. In addition, typical PEM have a softening point temperature around 80°C, and the dependence on temperature is assumed to be higher than the dependence on humidity, so the material limit line was determined at each temperature with the humidity fixed to RH 95% in a constant temperature and humidity chamber. Table 3 shows the environmental conditions used for measurement.

The shape of the sample used to determine the Stress-Number (S-N) diagram was a 10 mm × 50 mm rectangle, the distance between chucks was set to 20 mm, and the repetition rate was set to 20 mm/min.

3.4. Life Prediction of PEM under Mechanical Degradation

3.4.1. Calculation method of life consumption rate using cumulative fatigue damage law

The cumulative fatigue damage law is an empirical law related to material fatigue that predicts the life until fatigue breakdown when subjected to fluctuating stress. Figure 7 shows the S-N diagram and the stress frequency. The number of cycles to breakdown of repeated stress P_i on the material limit line is defined as N_i, and the repeated stress P_i frequency is defined as n_i. When the degree of fatigue damage is defined as ΔD_i, this can be expressed as shown in Eq. (2).

Table 3 Measurement conditions of S-N diagram

	Temperature (°C)	RH (%)
S-N diagram	70	95
	80	
	90	

$$\Delta D_i = n_i / N_i \tag{2}$$

In addition, when the cumulative degree of fatigue stress D is expressed as the cumulative value of each fatigue damage value in accordance with the frequency of various stress amplitudes, this can be arranged as shown in Eq. (3).

$$D = \sum \Delta D_i = \sum (n_i / N_i) \tag{3}$$

The value obtained by expressing the cumulative degree of fatigue stress as a percentage is defined as the life consumption rate (*Lcr*), and is shown in Eq. (4). The impact on life can be understood by expressing the relationship between the material limit line and each stress frequency using *Lcr*.

$$Lcr\,[\%] = \sum (n_i / N_i) \times 100 \tag{4}$$

The PEM properties and material limit line change according to the temperature conditions, so it is necessary to calculate *Lcr* from the material limit line and the generated stress value in accordance with the environment. *Lcr* was calculated using the cumulative fatigue damage law from the relationship between the generated stress value obtained by stress analysis using FEM as described in section 3.2. and the PEM material limit line described in section 3.3.

3.4.2. Creation of *Lcr* - membrane thickness conversion formula

The generated stress depends on the difference in the water content of the electrolyte membrane under a dry-wet environment, so a dry-wet cycle durability test was

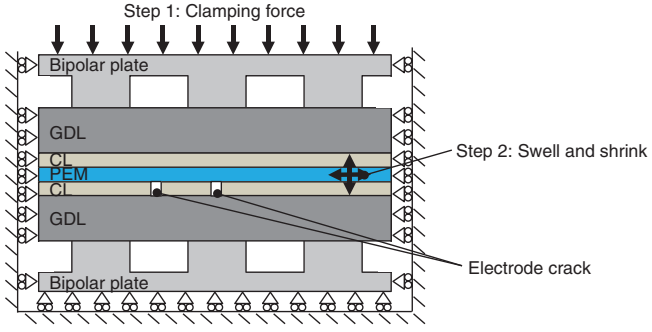


Fig. 6 FEM analysis model for dry-wet cycle

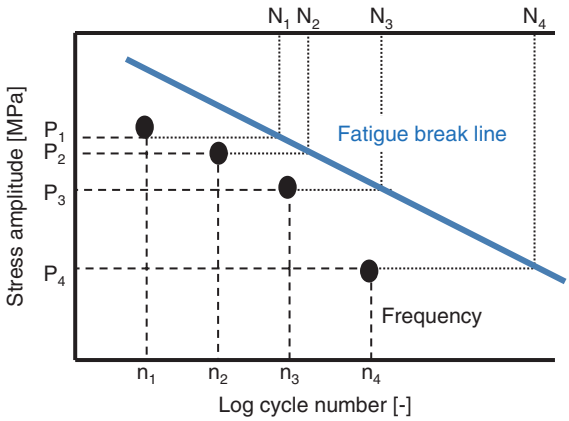


Fig. 7 Cumulative fatigue damage law

Table 4 Conditions of RH cycle test

	Test condition
Temperature (°C)	90
RH (%)	30, 70, 120
Gas supply	Gas: N_2 (Both anode and cathode) Pressure supply: Normal pressure Flow rate: 2 L/min (Both anode and cathode)

performed. The dry-wet cycle durability conditions set the low-humidity side as the dry condition, and the test was performed with three high-humidity-side conditions as shown in Table 4. An on-board-size MEA has a power-generating area on the order of several hundred cm^2, and an in-plane humidity distribution occurs during the dry-wet cycle. Therefore, the test was performed using a 40 mm × 60 mm-size MEA to reduce the effect on the in-plane humidity distribution.

The PEM thickness at electrode cracks after the dry-wet cycle durability test was analyzed to determine the correlation between the *Lcr* described in term 3.4.1. and the membrane thickness, and a correlation line was created for deriving the membrane thickness from the *Lcr*.

3.5. Verification Using On-board-size MEA

3.5.1. Verification of prediction accuracy using on-board-size MEA

The prediction accuracy was verified using an on-board-size MEA with a power-generating area on the order of several hundred cm^2. Figure 8 shows the durability test conditions used for verification. The durability conditions were set to accelerate mechanical degradation of the PEM by applying dry and wet conditions and pressure differences under a high-temperature environment. The temperature was set to 90°C, which is a condition that reduces PEM fatigue resistance under mechanical degradation. In addition, the dry-wet conditions set the wet side to RH 100% and the dry side to RH 1% to produce a large water content difference. Regarding the pressure difference conditions, the anode pressure was kept constant, and a pressure difference was applied by varying the cathode pressure. An in-plane humidity distribution occurs as the MEA area increases, but the in-plane condition was understood by measuring the in-plane humidity distribution and by using technology to predict the in-plane water content distribution[7), (8), (10)]. Mechanical degradation of the PEM progresses in locations where an in-plane water content difference occurs in the power-generating area, so the PEM life prediction accuracy was verified at electrode cracks in the location where the greatest water content difference occurred.

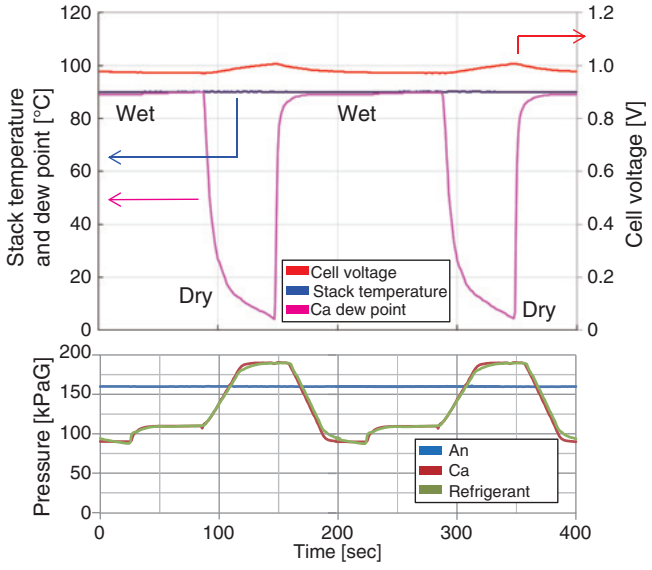


Fig. 8 Profile of accelerated stress test for mechanical degradation of PEM

4. Verification Results

4.1. PEM and CL Property Results for Reflection to Stress Analysis

4.1.1. PEM and CL Young's modulus results

Figure 9 shows the temperature dependence of the Young's modulus of the CL and PEM calculated using Eq. (1). These results show that each Young's modulus decreases as the temperature rises. In addition, the Young's modulus decreases additionally under high RH conditions. The CL was confirmed to have a higher Young's modulus than the PEM in each temperature and humidity region.

4.1.2. PEM dimensional change rate results

Figure 10 shows the measurement results of the PEM and CCM dimensional change rates in the in-plane direction. Compared to the dimensions at room temperature, the CCM swells at the high-humidity side and shrinks at the low-humidity side. In addition, these results also show that coating with a CCM reduced the dimensional change in the in-plane direction compared to that of only the PEM. This indicates that the CL has a higher Young's modulus than

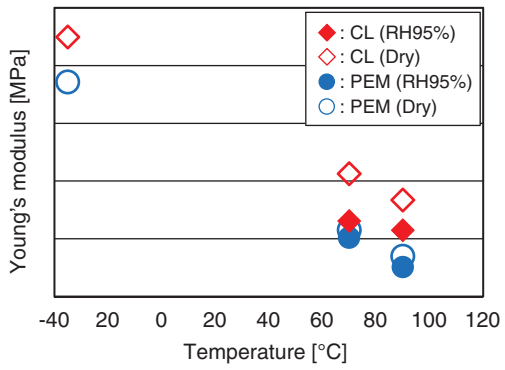


Fig. 9 Results of Young's modulus at various conditions

the PEM, which effectively reduces the PEM dimensional change in the in-plane direction.

Figure 11 shows the measurement results of the PEM dimensional change rate in the thickness direction. This shows that the PEM dimensional change amount in the thickness direction increases together with the temperature and RH.

4.2. Results of Stress Analysis Using FEM

The PEM and CCM properties in each temperature and humidity environment described in terms 4.1.1. and 4.1.2. were reflected to the FEM model shown in Fig. 6, and the PEM deformation behavior in each environment was analyzed. Figure 12 shows the results of using FEM to analyze the deformation behavior when the PEM swells at an electrode crack. The tendency of the PEM to swell as the water content increases was described in term 4.1.2., and it was found that when an electrode crack exists, the PEM deforms in a manner so as to enter the crack. Figure 13 shows an enlarged view of the red frame in Fig. 12, indicating that tensile stress concentrates at the edges of the electrode. This can be explained as a result of the CL having a higher Young's modulus than the PEM, as described in term 4.1.1. These results show that stress concentration at the edges of the electrode in a dry-wet environment results in high stress and is a factor promoting mechanical degradation of PEM at electrode cracks. Water is produced in accordance with the load during fuel cell power generation, and the PEM repeatedly swells and shrinks according to the amount of water produced. Therefore, it is thought that high stress is repeatedly input to the PEM around the edges of the electrode at electrode cracks, which promotes mechanical fatigue degradation.

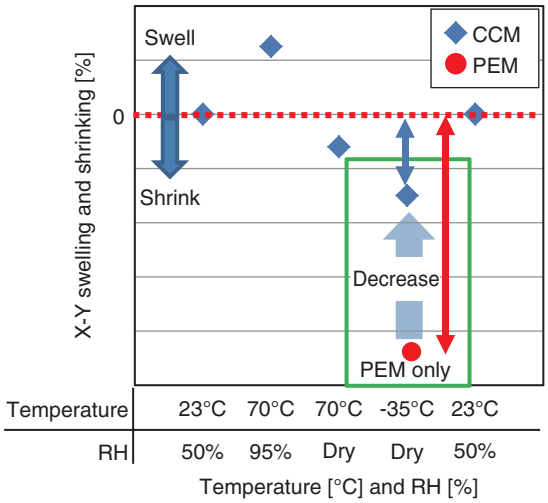


Fig. 10 Results of X-Y dimensional change rate of CCM and PEM

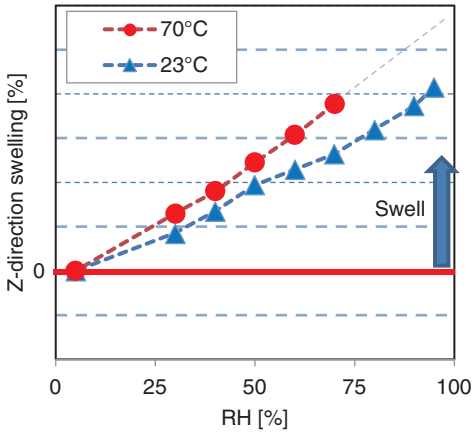


Fig. 11 Results of Z dimensional change rate of PEM

4.3. Material Limit Line Results

Figure 14 shows the PEM S-N diagram results. These results confirm that the stress fatigue durability of the PEM drops as the temperature rises. It was also confirmed that breakdown due to cumulative fatigue occurred even at high fatigue cycle counts in excess of

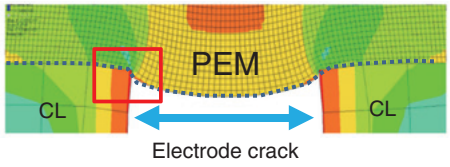


Fig. 12 Stress distribution in PEM simulation at PEM swelling

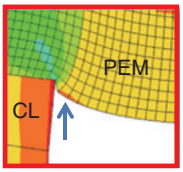


Fig. 13 Enlarged view of red frame in Fig. 12

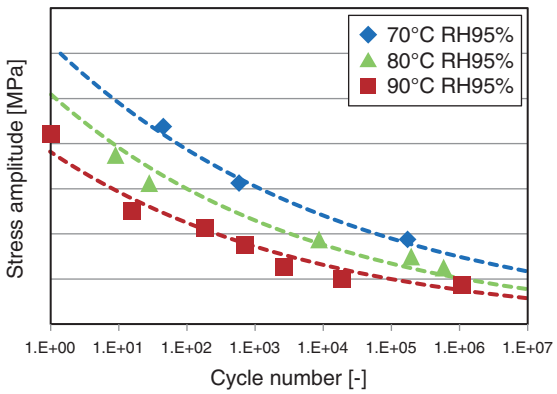


Fig. 14 Results of S-N diagram at various temperature conditions

10^6 times on the PEM fatigue curve. Therefore, when calculating the *Lcr* shown in Eq. (4), the fact that stress fatigue is input even at low stress was reflected, and the material limit line was calculated from the cumulative fatigue including low stress input.

4.4. *Lcr* Calculation Using Cumulative Fatigue Damage Law

4.4.1. Generated stress prediction by stress analysis using FEM

The stress analysis using FEM described in section 4.2. was performed to calculate the generated stress from the Young's modulus and dimensional change rate described in section 4.1. and the actual electrode crack width.

Figure 15 shows the relationship between the PEM dimensional change rate in the thickness direction at electrode cracks and the generated stress at each electrode crack width. These results show that the stress generated on the PEM at electrode cracks increases together with both the PEM swelling rate in the thickness direction and the crack width.

4.4.2. *Lcr* calculation

Lcr was calculated from the material limit line and generated stress values using the cumulative fatigue damage law as described in section 3.4. In addition, the calculations at each condition used the environmental conditions of the dry-wet cycle test at different RH described in term 3.4.2. Figure 16 shows the calculation results. These results show that *Lcr* increases together with the dry-wet difference, and the PEM is predicted to break at electrode cracks with a width of approximately 30 μm or more under durability test conditions of repeated RH 120% to dry cycle. However, the results also show that *Lcr* decreases as the dry-wet difference becomes smaller, and that fatigue degradation has little impact on the PEM under durability test conditions of repeated RH 30% to dry cycle.

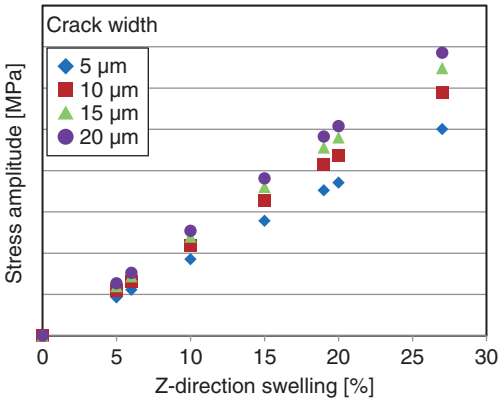


Fig. 15 Calculation results of stress amplitude at various conditions (FEM)

4.4.3. Results of membrane thickness analysis after dry-wet cycle test at different RH

Figure 17 shows the measurement results of the PEM thickness at electrode cracks after the dry-wet cycle test at different RH. The rate of decrease in the membrane thickness becomes more pronounced as the crack width increases, and the PEM was confirmed to break at an electrode crack width of approximately 30 μm. In addition, reducing the membrane thickness was confirmed to have an increased impact on membrane degradation at electrode cracks under conditions with a large dry-wet difference in the dry to wet direction, and this tendency matches the prediction obtained by stress analysis using FEM. This indicates that the dominant factor influencing the phenomenon of mechanical degradation of PEM is the increase in the stress generated at electrode cracks due to PEM swelling variation.

4.4.4. *Lcr* - membrane thickness conversion formula

The *Lcr* results relative to crack width calculated under each durability condition described in term 4.4.2. and the analysis results described in term 4.4.3. were used to determine the relationship between *Lcr* and the rate of

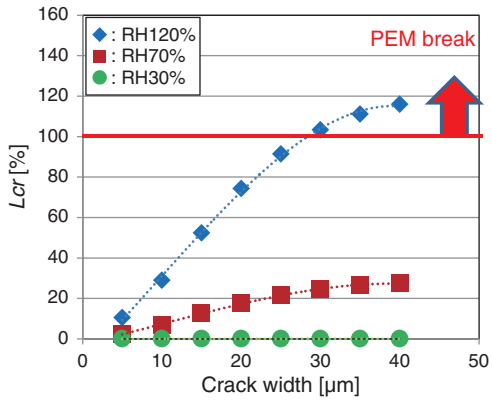


Fig. 16 Calculation results of *Lcr* in RH cycle test

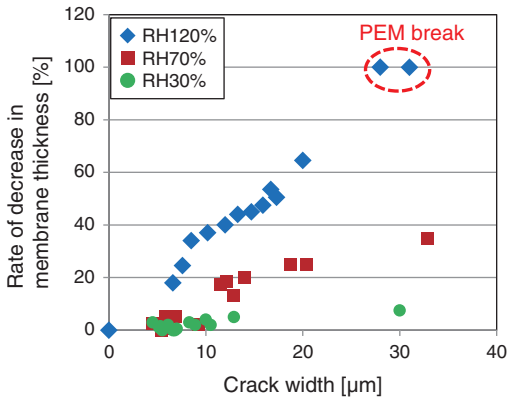


Fig. 17 Analysis results of membrane thickness in RH cycle test

decrease in the membrane thickness.

Figure 18 shows these results, indicating that the rate of decrease in the membrane thickness increases together with *Lcr*. This indicates that high stress is generated on the PEM at electrode cracks, which promotes mechanical degradation of the PEM, and that the *Lcr* determined from the relationship between the material limit line and the generated stress influences the rate of decrease in the membrane thickness. In addition, *Lcr* and the rate of decrease in the membrane thickness exhibited a high correlation even under durability conditions with different dry-wet differences. Based on these results, the membrane thickness, which decreases under the durability conditions, can be predicted by replacing the mechanical degradation stress with *Lcr*, even under different durability conditions. Potential methods for reducing mechanical degradation of PEM at electrode cracks include methods of controlling PEM water content fluctuation, enhancement of CL manufacturing technology, and increasing PEM fatigue durability. Use of the developed life prediction technology makes it possible to quantify the PEM thickness life-enhancing effects of each countermeasure method, which in turn enables investigation of the optimum countermeasure methods that can secure both sufficient power generation performance and durable reliability.

4.5. Results of Verification of Prediction Accuracy Using On-board-size MEA

Figure 19 shows the measurement results of membrane thickness after a mechanical degradation durability test using an on-board-size MEA. These results confirmed that mechanical degradation progresses in accordance with the electrode crack width, even in an on-board-size MEA. In addition, the results of analyzing the rate of decrease in the membrane thickness matched the trend in the predicted rate of decrease in the membrane thickness calculated using the developed life prediction technology. This confirmed that the developed life prediction technology can also be applied to an on-board-size MEA.

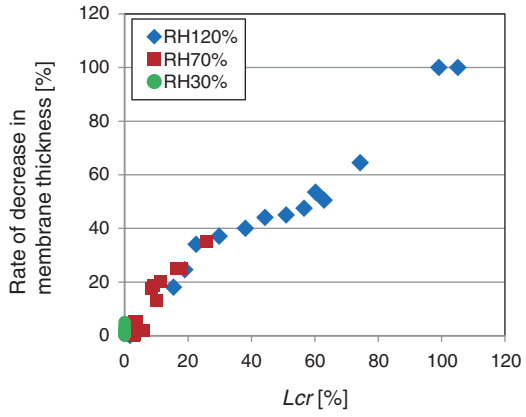


Fig. 18 Relationship between *Lcr* and rate of decrease in membrane thickness

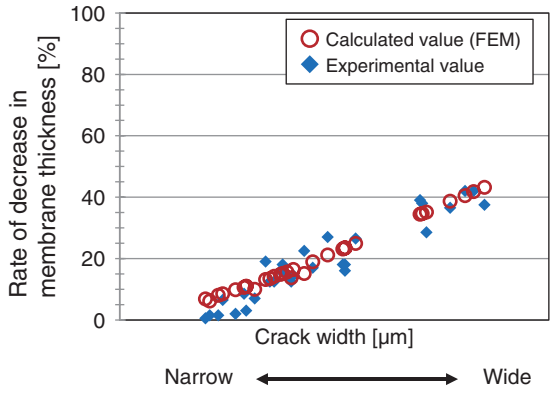


Fig. 19 Analysis results of membrane thickness in accelerated stress test using on-board-size MEA

5. Conclusion

Life prediction technology was established for PEM under mechanical degradation.

(1) The PEM and CL property results showed that the CL has a higher Young's modulus than the PEM, which helps to reduce dimensional change in the in-plane direction. However, FEM analysis also showed that when electrode cracks are present, this is a factor increasing the stress in accordance with the electrode crack width.

(2) The stress generated on the PEM in each temperature and humidity environment can be estimated by applying the material property values at each temperature and humidity to the FEM model, and this estimated stress is correlated with the results of dry-wet cycle tests at different RH.

(3) The impact of mechanical degradation on life can be quantified by using the cumulative fatigue damage law to define the PEM *Lcr*. In addition, it was confirmed that the membrane thickness after mechanical degradation durability can be predicted for an on-board-size MEA.

References

(1) Hiraide, A.: Life Prediction Model Estimating Chemical Degradation of Polymer Electrolyte Membrane for Fuel Cells, Honda R&D Technical Review, Vol. 28, No. 1, p. 50-58

(2) Lai, Y. H., Dillard, D. A.: Handbook of Fuel Cells: Advances in Electrocatalysis, Materials, Diagnostics and Durability, Vol. 5, ed. Vielstich, W., Gasteiger, H. A., Yokokawa, H., John Wiley & Sons, Ltd., p. 403-419, (2009)

(3) Gittleman, C. S., Coms, F. D., Lai, Y. H.: Chapter 2: Membrane Durability: Physical and Chemical Degradation, Polymer Electrolyte Fuel Cell Degradation, Ed. Mench, M. M., Kumbur, E. C.,

Veziroglu, T. N., Elsevier, (2012)
(4) Tang, H., Peikang, S., Jiang, S. P., Wang, F., Pan, M.: A Degradation Study of Nafion Proton Exchange Membrane of PEM Fuel Cells, J. Power Sources, 170(1), p. 85-92, (2007)
(5) Uchiyama, T., Kato, M., Ikogi, Y., Yoshida, T.: Mechanical Degradation Mechanism of Membrane Electrode Assemblies in Bucking Test Under Humidity Cycles, ASME J. Fuel Cell Sci. Technol., Vol. 9 (6) p. 0210071-0210078, (2012)
(6) Kai, Y., Kitayama, Y., Omiya, M., Uchiyama, T., Kumei, H.: In Situ Observation of Deformation Behavior of Membrane Electrode Assembly Under Humidity Cycles, ASME J. Fuel Cell Sci. Technol., Vol. 11 (5), p. 0510061-0510067, (2014)
(7) Iwanari, T., Miyajima, K., Furusawa, K., Inoue, M.: Real-time Measurement of Water Content of CCM in On-board Fuel Cell Stack System, Honda R&D Technical Review, Vol. 28, No. 1, p. 34-40
(8) Sato, M., Chiba, H., Inoue, M.: Development of CCM Water Content Distribution Measurement System for Fuel Cell Stack, Honda R&D Technical Review, Vol. 28, No. 1, p. 16-25
(9) Uchiyama, T.: Mechanical Model and Mechanical Durability in Membrane Electrode Assembly for Polymer Electrolyte Fuel Cells, NIPPON GOMU KYOKAISHI, 87 (6), p. 236-242, (2014) (in Japanese)
(10) Nagumo, K., Inoue, M.: Numerical Prediction of Water Content Distribution of Catalyst Coated Membrane of Fuel Cell Stack using Simulation, Honda R&D Technical Review, Vol. 28, No. 1, p. 26-33

■ Author ■


Masashi SUGISHITA


Suguru OHMORI

A Pore-Scale Multiphysics Method to Study PEMFC Catalyst Layers

Koji MORIYAMA* Jinfen KANG** Seung Hyun KIM**

ABSTRACT

Three dimensional pore-scale numerical approach to study the effects of structural parameters, material properties, and operating conditions on the performance of catalyst layer of proton exchange membrane fuel cell is developed. The proposed approach includes a novel stochastic reconstruction method and a pore-scale fully coupled simulation model. The pore-scale simulation model is based on a hybrid lattice Boltzmann-Finite Difference method. Multi-physics phenomena are taken into account and fully coupled in the model including the electrochemical reactions, water generation and evaporation, mass transport through electrode pores and ionomer, electron transport through carbon support and catalyst particles, and proton transport through ionomer. The proposed method is validated with experimental data and shows good agreement. The case studies show that the structure of catalyst layer and operating condition impacts on the overall electrode performances.

1. Introduction

To achieve high performance with a low-Pt loading electrode is an important issue for the mass production of low cost Proton Exchange Membrane Fuel Cells (PEMFCs) and has been intensively studied through experiments and computation[1]. Among the main issues to realize ultra-low Pt loading is optimizing the microstructure of the catalyst layer (CL). As in Fig. 1, the PEMFC CL is composed of four components: carbon agglomerate, ionomer, Pt particles, and pore-space. Water is generated by electrochemical reaction on the Pt surface by use of oxygen, proton, and electron. Oxygen is transported in pore and is dissolved and diffused in the ionomer, electron is transported in Pt and carbon support, and proton is transported in the ionomer. Therefore, transport of reactants and products strongly depends on the CL microstructure. In particular, at high current density operating conditions, the substantial oxygen mass transport loss caused by liquid water, ionomer transport resistance, and interfacial resistances between different phases significantly limits the output power density. The variation of ionomer morphology also affects the Ohmic loss due to proton transport.

To find an optimal CL structure, pore scale modeling has been a focus of attention[2]-[4]. However, no previous work on pore scale modeling has considered complex phenomena such as two phase flow including phase change, which impact the performance substantially.

Therefore, we propose a novel pore-scale modeling platform to study the influences of various CL microstructures on the performance. It was developed to perform a detailed analysis to understand physico-chemical processes in the CL, and to evaluate the influence of pore-scale structures. The computational platform consists of a novel stochastic reconstruction method and a pore-scale fully-coupled simulation model. The reconstruction method is designed to generate 3-D geometries of the CLs including all the components, at a high level of details. A number of pore-scale and macroscopic structural properties are introduced and specified in advance, leading

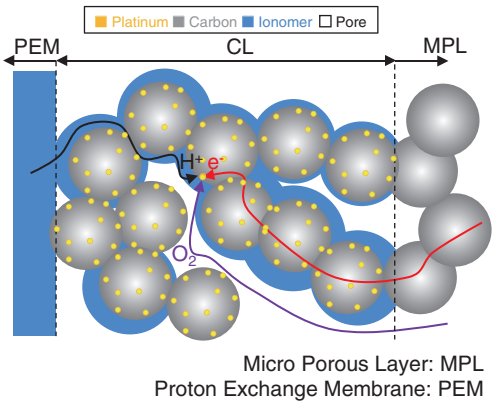


Fig. 1 CL in PEMFC

* Automobile R&D Center

** The Ohio State University

to a customized CL reconstruction method. In addition, anisotropic CLs with graded structural properties can also be reconstructed. In such structures, the electrochemical and transport properties vary along the thickness of the CL. The multi-physics pore-scale model describes important physical and chemical processes in different components of the CL, including liquid water generation, transport, and phase-change. A hybrid lattice Boltzmann-Finite Difference (LBFD) method is used to describe multiphase reactants and products transport. Several new models and methods are introduced to describe processes related to mass transport and Ohmic losses. Furthermore, results from validation and case studies are presented.

2. Stochastic Reconstruction of Catalyst Layer

Pore scale modeling needs the information on the detailed three dimensional structures to predict the phenomena in the CL microstructure. However, it is challenging to measure the real three dimensional geometries due to the weak material characteristics of ionomer to electron beam. So, a numerical reconstruction method based on the knowable structural properties is necessary. In the literature, the efforts on numerical reconstruction of CLs are mainly focused on reproducing CL structures resembling the digitized ones obtained by a microscope. However, due to the technical limitations, it is challenging to distinguish the ionomer from carbon components. The CL reconstruction study was therefore mainly limited to carbon structure reconstruction. The ionomer is added in the system following simple rules, such as uniform thickness[2-5]. Pt size distribution has not been considered.

In order to optimize the electrode structure and enhance the fuel cell performances in an efficient way, it is helpful to develop a customized CL reconstruction approach, such that we can stochastically reconstruct the CLs not only having the overall desired statistical properties but also having numerous detailed structural features, including ionomer thickness variations and Pt loading. In addition to isotropic CLs, it is also desirable to reconstruct graded anisotropic ones, which are often observed in real experiments. In this study, we extended a previously proposed stochastic reconstruction method[5] to provide such features. Numerous structural properties can be flexibly specified in advance, such as volume fraction of each phase, Pt loading, ionomer distribution form and coverage, Pt dispersion and coverage, etc. The structural properties can be globally or locally adjusted and the reconstructed CL can have various graded anisotropic properties.

2.1. Carbon Structure Reconstruction

For the generation of carbon structures, a sphere-based simulated annealing method[5] is used. Among several approaches which are used to virtually construct a porous media structure, the sphere-based simulated annealing method has recently become popular due to its outstanding features in generating the CL microstructures.

The sphere-based simulated annealing method is based on the stochastic optimization method to minimize the structural differences between the specified and generated carbon structures. Initially, spherical particles representing primary carbon particles are stochastically added and located in a computational domain until their volume fraction reaches a prescribed limit. Then, the spheres are moved arbitrarily and relocated to a new position according to certain distribution functions and restrictions. This optimization process continues until the structure reaches a status that satisfies the prescribed statistical status. In this study, the status is described by a two-point correlation function[5].

2.2. Ionomer Distribution

Ionomer is used to transport proton to the catalyst surfaces and is used same polymer with PEM. In the cathode CL, the structure of the ionomer thin film strongly affects the performance. An ideal coverage and thickness will provide the maximum active catalyst sites and mass transport. In a real manufacturing process, the ionomer may not distribute uniformly on the surface of the agglomerates and even it is not uniform on each carbon particle[6]. In order to mimic these real scenarios to the largest extent, we introduce five parameters to guide the reconstruction of ionomer layers: ionomer average thickness $\delta_{i,avg}$, ionomer to carbon mass ratio I/C, ionomer coverage percentage (i.e. percentage of carbon particles covered by ionomer) c_i, maximum offset value between an ionomer layer center and its covered carbon particle center $d_{i,max}$, and the Relative Humidity RH.

The ionomer layer was added in the CL according to multiple restrictions with these controlling parameters. The reconstructed ionomer layer has non-uniform thickness on different carbon particles with the average thickness $\delta_{i,avg}$. By defining the ionomer coverage percentage and the maximum offset value $d_{i,max}$, we are able to reproduce carbon particles that are not covered with ionomer or that are partially covered as in Fig. 2.

During fuel cell operation, the thickness of the ionomer layer changes due to humidification. In this work, this ionomer swelling effect is taken into account. By defining

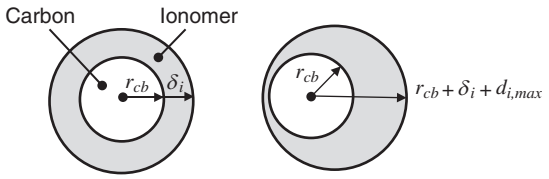


Fig. 2 Schematics of ideal uniform ionomer layer coverage and non-ideal coverage on carbon particle

the *RH* and *I*/*C* ratio, the ionomer volume fraction $\varepsilon_{i,RH}$ is calculated as[7],

$$\varepsilon_{i,\,RH} = \left(\frac{I}{C}\right)\frac{10}{f_t \rho_{i,dry}}\left(1+\frac{M_w \rho_{i,dry}\lambda}{\rho_w EW}\right), \quad (1)$$

where f_t = 28±2 mg/cm^2 for I/C<3, $\rho_{i,dry}$ is the density of dry ionomer, ρ_w is the density of water, M_w is the mole number of water, λ is the water content of the ionomer at a specific *RH*, and *EW* is the equivalent weight of ionomer material. The ionomer layers are added to the reconstructed CL according to the *RH*-dependent volume fraction given by Eq. (1).

2.3. Catalyst Particle Distribution

To represent or control the characteristics of the catalyst particle distribution in the CLs, four controlling parameters are introduced: Pt loading m_{Pt}, Pt weight percentage $Pt_{\mathrm{wt\%}}$, Pt/C ratio c_{Pt}, and Pt distance η_{Pt}. The m_{Pt} is the total amount of Pt particles distributed in a unit area of the CL with the unit of mg/cm^2. The $Pt_{\mathrm{wt\%}}$ is the ratio between the weight of Pt and that of carbon and Pt in the CL. The c_{Pt} describes the fraction of carbon particles that contain Pt particles. The η_{Pt} is used to specify the minimum distance between any arbitrarily distributed Pt particles on the surface of carbon agglomerates.

Based on these controlling parameters, the volume fraction of Pt particles ε_{Pt} can be calculated as,

$$\varepsilon_{Pt} = \varepsilon_s \frac{Pt_{\mathrm{wt\%}}}{\rho_{Pt}}\left(\frac{Pt_{\mathrm{wt\%}}}{\rho_{Pt}}+\frac{1-Pt_{\mathrm{wt\%}}}{\rho_{cb}}\right)^{-1}, \quad (2)$$

where ρ_{Pt} and ρ_{cb} are the density of platinum and carbon, respectively, and ε_s is the total volume fraction of carbon and Pt particles. This amount of Pt catalyst voxels is distributed in a stochastic way according to specified restrictions. Assuming the solid carbon, the Pt particles are located at the surface of each carbon particle. If c_{Pt} is unity, then the Pt particles will have a nearly uniform distribution in the system. The minimum distance between every two Pt particles can be specified to control the degree of particle dispersion. The c_{Pt} can be adjusted flexibly, giving a specific percentage of bare carbon particles are introduced. No catalyst particles are attached to the bare carbon particles. The bare carbon particles are randomly selected among the carbon agglomerate, until the specific percentage is reached. In this way, the Pt distribution will be reproduced to mimic the real situation to the largest extent.

If the percentage of bare carbon particles is 0, and considering the Pt supported carbon has constant $Pt_{\mathrm{wt\%}}$, then the $Pt_{\mathrm{wt\%}}$ is equal to the ratio between the total Pt weight and the total Pt and carbon weight. Therefore, the $Pt_{\mathrm{wt\%}}$ and Pt loading have the following relationship:

$$Pt_{\mathrm{wt\%}} = \left[\left(\frac{\varepsilon_s L}{m_{Pt}}-\frac{1}{\rho_{Pt}}\rho_{cb}+1\right)\right]^{-1}, \quad (3)$$

where L is the thickness of the CL.

2.4. Anisotropic Graded Structure

The manufactured CLs can easily be inhomogeneous and anisotropic. In order to capture this property, we also extended the current reconstruction method. In the literature, no study has been reported to reconstruct such CLs. In order to reconstruct such structures, two approaches can be considered. The first is to design a reference trial two-point correlation function that describes correctly the graded structure characteristics in the whole system. The second is to generate several different CL domains that have customized properties in each domain and then to combine them together. The first method needs a lot of time to obtain the structure. On the other hand, the second method is more straight forward and easy to realize. However, the main issue for this second approach is the abrupt change of carbon structures, e.g., broken carbons, at the domain boundaries. In order to solve this issue, we propose the following method. First, the carbon agglomerate structure for the first domain is generated. When generating the second domain, the carbon particles in the interfacial region between the first and second domains are subject to some constraints to maintain the continuity of the structure. Specifically, the carbon particles are restricted from relocation or addition. In addition, all the other carbon particles in the bulk region are required to skip the interfacial region when they have to be relocated in the optimization process. After stochastically reconstructing all the domains, good continuity property is obtained at the domain interfaces in the final graded structure.

3. Multiphysics Pore-scale Modeling

In this study, multiphase reacting flows and transport phenomena in different components of the CL are simulated by using a hybrid LBFD method. The velocity field is solved by using the lattice Boltzmann method. The liquid-gas interface is described by using the finite difference phase-field method. The species transport is solved using the macroscopic conservation equation supplemented by the Knudsen diffusion correction. The electrochemical reactions, water generation, and evaporation are fully coupled with the mass transport through pores and ionomer. In the experiments, it has been observed that ionomer layer geometry and transport properties are strongly influenced by the *RH* and the liquid water in the pores. Ionomer swells and ionic conductivity increases when the ionomer uptakes water. The effects of ionomer swelling are considered in the CL reconstruction process, while the ionic conductivity variation is taken into account in the pore-scale modeling.

3.1. Multiphase Reactive Flow with Phase Change

The phase-field method for two-phase flows with phase change has been developed in this research. The equation

for the order parameter C that describes the liquid-gas interfaces is given as,

$$\frac{\partial C}{\partial t}+u_\alpha\frac{\partial C}{\partial x_\alpha}=\frac{\partial}{\partial x_\alpha}\left(M\frac{\partial \phi}{\partial x_\alpha}\right) +\beta_p\frac{c_{w,sat}-c_{w,g}}{c_{w,sat}}C^2(1-C^2), \tag{4}$$

where M is the mobility. ϕ is the chemical potential. The parameter β_p is related to the water evaporation and condensation rate. $c_{w,g}$ is the concentration of water vapor in the gas phase. $c_{w,sat}$ is the saturation concentration of water vapor, and is evaluated by the Clausius-Clapeyron equation[8].

The continuity, momentum, species, and energy equations can be written as,

$$\frac{\partial u_\alpha}{\partial x_\alpha}=\frac{\Delta\rho}{\rho}\omega_c, \tag{5}$$

$$\rho\frac{\partial u_\beta}{\partial t}+\rho u_\alpha\frac{\partial u_\beta}{\partial x_\alpha}=-\frac{\partial p}{\partial x_\alpha} +\frac{\partial}{\partial x_\alpha}\left[\nu\left(\frac{\partial u_\beta}{\partial x_\alpha}+\frac{\partial u_\alpha}{\partial x_\beta}\right)\right]+\rho F, \tag{6}$$

$$\frac{\partial C_i}{\partial t}+u_\alpha\frac{\partial C_i}{\partial x_\alpha}=\frac{\partial}{\partial x_\alpha}\left(D_i\frac{\partial C_i}{\partial x_\alpha}\right)+\omega_i, \tag{7}$$

$$\frac{\partial T}{\partial t}+u_\alpha\frac{\partial T}{\partial x_\alpha}=\frac{\partial}{\partial x_\alpha}\left(k\frac{\partial T}{\partial x_\alpha}\right)+\omega_T\frac{\rho\omega_c h_{fg}}{\rho c_p}, \tag{8}$$

where

$$\omega_c=\beta_p\frac{c_{w,sat}-c_{w,g}}{c_{w,sat}}C^2(1-C^2), \tag{9}$$

and $\omega_{H_2O}=a_{C,H_2O}\omega_C$. The parameter a_{C,H_2O} is the conversion factor between the order parameter and the water vapor concentration. ω_i and ω_T are the source terms of species conservation equation and temperature equation, respectively. The velocity field is solved by using the lattice Boltzmann method, while the finite difference method is used to solve other scalar equations. The details of the hybrid LBFD method will be presented in future publications.

3.2. Oxygen Reduction Reaction (ORR)

At high potentials, O and OH coverages on the Pt surface are significant[9]-[11]. The adsorbed O and OH therefore block available reaction sites on which O_2 can sit. As a result, the available reaction sites decrease as the potential increases. The oxygen reduction reaction considering the oxide coverage effect can be expressed by the following kinetic model[12]:

$$j=j_0\left(\frac{p_{O_2}}{p_{O_2,0}}\right)^\gamma(1-\theta)\exp\left(-\frac{\alpha F}{RT}\eta\right)\exp\left(-\frac{\omega\theta}{RT}\right), \tag{10}$$

where η is the overpotential, F is the Faraday constant, R is the gas constant, j_0 is the exchange current density, and γ is the oxygen reaction order. ω is the energy parameter for the Temkin isotherm, which defines the coverage-dependent rate of change of the apparent Gibb's energy of adsorption of adsorbing species. The cumulative oxygen coverage θ is a function of potential and was given by experimental data (refer to Fig. 6(a) of Ref. (13)).

3.3. Coupling of Electrochemistry and Transport

3.3.1. Water production and transport

In the particle-type CL, water is produced at the catalyst particle surface, transports through the ionomer, and finally emerges at the ionomer-pore interface. A simple water transport model involving only diffusion is solved since water production at Pt surface and emergence in the pores is of major interest. On Pt surfaces, the water production is considered as a flux boundary condition:

$$\omega_{w,Pt}=j/2F, \tag{11}$$

where $\omega_{w,Pt}$ is the water production rate.

At the ionomer-pore interface, water emerges from the ionomer. The water flux on the ionomer-pore boundary is modeled as,

$$\omega_w=c_{lf}(c_{w,i}-c_{w,sat}), \tag{12}$$

where $c_{w,i}$ is the water concentration at the ionomer-pore boundary. c_{lf} is the coefficient that controls the water emergence speed and can be written as,

$$c_{lf}=c_{lf,0}D_{w,i}/l_i^2. \tag{13}$$

The $c_{lf,0}$ is an adjustable parameter, $D_{w,i}$ is the diffusivity of water in ionomer, l_i is the characteristic thickness of the ionomer. Hence, $D_{w,i}/l_i$ represents the velocity scale of the process. Currently we set $c_{lf,0}=l_i$ assuming the water emergence speed has a similar order to that of water diffusion in the ionomer.

In this work, when water emerges from ionomer or Pt to the pores, it is assumed that water is in the liquid phase. As of now, there is no clear evidence of whether the emerging water is in gas phase or in liquid phase. However, when the RH is less than 100%, the emerged liquid water evaporates, which is considered in the present modeling.

Since the order parameter is unity for liquid water, the velocity at the water-emerging boundary can be given as,

$$v_c=\omega_C/C_l, \tag{14}$$

where C_l is the order parameter for liquid water, and it is unity. ω_C is the water flux of $\omega_{w,i}$ in the unit of the order parameter.

3.3.2. Electron and proton transport

The potentials for the solid and electrolyte phases

are governed by the Poisson's equation. The boundary conditions are set as follows. For the cathode MPL/CL interface,

$$\phi_s = V_{cell},\ \partial\phi_e / \partial n = 0, \tag{15}$$

where V_{cell} is the potential at the MPL/CL interface. For the cathode PEM/CL interface,

$$\phi_e = \phi_{e,0},\ \mathbf{n} \cdot \nabla\phi_s = 0, \tag{16}$$

where $\phi_{e,0}$ is the electrolyte-phase potential at the PEM/CL interface and $\mathbf{n}$ is the surface normal vector. At the ionomer/carbon interface,

$$\mathbf{n} \cdot \nabla\phi_e = 0,\ \mathbf{n} \cdot \nabla\phi_s = 0. \tag{17}$$

At the electrochemically active surface,

$$-k_e \nabla\phi_e \cdot \mathbf{n} = -j,\ -k_s \nabla\phi_s \cdot \mathbf{n} = j. \tag{18}$$

In the simulation, Ohmic losses from other components of fuel cells are also calculated based on the electronic and ionic resistance. The resistances are converted from the Ohmic loss of each component predicted by the down-the-channel model[14].

3.3.3. Ionomer humidification and relative humidity

The water plays an important role in CL. It emerges at the ionomer/pore interface, evaporates from liquid water to vapor in the pores, and it can be taken up by ionomer again. It alters the oxygen transport by blocking the pores directly or by making the ionomer swell. It also influences the *RH* in the CL and proton conductivity in the ionomer. The interactions among these processes are important and are modeled as follows.

When the water concentration in the ionomer $c_{i,w}$ is lower than the saturated concentration, the ionomer uptakes water. The saturated water concentration in the ionomer $c_{i,w,sat}$ is calculated as below[15].

$$c_{i,w,sat} = \lambda / (\lambda \overline{V_w} + EW / \rho_{i,dry}), \tag{19}$$

where $\overline{V_w}$ the molar volume of water, $\rho_{i,dry}$ is density of dry ionomer, and the water content λ is a function of temperature and *RH*:

$$\lambda = \begin{cases} \left[1 + 0.2325RH^2\left(\frac{T-30}{30}\right)\right] \times \\ [14.22RH^3 - 18.92RH^2 + 13.41RH], \\ if\ RH < 100\%, \\ 9.22 + 0.181T,\ if\ RH > 100\%. \end{cases} \tag{20}$$

The *RH* is calculated based on the water vapor concentration $c_{w,g}$ and temperature *T*. When the water concentration $c_{i,w}$ in the ionomer becomes larger than $c_{i,w,sat}$, the water emerges from the ionomer and appears in the pores at the ionomer/pore interface. The liquid water evaporates, which increases the *RH* simultaneously. When the *RH* varies, the ionomer saturated water concentration $c_{i,w,sat}$ is calculated accordingly in the next time step. The water emergence rate from the ionomer varies accordingly.

Table 1 Parameters of CL sample for studying pore size distribution and transport properties

Parameter	Value	Unit
Thickness	1	μm
Porosity	42	%
Carbon volume	28	%
Structure parameter *d*	40	nm
Carbon particle diameter	40	nm
Pt loading	0.0129	mg/cm^2
$Pt_{wt\%}$	19	%
Pt particle diameter	5.7	nm
Pt/C ratio c_{Pt}	100	%
ESA	45	m^2/g-Pt
I/C	1	-
EW	900	g/cm^3
Ionomer volume fraction	29.5 (RH0%)	%
	32 (RH20%)	%
	34 (RH45%)	%
	39 (RH85%)	%
Ionomer coverage c_i	100	%
Voxel size	5×5×5	nm^3
Grid number	200×200×200	-

4. Validation Study

4.1. Validation Study: Reconstruction

We reconstructed cathode CLs (CCLs) by applying the proposed method. For validation, we examined the structural and transport properties of the reconstructed CLs and compared with experiments and literature data at different *RH* values. These properties include Pore Size Distribution (PSD), Electrochemical Surface Area (ESA), proton resistivity, electronic conductivity and gas diffusivity. The ionomer thickness and volume fraction vary with *RH*, which changes the porosity and tortuosity accordingly. This volume variation effect was taken into account in the reconstruction process. The CLs were reconstructed with the setup specified in Table 1.

The reconstructed CL is presented in Fig. 3. The pore size distribution at dry condition (*RH*=0%) was evaluated

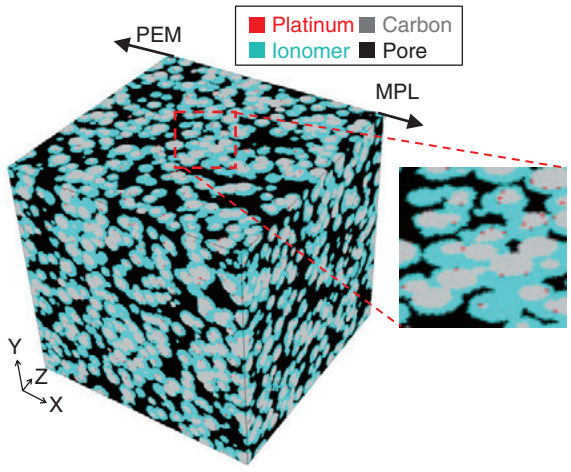


Fig. 3 Reconstructed CL using proposed general stochastic reconstruction method

and compared with experimental data in Fig. 4. At different *RH* conditions, the ionomer volume fraction was calculated in advance and used for the reconstruction. Several macroscopic properties of the CLs were evaluated based on the reconstructed CLs. ESA is about 45 m^2/g-Pt. For each CL sample at different *RH*, single phase simulations were conducted to examine the transport properties. In Fig. 5, the proton resistivity with respect to *RH* is shown. The results predicted by the model are in good agreement with the experimental data. In Fig. 6, the gas diffusivities and electronic conductivity at *RH*=30% are compared with literature data[16]. The simulation results of gas diffusivity and electronic conductivity also agree with the experimental data.

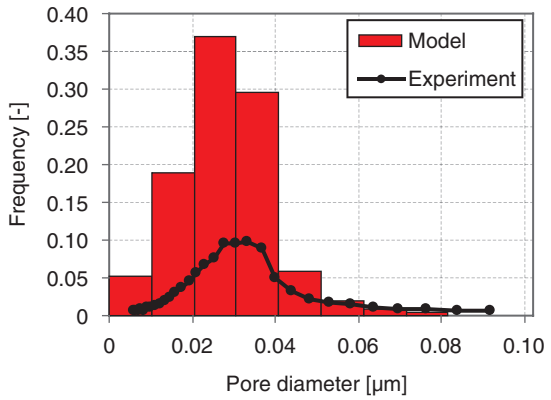


Fig. 4 Pore size distribution

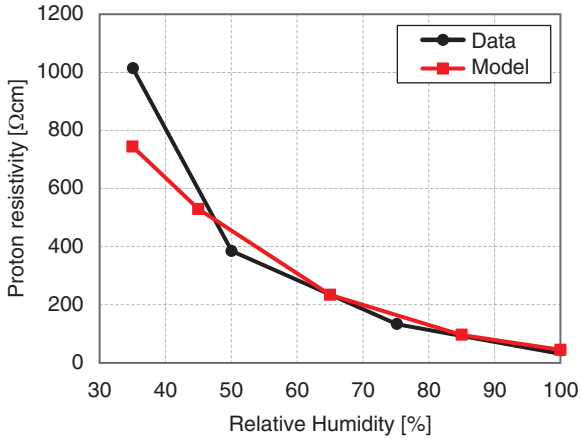


Fig. 5 Validation study: proton resistivity of reconstructed CL

Table 2 Parameters of CL reconstruction for validation

Parameter	Value	Unit
Thickness	15.5	μm
Porosity	42	%
Carbon volume	28	%
Structure parameter *d*	90	nm
Carbon particle diameter	60	nm
Pt loading	0.2	mg/cm²
$Pt_{wt\%}$	23.4	%
Pt particle diameter	5.7	nm
Pt/C ratio c_{Pt}	100	%
ESA	45	m^2/g-Pt
I/*C*	1	-
EW	900	g/cm³
Ionomer volume fraction	29.5 (RH0%)	%
	35.5 (RH65%)	%
Ionomer coverage c_i	100	%
Voxel size	16×16×16	nm³
Grid number	960×64×64	-
RH	65	%
Cathode inflow	Air	-
Anode inflow	Pure hydrogen	-
Temperature	353	K
Pressure	150	kPa

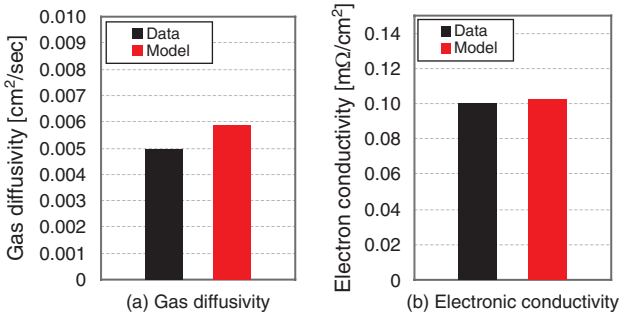


Fig. 6 Data comparison of gas diffusivity and electronic conductivity of reconstructed CL at *RH*=30%

4.2. Validation Study: Simulation

In this case, a cathode CL with full thickness from PEM to MPL was reconstructed and used for fully coupled multi-physics simulations. Numerical results of the model are compared with experimental data. In Fig. 7, the reconstructed structure is demonstrated with the view of the X-Y cross-section at the center of Z-coordinate. The parameters of CL reconstruction are given in Table 2. Carbon particle diameter is measured to be approximately 40 nm. Due to limited resolution in the numerical reconstruction, 60 nm was used. Similarly, the agglomerate structure parameter *d* is set to be 90 nm. At the interface between CCL and MPL, the boundary value of oxygen concentration, *RH* and temperature

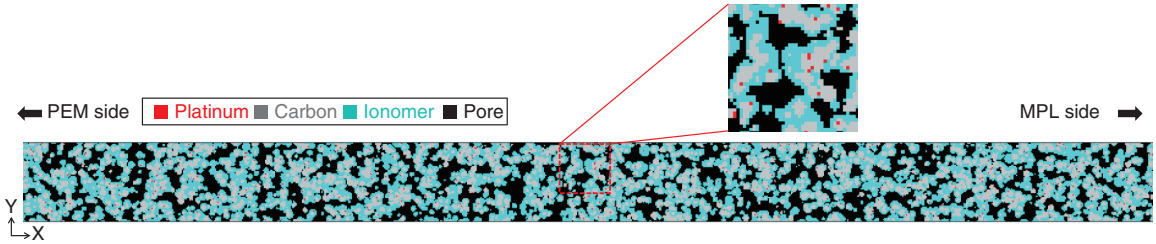


Fig. 7 Validation study: 2-D view of XY plane at center of Z-coordinate of reconstructed 3D CCL structure

were all defined with the values predicted with the down-the-channel model[14]. In the simulation, single-phase calculation was conducted first to get the converged ionic potential field. Then, the multiphase simulation is performed by using the single phase results as the initial condition.

In Fig. 8, the V-I polarization curves are shown. The predicted results are in good agreement with experimental data, while at high current density (1.5 A/cm^2 – 2 A/cm^2) the model slightly under-predicts the current density. In CCLs, the water generation rate changes with current density. The relationship between water saturation and current density is shown in Fig. 8. The saturation increases with current density. At the current density of 1.5 A/cm^2, the saturation level is about 12%. The distributions of liquid water, water vapor concentration, oxygen concentration, electrolyte -phase potential, and temperature are shown in Fig. 9. The average saturation and current density profiles along the CCL thickness (X-direction) are shown in Fig. 10. The results of

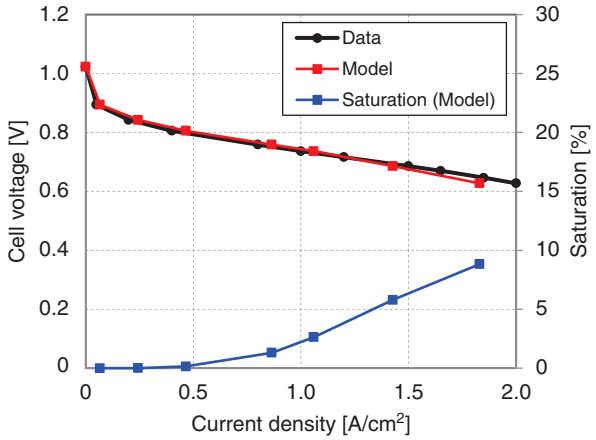


Fig. 8 Validation study: comparison of V-I polarization curve between simulation and experiment data, and simulation result of water saturation

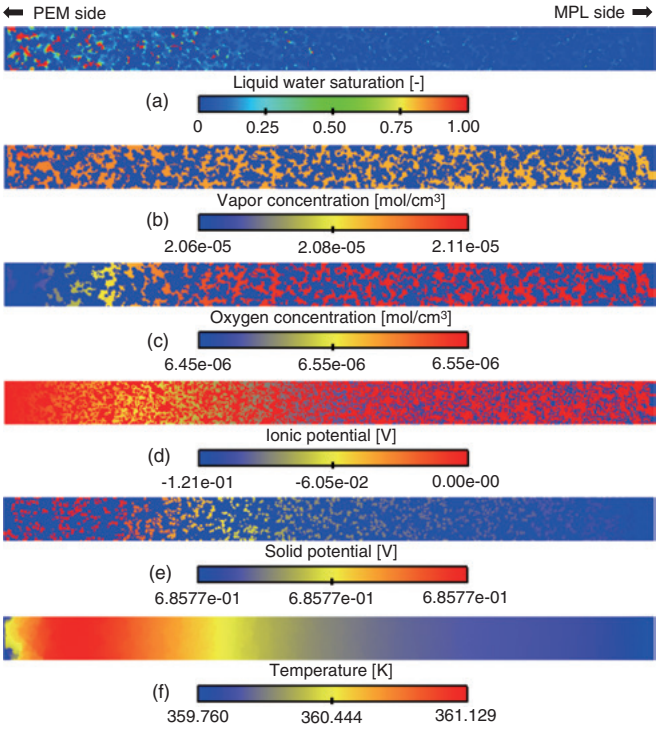


Fig. 9 Validation case: 2-D profiles of flow and electronic field properties on center XY plane of CCL

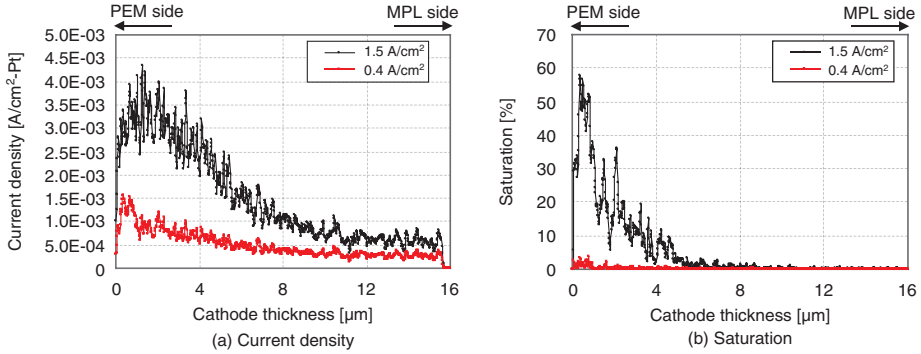


Fig. 10 Current density and saturation distribution along thickness of CL at I = 1.5 A/cm^2 and 0.4 A/cm^2 (RH=65%)

two cases are shown, the higher current density case at $I = 1.5$ A/cm^2 and the lower current density case at $I = 0.4$ A/cm^2.

In Figs. 9 and 10, the left end corresponds to PEM, while the right end MPL. The ionic potential is the highest at the PEM boundary. The maximum current density occurs slightly away from PEM. This is because most of the liquid water exists near PEM. The oxygen concentration is significantly decreased in this region due to the blockage of the pathways by liquid water.

5. Case Study

In order to evaluate the impact of various CL structure properties on the electrode performance, CL samples with different specifications were reconstructed to conduct the case study. Here, results for 4 representative non-graded CLs (N1-N4) and 4 graded CLs (G1-G4) are summarized.

5.1. Non-graded CLs

In the reconstruction process, we adjusted only one parameter for each case, while keeping other structure properties the same. The base non-graded CL sample, N1, was generated with the parameters shown in Table 3. The difference of N2, N3, and N4 from N1 is only RH to examine the effect of *RH* on the CL structure, water saturation, and performance. *RH* of N2, N3, and N4 are 95%, 70%, and 30%, respectively.

The fully coupled multiphase simulation results for all cases are collected and compared. In Fig. 11, V-I polarization improves according to the increase of *RH* due to the increase of proton conductivity. And the polarization curves show that 95% RH case has the best performance due to the best balance between oxygen transport and proton transport. As shown above, the developed model can be applied to show the optimal combination of CL structure and operating condition with the understanding of liquid water and current density distributions.

5.2. Graded CLs

Three graded CLs (G2 to G4) and a reference CL (G1) are reconstructed and simulated with low-Pt loading CL, 0.05 mg-Pt/cm^2. The main parameters, which are different from those for the non-graded case N1, are listed in Table 4. G1-G4 have the same overall *I*/*C* ratio, carbon volume fraction, and Pt loading, but their structures are graded and locally different from each other. G2 is chosen to examine the effect of I/C ratio and porosity distribution, and G3 and G4 are chosen to examine the effect of Pt distribution on the performance and water and current density distribution.

Figure 12 shows the performance and water saturation

Table 3 Parameter setup of reconstruction and simulation for reference CL sample, N1

Parameter	Value	Unit
Thickness	12	μm
Porosity	42	%
Carbon volume	28	%
Structure parameter *d*	90	nm
Carbon particle diameter	60	nm
Pt loading	0.2	mg/cm^2
$Pt_{wt\%}$	23.4	%
Pt particle diameter	5.7	nm
Pt/C ratio c_{Pt}	100	%
ESA	45	m^2/g-Pt
I/*C*	1	-
EW	900	g/cm^3
Ionomer volume fraction	29 (RH0%)	%
	42 (RH100%)	%
Ionomer coverage c_i	80	%
Computational domain	16×16×16	nm^3
Grid number	760×64×64	-
RH	100	%
Cathode inflow	Air	-
Anode inflow	Pure hydrogen	-
Temperature	353	K
Pressure	150	kPa

Table 4 Changed reconstruction parameters for non-graded CL samples, G1-G4, from reference CL

Cases	Parameter	Value (6 domains from PEM to MPL)	Unit
G1	Uniform		
G2	*I*/*C*	1.2, 1.1, 1.0, 0.9, 0.9, 0.9	-
	Porosity	23.2, 26.1, 29.0, 31.9, 31.9, 31.9	%
G3	$Pt_{wt\%}$	13.1, 13.1, 7.0, 7.0, 0.0, 0.0	%
G4	$Pt_{wt\%}$	0.0, 0.0, 7.0, 7.0, 13.1, 13.1	%

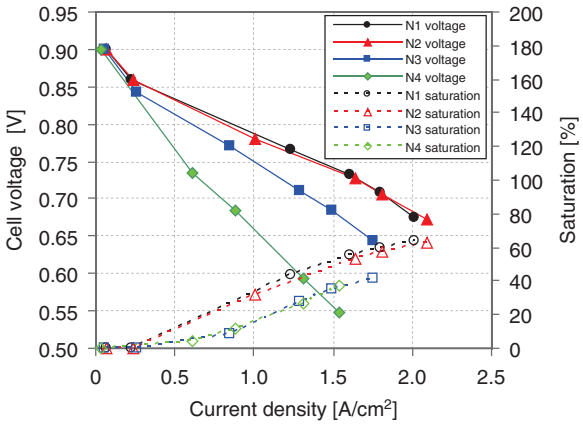


Fig. 11 Case study for N1-N4: Effects of *RH* on CL performance

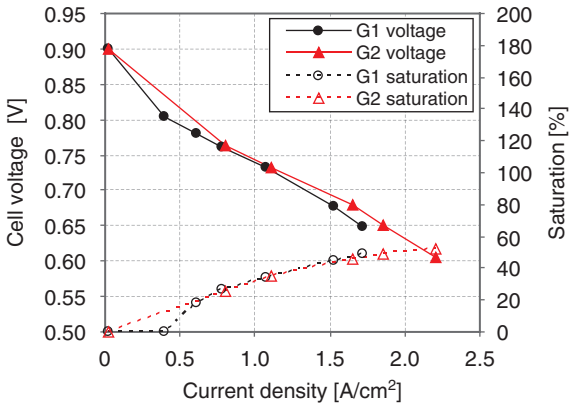


Fig. 12 Case study at *RH* 100%: Effects of graded I/C ratio and porosity on CL performance

comparison for cases G1 and G2 at 100% RH. The performance of the CL with *I/C* ratio and porosity gradient (G2) is found to be better due to its high proton conductivity from PEM to MPL and high gas diffusivity from MPL to PEM.

Figure 13 shows the performance and water saturation comparison for cases G1, G3, and G4 at 100% RH. And Fig. 14 shows water saturation and current density per Pt surface distribution along the CL thickness for cases G1, G3, and G4. The performance of CL structure with no Pt loading near the PEM (G4) is found to be the lowest because there is no electrochemical reaction near PEM and proton transport path gets longer and proton transport resistance gets higher. The performance of CL structure with high Pt loading near the PEM (G3) is found to be not better than uniform structure because more liquid water accumulates and the reactive sites are not utilized effectively near the PEM. To examine the effect of *RH* on the performance and water saturation for G1 and G3, comparison at *RH* = 65% is conducted as Fig. 15. At low relative humidity condition, the performance of case G3 is better than case G1 due to less liquid water accumulation and lower proton transport resistance, and the reactive sites are utilized effectively near the PEM accordingly. As shown above, the developed model can be applied to show the direction of low-Pt loading CL structure and optimal operating conditions for it with the understanding of the phenomena to improve the CL performance.

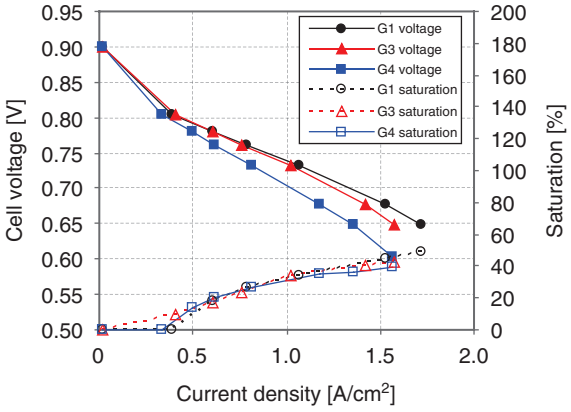


Fig. 13 Case study G1, G3, and G4 at *RH* 100%: Effects of graded Pt loading on CL performance

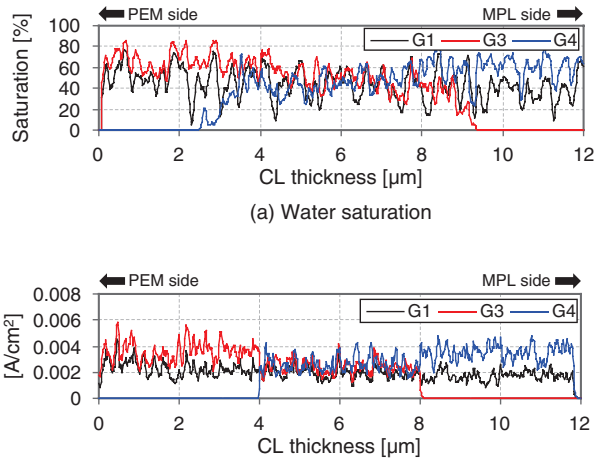


Fig. 14 Water saturation and current density per Pt surface distribution along CL thickness

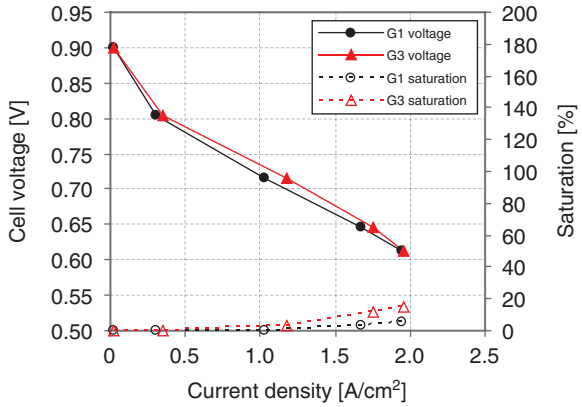


Fig. 15 Case study G1 and G3 at *RH* 65%: Effects of graded Pt loading on CL performance

6. Conclusion

We have proposed a novel computational framework to simulate the detailed physico-chemical processes in the reconstructed CLs of PEMFC. First, a general stochastic reconstruction method was developed based on the sphere-based simulated annealing method. This method is the general stochastic reconstruction method that can generate customized uniform and graded CLs with specified structural parameters. Second, a 3-D pore-scale multi-physics simulation model has been proposed. It can simulate fully coupled multiphase reactive flows and electrochemical phenomena in PEMFC CLs. The model was developed based on the hybrid lattice Boltzmann-Finite Difference method. All important processes occurring in the CL are taken into account, including the electrochemical reactions, water generation and evaporation, mass transport through electrode pores and ionomer, and the electron transport through carbon and catalysts, and proton transport through ionomer.

Reconstruction method is validated by the experimental data of PSD, gas diffusivity, proton resistivity, and electron conductivity. And the fully-coupled model is validated for the experimental V-I polarization curve. The simulation results demonstrate that this approach can be used to predict the performance of the electrode and to investigate detailed transport phenomena in the pore structures including distributions.

References

(1) Owejan, J. P., Owejan, J. E., Gu, W.: Impact of platinum loading and catalyst layer structure on PEMFC performance, Journal of the Electrochemical Society, 160, F824-F833, (2013)

(2) Lange, K. J., Sui, P. C., Djilali, N.: Pore Scale Simulation of Transport and Electrochemical Reactions in Reconstructed PEMFC Catalyst Layers, Journal of the Electrochemical Society, 157, B1434-B1442, (2010)

(3) Lange, K. J., Sui, P. C., Djilali, N.: Determination of effective transport properties in a PEMFC catalyst layer using different reconstruction algorithms, Journal of Power Sources, Vol. 208, p.354-365, (2012)

(4) Singh, R., Akhgar, A. R., Sui, P. C., Lange, K. J., Djilali, N.: Dual-Beam FIB/SEM Characterization, Statistical Reconstruction, and Pore Scale Modeling of a PEMFC Catalyst Layer, Journal of the Electrochemical Society, 161, F415-F424, (2014)

(5) Kim, S. H., Pitsch, H.: Reconstruction and effective diffusivity of the catalyst layer in PEM fuel cells, Journal of the Electrochemical Society, 156, B673-B681, (2009)

(6) Song, J. M., Suzuki, S., Uchida, H., Watanabe, M.: Preparation of high catalyst utilization electrodes for polymer electrolyte fuel cells, Langmuir, Vol.22, p.6422-6428, (2006)

(7) Yu, Z., Carter, R. N.: Measurement of effective oxygen diffusivity in electrodes for proton exchange membrane fuel cells, Journal of Power Sources, Vol.195, P.1079-1084, (2010)

(8) Wark, Kenneth.: Generalized Thermodynamic Relationships, Thermodynamics (5th ed.), New York, NY: McGraw-Hill, Inc., ISBN 0-07-068286-0, (1988)

(9) Wang, J. X., Markovic, N. M., Adzic, R. R.: Kinetic analysis of oxygen reduction on Pt(111) in acid solutions: Intrinsic kinetic parameters and anion adsorption effects, Journal of Physical Chemistry B, Vol.108, p.4127-4133, (2004)

(10) Wang, J. X., Zhang, J., Adzic, R. R.: Double-trap kinetic equation for the oxygen reduction reaction on Pt(111) in acidic media, Journal of Physical Chemistry A, Vol.111, p.12702-12710, (2007)

(11) Rai, V., Aryanpour, M., Pitsch, H.: First-principles analysis of oxygen-containing adsorbates formed from the electrochemical discharge of water on pt(111), Journal of Physical Chemistry C, Vol.112(26), p.9760-9768, (2008)

(12) Markovic, N. M., Gasteiger, H. A., Grgur, B. N., Ross, P. N.: Oxygen reduction reaction on Pt(111): effects of bromide, Journal of Electroanalytical Chemistry, Vol.467, p.157-163, (1999)

(13) Subramanian, N. P., Greszler, T. A., Zhang, J., Gu, W., Makharia, R.: Pt-oxide coverage-dependent oxygen reduction reaction (ORR) kinetics, Journal of the Electrochemical Society, Vol.159, B531-B540, (2012)

(14) Gu, W., Baker, D. R., Liu, Y., Gasteiger, H. A.: Proton exchange membrane fuel cell (PEMFC) down-the-channel performance model advances in electrocatalysis, materials, diagnostics and durability, In Vielstich, W., Yokokawa, H., Gasteiger, H. A., editors, Advanced diagnostics, models and design Low-temperature fuel cells, Vol.6, John Wiley & Sons, (2009)

(15) Kusoglu, A., Weber, A. Z.: Water transport and sorption in nafion membrane. In Page, K., et al. editors, In Polymers for Energy Storage and Delivery: Polyelectrolytes for Batteries and Fuel Cells, p.175-199, American Chemical Society, (2012)

(16) Yeong, C. L. Y., Torquato, S.: Reconstructing random media, Physical Review E, Vol.57(1), p.495-506, (1998)

Author



Koji MORIYAMA



Jinfen KANG



Seung Hyun KIM

Three Dimensional Large Scale Numerical Simulation of PEMFC with Low-Pt Loading

Koji MORIYAMA* Wenbin GU**
Liang HAO*** Chao-Yang WANG***

ABSTRACT

The developed multiphase mixture model for low-Pt loading electrode is applied to examine the effects of Pt loading and operating condition on current density and water distribution in realistic scale proton exchange membrane fuel cells. The predicted fuel cell voltage, high-frequency resistance, as well as current density and temperature distributions all show good agreement with the experimental data under various operating conditions and for two Pt loadings of 0.3 mg/cm^2 and 0.1 mg/cm^2. In particular, the present study demonstrates quantitative comparisons of the liquid water distribution in the proton exchange membrane fuel cell with the neutron imaging measurements. Such a comprehensive data comparison gives a fundamental understanding of the physical phenomena in the proton exchange membrane fuel cells and findings to design and develop the next generation of proton exchange membrane fuel cell with low-Pt loading.

1. Introduction

In the past decade, significant advancements have been achieved in proton exchange membrane fuel cell (PEMFC) technology. However, commercialization of this promising power source for automotive applications is still hindered by high cost and slow development cycle. Spatially resolved measurements of reaction and transport parameters in a fuel cell, while critical for a basic understanding of the complex electrochemical and transport behaviors, are expensive and challenging, if not impossible, to obtain. Modeling and simulation, therefore, play an important role in meeting the increasing demand for details in fuel cell research and development. Additionally, computer simulations become an increasing part of the discovery and design process for a next generation of highly efficient and compact PEMFCs.

A number of modeling studies have been performed with the computational fluid dynamics (CFD) framework to solve the complete set of transport equations governing mass, momentum, species, energy, and charge conservation in PEMFC[(1)-(4)]. However, the majority of prior work is limited to simple geometries such as straight channels, simplified dimensional assumptions such as 1D, 2D, unrealistic operating conditions such as fully humidified gas feed, or small-scale calculations with computational mesh smaller than a million grid points. While these prior studies helped to understand transport phenomena and reaction occurring in PEMFCs, the current challenge facing PEMFC technology is to address real issues arising in development of next generation fuel cells with low cost and high durability with low-Pt loading. Such PEMFCs of the future usually feature a complex 3D flow filed, and have auxiliary components, such as coolant channels and inlet and outlet manifolds. Shimpalee[(5)] employed a single-phase model to study the dynamic response of a PEMFC during a 20-second cycle with realistic fuel cells. However, the single-phase computations failed to address water flooding and ensuing mass transport loss inherently existing in the PEMFCs under normal operating conditions. Moreover, there has never been an attempt to validate the realistic fuel cell simulations against a wide range of experimental measurements including distribution data. Until most recently, experimental validation studies were limited to small-scale calculations. For example, Fink et al.[(6)] and Carnes et al.[(7)] performed validation studies on PEMFCs with parallel serpentine flow field, but only the current density (CD) distribution was examined.

In this work, a series of 3D computations and experimental validation on a PEMFC with realistic scale and geometry used in a U.S. Department of Energy (DOE) project[(8)] is performed using the multiphase-mixture model.

* Automobile R&D Center
** General Motors Company
*** The Pennsylvania State University

Table 1 Physical properties and correlations

Parameters	Value	Parameters	Value
Dry membrane density (g/cm^3), ρ_e	1.9	Volume fraction of ionomer in the catalyst layer, ε_e	$\varepsilon_e = (I/C)\,\varepsilon_c \frac{\rho_c}{\rho_e}\left(1 + \frac{M_w \rho_e}{\rho_w EW}\lambda\right)$
EW of dry membrane (g/mol), *EW*	950		
Anode Pt loading (mg/cm^2)	0.05	Proton conductivity of ionomer (S/m), κ	$\kappa = 22.0 \exp\left[-\frac{E_\kappa}{R}\left(\frac{1}{T} - \frac{1}{353.15}\right)\right]$ $a^{2.24}$, E_k = 12 kJ/mol
Cathode Pt loading (mg/cm^2)	0.3/0.1		
Anode ionomer carbon weight ratio (I/C)	0.6	Tortuosity of the ionomer phase in the catalyst layer, τ_e	$\tau_e = \begin{cases} 0.0845\,(\varepsilon_e - 0.04)^{-1.17} & \varepsilon_e < 0.16 \\ 1.0 & \varepsilon_e \geq 0.16 \end{cases}$
Cathode ionomer carbon weight ratio (I/C)	0.95		
GDL porosity, ε_{GDL}	0.625	Water uptake in ionomer, λ	$\lambda = \begin{cases} \left[1 + 0.2325a^2\left(\frac{T-303}{30}\right)\right]\left[14.22a^3 - 18.92a^2 + 13.41a\right] & a \leq 1 \\ 8.71\left[1 + 0.2325\left(\frac{T-303}{30}\right)\right](1-s) + [9.22 + 0.181\,(T - 273.15)]\,s & a > 1 \end{cases}$
MPL porosity, ε_{MPL}	0.5		
Carbon fraction in CL, ε_c	0.696		
Carbon density (g/cm^3), ρ_c	1.95		
GDL thermal conductivity (W/m K)	0.5	Water permeability in the membrane (mol/(m*Pa*s)), p_w	$p_w = 3.2 \times 10^{-11} \exp\left[\frac{E_w}{R}\left(\frac{1}{T} - \frac{1}{363}\right)\right]$ exp (3.4a), E_w = 22 kJ/mol
MPL thermal conductivity (W/m K)	0.25		
CL thermal conductivity (W/m K)	0.2	Oxygen permeability in ionomer (mol/(m*Pa*s)), p_{O_2}	$p_{O_2} = p_{dry} \exp(-E_{dry}/RT) + \upsilon_w p_{wet} \exp(-E_{wet}/RT)$
Electrical contact resistance (Ω cm^2)	0.012		$\rho_{dry} = 0.674 \times 10^{-11}$, $\rho_{wet} = 5.05 \times 10^{-11}$ mol/(mPa S), E_{dry} = 21.28 kJ/mol, E_{wet} = 20.47 kJ/mol
Coolant specific heat (J/(g*K))	4.18	Water volume fraction in ionomer, u_w	$u_w = 18\lambda/(18\lambda + EW/\rho_e)$

The predicted cell voltage and high-frequency resistance (HFR), current density and temperature distributions, as well as liquid water distribution are compared to the experimental data under various operating conditions and at two platinum (Pt) loadings of 0.3 mg/cm^2 and 0.1 mg/cm^2, respectively. The details of the operating conditions and the corresponding experimental data can be found on the DOE project website[8].

2. Numerical Model and Procedure

This modeling study employed the non-isothermal, electrochemistry-transport fully coupled model based on the multiphase mixture model[1]. The two-phase flow in both porous components and gas flow channels in PEMFCs is taken into account. Conservation equations of mass, momentum, energy, species and charge under two phase condition can be summarized as follows:

Continuity equation:

$$\nabla \cdot (\rho \vec{u}) = 0 \tag{1}$$

Momentum conservation:

$$\nabla \cdot \left(\frac{\rho \vec{u}\vec{u}}{\varepsilon^2}\right) = -\nabla P + \nabla \cdot (u \nabla \vec{u}) + S_u \tag{2}$$

Energy conservation:

$$\nabla \cdot (\gamma_T \rho c_p \vec{u} T) = \nabla \cdot (k^{eff} \nabla T) + S_T \tag{3}$$

Species conservation:

$$\nabla \cdot (\gamma_C \vec{u} C^i) = \nabla \cdot (D_g^{i,eff} \nabla C_g^i) - \nabla \cdot \left[\left(\frac{m f_l^i}{M^i} - \frac{C_g^i}{\rho_g}\right)\vec{J}_l\right] + S_C^i \tag{4}$$

Electron conservation:

$$0 = \nabla \cdot (\sigma_s^{eff} \nabla \Phi_s) - j \tag{5}$$

Proton conservation:

$$0 = \nabla \cdot (\kappa_e^{eff} \nabla \Phi_e) + j \tag{6}$$

where, ρ, u, P, T, C^i, j, Φ_s and Φ_e are the density, superficial fluid velocity vector, pressure, temperature, molar concentration of species i, volumetric reaction current, electronic phase potential, and electrolyte phase potential, respectively. More details about this model can be found in references[1] and thus are not repeated here. For low-Pt loading (0.1 mg/cm^2) simulations, the microscopic transport resistance of oxygen in cathode catalyst layer (CL) will play an important role on PEMFC performance. We used our recently developed electrode model to account for low-Pt loading effect[9]. The physical parameters relevant to the present study are listed in Table 1.

Figure 1 shows the computational geometry and mesh of the modeled PEMFC in this work. This fuel cell includes

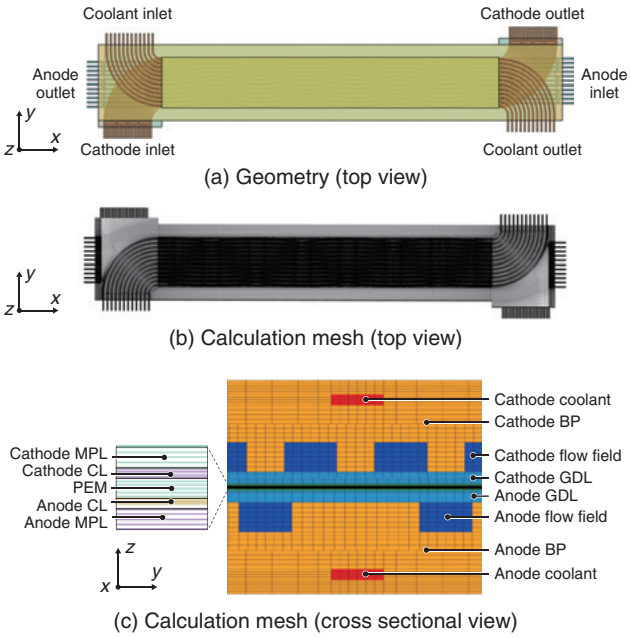


Fig. 1 Computational geometry and mesh of modeled PEM fuel cell

Table 2 Geometry parameters of modeled fuel cell

Parameters	Value
Membrane thickness (μm)	18
CCL thickness (μm)	16
ACL thickness (μm)	6
MPL thickness (μm)	30
GDL thickness (μm)	160
Gas channel width (mm)	0.4
Gas channel height (mm)	0.7
Gas channel length (mm)	183
Coolant channel width (mm)	0.7
Coolant channel height (mm)	0.15
Anode land width (mm)	1.5
Cathode land width (mm)	0.5

11 wavy rectangular flow channels on the anode side and twice as many on the cathode side. Each side has 12 coolant channels with the arched part near the inlet and outlet. Due to the complex geometry of the gas flow channels and coolant channels, the bipolar plates (BP) and coolant flow channels, gas diffusion layers (GDL), and membrane electrode assembly (MEA) are meshed separately in order to simplify the meshing process and reduce the mesh element number. This results in the non-conformal meshes in both anode and cathode BP, and in cathode GDL as shown in Fig. 1(c). The total number of the mesh elements is about 9.2 million with 95 mesh layers along the through-plane direction of the cell. Details of the geometrical dimensions of the cell are listed in Table 2.

The governing Eqs. (1)-(6) coupled with the low-Pt loaded electrode model for the cathode CL are solved within the commercial CFD software, ANSYS Fluent, using SIMPLE algorithm and algebraic multigrid (AMG) method. User defined functions (UDFs) are added to update the source terms, transport properties, boundary conditions and electrochemical reactions in these equations during calculation. For a typical two-phase simulation case, several thousand iterations are required to reach convergence with the water balance less than 2% and species balance less than 1%.

3. Results and Discussion

3.1. Calculation Condition and Calculation Result

The present validation studies are performed on 8 cases, including 5 cases with 0.3 mg/cm^2 Pt loading and 3 cases with 0.1 mg/cm^2 Pt loading. These cases have different inlet boundary conditions and operating temperatures. Table 3 lists the operating conditions of these cases, in which Letters B and L in Case No. indicate the case with 0.3 mg/cm^2 Pt loading and 0.1 mg/cm^2 Pt loading, respectively. Numerous comparisons with the experiments were conducted. The prediction of water balance between anode and cathode is challenging in the case where cathode inlet gas is dry and anode inlet gas is wet or conversely, where cathode inlet gas is wet and anode inlet gas is dry. Thus, 8 cases are chosen herein to compare between simulations and experiments here.

Figure 2 shows the contours of the simulated current density (a) and temperature (b) distributions in the membrane, temperature distribution on the cathode BP (c), as well as water saturation distribution in the cathode gas flow channel (d) and GDL (e) for Case B1 at 1.5 A/cm^2. It can be seen that the current density decreases somewhat with increasing water saturation in the GDL along the cathode flow channels as shown in Fig. 2(e). Some regions with much smaller current density exist near the top and bottom edges where gas flow is detoured by the cathode wavy channels such that it becomes easy to accumulate liquid water. The temperature distribution in the membrane appears to reflect the different patterns of the wavy channels in anode and cathode sides. At the cathode BP, the region with the highest temperature exists near the outlet of the coolant channels. The water saturation in the cathode gas channel and GDL increases along the cathode flow. Although the anode inlet is almost completely dry, the cathode side still accumulates considerable liquid water through condensation, due to the low operating temperature in this case.

The detailed distributions of the reaction current, temperature and water saturation in the PEMFC shown in Fig. 2 are obtained from the 3D computations with fine mesh. However, it is challenging to obtain these distributions with such high spatial resolution from the experiments. In particular, the difference of current density and temperature in the membrane and water saturation in the cathode GDL between the region under the land and under the channel can be clearly observed in the simulation result with high spatial resolution mesh as seen in Fig. 2(a) and (e). As shown in Fig. 2, this developed method can give the deep insight into distributions in the cell such as differences of water, current density, and temperature in the MEA under the lands and under the flow channels which are challenging to measure with experimental approaches.

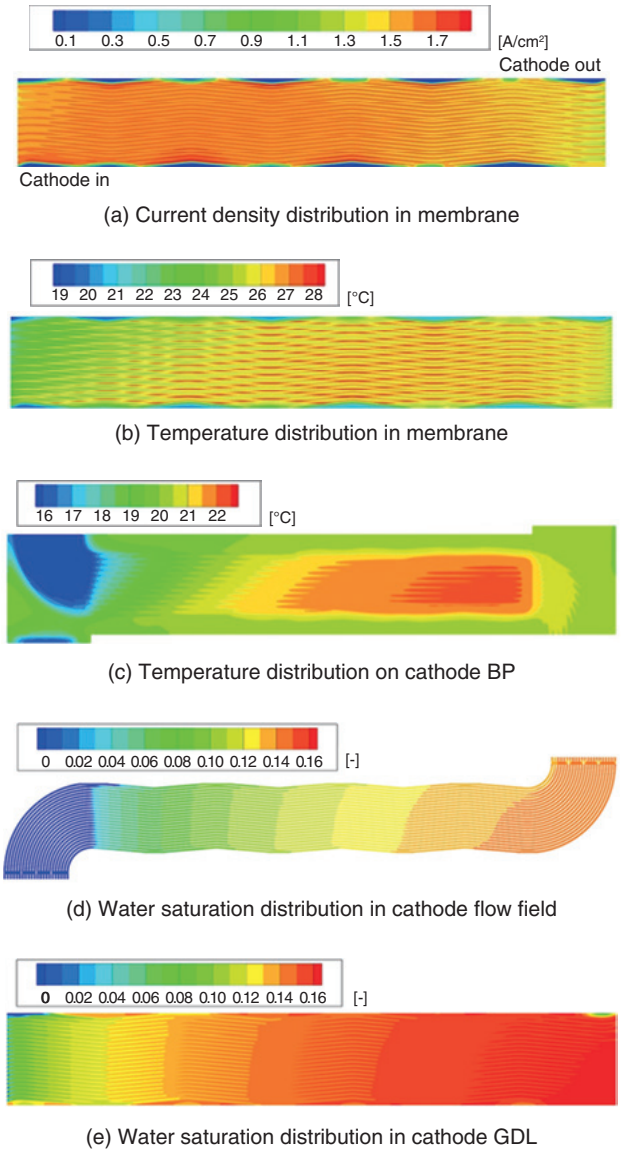
3.2. Comparison of Current Density and Temperature Distribution between Simulation and Experiment

It is challenging to measure the distributions by experimental approaches with such a high spatial resolution as shown in Fig. 2. According to reference[8], two 25 (length) × 4 (width) segmented collectors were used to measure the current density and temperature distributions on anode and cathode BPs, respectively. In order to make direct comparisons, we also divided the simulated results into the same 100 (25 × 4) segments as in the experiment. In each segment, the simulated values are averaged based on the weight of the mesh area in that segment. Figure 3(a) and (b) show a comparison of the segmented current density and temperature distributions between the simulation and experiment for Case B2, and Fig. 3(c) shows a comparison of the corresponding 1D profiles

Table 3 Operating conditions for validation cases

Case	Loading (mg/cm²)	Current density (A/cm²)	Cathode			Anode			Cell temperature (°C)	Coolant	
			Stoich.	Inlet Temp. /Dew point (°C)	Inlet pressure (atm)	Stoich.	Inlet Temp. /Dew point (°C)	Inlet pressure (atm)		Inlet T (°C)	Outlet T (°C)
B1	0.3	1.5	2	15.1/9.8	1.6	1.5	18.7/-100.0	1.0	20	11.8	18.9
B2	0.3	1.5	2	36.1/38.2	1.6	1.5	38.7/-100.0	1.0	40	30.9	38.3
B3	0.3	1.5	2	56.8/58.0	1.6	1.5	58.6/-100.0	1.0	60	50.6	58.3
B4	0.3	1.5	2	77.6/77.8	1.6	1.5	78.7/-100.0	1.0	80	73.3	78.5
B5	0.3	1.5	2	37.0/10.1	1.1	1.5	39.9/39.2	1.5	40	33.2	39.8
L1	0.1	1.5	2	35.4/38.1	1.7	1.5	38.7/-100.0	1.1	40	30.1	17.0
L2	0.1	1.5	2	55.9/58.0	1.7	1.5	58.4/-100.0	1.1	60	50.0	58.2
L3	0.1	1.5	2	34.4/10.1	1.2	1.5	38.8/39.2	1.5	40	29.5	18.9

along the cathode flow channels for the same case. It can be seen that the multiphase-mixture model predictions are in accord with measured current density and temperature distributions. Moreover, the 1D results successfully capture the trend change of current density and temperature along the cathode channels. Similar agreement is also achieved in



(a) Current density distribution in membrane

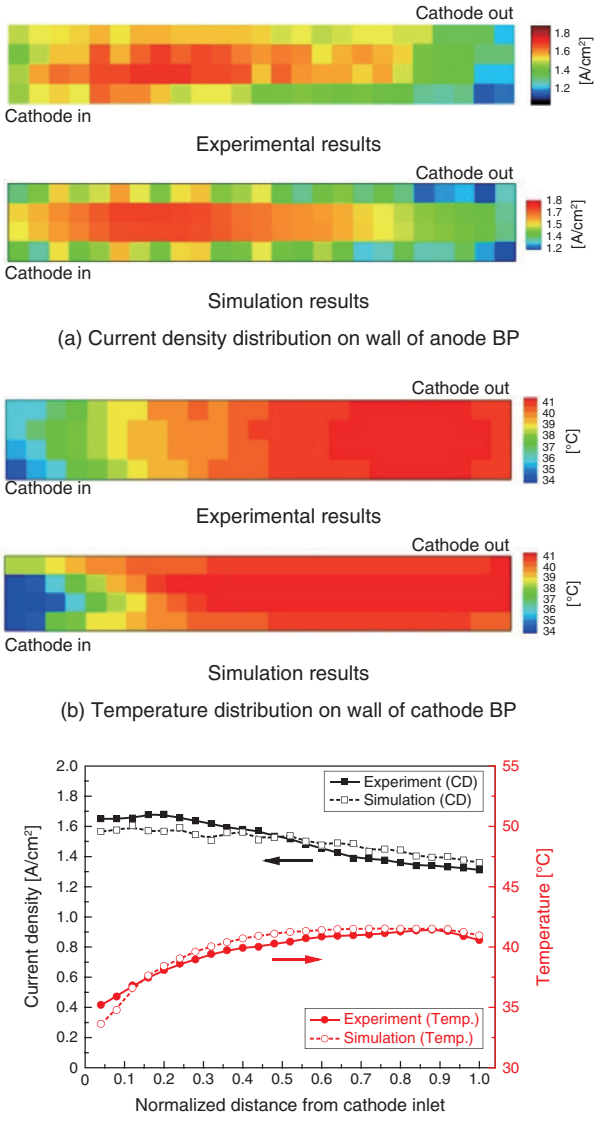
(b) Temperature distribution in membrane

(c) Temperature distribution on cathode BP

(d) Water saturation distribution in cathode flow field

(e) Water saturation distribution in cathode GDL

Fig. 2 Contours of calculation results of distributions for Case B1



(a) Current density distribution on wall of anode BP

(b) Temperature distribution on wall of cathode BP

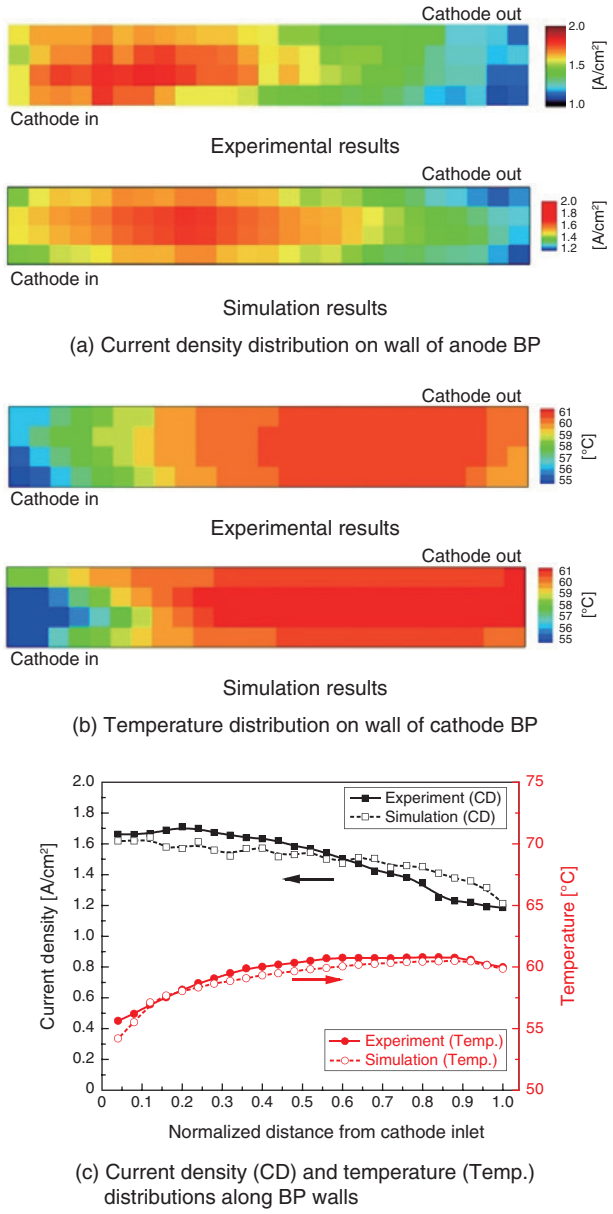
(c) Current density (CD) and temperature (Temp.) distributions along BP walls

Fig. 3 Current density and temperature distributions for Case B2

other cases considered as shown in Fig. 4 - Fig. 7 for Case B3, Case B5, Case L2 and Case L3.

The effects of Pt loading on current density distribution are examined in Fig. 4(c) and Fig. 6(c). The operating conditions of Case B3 and Case L2 are almost same. Although experimental data of current density distribution along the channel doesn't show much difference between 0.3 mg/cm^2 and 0.1 mg/cm^2 cases, the simulation results indicate that current density distribution along the channel becomes more uniform and the peak of the current density is shifted from near the cathode inlet to the middle of the cathode flow path when Pt loading is decreased from 0.3 mg/cm^2 to 0.1 mg/cm^2. It is assumed that CL with low-Pt loading is unable to deal with high current near the cathode inlet due to its low active surface area and the peak of the current density is shifted to the downstream of the cathode flow path.

Figures 8 and 9 show the comparisons of the predicted voltage and HFR with the experimental data for all cases with Pt loading of 0.3 mg/cm^2 and 0.1 mg/cm^2, respectively. From the results of Case B2 and L1, B3 and L2, and B5 and L3, cell voltages are decreased by 50 to 100 mV and HFR is increased by about 10 mΩcm^2 corresponding to the decrease of Pt loading from 0.3 mg/cm^2 to 0.1 mg/cm^2. The simulations capture the voltage and HFR changes in a wide range of operating conditions for both Pt loadings. Good agreement of the voltage and HFR between simulations and experiments are obtained.

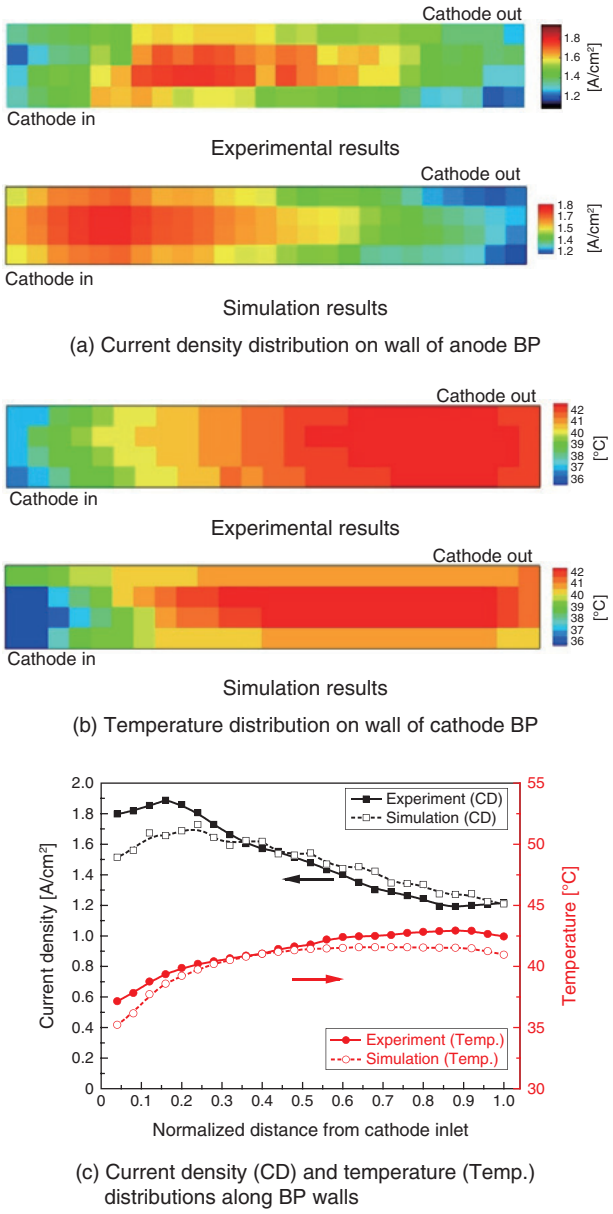


(a) Current density distribution on wall of anode BP

(b) Temperature distribution on wall of cathode BP

(c) Current density (CD) and temperature (Temp.) distributions along BP walls

Fig. 4 Current density and temperature distributions for Case B3



(a) Current density distribution on wall of anode BP

(b) Temperature distribution on wall of cathode BP

(c) Current density (CD) and temperature (Temp.) distributions along BP walls

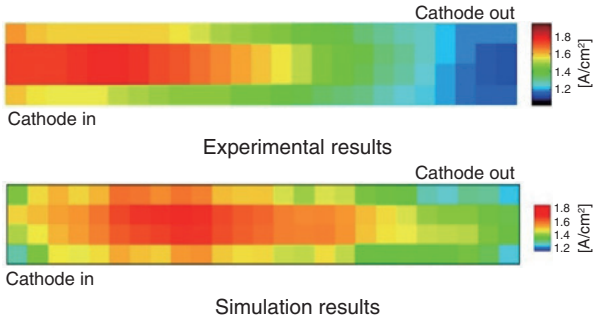
Fig. 5 Current density and temperature distributions for Case B5

3.3. Comparison of Water Distribution between Simulation and Experiment

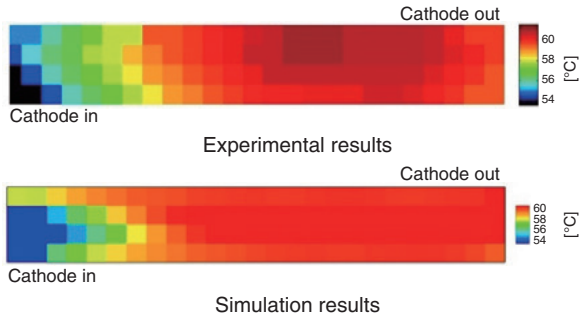
Figure 10 compares the water thickness distribution measured by neutron imaging with the simulated one for Case B2, B3, B4 and B5, respectively. The water thickness in the simulations is calculated by,

$$t_w = \int s_k \varepsilon_k dx \qquad (7)$$

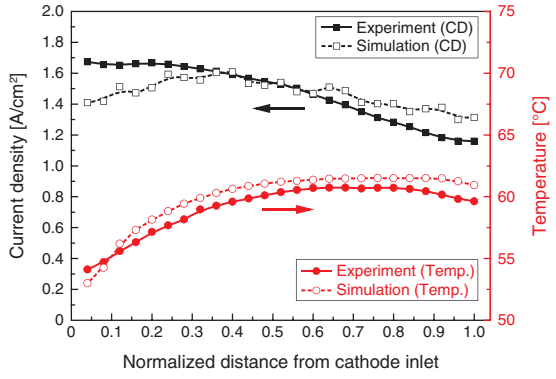
where s_k and ε_k are the water saturation and porosity in the cell components including gas channel, GDL or CL. The integration is performed across the entire thickness of the cell. It is seen from Fig. 10 that the simulated water thickness distribution agrees with the neutron imaging quite well. The liquid water in the cell decreases gradually as the temperature increases. In Case B2 at 40°C, liquid water nearly spreads through the whole cell, while the cell has almost no liquid water in Case B4 at 80°C. In addition, although Case B2 and Case B5 work at the same temperature, different water distribution patterns appear due to the different inlet conditions. In Case B2, the cathode inlet has high relative humidity (RH) and the anode inlet is completely dry. Consequently, there is little liquid water in the region near the anode inlet. In Case B5, the anode inlet is nearly fully saturated, but the cathode inlet RH is very low, thus resulting in a drier region near the cathode inlet. The simulations correctly capture the water distribution change under different operating conditions. The simulation study achieves a quantitative agreement of the water



(a) Current density distribution on wall of anode BP

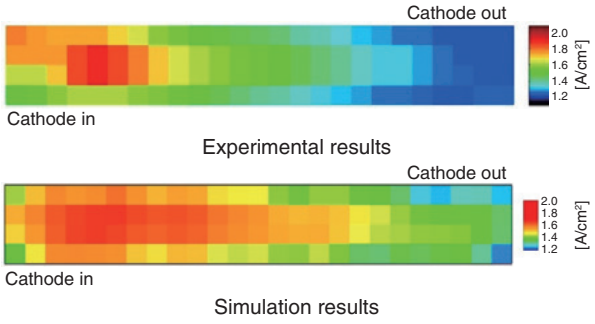


(b) Temperature distribution on wall of cathode BP

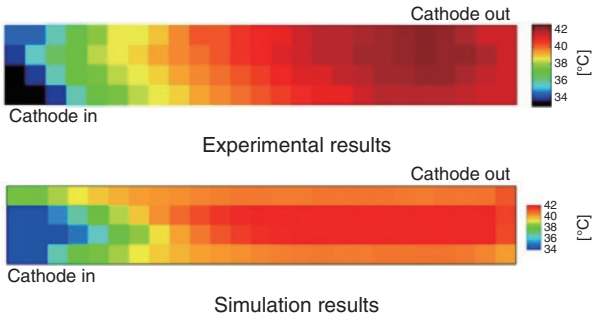


(c) Current density (CD) and temperature (Temp.) distributions along BP walls

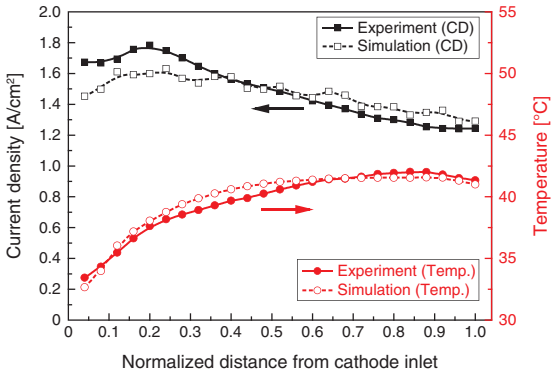
Fig. 6 Current density and temperature distributions for Case L2



(a) Current density distribution on wall of anode BP

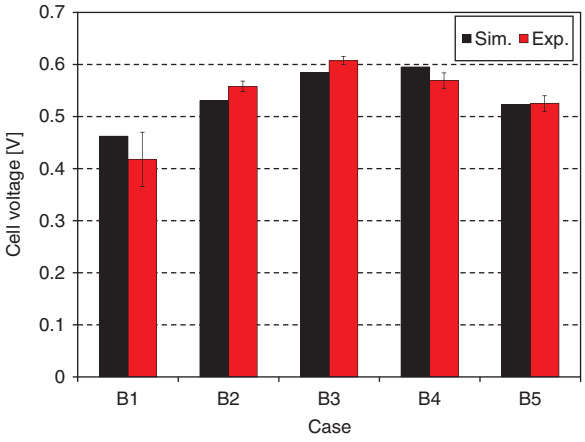


(b) Temperature distribution on wall of cathode BP

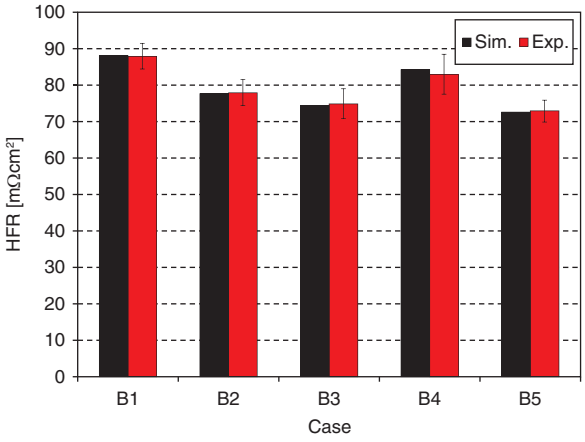


(c) Current density (CD) and temperature (Temp.) distributions along BP walls

Fig. 7 Current density and temperature distributions for Case L3

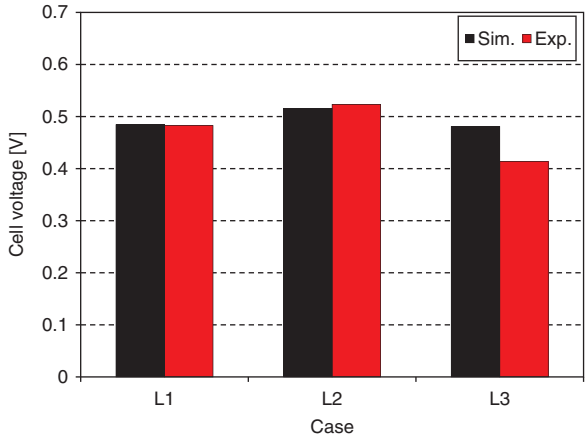


(a) Voltage

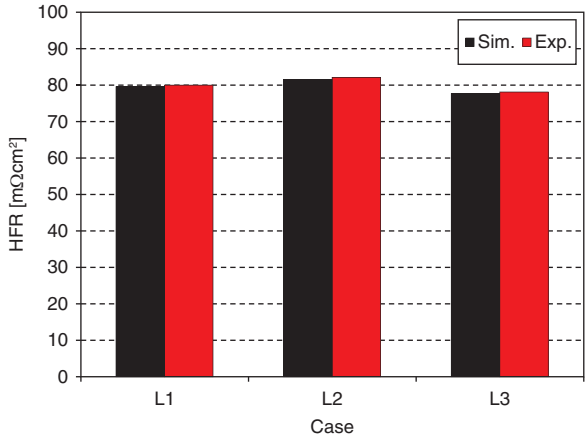


(b) High Frequency Resistance

Fig. 8 Comparison of voltage (a) and HFR (b) between simulation and measurement for 0.3 mg/cm^2 Pt loading cases

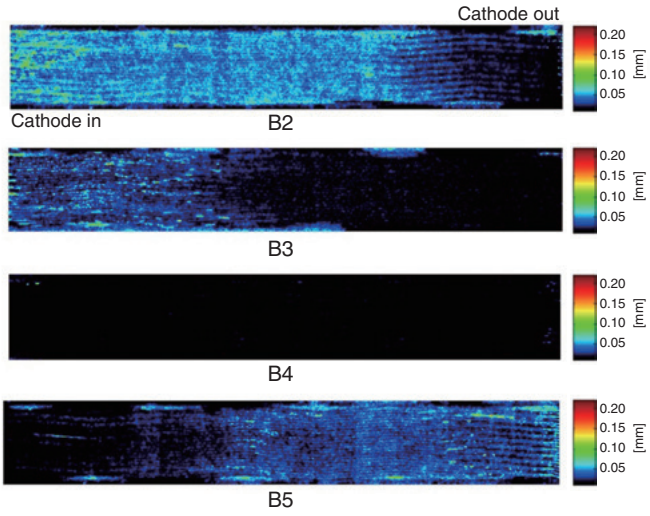


(a) Voltage

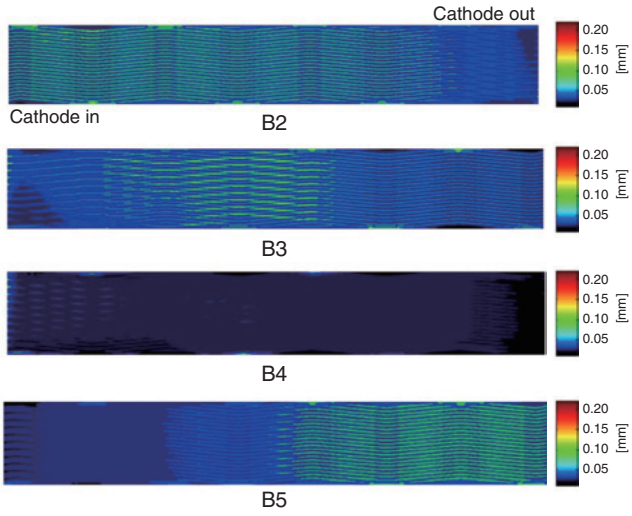


(b) High Frequency Resistance

Fig. 9 Comparison of voltage (a) and HFR (b) between simulation and measurement for 0.1 mg/cm^2 Pt loading case



(a) Experimental data (Neutron Imaging)



(b) Simulation results

Fig. 10 Comparison of water distribution between simulation and neutron imaging for cases B2, B3, B4, and B5

distribution in the cell with neutron imaging measurements, demonstrating that the multiphase-mixture model is quite capable of predicting water transport and distribution in PEMFCs with realistic flow field geometries. Also, simulation results show the ability of the model to find the optimal combination of operating condition, flow field and MEA design to utilize a low-Pt loading CL and realize low cost cell.

4. Conclusion

Large-scale computations of a PEMFC with parallel wavy flow field have been carried out using the multiphase-mixture model. We demonstrate the vast computational capability of the model in simulating the comprehensive two-phase phenomena in a PEMFC. Eight case studies are performed to examine the validity of these simulations. Reasonable agreement in cell voltage, HFR, and current density and temperature distributions is achieved between simulations and experiments in these cases under various operating conditions with two Pt loadings of 0.3 mg/cm^2 and 0.1 mg/cm^2, respectively. Of particular importance, we obtain a quantitative agreement between the predicted and measured liquid water distributions in a practical PEMFC.

References

(1) Wang, Y., Wang, C. Y.: A Nonisothermal, Two-Phase Model for Polymer Electrolyte Fuel Cells, Journal of the Electrochemical Society, 153, A1193-A1200, (2006)

(2) Meng, H.: A Three-dimensional Mixed-domain PEM Fuel Cell Model with Fully-coupled Transport Phenomena, Journal of Power Sources, 164, p.688-696, (2007)

(3) He, M., Huang, Z., Sun, P., Wang, C.: Modeling and Numerical Studies for a 3D Two-Phase Mixed-Domain Model of PEM Fuel Cell, Journal of the Electrochemical Society, 160, F324-F336, (2013)

(4) Cao, T. F., Lin, H., Chen, L., He, Y. L., Tao, W. Q.: Numerical Investigation of the Coupled Water and Thermal Management in PEM Fuel Cell, Applied Energy, 112, p.1115-1125, (2013)

(5) Shimpalee, S., Greenway, S., Spuckler, D., Van Zee, J. W.: Predicting Water and Current Distributions in a Commercial-size PEMFC., Journal of Power Sources, 135, p.79-87, (2004)

(6) Fink, C., Fouquet, N.: Three-dimensional Simulation of Polymer Electrolyte Membrane Fuel Cells with Experimental Validation, Electrochimica Acta, 56, p.10820-10831, (2011)

(7) Carnes, B., Spernjak, D., Luo, G., Hao, L., Chen, K. S., Wang, C. Y., Mukundan, R., Borup, R. L.: Validation of a Two-phase Multidimensional Polymer Electrolyte Membrane Fuel Cell Computational Model using Current Distribution Measurements, Journal of Power Sources, 236, p.126-137, (2013)

(8) http://pemfcdata.org.

(9) Hao, L., Moriyama, K., Gu, W., Wang, C. Y.: Modeling and Experimental Validation of Pt Loading and Electrode Composition Effects in PEM Fuel Cells, Journal of the Electrochemical Society, 162 (8), F854-F867, (2015)

Nomenclature

Latin Symbols

c_p	Specific heat (J/kg K)
C^i	Molar concentration of species i (mol/m^3)
$D^{i,eff}$	Effective diffusivity of species i (m^2/s)
j	Volumetric reaction current density (A/m^3)
P	Pressure (Pa)
S	Source term in transport equations
s	Saturation
T	Temperature (K)
u	Velocity vector (m/s)

Greek Symbols

ε	Porosity
κ	Ionic conductivity (S/m)
λ	Water content in ionomer
ρ	Density (kg/m^3)
σ	Electronic conductivity (S/m)

Subscripts/Superscripts

e	Ionomer
eff	Effective value
g	Gas
i	Species
k	Component in cell
s	Electronic phase

Author


Koji MORIYAMA


Wenbin GU


Liang HAO


Chao-Yang WANG

Development of 70 MPa Differential-pressure Water Electrolysis Stack

Hiroyuki ISHIKAWA* Eiji HARYU*
Nobuyuki KAWASAKI* Hayato DAIMON*

ABSTRACT

In order to accommodate the increased fuel tank storage pressure of fuel cell vehicles to 70 MPa, measures were taken to enable hydrogen stations that use Honda's proprietary differential-pressure water electrolysis technology to support higher pressures. Specifications capable of enduring long-time operation at 70 MPa were established by using a sealing structure with a high-pressure hydrogen channel in the center of the cell. In addition, the break mechanism of the proton exchange membrane was clarified, and specifications capable of sustaining the differential pressure were set. A high-pressure water electrolysis stack based on this know-how was manufactured and compared with existing hydrogen stations that use a mechanical compressor, and it was confirmed that the electric power needed to produce hydrogen compressed to 70 MPa was reduced by approximately 30%. Moreover, the water content of the hydrogen was reduced by 60% compared to that of hydrogen compressed to 35 MPa, which reduced the dehumidification energy needed for use as hydrogen fuel for fuel cell vehicles.

1. Introduction

Honda is continuing development of fuel cell vehicles (FCV) that use hydrogen as an energy source to address the two issues of reduction of CO_2 emissions and depletion of fossil fuels. Efforts are being made to increase the FCV fuel tank storage pressure from 35 MPa to 70 MPa to extend FCV cruising ranges and increase user convenience. However, there are also calls to manufacture the hydrogen used as fuel from renewable energy without using fossil fuels as much as possible. Therefore, proving tests are under way worldwide for solar hydrogen stations that use solar cells as the input power source to help expand the hydrogen supply infrastructure in parallel with FCV development[(1)-(4)]. In addition, smart hydrogen stations, which are the first known stations to combine all elements from hydrogen production to the dispenser in a single package, have been operated in Saitama City and Kitakyushu City since 2014[(5), (6)]. These hydrogen stations use Honda's proprietary differential-pressure water electrolysis technology that integrates water electrolysis and hydrogen pressurization functions, and realize a more compact, space-saving size compared to existing stations that use a mechanical compressor (Fig. 1). However, the existing differential-pressure water electrolysis stacks used in these stations have 35 MPa specifications, so measures are needed to support 70 MPa.

Figure 2 shows a schematic of differential-pressure water electrolysis. The water electrolysis reaction at high pressure is the same as that at normal pressure, and is the water electrolysis reaction using a proton exchange membrane (PEM). In addition, electrochemical hydrogen pressurization methods operate on the principle of setting only the cathode to high pressure to obtain high-pressure hydrogen. Therefore, unlike methods that use a mechanical compressor, there is no vibration noise and motor rotation noise during hydrogen pressurization, realizing excellent quietness, and there is also no friction loss or motor loss, increasing efficiency. However, the cell structure should provide both electrochemical reactor and high-pressure hydrogen vessel functions, so a sealing structure is considered necessary to prevent external gas leaks. At the same time, the structure should have water supply performance and gas exhaust performance that do not impede the water electrolysis reaction. During the course of research on differential-pressure water electrolysis at 35 MPa, the authors established a structure that satisfies water electrolysis performance, differential-pressure sustaining performance, and external sealing performance[(7), (8)]. Development typically has the goal of realizing differential-pressure water electrolysis with a pressure difference on the order of about a dozen MPa[(9)], and there are no known reports of obtaining 70 MPa hydrogen by differential-pressure water electrolysis without using a mechanical compressor.

This study investigated a structure that realizes 70 MPa differential-pressure water electrolysis, manufactured an actual stack using that structure, and evaluated the performance.

* Automobile R&D Center

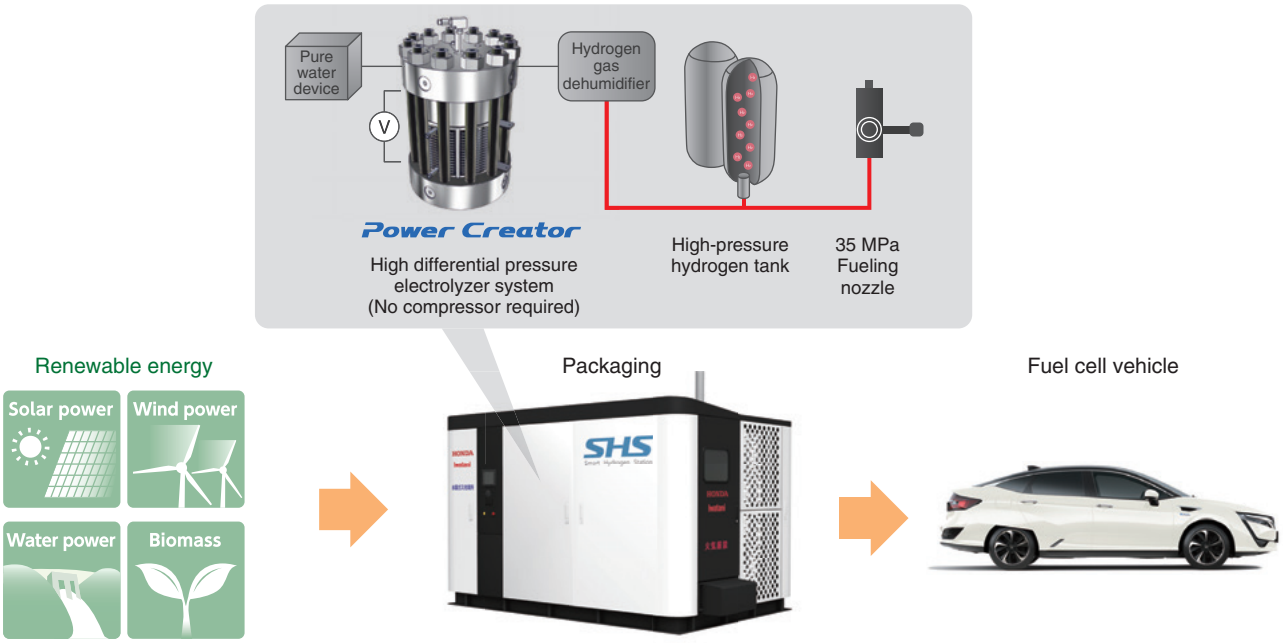


Fig. 1 Concept of Honda original smart hydrogen station

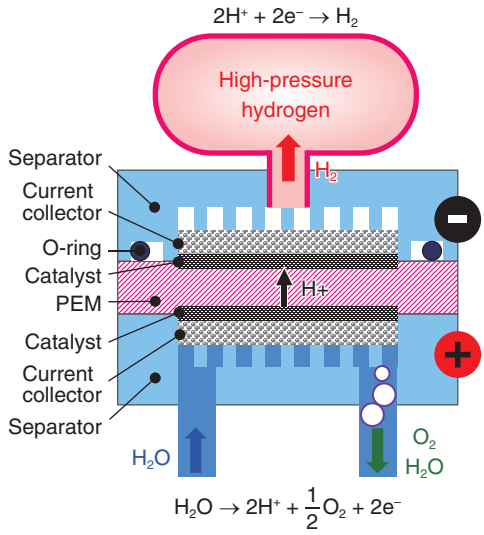


Fig. 2 Overview of high differential pressure water electrolysis

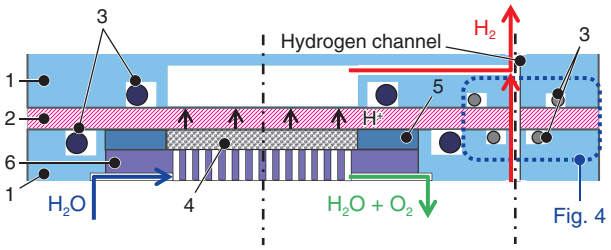
2. Approach toward Construction of Differential-pressure Water Electrolysis System that Supports 70 MPa

2.1. Understanding of Differential-pressure Sustaining Mechanism

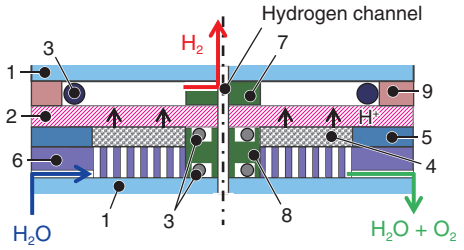
In differential-pressure water electrolysis, the differential pressure is sustained by the PEM, so the PEM needs pressure resistance capable of enduring the differential pressure between the target hydrogen pressure and the anode-side pressure. This pressure resistance is provided by the anode current collector, so the current collector itself should not deform and should also suppress PEM deformation relative to the pores on the current collector surface. Therefore, to help ensure that the membrane does not break even if differential pressure of 70 MPa is produced on the PEM, it is necessary to understand the minimum membrane thickness capable of sustaining this differential pressure and to clarify the differential-pressure sustaining mechanism.

2.2. Establishment of 70 MPa Sealing Structure

Figure 3(a) shows the conventional 35 MPa sealing structure, and Fig. 4 shows the location where different membrane thickness occurs due to the difference of dry-wet in the conventional structure. In the conventional structure, the PEM is exposed to the outside air, and different membrane thickness occurs between the part next to the high-pressure hydrogen channel that is kept in the wet state by the water content of the generated hydrogen and the part outside the O-rings. As shown in Fig. 5, this difference in dry-wet membrane thickness is greater at 70 MPa than at 35 MPa. Generally speaking, in order to seal with an O-ring, the design should clasp the O-ring in the installation gap and help prevent O-ring extrusion. This gap needs to be reduced as the pressure received by the O-ring increases, but the allowable gap is not specified at the high pressure of 70 MPa[10], so likewise there should be no gap in order to help achieve 70 MPa sealing durability. Therefore, a structure with the high-pressure hydrogen channel parts [parts 7 and 8 in Fig. 3(b)] in the center of the cell was devised as shown in Fig. 3(b). In this structure, no part of the PEM is exposed to the outside air, so there is no concern



(a) Conventional structure



(b) 70 MPa structure

1: Separator	2: PEM
3: O-ring	4: Anode current collector
5: Frame	6: Water passage plate
7: Cathode continuous hole part	8: Anode continuous hole part
9: Pressure-resistant body	

Fig. 3 Schematic of conventional and 70 MPa sealing structures

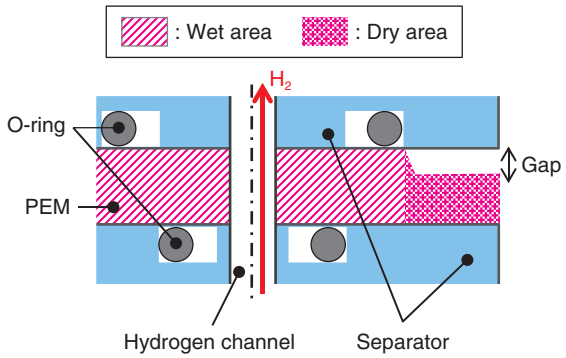


Fig. 4 Enlarged view of PEM dry-wet area in conventional sealing structure

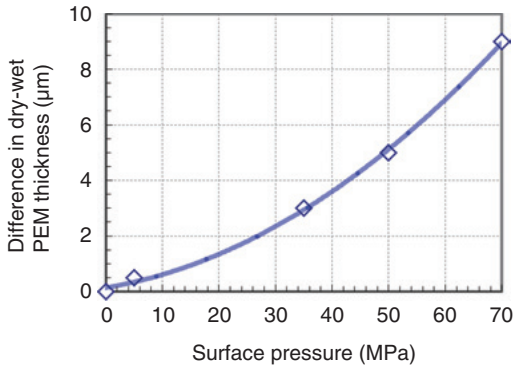


Fig. 5 Relation between surface pressure and difference in dry-wet PEM thickness (50°C, 100 μm)

of O-ring extrusion due to different dry-wet membrane thickness. Next, it was necessary to demonstrate durability to confirm that this sealing structure secures pressure resistance at 70 MPa and that there is no damage to the cell parts.

3. Experimental Method

3.1. Method for Understanding Minimum PEM Thickness

Figure 6 shows a cross-sectional view of the cell used to investigate a 70 MPa pressure-resistant structure. As described above, the structure has a hydrogen channel in the center of the cell, the current collector supports the PEM, and the O-ring provides the sealing function. A constant surface pressure is applied to the cell by a spring inside the piston, and the overall cell was manufactured in accordance with the design guidelines for high-pressure hydrogen vessels. The nitrogen gas used in the test was pressurized in steps using a gas pressurization compressor, and it was confirmed that pressures up to 70 MPa can be sustained. In addition, it was also confirmed whether there was damage to the O-ring that provides sealing performance and to the current collector parts. The test temperature for the pressure resistance test was set to 80°C, and this temperature was maintained by circulating hot water within the cell. The PEM thickness used in the test was reduced in steps starting from 200 μm to determine the minimum membrane thickness at which the differential pressure can be sustained. Based on these results, the cross-section of the PEM after the test was observed in locations with different membrane thickness to examine the mechanism by which differential pressure can be sustained.

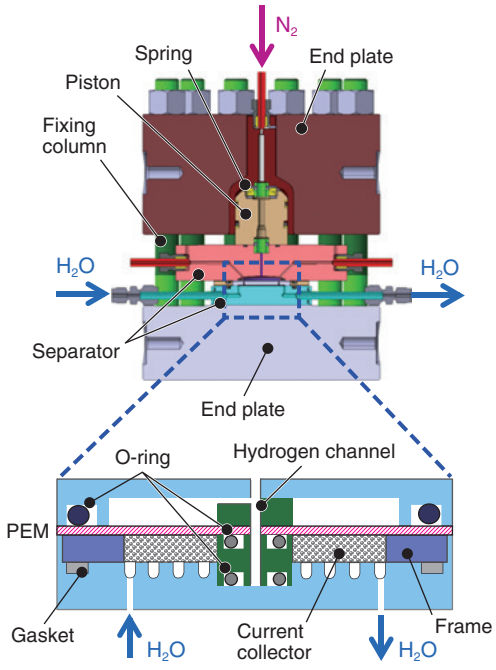


Fig. 6 Structure of 70 MPa pressure-resistant cell

3.2. Structural Durability Test Method

Figure 7 shows the evaluation system used in the 70 MPa cell structure durability test. A pressure cycle test that repeats pressurization to a maximum of 85 MPa and pressure reduction to normal pressure was performed with the target of 1000 cycles as the durability mode. The reason for this is that the solar hydrogen station currently being verified in Japan performs start-stop approximately 100 times per year[4], so the target was set to the number of start-stop times for 10 years. The test medium was incompressible water, and the test was performed using an air-driven hydraulic pump with sufficient pressure resistance to make it easier to check for leaks and to shorten the durability test. Pressurization and reduction was performed by adjusting the valve output of the pressure regulator and the flow regulator beforehand and turning the solenoid valve on and off with a timer. In addition, from the viewpoint of safety, relief valves were installed before the high-pressure filter and after the pressure regulator. The temperature during the durability test was set to the maximum stack operating temperature of 65°C. Cell structure durability was evaluated by performing the above-mentioned nitrogen gas sealing test (25°C) at 70 MPa. The nitrogen permeation amount from the high-pressure side to the opposite side was collected by the water replacement method, and durability was judged by comparing the amount before and after the durability test.

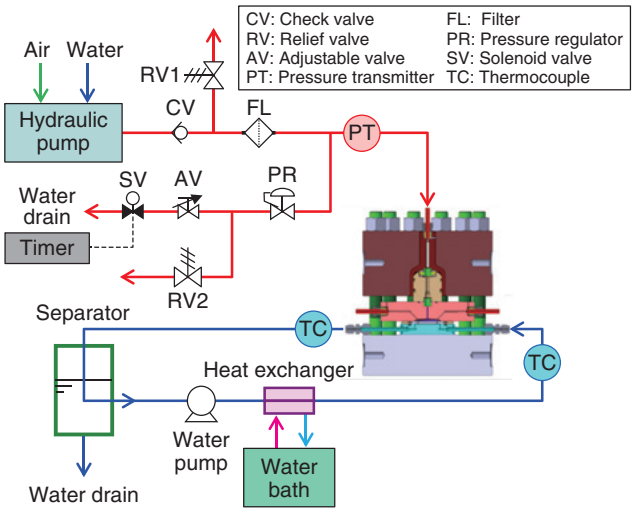


Fig. 7 Evaluation system of hydraulic durability test

4. Results and Discussion

4.1. Differential-pressure Sustaining Mechanism and Needed Membrane Thickness

Figure 8 shows the difference in differential-pressure sustaining performance at different PEM thicknesses. A differential-pressure of 70 MPa could be sustained at a membrane thickness of 60 μm or more, but at 50 μm the membrane broke four minutes after reaching 70 MPa, and at 30 μm the membrane broke immediately after reaching 50 MPa. In addition, after the test with a membrane thickness of 60 μm, it was found that there was no damage to the PEM, O-ring or current collectors, and that the structure with a high-pressure hydrogen channel in the center can satisfy both the differential-pressure sustaining and the sealing structure functions.

The membrane cross-section at each membrane thickness was observed after the above test. Figure 9 shows schematics of the differential-pressure sustaining condition and the membrane break condition. This shows that in the condition where the membrane broke, the entire membrane was in the tensile state relative to the current collector pores, but at a membrane thickness that sustained the differential pressure, the membrane maintained the compression state relative to the current collector pores. This clarified that in order to secure durability at 70 MPa, it is necessary to determine the minimum membrane thickness necessary to sustain the differential pressure, and also the

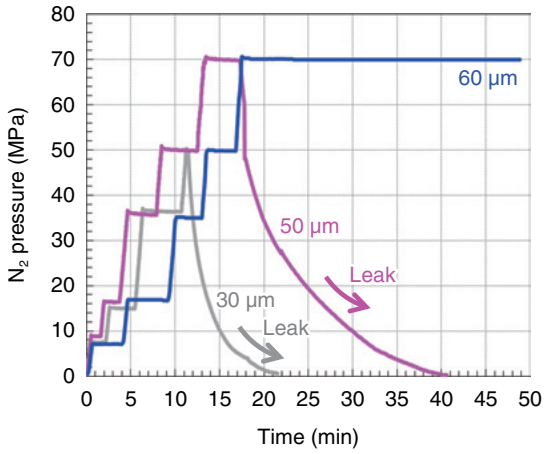


Fig. 8 Pressure sustaining characteristic by PEM thickness difference (80°C, N_2)

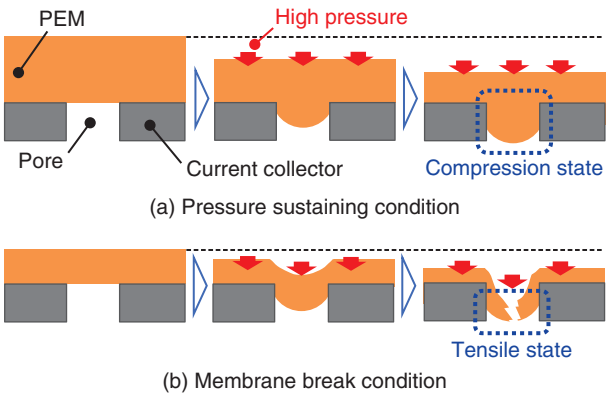


Fig. 9 Schematic of PEM cross section at pressure sustaining and membrane break conditions

Table 1 N_2 permeation amount before and after hydraulic durability test (25°C, N_2)

Measurement point	PEM permeation amount of N_2 ($cm^3/min/cm^2$)*
Before durability test	0.046
After 1000 cycles	0.046

* Average value of 3 times

amounts by which the membrane thickness decreases due to deformation at the current collector pores and due to compression creep. Therefore, PEM deformation to the pores was obtained by converting the pore volume into the membrane thickness, and was calculated to be 20 μm. In addition, PEM compression creep was determined by obtaining the property of the PEM alone, and it was found that 20 μm should be estimated. These results clarified that a PEM thickness of 100 μm or more satisfies the durability requirement.

4.2. Results of Structural Durability Test

Figure 10 shows the temperature and pressure profile in the hydraulic pressure rising and reduction durability test. The pressure rising and reduction test was performed for 1000 cycles at approximately 25 s per cycle. Table 1 compares the amount of nitrogen gas permeating to the opposite side at the start of the hydraulic pressure cycle test and after 1000 cycles in the 70 MPa sealing test. There was no difference in the nitrogen permeation amount before and after the durability test, which proved that this structure can endure extended use in terms of both differential-pressure sustainment and sealing structure performance. In addition, there was no damage to the PEM, O-ring or current collectors after the durability test, which also confirmed the durability of the parts.

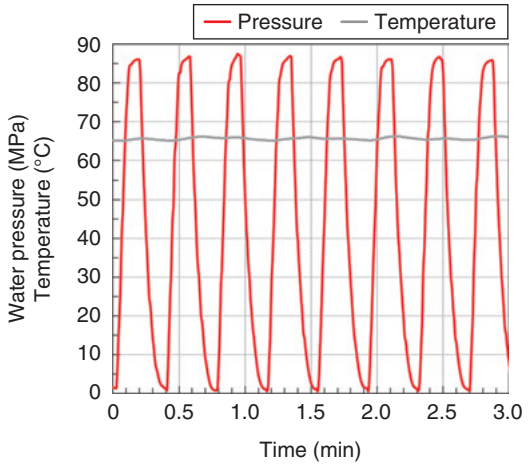


Fig. 10 Water pressure and temperature profile in hydraulic durability test

5. Evaluation of 70 MPa Stack Performance

5.1. Performance Evaluation Items

It is necessary to confirm whether changing the cell structure affects the electrolysis performance in a 70 MPa stack. Therefore, this was verified by comparing the difference in the electrolysis voltage during high-pressure water electrolysis with that of the conventional 35 MPa stack. In addition, the compressor power consumed by existing 70 MPa hydrogen stations and the pressurization energy needed by high-pressure water electrolysis were compared, and the advantage of differential-pressure water electrolysis was verified.

Meanwhile, in order to use hydrogen generated by 70 MPa high-pressure water electrolysis as hydrogen fuel for FCVs, the hydrogen quality should be as specified by SAE J2719[11] and ISO 14687-2[12], and the water concentration should be less than 5 ppm. In the water electrolysis reaction, water accompanies the protons moving within the PEM, so the generated hydrogen always contains some water. The energy needed to remove the water contained in the hydrogen in a subsequent process can be estimated by quantitatively determining this amount of water, so this is important for system design. Therefore, the amount of water contained in hydrogen generated by high-pressure water electrolysis was measured in the manufactured 70 MPa stack.

5.2. Stack Performance Evaluation Method

The PEM used in the test had a membrane thickness of 100 μm, and used an Ru-Ir complex oxide catalyst as the anode catalyst and a platinum black as the cathode catalyst. These catalysts were hot-pressed to both surfaces of the PEM to manufacture the stack used in the test. Figure 11 shows the evaluation system used to evaluate the performance of the manufactured 70 MPa differential-pressure water electrolysis stack. Hydrogen permeating

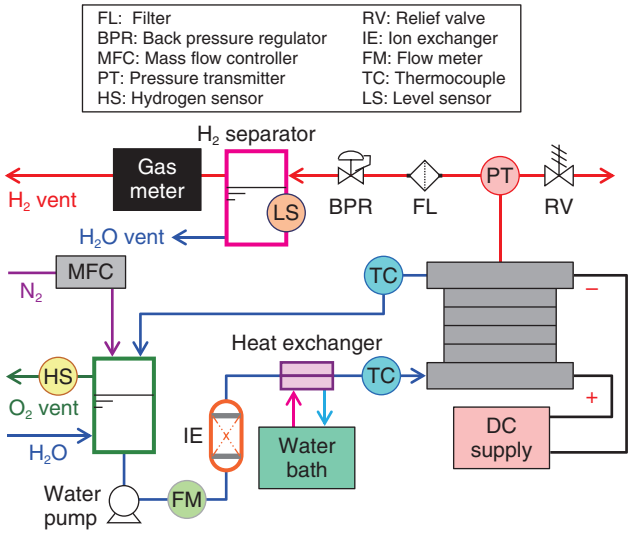


Fig. 11 Evaluation system of electrolysis stack

from the opposite electrode during high-pressure water electrolysis is included in the oxygen side, so for reasons of hydrogen safety, the test was performed by diluting with nitrogen at the oxygen-water separator and measuring with a hydrogen sensor to make sure that the hydrogen concentration was sufficiently low.

The test conditions adjusted the temperature to the stack operating temperature of 60°C using the temperature of the water circulating through the stack. The water quality was pure water, and the current density was set to 1.2 A/cm^2. Stack performance was evaluated by comparing the calculated and measured values of the electrolysis voltage needed to raise the pressure to 70 MPa, and by performing I-V measurement with different current values at each pressure to compare the cell voltage at different pressures. In addition, the amount of hydrogen produced was measured using a wet gas flow meter after lowering the pressure to normal pressure with the back pressure regulator. Furthermore, the amount of water permeating to the high-pressure hydrogen side during high-pressure water electrolysis was obtained by adding the rate of increase in the water level of the hydrogen-water separator on the hydrogen side and the amount of saturated vapor contained in the generated hydrogen.

5.3. Results of Stack Performance Evaluation

The know-how described above related to differential-pressure sustaining performance, sealing performance, and water electrolysis performance was used to manufacture a 70 MPa differential-pressure water electrolysis stack. Figure 12 shows a photograph of the exterior.

Figure 13 shows a graph comparing the electrolysis voltage needed to raise the pressure to 70 MPa with that of the conventional 35 MPa stack. These results clearly show that the pressurization curve up to 35 MPa matches that reported thus far. This demonstrates that the changes in the cell structure between the 70 MPa stack and the conventional 35 MPa stack do not have an adverse effect on water electrolysis performance. In addition, Table 2 compares the measured value with the calculated value of the electrolysis voltage E_{WE} needed for high-pressure water electrolysis as derived when ir is zero in Eq. (1)[13]. The reason why the measured value is 42 mV larger than the calculated value is assumed to be due to the increase in the direct-current resistance component resulting from the rise in PEM resistance when the PEM is highly compressed.

Table 2 Electrolysis voltage for 70 MPa compression

	Electrolysis voltage for 70 MPa compression (mV)
Calculated value	78
Measured value	120

$$E_{WE} = E_0 + \frac{RT}{2F} \ln \frac{P_1}{P_2} + ir \quad (1)$$

E_{WE}: Electrolysis voltage measured value [V]
E_0 : Theoretical electrolysis voltage [V]
R : Gas constant [J/(K·mol)]
T : Absolute temperature [K]
F : Faraday constant [C/mol]
P_1 : Hydrogen partial pressure on high-pressure side [MPa]
P_2 : Hydrogen partial pressure on low-pressure side [MPa]
ir : Direct-current resistance voltage [V]

Based on these results, Table 3 compares the amount of power needed to compress 1 kg of hydrogen to 70 MPa with that of existing hydrogen stations[14]. These results show that the hydrogen pressurization energy needed by differential-pressure water electrolysis is less than that for any currently operated hydrogen station, and that power consumption can



Fig. 12 Photograph of 70 MPa differential-pressure water electrolysis stack

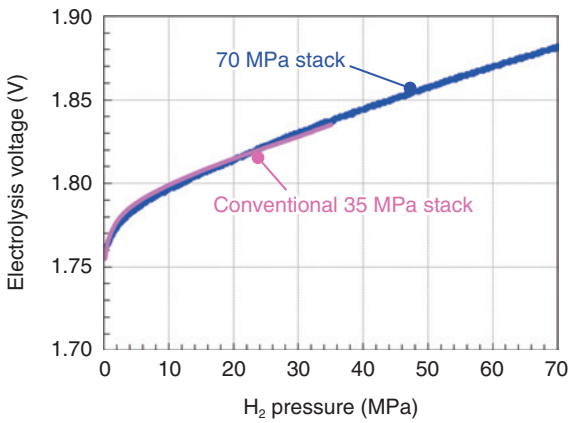


Fig. 13 Hydrogen compression curve of 70 MPa stack and conventional 35 MPa stack (60°C, 1.2 A/cm^2)

Table 3 Comparison of energy consumption for hydrogen compression

Manufacturer (Location)	Energy consumption for Hydrogen compression (kWh/kg-H_2)
Honda 70 MPa stack	3.71
JHFC (Asahi, Yokohama)	6.44
JHFC (Daikoku, Yokohama)	4.54
JHFC (Senju, Tokyo)	4.82

be reduced by approximately 30% compared to the amount of power consumed by a mechanical compressor.

Figure 14 shows the graph obtained by performing I-V measurement at each pressure and using Eq. (2) below to obtain the voltage efficiency (HHV conversion). The I-V slope at 70 MPa is larger than that at 35 MPa, and this is presumed to be due to an increase in the direct-current resistance component [*ir* term in Eq. (1)] accompanying the increase in PEM resistance. As a result, the obtained voltage efficiency is 78% at 70 MPa and 1.2 A/cm^2. This is lower than the voltage efficiency of 81% at 35 MPa, but also higher than the initially predicted 75%, so better than expected efficiency was obtained.

$$\eta_V = \frac{E_0}{E_{WE}} \times 100 \qquad (2)$$

η_V : Voltage efficiency [%]

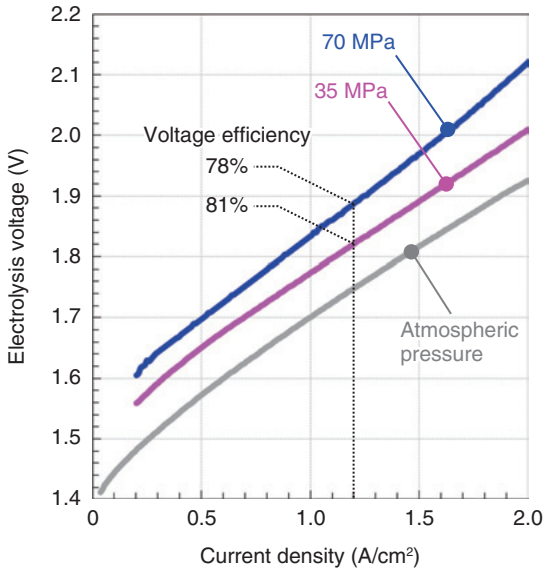


Fig. 14 Effect of H_2 pressure on I-V curve (60°C)

Figure 15 shows the transition in current efficiency due to pressure. Current efficiency indicates the production rate of hydrogen generated relative to the force current, and is calculated from Eq. (3). It was found that the current efficiency decreases as the pressure increases, but the rate of decrease lessens at higher pressures of 35 MPa or more. Current efficiency was initially thought to decrease in inverse proportion to the pressure, so 75% had been assumed[7], but the results showed that current efficiency of 83% was achieved at 70 MPa.

$$\eta_A = Q \cdot \left(\frac{I_{WE} \cdot 3600}{F} \cdot \frac{1}{2} \right)^{-1} \times 100 \qquad (3)$$

η_A : Current efficiency [%]
Q : Amount of hydrogen generated [mol/hr]
I_{WE} : Electrolysis current [A]

Figure 16 shows the relationship between the pressure and the amount of water permeating to the high-pressure cathode. This shows that the amount of water decreases as

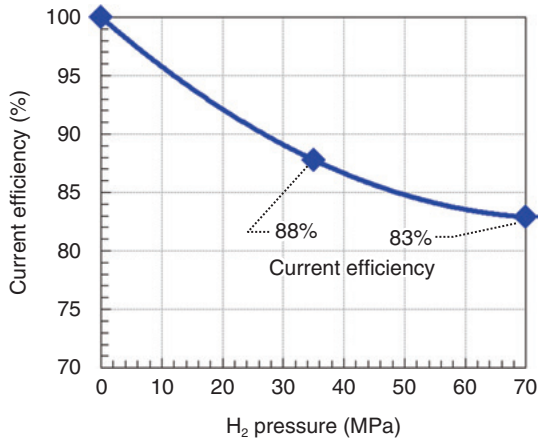


Fig. 15 Effect of H_2 pressure on current efficiency (60°C, 1.2 A/cm^2)

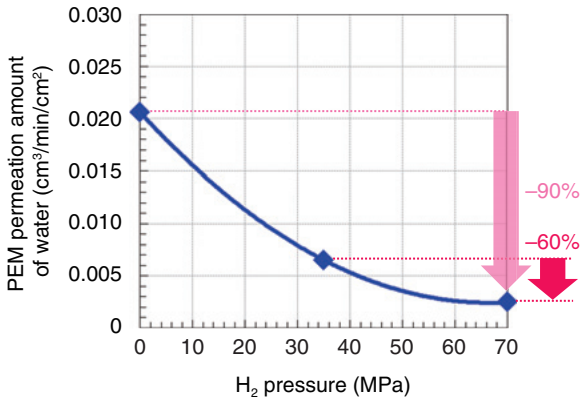


Fig. 16 Effect of H_2 pressure on PEM permeation amount of water to cathode (60°C, 1.2 A/cm^2)

the pressure increases, and at 70 MPa is 60% less than that at 35 MPa, and 90% less than that at normal pressure. This indicates that the water content of the generated hydrogen decreases, which suggests that the internal volume of the high-pressure hydrogen-water separator can be reduced, and that the energy required for dehumidification can also be reduced compared to that at 35 MPa. This provided prospects for additional system simplification.

6. Conclusion

A pressure-resistant structure for a 70 MPa differential-pressure water electrolysis stack was investigated and durability tests of this structure were performed. As a result, the following conclusions were obtained.

(1) The membrane thickness limit capable of sustaining a differential-pressure of 70 MPa was determined, and the mechanism by which differential-pressure can be sustained by the PEM was clarified.
(2) The sealing structure with a high-pressure hydrogen channel in the center used by a 70 MPa stack was proven to have durability capable of enduring the equivalent of 10 years of operation.

A 70 MPa differential-pressure water electrolysis stack that takes into account the above know-how was manufactured and the performance was verified. The following results were obtained.

(1) Use of 70 MPa differential-pressure water electrolysis successfully reduced the electric power needed to generate hydrogen compressed to 70 MPa by approximately 30% compared to that for existing hydrogen stations that use a mechanical compressor.
(2) The water content of the generated 70 MPa hydrogen was 60% lower than that at 35 MPa, so the energy required for dehumidification decreases, providing prospects for further simplifying the system.

References

(1) Nakazawa, K., Nagaoka, H., Takeuchi, J., Moburg, F., Yamashita, I., Okabe, M.: Introduction of High Differential Pressure Water Electrolysis-type Solar Hydrogen Station (SHS2), Honda R&D Technical Review, Vol. 22, No. 2, p. 28-35
(2) Nagaoka, H., Yoshida, N., Cun, D., Yamashita, I., Okabe, M.: Verification Test of High Differential Pressure Water Electrolysis-type Solar Hydrogen Station (SHS2), Honda R&D Technical Review, Vol. 24, No. 2, p. 74-81
(3) Takeuchi, J., Nakazawa, K., Yoshida, N., Ito, J., Okabe, M., Yamashita, I.: Introduction of Solar Hydrogen Station Installed in Japan, Honda R&D Technical Review, Vol. 25, No. 1, p. 86-92
(4) Yoshida, N., Miyake, A.: Verification Test Results for Solar Hydrogen Station in Japan, Honda R&D Technical Review, Vol. 26, No. 2, p. 200-206
(5) http://www.honda.co.jp/news/2014/4140918.html
(6) http://www.honda.co.jp/news/2014/4141215.html
(7) Haryu, E., Nakazawa, K., Taruya, K., Ishikawa, H., Okabe, M.: Mechanical Structure and Performance Evaluation of High Differential Pressure Water Electrolysis Cell, Honda R&D Technical Review, Vol. 23, No. 2, p. 97-105
(8) Kawasaki, N., Haryu, E., Ishikawa, H., Nakazawa, K., Okabe, M.: Study of Seal Structure of High-differential-pressure Water Electrolysis Cell, Honda R&D Technical Review, Vol. 25, No. 2, p. 137-144
(9) Grigoriev, S. A., Porembskiy, V. I., Korobtsev, S. V., Fateev, V. N., Auprêtre, F., Millet, P.: High-pressure PEM water electrolysis and corresponding safety issues, International Journal of Hydrogen Energy, Vol. 36, No. 3, p. 2721-2728, (2011)
(10) JIS B2401-2: 2012, O-Rings-Part 2: Housing dimensions and sizes
(11) SAE J2719: 2011, Hydrogen Fuel Quality for Fuel Cell Vehicles
(12) ISO/TS 14687-2: 2008, Hydrogen fuel - Product Specification - Part 2: Proton exchange membrane (PEM) fuel cell applications for road vehicles
(13) The Electrochemical Society of Japan: Electrochemical handbook, Vol. 5, p. 155, (2000)
(14) Japan Automotive Research Institute: Analysis of Total Efficiency and Greenhouse Gas Emission, p. 58, (2011)

Author


Hiroyuki ISHIKAWA


Eiji HARYU


Nobuyuki KAWASAKI


Hayato DAIMON

Design of Next-generation Environmental Vehicle CLARITY FUEL CELL, realizing Harmony between Vehicles and Society

Fumihiro YAGUCHI* Kei KOBAYASHI*
Ken SAHARA* Saki TOMITA*

ABSTRACT

The new model CLARITY FUEL CELL is the third generation of the FCX fuel cell vehicle, which was the world's first fuel cell vehicle made available for lease. In addition to the world's highest level of environmental performance (zero emissions), the development of the new vehicle sought to realize both the aesthetic form and practicality of a sedan, and a sense of luxury.

The concept for the new package design was "BOLD & AERO PACKAGE", balancing a low total height for aerodynamic performance with a roomy interior space. Based on this vision, the concept for the exterior of the vehicle was "BOLD & AERO." For the exterior, the development realized an imposing body through the use of low and wide proportions combined with an advanced and aesthetic streamlined design. The concept for the interior was "Advanced Modern Lounge". The interior design realized harmony between advanced technology and a satisfying interior space. "FUTURE LUXURY" was set as the concept for the color and materials employed in the vehicle, expressing a new vision of luxury that redefines the image of environmental vehicles. These elements have realized a new level of commercial appeal for the CLARITY FUEL CELL.

1. Introduction

The goal for the development of the FCX CLARITY, announced in 2008 (the previous CLARITY model; Fig. 1), was to create a fuel cell system with a view toward mass production, and to promote diffusion of fuel cell systems in the market in a passenger vehicle in order to address environmental issues including air pollution, global warming, and the depletion of fossil fuels. The previous FCX CLARITY used a sedan design that revolutionized the image of fuel cell vehicles (FCV) by positioning the fuel cell (FC) in the center console making it possible for the FCX CLARITY to seat four passengers.

The new CLARITY FUEL CELL (the new CLARITY) uses revolutionary package technologies to position a smaller FC stack under the front hood. This technology realizes a spacious and comfortable cabin that seats five passengers representing a major evolution against the preceding CLARITY.

It was considered that merely realizing environmental



Fig. 1 2008 model year FCX CLARITY

* Automobile R&D Center



Fig. 2 Grand concept

performance would not win customers over. It was necessary for the vehicle to also be appealing as a car. This appeal would result from a combination of beauty, dynamic performance, user-friendliness, and a body with an upper-middle sedan feel. It was felt that sedan styling that incorporated these goals would realize this appeal in the new CLARITY.

The grand concept born from this thinking was "Red Carpet to a New Era" (Fig. 2). It was considered that the fusion of outstanding environmental performance and the appeal of an upper-middle sedan would create new value. The design theme was to make this value match customer desires through a unique design.

2. Package Design

2.1. Package Concept

Two types of product value were pursued in order to give form to the grand concept in the new CLARITY's package design.

The first of these was a body that would promote a sense of satisfaction and pride in ownership of an FCV. In order to not simply offer environmental performance but to also realize a product that was appealing as a car, it was considered necessary to achieve levels of style and comfort that would be seen as outstanding even when compared to an upper-middle sedan like the ACCORD.

The second type of value was the realization of the top driving range for an FCV. Because, as of 2016, the number of hydrogen stations remains limited compared to the number of gasoline stations, it is important to offer FCV owners an extended driving range for one filling. Designers sought to realize this value by boosting aerodynamic performance through the vehicle's framework. "BOLD & AERO PACKAGE" (Fig. 3) was set as the package concept balancing these two types of value. The aim was to create a next-generation FCV in which both the exterior and the interior fittings gave the sense of a BOLD body, and to balance this with high-efficiency aerodynamic performance.

2.2. Comfort and Sedan-like Overall Height

In order to give the new CLARITY's body the feel of an upper-middle sedan, the vehicle was provided with an interior space able to comfortably seat five adults. In addition, in order to offer users the sense of a clear difference from a standard compact-class passenger vehicle with an upright posture, the goal was to realize a sedan-like posture and overall height.

To realize a five-passenger vehicle, the FC stack that had been positioned in the center console in the previous CLARITY was reduced in size and positioned under the front hood together with the Voltage Control Unit (VCU), concentrating the FC powertrain into a size similar to a V6 engine. With this change, the rear of the center console and the floor tunnel no longer impinged on the rear seats, making it possible to increase the number of passengers from four in the previous CLARITY to five in the new model. In addition, in order to create a comfortable space for five adults, the vehicle was given the same distance between the front and rear seats as the 2013 model year ACCORD and rear seat shoulder room of more than 1450 mm.

Next, in order to realize a sedan-like posture and overall height, the drive batteries were positioned in the space under the floor, and the floor area where passengers place their heels and the hip points of the front seats were lowered.

Design of the shape of the battery pack and the surrounding body framework helped to control the floor from protruding in height. Additionally, the gap between

the front seat frames and the floor was reduced making it possible to efficiently position the drive batteries in the space under the front seats, and the realization of a height difference of less than 265 mm between the passenger heel area and the front seat hip points. This made it possible to realize a sedan-like posture and an overall height of 1475 mm (Fig. 4). If the gap between the front seat frames and the floor was too small, rear passengers would not be able to place their feet under the front seats, reducing passenger comfort. Given this, volume was controlled by first shifting the position of the battery pack towards the front within a range that would make it possible to offer front seat passengers sufficient room to draw their feet back, and secondly by taking the positions of the rear passengers' toes into consideration in the shapes of the battery pack and the lower sections of the front seats. Further, rear seat comfort was balanced with a low front-seat posture by shifting the rear heater duct, conventionally positioned under the floor beneath the front seats, towards the center console.

2.3. High-deck Sedan Framework

In order to realize the top driving range for an FCV, designers aimed to boost aerodynamic performance from a basic framework. A distinctive high-deck sedan framework, in which the lid of the trunk is in a high position, was adopted in order to balance comfortable passenger space with a smooth, spindle-shaped silhouette effective in boosting aerodynamic performance. This high-deck sedan framework made it possible to realize sufficient head clearance despite the adoption of a spindle-shaped roof design with the rear windshield at a stronger slant than in a conventional sedan.

In addition, the layout for the new CLARITY positions a small high-pressure hydrogen tank under the rear seats and a large high-pressure hydrogen tank under the floor

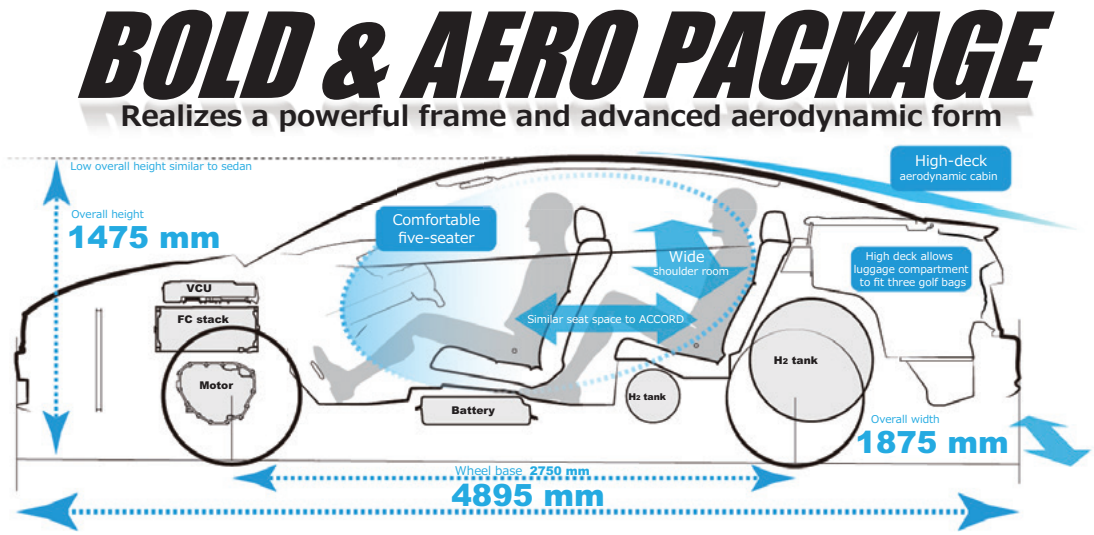


Fig. 3 Image of package concept (North American model)

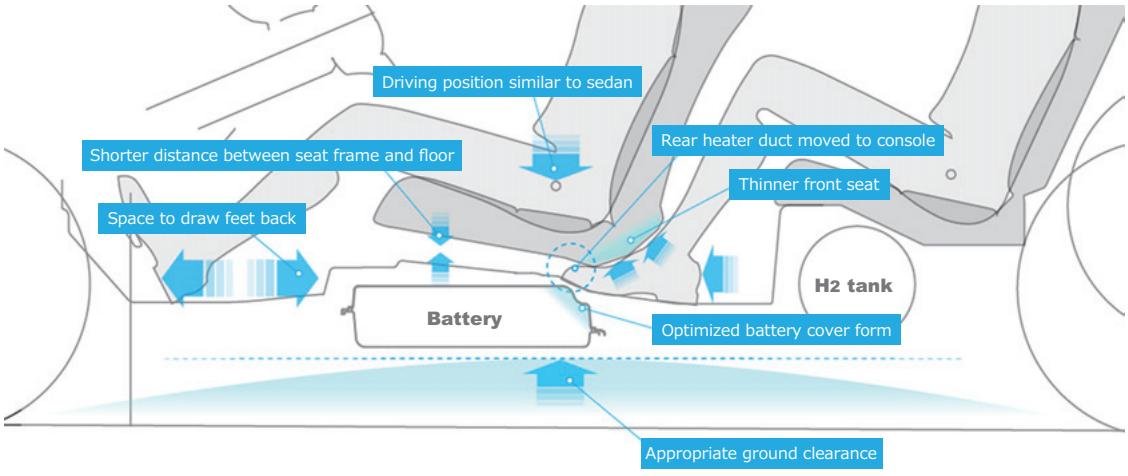


Fig. 4 Details of battery and floor layout

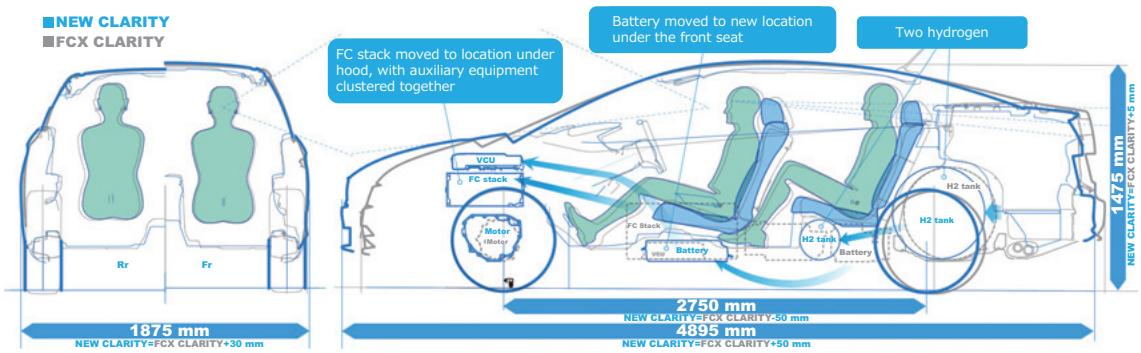


Fig. 5 Comparison of CLARITY package layout

of the trunk. The hydrogen pressure of the tanks has been increased to 70 MPa, increasing hydrogen storage volume by 33% against the previous CLARITY. In a conventional sedan framework, trunk space is dramatically reduced, but the adoption of a high-deck sedan framework has increased the volume of the trunk space vertically making it possible to realize a trunk opening with large vertical dimensions.

These innovations have made it possible to increase hydrogen storage volume against the previous CLARITY while realizing a trunk space able to hold three 9.5-inch (diameter) golf bags or two 29-inch suitcases (Fig. 5).

2.4. Balancing Aerodynamic Performance and Rear Field of Vision

Designers considered means of helping to prevent the trunk lid, which was elevated as a result of the adoption of the high-deck sedan framework, from impeding the rear field of vision. In the new CLARITY, two small extra windows have been positioned behind the rear seat back and in the trunk lid to aid visibility in the rear downward direction. The position and shape of the rear spoiler were optimized in order to reduce the blind spot between the rear windshield and the extra windows against the previous CLARITY, which used the same extra window configuration. In order to also increase diagonal rear visibility, a six-light configuration was employed featuring a rear quarter-window that is a new addition against the previous CLARITY. These measures not only increased the rear field of vision, but also contributed to allowing more light into the cabin creating a bright and open cabin that feels more spacious and comfortable than its dimensions would suggest.

3. Exterior Design

3.1. Concept

The concept for the exterior of the new CLARITY was “BOLD & AERO.” The design sought to realize an imposing sedan form and advanced and aesthetic aerodynamic styling (Fig. 6).



Fig. 6 Exterior design concept

3.2. Elegant Cabin and Powerful Body

In order to achieve an advanced and aesthetic design while realizing the space that would make the vehicle the first FC sedan to seat five people and maintaining an adequate field of vision, the design of the cabin featured a sleek, coupe-like silhouette. In addition, a spacious and advanced design with the feel of a glass canopy was realized by enlarging the rear quarter-window and blacking out the pillars and the roof. Emphasizing the curvature of the windows close to the B pillar in the plan view from above and extending the curvature outwards made it possible to realize an aesthetic and well-shaped cabin form (Fig. 7).

To actualize an imposing sedan form at the sides of the vehicle, forms with extensive modulations were adopted, and the 18-inch wheels present a sporty feel for an environmentally conscious vehicle. At the rear, the bracing of the package's high deck with a large spoiler has created a sharp and powerful body.

The combination of an elegant cabin and a powerful body realized in this way formed the basis for the design of a new era FC sedan (Fig. 8).

3.3. Framework and Detailing for Increased Aerodynamic Performance

Because driving range is an important issue for FCV vehicles, boosting aerodynamic performance through exterior design is an important factor in their design. Sedans normally display good aerodynamics, but designers sought to boost aerodynamic performance to an even greater extent in the new CLARITY, therefore the framework was designed to optimize aerodynamics from the initial stage of the development.

In normal sedans, turbulence is generated at points where vertical eddies produced by the A pillars strike eddies at the C pillars at the rear, and the resulting induced drag causes aerodynamic performance to decline. In the new CLARITY, the position and the inclination of the A pillars, the curvature of the surfaces of the pillars, and the difference in level between the pillars and the windows were taken into consideration in order to reduce the occurrence of eddies at the A pillars. Eddies at the C pillars have also been reduced by setting the rear windows close to the C pillars further in and narrowing them to a greater extent than they would be in a standard sedan, while also shifting the lower ends of the C pillars towards the rear. In addition, induced aerodynamic drag was greatly reduced through the styling from the sides of the vehicle to the rear spoiler. This helped ensure that eddies at the C pillars flow to the rear without wrapping around the upper section of the vehicle. The application of these measures produced a framework possessing a high level of aerodynamic potential (Fig. 9).

The design of the details sought to further draw out the aerodynamic potential of the basic framework.

Air curtains fitted to the lower part of the front bumper and the rear of the rear doors were effective in controlling turbulence produced by the tires. The rear door air curtains in particular represented an experiment that had never

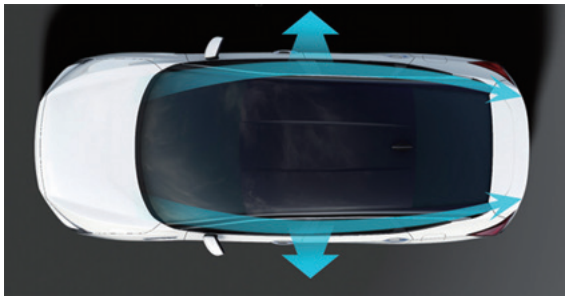


Fig. 7 Top view of exterior design

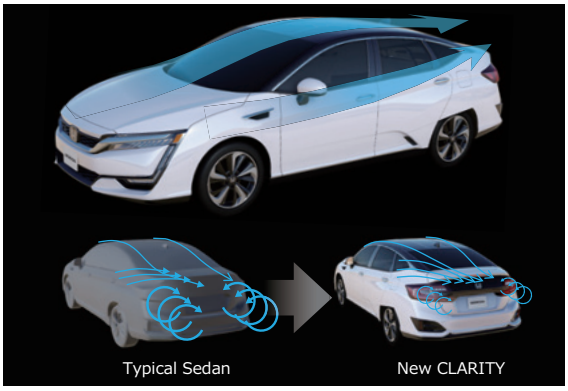


Fig. 9 Image of aerodynamic styling performance

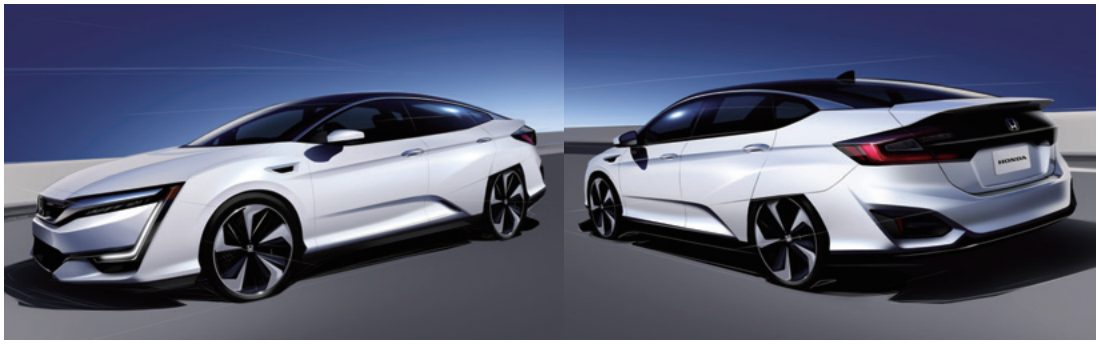


Fig. 8 Exterior design sketch

before been applied to a sedan. A normal sedan features an outer panel on the body between the rear edges of the rear doors and the tire housing, but this structure does not serve an aerodynamic function. In the new CLARITY, the rear doors extend to the front section of the rear wheel housing, and tunnel-shaped plastic parts (Fig. 10) have been attached in this area. Air introduced through these rear door tunnels passes over the outer sides of the rear tires thus controlling turbulence produced by the tires (Fig. 11).

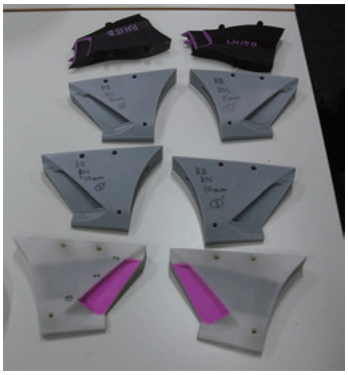


Fig. 10 Study of air curtains

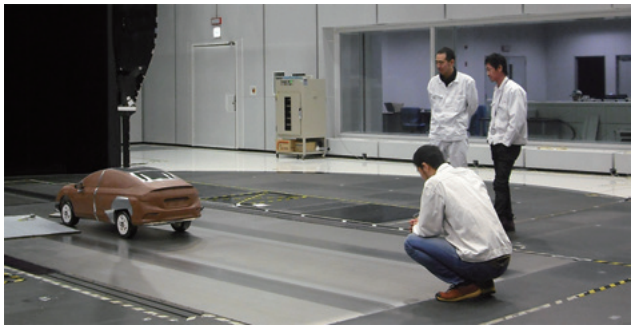


Fig. 11 Wind tunnel experiment

Tire covers on the upper sections of the rear tires represent a distinctive design feature on the sides of the new CLARITY. It would have been possible to achieve a major increase in aerodynamic performance by completely covering the rear tires. However, this would have reduced the track width, making the vehicle appear less robust from the rear. This and other considerations resulted in the adoption of a method not employed in normal sedans. The new CLARITY's use of the side outer panels to cover only the upper sections and fronts of the tires is a most effective means of controlling turbulence from the rear tires without the use of a rear cover while maintaining a wide tread (Fig. 12).

For the new CLARITY, from the design of the overall shape of the body to the detail parts, designers would first create the basic shape. Aerodynamics engineers followed by running simulations (using computational fluid dynamics: CFD) in order to study directions for increasing aerodynamic performance. The results of these simulations were reflected in clay models which were tested in model wind tunnels. The repetition of this process enabled a design displaying a high level of aerodynamic performance with a driving range of approximately 750 km per filling (reference value) (Fig. 13).



Fig. 13 Mass production model

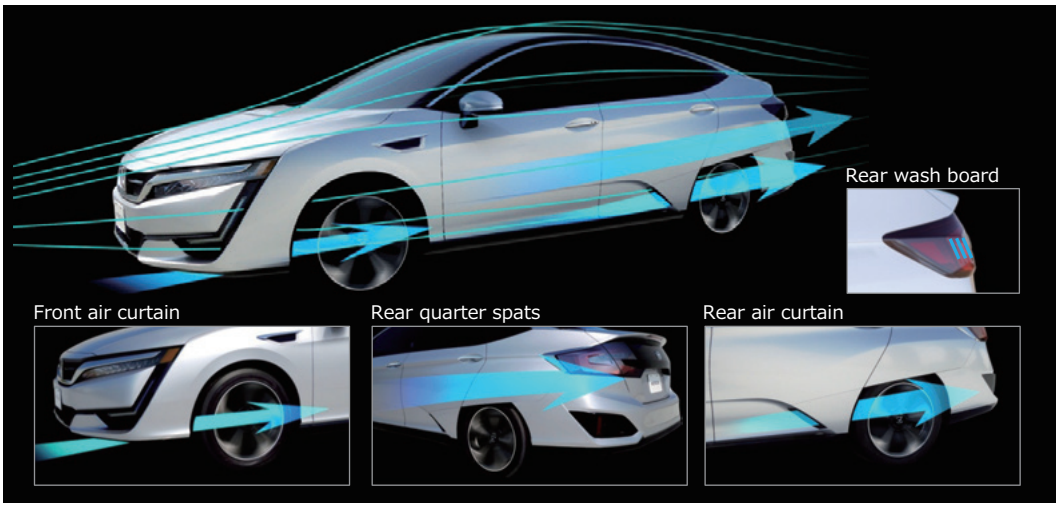


Fig. 12 Aerodynamic features

3.4. Advanced Front Face and Rear Combination Lamps that Prioritize Aesthetics

The front face of the new CLARITY is an expression of Honda's SOLID WING FACE (Fig. 14), the company's characteristic front design using the latest technologies.

The end of the front hood wraps around the front grille at an acute angle, and a low, sharp nose is realized by pushing down the central section of the chrome garnish molding. In addition, the grille and the chrome garnish molding of the inner section of the headlights are continuously connected, and thin full-LED turn signals and in-line high and low beam lamps have been positioned above and below, producing a wide front expression and giving the vehicle a sense of advancement (Fig. 15). Daytime Running Lights (DRL) extending from the headlights to the lower section of the bumper in a large L-shaped configuration not only produce a distinctive appearance, but also represent a design proceeding from considerations of safety helping to ensure vehicle awareness from a distance even during the day.

The rear combination lamps are integrated with the extra windows carried over from the previous CLARITY, creating a distinctive design with a sense of width and unity. The design prioritized good visibility, and the beauty of the lights when lit which have an external appearance suggesting lumps of glass. This is realized through the use of inner lenses of greater-than-normal thickness to reflect indirect light (Fig. 16).

3.5. Hybrid Wheels fusing Function and Design

In order for the new CLARITY to achieve an imposing sedan body it has been fitted with 18-inch wheels, two inches larger than the wheels used for the previous CLARITY.

It is standard practice for environmental vehicles to reduce the area of the wheel opening, increasing aerodynamic performance, and to use low-diameter dish-type wheels in order to reduce weight and contribute to an increased driving range. However, because electric vehicles do not use engine brake mechanisms, cooling of the brakes becomes an issue when descending a continuous slope, making it necessary to increase the size of the wheel opening. The task in the case of the new CLARITY was to balance weight reduction, cooling performance, and aerodynamic performance while using large-diameter wheels. The use of aluminium wheels and large wheel openings reduced weight and increased cooling performance, while the use of plastic covers boosted aerodynamic performance. The result was a hybrid wheel with an advanced design (Fig. 17).

The shapes of the base aluminium wheel needed to ensured sufficient strength for the weight of the vehicle with a low wheel weight. Design efforts were restricted to the area that would not be hidden by the plastic cover thus reducing the amount of aluminium demanded by the design.

CFD was applied to the plastic covers (Fig. 18) enabling a design that blocked the flow of air into the wheels and helping to ensure an opening for the discharge of heat in the direction of rotation, while also balancing aerodynamic performance and cooling performance.



Fig. 14 Honda Solid wing face image

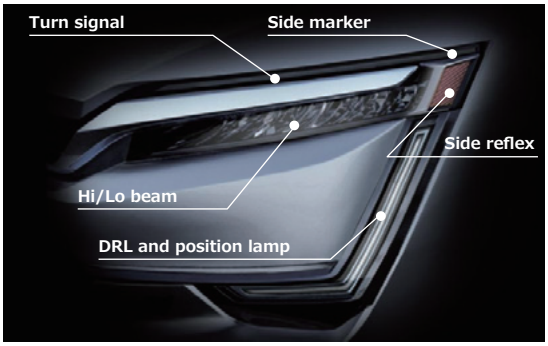


Fig. 15 Full LED head light

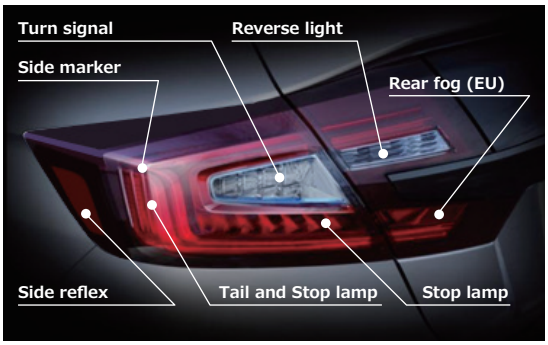


Fig. 16 Rear combination lamp

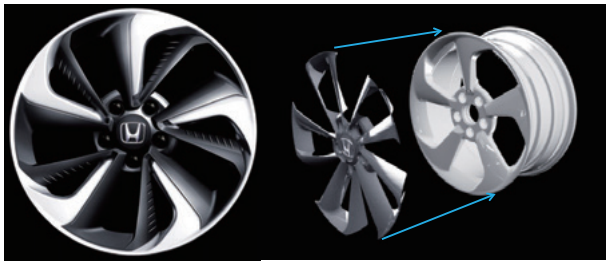


Fig. 17 Hybrid wheel

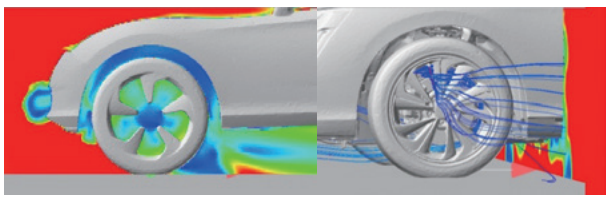


Fig. 18 CFD air flow simulation

4. Interior Design

4.1. Concept

The interior design concept for the new CLARITY was “Advanced Modern Lounge” (Fig. 19). This concept brought advanced interfaces based on Honda’s design concept of instantaneous recognition and intuitive operation into harmony with a space featuring materials that appeal to the senses to create a satisfying interior space.

4.2. Creation of a Relaxing Space

In order to create a satisfying and relaxing space, a horizontal from the center of the instrument panel to the doors was formed with a focus on realizing a free and unconstrained left to right sweep. In addition, the use of a difference in level from front to rear creates a sense of depth producing a cabin that feels more spacious than its dimensions would suggest.

Soft padding is used on the instrument panel and the upper door trims to create a pleasing texture. The use of warm materials and high-quality, carefully sewn, soft and pleasantly textured materials in areas that passengers constantly touch and see has created a comfortable space that resonates with the feelings (Fig. 20).

The step between the front and rear of the instrument panel (Fig. 21) also plays an important role in the composition of the cabin space. If the dimensions of the lower level in the depth direction were too small, it would create a narrow impression. If they were too large, it would create a sense of space, but it would not be possible to reach the knobs of the air conditioner outlets, impeding

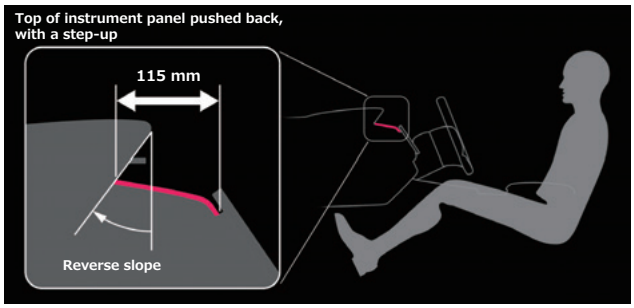


Fig. 21 Instrument panel design

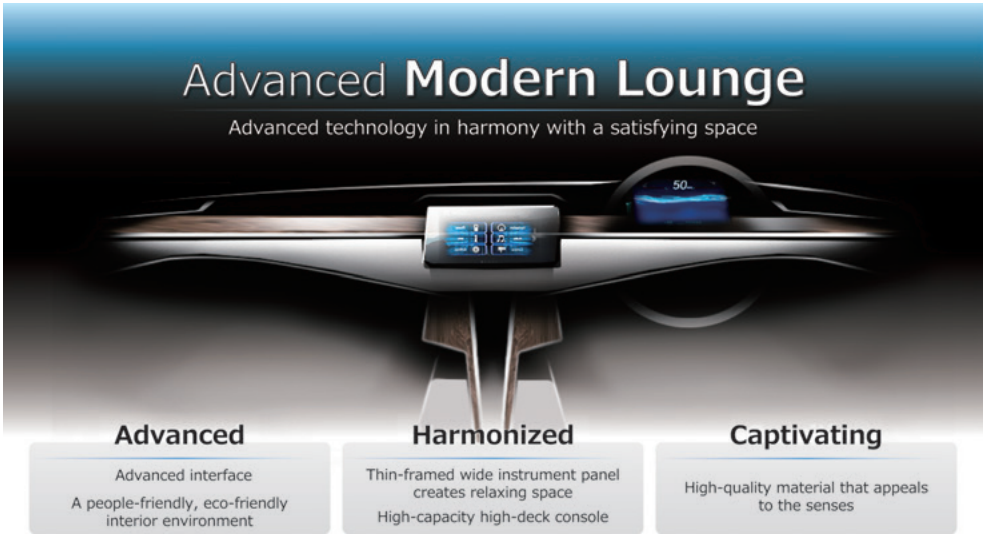


Fig. 19 Interior design concept

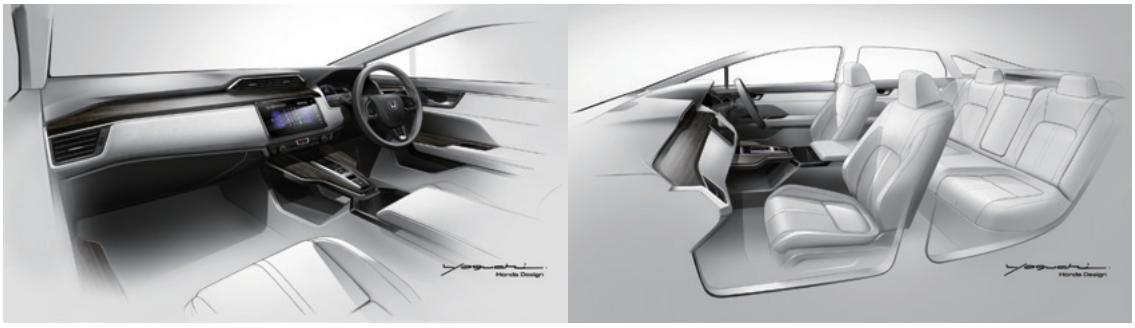


Fig. 20 Interior design sketch

functionality. It was decided that the use of a reverse slope based on these considerations would maintain the knobs within reach, while also extending the lower section forwards. Tests using clay models and package models led to the conclusion that a depth of 115 mm would be the optimal dimension to create a sense of spaciousness while allowing users to reach the knobs of the air conditioning outlets.

High-backed seats that passengers could relax their bodies into, but that would also firmly hold them, were adopted for the new CLARITY. This design helps to ensure that the seat back supports the passenger from shoulders to back, offering a sense of security and making it possible to sit for long periods with a stable posture. The design also used a shape that narrows at the top thus giving consideration to rear seat passengers by helping to prevent them from feeling crowded, and attempt to ensure that the shoulder section of the seat back did not obstruct their view of the center panel from a sitting position (Fig. 22).

4.3. Functional Sedan Console

The layout of the previous CLARITY positioned the FC stack in the center console. In the new CLARITY, revolutionary package technologies have made it possible to reposition the FC stack under the front hood. The use of a high-deck console was proposed in order to effectively utilize the space in which the FC stack was previously positioned (Fig. 23).

Positioning the miniaturized switch-type shift-by-wire (SBW) and electric parking brake (EPB) at a height that made them easy to operate freed up the lower section as a utility space. The design allows vehicle users a convenient space to place smartphones or tablets for charging, and the tray in the lower section can be accessed from a sitting position. This area also doubles as a wrist-rest to aid in smooth operation of the air conditioning while driving, offering a new level of ease of use that responds to user needs.

4.4. Advanced Interfaces

The new CLARITY features Honda's latest interface devices, based on the design concept of instantaneous recognition and intuitive operation, creating an environment that allows the driver to concentrate on driving (Fig. 24).

The meter design positions a large liquid crystal display capable of presenting an array of information in the center of the instrument panel. This interface organizes and displays information using simple graphics and colors.

The fuel cell power monitor (Fig. 25) provides an intuitive visual representation of the amount of hydrogen consumption through the expansion and contraction of a



Fig. 24 Interface design

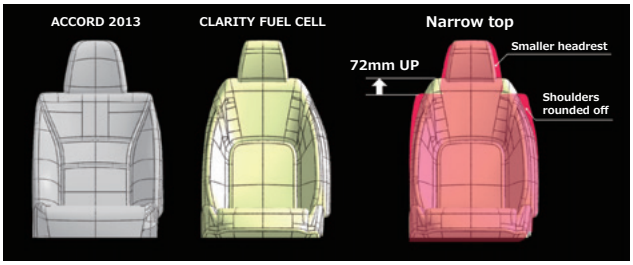


Fig. 22 Front seat design

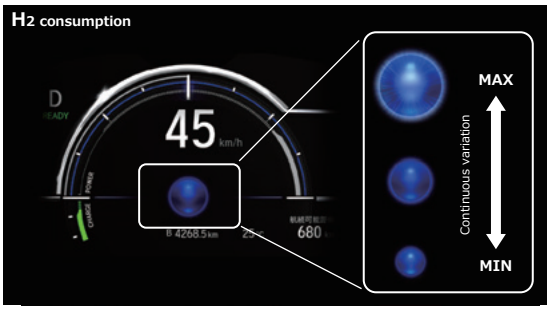


Fig. 25 Fuel cell power monitor



Fig. 23 Console design (Mock-up model)

blue ball. The power/charge indicator (Fig. 26), presented in the form of an arc, displays total power output and regeneration at the same time as indicating the power source being used for vehicle operation. The graphic display has been designed to make it possible to instantly read off the constantly changing system status via the movement of a needle.

Surrounding the displays with a silver frame isolates and organizes their information and increases their visibility. The frame design emphasizes the margin between the remaining hydrogen indicator and the frame (Fig. 27) providing instant awareness of the remaining amount of hydrogen.

4.5. Forms that Use Materials to Their Fullest Extent

Conventional vehicle interior design has tended to involve the decoration of forms. Today, with the evolution of element technologies, it is possible to realize design expressions that would not have been possible using existing materials. However, decorating forms in unnatural ways creates the risk of negatively affecting the feel of the interior.

The design for the new CLARITY placed the priority on forms emerging naturally from the materials themselves. For example, parts coated in silver were given hard forms to suggest that they had been cut from metal. The forms of wood grain panels were created with consideration of techniques similar to those employed for wood veneers in which thin strips of wood are cut and applied to a base. Close attention to the characteristics and methods of creation of the materials has heightened the feel of the interior enabling realization of the interior concept: A satisfying interior space (Fig. 28).

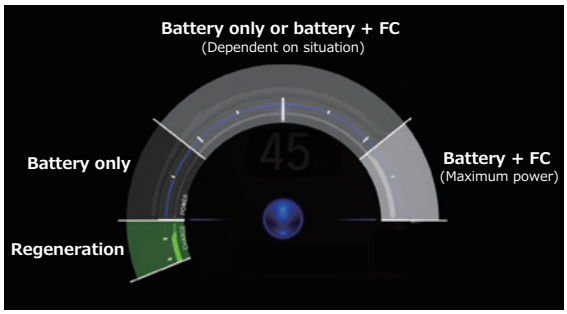


Fig. 26 Power/charge indicator

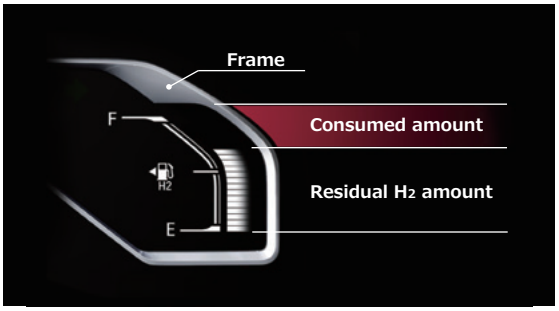


Fig. 27 Display integrated with frame and indicator

5. Color Design

5.1. Concept

The goal of color design for the new CLARITY was to balance environmental consciousness with a sense of high quality as a sedan that promoted pride of ownership. Departing from the conventional concept of environmental vehicles and sedans, which each embodied just one of these qualities, it was felt that a vehicle possessing both qualities would create luxurious value for a new era. The design concept was therefore set as “FUTURE LUXURY.”

5.2. Exterior Colors

The new CLARITY is offered in a three-color lineup (Fig. 29).

The new color PREMIUM BRILLIANT GARNET



Fig. 29 Color lineup



Fig. 28 Mass production model

M., a highly appealing color that attracts attention, creates feelings of exhilaration and pride of ownership.

WHITE ORCHID P. is a clean and progressive color that highlights the sense of the new CLARITY as a vehicle of the future.

CRYSTAL BLACK P. suits the vehicle to formal occasions and is a color that combines a sense of high quality with a feeling of calm.

Each of these body colors has its individual place, and each powerfully emphasizes the image of the new CLARITY.

5.2.1. New PREMIUM BRILLIANT GARNET M.

The color STAR GARNET M., used on the previous CLARITY, changed the image of environmentally conscious vehicles by creating a feeling of luxury. This concept was carried over to the new CLARITY, but designers sought to more strongly emphasize the beauty of the vehicle's shapes by increasing the feeling of shading. For its top coat, the newly developed color PREMIUM BRILLIANT GARNET M. employs a high-dispersion, red-pigmented semi-transparent coat, producing a vivid color and strong shading (Fig. 30). The realization of a color that appears more vivid in the highlighted areas struck by the light and produces a feeling of depth and calm in the shaded areas gives the vehicle a sense of solidity and three-dimensionality. As the name BRILLIANT GARNET suggests, this is an evolution to a color that shines from the inside like a raw gemstone polished into a jewel.

5.3. Interior Colors

The goal for the interior color design was to create a comfortable and harmonious space. The coordination between colors and materials was defined from the initial stage of design resulting in highly refined interior fittings.

The new CLARITY offers two choices of interior color: A chic and luxurious black, and a progressive and glamorous platinum grey (Fig. 31). In each case, monotones are coordinated in order to make the simple forms stand out to greater effect.

5.4. Materials that Consider the Environment

Environmentally conscious materials were actively employed in the new CLARITY. Materials were developed for the vehicle that would offer a rich texture and a sense of quality despite being recycled or derived from plants.

The roof lining and the floor mat employ plant-derived polyester thread made from the residue produced by crushing sugarcane. This thread is used as the lining of the synthetic leather employed for the seats and armrests (Fig. 32).

The material employed on the instrument panel and the mid-sections of the door pads, distinctive features of the interior, is an artificial suede leather produced using recycled polyester (Fig. 33). Soft and pleasant to the touch

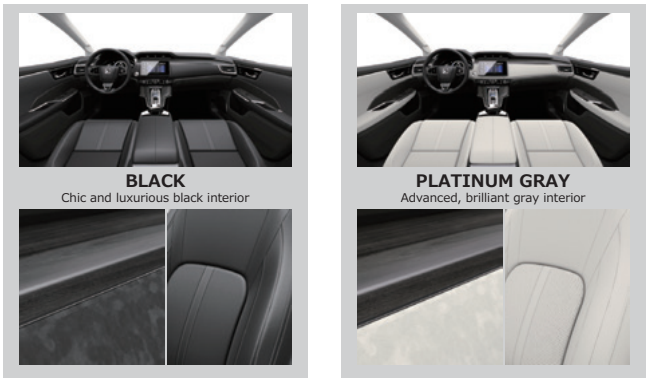


Fig. 31 Interior color and material coordination

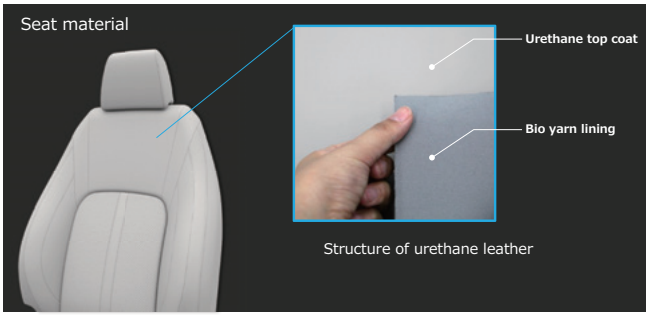


Fig. 32 Seat materials

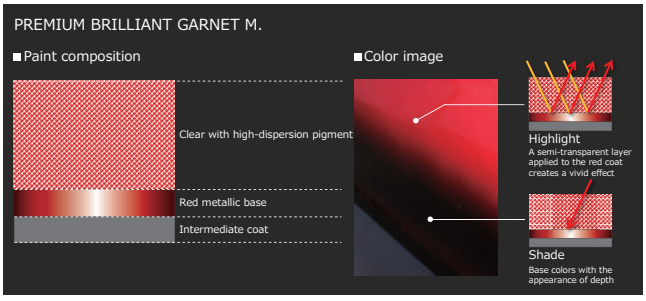


Fig. 30 Paint composition



Fig. 33 Artificial suede leather

while suggesting warmth and high quality, the use of this material on broad areas of the interior contributes to the sense of enveloping comfort.

5.5. Realization of High-quality Sedan Interior

The interior design of the new CLARITY sought to realize the high-quality finish and detailing of a sedan while using environmentally conscious materials. Decorative wood grain patterns were produced by gravure printing rosewood grain (a wood known for its use in furniture and musical instruments) on a base. The calm and fluctuating rosewood grain pattern creates a high-quality and luxurious impression. The reproduction of the feel of wood grain (creating an impression of convexities and concavities) offers a sense of the warmth of wood to the touch despite the fact that the material is a film. Decorative silver pin striping at the ends of these parts coordinate with the wood grain to make it stand out all the more effectively (Fig. 34).

A single color is used for the seats in order to make them appear spacious and inviting like a roomy sofa. Looking closely, passengers will be aware of intricate patterning and stitching down to the finest details, in addition to the use of center accents, for a finish suggesting high-quality tailoring.

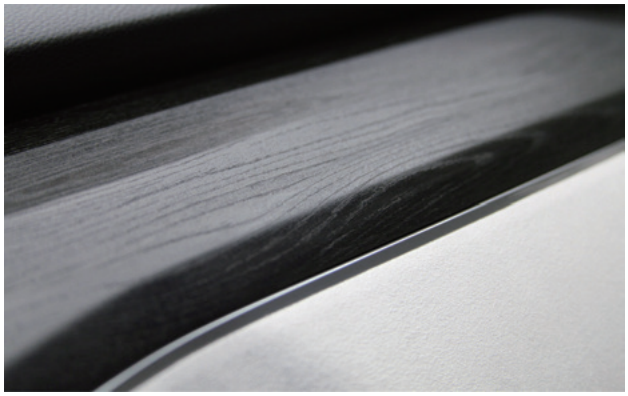


Fig. 34 Wood film panel

6. Conclusion

The design of the next-generation environmental vehicle CLARITY not only realized aerodynamic performance from the foundational level of the framework in addition to environmental performance, but also achieved a presence, practicality, and sense of quality that will make the vehicle an FCV that delights customers.

With a focus on achieving the comfort and practicality demanded from an upper-middle sedan, the design succeeded in realizing space for five passengers and a level of user-friendliness comparable to that of the Accord, despite the employment of different mechanisms to an internal combustion engine vehicle. In order to realize an imposing framework, vehicle height was kept low despite the positioning of the batteries under the floor, producing an aesthetic low and wide form. In addition, the increased aerodynamic performance ensured by the streamlining of the cabin, the use of a high deck, and the fitting of air curtains to the front and rear wheels has further emphasized the individuality of the new CLARITY.

The interior achieves the quietness and smoothness that characterize FCV while also offering a roomy and relaxing space. Carefully chosen high-quality interior materials are pleasant to the touch and appeal to the senses while being derived from plants, thus reducing environmental impact. The warm and relaxed interior space will make users wish to continue driving forever.

The promotion of more widespread use of an FC vehicle like the new CLARITY necessitated a level of driving pleasure and enjoyment that appealed to the senses and the feelings in a way that could not be expressed in numbers. In order to make Honda's company goal of a sustainable society a reality, it will be necessary to increase the appeal of products to customers through design. Honda is confident that the new CLARITY will contribute to society and respond to the demands of customers through its fusion of environmental technologies and design.

■ Author ■



Fumihiro YAGUCHI



Kei KOBAYASHI



Ken SAHARA



Saki TOMITA

Styling Design of the Forza125

Taro NISHIMOTO*

ABSTRACT

The Forza125 was developed targeting 125 cc GT scooter market in Europe, especially focusing on the market in France. The name GT scooter stands for the category of scooters with larger body size primarily used for long distance commuting. Prior to the development, market survey was conducted and customer's real needs were revealed through the results. Based on these findings, the development goal of the Forza125 was defined as a next generation standard scooter under the concept theme of "New Stylish Sport." As the vehicles of this category are used for commuting, it was pursued to fulfill both requirements in performances needed for highway driving and for city driving to highly satisfying level. In its styling design, representation of superior performance of this vehicle was endeavored. In addition, air flow managements were thoroughly investigated by applying appropriate exterior designs. One of such examples is application of an adjustable screen that is the first in this vehicle class. The developed model was favorably received in the marked winning the category top model in the cumulative sales volume after the product release.

1. Introduction

The scooter market in Europe is continuously shrinking after the Bankruptcy of Lehman Brothers in 2008. In this circumstance, 125 cc scooters have been maintaining a certain size of market within overall scooter market in Europe. Honda has been responding to the varying demands and preferences of users for this market by renewing existing core models, such as the SH125 or by introducing new models, such as the PCX. As a consequence, Honda had successfully gained a firm support from the customers of scooter market in Europe, primarily for the models with small-sized body and in lower price range. However, the situation was different in French market. In France, GT scooters, which are larger sized scooters in 125 cc category usually used for a long distance commuting, are leading models in the market instead of compact models like the SH or the PCX.

With these backgrounds, the development of the Forza125 was started in 2013 setting 125 cc GT scooter market in France as a main target. In the development, we tried to identify the real needs that the customers who were not satisfied with the SH or the PCX have and create a design that can meet those needs.

2. Market Backgrounds

One of the significant characteristics of two-wheeler market in Europe is that, in many countries, people can ride two-wheeled vehicles with the license accompanied to a car license if the displacement is not exceeding 125 cc. Two-wheelers of 125 cc class have several benefits. Their maintenance cost is reasonable and the price is within affordable range. Moreover, it does not require any exclusive license to drive a 125 cc class two-wheeler. With those economical features and their high usability, 125 cc two-wheelers have been supporting the peoples' lives as handy transport means in Europe for a long time. Especially, scooters of 125 cc class, which are equipped with automatic transmission, do not require any special attire or skill to ride. Those scooters are also provided with sufficient utility spaces. Because of those reasons, these scooters have already established the status of existence completely diffused into the peoples' lives to the extent of being deemed as a part of their cultural assets.

The economy has been stagnant since the Bankruptcy of Lehman Brothers and the motorcycle market has been in a contractive tendency. However, scooters in 125 cc class are well supported by users with the values of good economy and utility as a transport means, and those scooters account for a large percentage of 50% in the European scooter market (Fig. 1). Even though the number of the sales units has been declined compared to the peak period, this market is still one of the important segments in the entire market.

In the European 125 cc class scooter market as described above, models representing the presence of Honda are the PCX125 (Fig. 2) and the SH125 (Fig. 3).

PCX125 is one of the favorably received models, which was released all over the world in 2010 targeting a global model. This model was provided with sufficient specification and equipment achieving high quality

* THINK Lab., Honda R&D

appearance and usability yet was released with affordable price by making use of the advantage of a large production volume only realized by a global model.

On the other hand, the SH125 has been gaining a large market share in South Europe and its neighboring areas where people tend to show favor in scooters with large diameter wheels. The SH is a model with a long history since its first release in Europe in 1984 and is one of the representing models from Honda for commuters' scooter category.

Thanks to these core popular models, Honda can have a large market share in 125 cc class scooter market in Europe. On the contrary, the situation has been lasting long for Honda that it cannot establish a sufficient presence in the same market category in France. Since its release, the PCX125 surely gained a certain size of the market share in the smaller size scooter market but it couldn't fully capture the customers' minds (Fig. 4).

In France, the scooter category called GT scooter is the main category and accounts for about 50 percent of the market. In Honda's scooter product lineup, the S-Wing (Fig. 5) is the model that belongs to the GT scooter category. When they are compared to the models with a compact body, such as the PCX125 or the SH125, scooters of this category usually employ, despite of its small engine displacement of 125 cc, a body with generous size almost equivalent to 250 to 300 cc class scooters. They also have a large storage capacity and wind protection performance as the vehicle features.

More than eight years have passed since the S-Wing was put on the market in 2007. When it was introduced, the

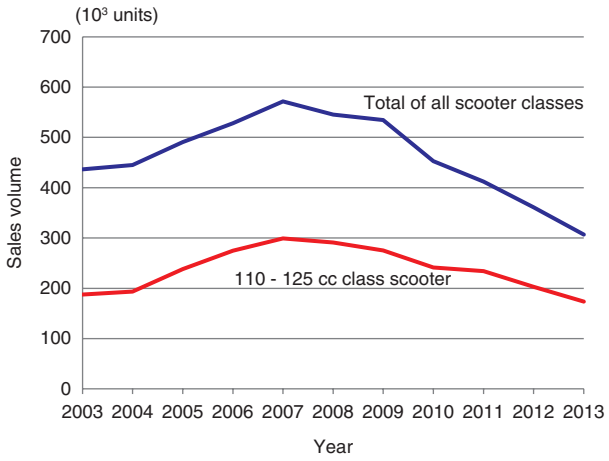


Fig. 1 Transitions of scooter market size for ten major countries in Europe (from Honda internal material)



Fig. 2 The PCX125



Fig. 3 The SH125

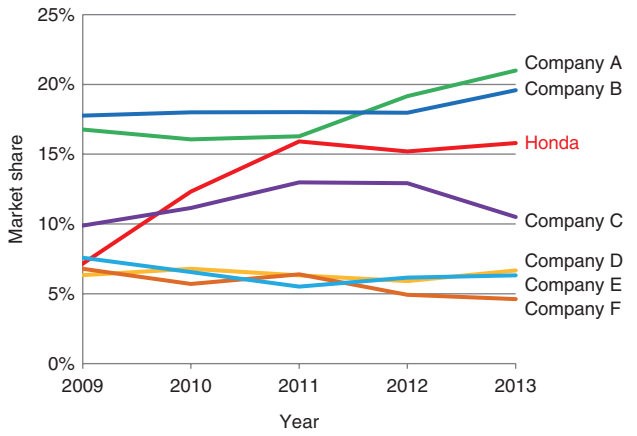


Fig. 4 Transitions of market shares for 110 to 125 cc class scooters among manufactures in France (from Honda internal material)



Fig. 5 The S-Wing

model had technical advantages against competing models. Such technologies included Antilock Braking System that was applied to a scooter in that class for the first time. However, in recent years, ABS is already widely applied and has no significance at all. Moreover, the performances in fuel economy and drive power cannot be counted as characteristics superior enough to the products from competitors.

To overcome those situations, the development of the Forza125 was started in 2013 targeting the 125 cc GT scooter market in France as the main target. To start with, a market survey was conducted to know what would be necessary to attract customers' minds.

3. Market Survey in France

This survey was conducted to identify what the customers want in the market of France. For that purpose, we researched on background situations of their scooter use and the way they use them in the real world. In addition, the subjects also included in the research were the reason why they favor GT scooters and what is the missing feature in existing GT scooters such as the S-Wing. Through these researches, we endeavored to find intimations that may lead us to know what kind of vehicle the developing Forza125 should be.

3.1. Purpose and Background Situations of 125 cc Class Scooter Usage

The purposes and background situations for users in France to use 125 cc class scooters were researched first.

Most of the users are using scooters for their commuting. Many of them privately own four-wheeled vehicles as well, and not a few of the cars are those in expensive price ranges. Two-wheeled vehicles are used mostly for commuting on weekdays. Cars are usually used for their transport needs with family on weekends.

The major reason why they do not use cars for their commuting but two-wheelers is the traffic congestion and unavailability of parking space. The central city areas in France are chronically congested in and around commuting hours on city streets as well as on highways. They use scooters of 125 cc class to evade the congestion. In addition, two-wheelers have been granted with citizenship in France and parking lots are readily available in many places in cities despite those for automobiles are insufficient (Fig. 6). It is assumed that they can choose two-wheeled vehicles without hesitation because these vehicles are publicly accepted totally without any perceived ideas to regard them as a nuisance or an antisocial existence.

Among two-wheeled vehicle categories, scooters are usually chosen because they are suitable for a ride in business attire, such as business suits or leather shoes and they accommodate a business bag to be stored in a body. In addition, it is another reason for choosing scooters that riders can have some protection against wind and rain with a leg shield and other vehicle body structures.

People in France basically deem 125 cc class scooters as convenient transport measures providing an excellent mobility with easy handling and sufficient drive power. Especially, users who use two-wheeled vehicles for commuting with an accompanied license do not have any interest in the two-wheelers over 125 cc as their vehicle options. It rather commonly happens that a business person without any interest or riding experience begins to use a scooter in order to evade traffic congestions. However, most of them actually have no interest in two-wheeled vehicles as their subject of hobby.

As mentioned above, a 125 cc scooter is recognized as a very convenient tool for commuting by many users in France. Moreover, they are selecting a 125 cc scooter not because it is reasonably priced compared to automobiles but it is one of their "smart options" under thorough considerations on the efficiency and the usability.

3.2. Reasons Why GT Scooters are Chosen

Why do the larger-bodied GT scooters have a large share of the 125 cc-class scooter market in France rather than the compact models such as the PCX and the SH? The single most important reason is the use on the highways for commuting to work. Unlike the other countries in Europe,



Fig. 6 Parking spaces spotted in a city area of France

125 cc motorcycles are allowed on highways in France. Because of this, urban areas that are fairly far away can be commuted to from suburbia by a 125 cc motorcycle. Many of them ride their scooters for approximately 30 km one way, totaling 50-70 km every day, between home in the suburbs and the office in the city center. That means that the French customers use the scooter for commuting at high speeds on highways and low speeds on congested general roads. As they travel at a speed above 100 km/h for a certain period of time on highways, they require functions and performance unavailable from compact models made mainly for use on general roads, such as the dynamic performance for high speed cruising, good protection to keep off rain and wind, wobble-free stability when on road, adequately padded seat for long-time comfort, high eye point for good front visibility. The 125 cc GT scooters with the above-mentioned features can be said as a category that has evolved in France having a unique environment that permits 125 cc motorcycles on highways.

In France, compact scooters such as the PCX are starting to gain recognition as a suitable commuter in town for having advantages in environmental protection, such as good fuel efficiency and the idle stop system. Many users choose such compact models since those living in the city use scooters for traveling short distances. Nevertheless, these company scooters do not prioritize dynamic performance for high speed cruising and wind as they are considered city commuters. They do not have the adequate level of usability for those users riding on highways.

3.3. Voices of GT Scooter Users

What has surfaced upon hearing voices from regular GT scooter users is that they are not necessarily satisfied with the current GT scooters.

First, although the engine power is a key feature of GT scooter, many users feel the power is insufficient when overtaking on a highway or launching and accelerating in town. Accordingly, the dynamic performance is a main concern when they choose a model. In other words, the performance the user felt as lacking in the existing GT scooter was the dynamic performance.

The next issue is the body size. GT scooters have evolved to meet user needs such as d wind protection and expanded luggage space. As such, some GT scooters grew much larger in body size to respond to those requests. A larger body was advantageous for wind protection and/or luggage space, but it began affecting their agility in town as a trade-off. Since agility is critical when navigating through heavy traffic, users have been seeking an appropriate body size for it. In other words, the users were seeking a model with a body size that best balances two contradicting demands: a large body size suitable for cruising on highways and a compact body size for agility in town.

Also clarified at this time was the importance of the styling. The GT scooters themselves are well accepted without any negative images. On the other hand, they were not recognized as being particularly “sporty” or “stylish.” The users were more concerned with the functions because a 125 cc scooter as a product was viewed as a utility commodity, not necessarily something for hobby. Notwithstanding that, a styling that is sportier and with a more advanced image is becoming desired even for a scooter for commuting. Needs are growing for a scooter to have a styling design that matches the dynamic performance, rather than having just high dynamic performance. In other words, the styling design of current models lacks a sporty and stylish image that represents the dynamic performance the users seek.

As mentioned earlier, many users in this category are also an automobile user as well. Accordingly, the quality of a scooter’s exterior design is compared to automobiles. Since such users ride in town wearing business attire, demands are high in the visual quality, its luxury image and design quality, even for a commuter. Anything that appears lower in cost or low in performance are not preferred. In other words, they seek from a scooter the same level of quality image as of an automobile.

Many users of scooters in this category are of a class having relative high income. They use a scooter not because they are unable to buy a car, but rather because it is a wise option taking into account its practicality and efficiency. Accordingly, they do not want to be seen as riding something lower in cost or economically pressed. A styling design that adequately meets such demands, however, has not necessarily been offered.

As such, our target users have had complaints in the styling design of existing models. They were not seeking to show off the scooter or attract attention from others; rather, it was a style that has the aura of a solid presence that gives the owner the satisfaction and pride of owning one. What is needed was not a styling as a tool but a design that surpasses that: a styling design that gives a sporty and intelligent image, which is also at the same time cutting edge and high-tech in image.

With such results obtained from the research, it has been concluded that there is a need of development of an entirely new GT scooter that responds to the market demands as mentioned above. In other words, the Forza125 was to become a truly new model that becomes a standard of next-generation GT scooters should be, rather than being an extension of the S-Wing model line.

Mentioned hereafter are the processes of the styling design actually conducted on the basis of the said direction of product development.

4. Aims of Product Development

Based on the findings of the research, the development team established the following six criteria that should be realized in the Forza125, the new development model.

(1) Dynamic performance

- No.1 dynamic performance (max speed, overtaking

acceleration, standing acceleration) in the category exceeding conventional GT scooters

(2) Sporty and intelligent design
- Sporty styling design that expresses high dynamic performance and evokes image of agility
- Styling that gives an intelligent image that makes the owner feel joy and pride in possession, a high-quality image and presence beyond the standards of class

(3) Highway use: Highway comfort, convenience
- Wind protection
- Wind noise countermeasure
- Wide vision and visibility
- Stability
- Safety devices such as ABS

(4) City use: City-use comfort, convenience
- Utility suitable for commuting to work
- Comfort, agility, and maneuverability suitable for city use
- Exhilarating feeling inherent in motorcycles and scooters

(5) Image of advanced technology
- Technology that captures the up-to-date, high-tech image

(6) Economy
- No.1 fuel efficiency in category
- Fuel capacity sufficient for commuting to work for a week

There are following issues when simultaneously satisfying all of the above criteria.

To improve wind protection, the size of the front cowl or screen is usually increased. A large cowl, however, hinders ability to pass through a narrow space on congested city roads, and spoils agility. An enlarged screen reduces exhilarating feeling that a motorcycle or scooter gives from exposure to wind.

An increased tire size is effective for improvement of comfort when riding in city. When the tire size is increased, however, a larger space is taken by the rear tire for movement, which reduces utility box space, and makes it hard to maintain sufficient utility spaces necessary for commuting to work.

While an extended wheel base is beneficial for high-speed stability, it hinders agility and maneuverability in town.

The 125 cc scooter to develop at this occasion is in a moderate price range and the body space is limited. A high engine power like a large scooter cannot hoped to be achieved. A big increase of body weight cannot be allowed from the standpoint of dynamic performance.

It can therefore be understood that the hurdles are very high for development of a product that satisfies performance requirements in two completely different working environments, i.e., highways and city roads. This is the reason why no models that satisfied all of the above existed.

Nevertheless, the development team members tackled the challenge with a goal set at achieving high levels of performance both on highways and city roads. We chose to refer to the new scooter as “New Stylish Sport.” This project is aimed at creation of a GT scooter that will become a standard and play a leading role in the next generation of scooters.

Table 1 Target specifications of the Forza125

Item	Specification
Engine	eSP engine. 4 valves
Power	11 kW/8,750 rpm
Curb weight	160 kg or less
Wheelbase	1,500 mm
Seat height	780 mm
Front tire size	120/70-15
Rear tire size	140/70-14
Fuel consumption	2.29 L/100 km
Fuel tank capacity	11.5 L
Utility space capacity	48 L Accommodating Full face helmet × 2 or Full face helmet × 1 + Business bag

5. Specifications to Serve as Bases of Styling Design

Keeping in mind the said concept, goals were set for specific performance, dimensions and key specifications. Among those, the specifications closely related to determine its exterior design are listed in Table 1.

The engine referred to as eSP is employed[1]. The eSP engine has been developed as Honda’s new generation engine that achieves both practical engine power and a good fuel efficiency. In this model, an even higher power output is targeted by incorporating 4-valve design into the base eSP engine. Regarding the key criterion of dynamic performance, goals were set at an engine power output of 11 kW/8750 rpm and a curb weight of 160 kg or less to achieve the best running performance in the category.

The target wheelbase was set at approximately 1500 mm to balance handling and stability.

Considering the visibility on highways and the ease for feet to touch ground on city roads, the seat height was set at 780 mm.

To best balance stability, agility and riding comfort, the tire size of 120/70-15 was selected for front, and 140/70-14 for rear. These are a size larger than S-Wing. Up-sized tires are keys to realization of styling that gives images of dynamic performance and improved riding comfort.

The fuel efficiency of 2.29 L/100 km and the 11.5 L fuel tank capacity are targeted to allow a maximum range of 470 km or more, which requires filling only once a week for most users.

The capacity and shape of the utility box are set presuming storage of two full-face helmets or a full-face helmet and a business bag.

6. Styling Theme and Proportions for Realization of Target Style

6.1. Styling Theme

At the start of styling design, the theme was first

set. GT scooter users are most concerned with dynamic performance, thus a design that matches it is desired. Accordingly, the design team deemed necessary to create a style that conveys to users the model's high performance capabilities at a glance. "A style that produces fast and agile image" was chosen straightforwardly as styling theme appropriate for "New Stylish Sport."

Moreover, it was decided to pursue a design that is appropriate for its functions rather than for differentiation. A target was set at realization of a highly stylish design by incorporating function into the styling design rather than spoiling the function by the styling design. That is because users never want to have the function spoiled for the sake of style in a scooter for daily commuting which in a sense is the harshest operating environment. If the design is too unique, it would fail to become a standard in the long run although it may draw attention for a limited period of time.

6.2. Design Proportions

First, we discussed what styling design would produce a fast and agile image. This was done because it is the proportions of an entire vehicle, more so than the styling of cowls and the details, that is the key for creating such an image.

Generally, a GT scooter body tends to be longer and/or larger relative to its undercarriage parts including the wheels, in order to provide both wind protection and luggage space. Such a balance, however, diminishes the sportiness, making it difficult to create a high dynamic performance image. Accordingly in this project, it was decided to employ two proportion-related elements, "mass forward balance" and "trapezoidal proportions," to create a fast and agile image through styling design.

The "mass-forward balance" in this instance refers to a means of styling design that can emphasize a strong forward motion and good wind protection as well as creating the image of man and machine as being one. Also, the "trapezoidal proportions" is effective to create a fast and agile image by keeping the body as compact as possible while emphasizing the undercarriage parts that connect the bike to the ground. These methods are often used for the styling design of motorcycles and are far different from the conventional approaches of scooter styling design (Fig. 7).

7. Styling Design Sketch

The style with a "mass-forward balance" and "trapezoidal proportions" was pursued keeping in mind the specifications and equipment to be applied. In the stage of design sketching, styling design was conducted to allow reflection of two intentions mentioned hereafter.

7.1. Styling Incorporating Function into Design

As mentioned in the section on the styling theme, many of the external shapes of the Forza125 were created not only for styling but also from functional requirements.

It was necessary to make the cowls and the body as compact as possible to achieve ideal body proportions, sporty style and agility for use in town. On the other hand, a certain cowl size is necessary for wind protection. To satisfy two contradicting requirements, thorough air flow management was considered when designing the shape. In other words, attempts were made to maintain adequate wind protection from a compact body.

From the stage of design sketch, the styling was created while well keeping in mind how the air should flow, such as how to let the air leave off the cowls, and how to intake and release the air. In particularly, the shape of the front cowl directly affects wind protection for rider's upper body and arms. Therefore with respect to the design of this part, many design considerations were taken such as letting air leave from the reverse surface in the rear ends on the sides of the front cowl (Fig. 8).

7.2. Styling Design That Exudes Intelligent Maturity

As the results of market researches indicate, the main target of this model is adult business persons. Moreover, taking into account that the users are mature Europeans, the obvious expectation was a design that would make

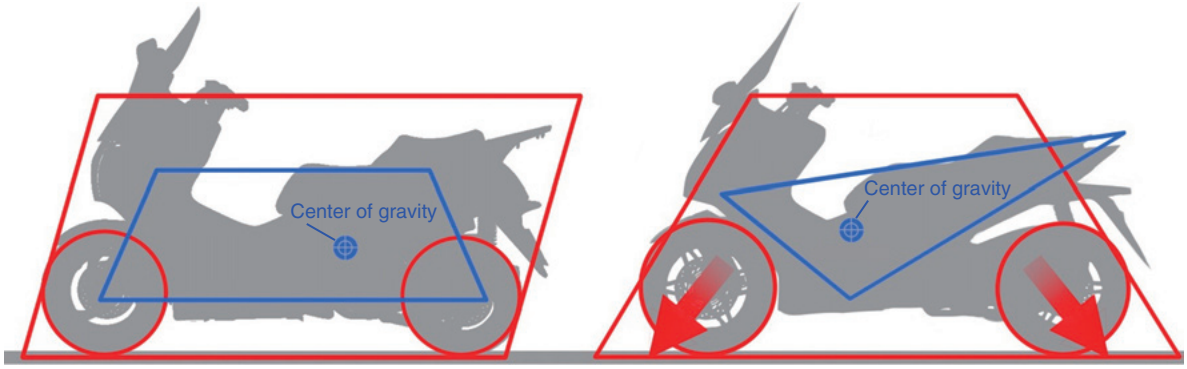


Fig. 7 Objective directions in design for the vehicular proportion of the Forza125

one feel that the product has the image of intelligence and matureness, allure and sexiness, and that it has a presence that gives its owner satisfaction of ownership. Accordingly, the design should satisfy user pride as well as having an intelligent and high-quality feel.

To create a mature, alluring and sexy image, dynamic yet elegant character lines and surface treatments were incorporated into the exterior parts such as the front body and the rear body (Fig. 9). At the same time, sharp and three-dimensional part shapes and the well-balanced layout of painted parts and material-colored parts emphasize sportiness that can satisfy mature users.

In the meantime, a mechanical and solid design was applied to the functional parts to produce an intelligent and high-quality feel give an advanced, high-tech impression. Meticulous attention was paid to designing even the smallest of details based on their functions (Fig. 10).

With the said considerations taken, the sporty yet elegant, aggressive yet intelligent, unique charm of the Forza125 was produced by the contrast of the elegant and glamourous body design against the mechanical and solid functional parts.

Thus completed was the styling sketches which should be well accepted by mature users in Europe while incorporating the function as a part of design (Fig. 11).

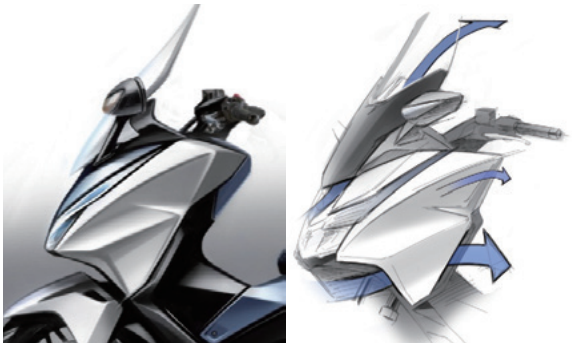


Fig. 8 Body shapes designed by thorough investigations on airflow management



Fig. 9 Character lines



Fig. 10 Design expressions evoking mechanical characteristics of functional parts



Fig. 11 Styling sketch of side view

8. Designing of Details

8.1. Design by 3D Modeling

As the next step, the proportions and the design concept were reflected on the 3D model by repeating the following procedures.

(1) Produce clay model
(2) Produce design data
(3) Produce prototypes
(4) Test functions and performance using prototypes

With the styling design for this project, more hours were spent than usual for the step (4), especially for the aerodynamic tests and the feedback of test results to the design team.

Prototypes were used to run tests in the wind tunnel to confirm where and how the wind blasts against the rider, with the following as targets to be achieved:

(1) Adequate wind protection from compact cowls
(2) Optimum wind protection for riders of various physical builds
(3) Considerations for comfort such as reduction of wind noise

Based on the test results, detailed shapes of the cowls were repeatedly refined by working together with the clay modelers and engineers. The styling was refined by conducting computer simulation verifications simultaneously with the wind tunnel tests.

At the same time, prototypes were taken to the test course for compound tests of various performance criteria other than the wind protection. Upon reviewing of the test results and hearing from the test riders, the styling was further refined.

In the process leading up to the finalization of styling design of this model, it was extremely challenging issue to achieve both handling stability and wind protection. The design was repeatedly modified without a compromise until reaching a fully satisfying level. The styling design of the Forza125 was finalized through such thorough validation processes (Fig. 12).

8.2. Adjustable Screen

The windscreen, which is a key part of wind protection, is an element that affects significantly to the styling impression. While the screen design started in an early stage, it was the most challenging part to design in the development of the Forza125. First, computer simulation was used to roughly estimate the approximate size, height and shape of screen for adequate wind protection, then the styling design was made based on it.

8.2.1. Advantages and disadvantages of screen

A larger screen provides better wind protection, improving comfort at high speeds. However, a large screen could create issues as well. As a motorcycle/scooter screen is made of plastic by injection molding or hot pressing, it is hard to attain clear and natural view of the windshield of an automobile. It is also vulnerable to scratches. When in rain, rider's vision may be hindered by irregular reflections from water drops on the screen. The fun and exhilarating feeling unique in motorcycle/scooter are attributable to the rider being exposed to wind, unlike in a car. An excessively large windscreen spoils such an exhilarating feeling.

8.2.2. Body size of rider and screen size

To balance such variety of requirements, a screen having a size that matches rider's body size is required. However, it is obvious that an optimum screen size varies depending on the height and build of the rider. An optimum screen size for a short rider may be too small for a tall rider to obtain adequate protection. On the other hand, if the screen is optimum for a tall rider, it may disturb front view for a short rider. The team repeatedly discussed how a screen should be to match a broad range of user physical constitutions.

8.2.3. Employment of adjustable screen and its limitations

The solution finally reached was to apply an adjustable screen.

Though adjustable screens are already employed in some large tourer models, none has ever been applied to 125 cc-class motorcycles. Nevertheless, it was concluded that it was the only option to have the rider feel exhilaration while offering adequate wind protection to a large number of users.

Considering the general price range of 125 cc scooters, any high-cost design requiring a large number of additional parts or high-cost parts had to be avoided. It is necessary



Fig. 12 Finalized exterior design (for mass production)

to make the styling feasible while ensuring screen adjuster rail protection, aerodynamic effects, durability and user-friendliness, taking into account the said limitations. As a means to fill the said needs, a visor as shown in Fig. 13 in front of the screen to cover up the adjuster was devised. Accordingly enabled was the screen appearing more compact than that of conventional GT scooters while protecting the adjuster. The design also contributes to the unique face appearance that gives the impression of individuality and presence while being stylish and sporty. Also to be noted is that the screen is stored behind the visor when lowered.

Additionally, the screen/visor design provides further improvement in wind protection by streamlining the air taken in from the duct under the visor and releasing out of the back of screen (Fig. 14).

8.2.4. Final screen design

The specifications and design of the adjustable screen was also refined gradually while conducting computer simulations and tests in the wind tunnel using actual scooter as with the development of body cowls (Fig. 15).

Finally, the screen height adjustment range was set at 120 mm with six positions to offer comfortable riding on highways to riders of various physical constitutions. If wind protection is not concerned, the screen can also be lowered to allow the rider to feel the exhilaration and thrill of riding a motorcycle/scooter.

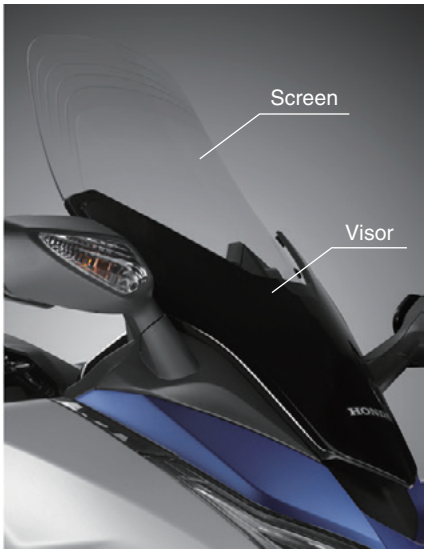


Fig. 13 Adjustable screen and visor

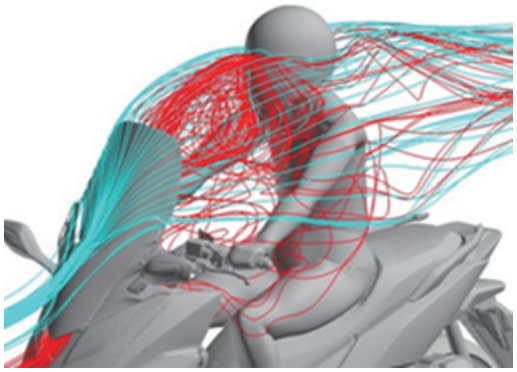


Fig. 14 Airflow straightening effects generated behind the screen, where red lines show the straightened flows behind the screen

8.3. Design Details

Aside from the entire proportions and cowls of the model, other details were also designed considering functionality, convenience, and safety. Among those, the specifications and design especially noteworthy are introduced hereafter.

8.3.1. Mirror with turn signal light

In France, it is common practice to keep turn signal lights blinking when a motorcycle/scooter maneuvers between automobiles on congested highways (Fig. 16). Taking this into consideration, the front turn signal lights were integrated into the mirrors located at a high position (Fig. 17). This reduces chances of turn signal lights being hidden behind an object such as an automobile, to make the scooter more recognizable. It also contributes to improved visibility from other riders or pedestrians on general roads.



Fig. 15 Design verification using wind tunnel



Fig. 16 Congested motor highway circulated around the city of Paris

8.3.2. Wheel and suspension

The front and rear wheels were designed to appear powerful yet agile by reflecting recent motorcycle trends to give a fast and high-performance image (Fig. 18). The rear suspension units are installed at an angle to emphasize the trapezoidal proportions while reducing vibrations and improving riding comfort.

8.3.3. Lighting system

The LED dual headlights were designed to appear sharp and intense to exude presence by integrating with LED position lights that emit light in linear patterns with light-directing plates enhance presence (Fig. 19). Moreover, the LED tail and brake light was designed with a unique M-shape to allow the Forza125 to be immediately recognized when seen from behind (Fig. 20).

8.3.4. Utility spaces

The Forza125 provides top-level capacity in utility spaces for its category. The utility box in the rear body has a 48-liter capacity and can accommodate various usages by using the attached separator plate (Figs. 21 and 22). Also, the glove compartment in the front body is equipped with a power socket to allow charging of devices such as a smart phone, etc. (Fig. 23).

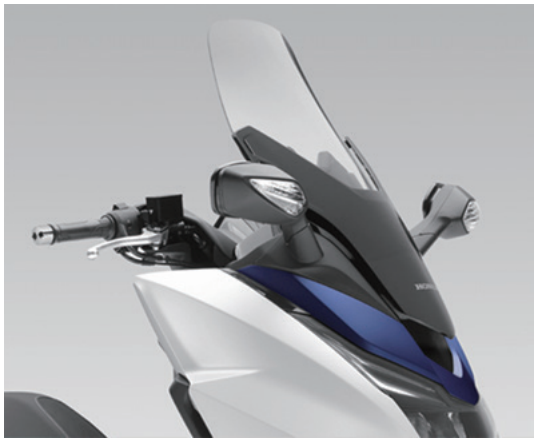


Fig. 17 Side mirrors installed with turn signal lights



Fig. 18 Front wheel and front fork with bottom case



Fig. 19 Dual LED head lights and LED position lights



Fig. 20 LED tail and brake light



Fig. 21 Utility space under the seat

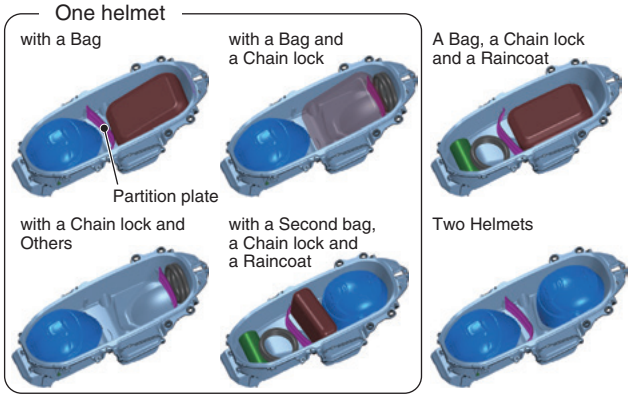


Fig. 22 Examples of practical uses of the utility box

8.3.5. Instrument panel

The instrument panel is an area that the user frequently looks at when using a scooter. It is therefore one of the critical areas in which users get the feel of a product's quality and a sense of satisfaction for ownership. The following was taken into account when designing so that users, whose standards are based on the quality of automobile, perceive that the simple and functional product has a feel of high quality (Fig. 24).

(1) The speedometer and tachometer are of an analogue type to produce a mature, gentle image.
(2) The area around the meter is framed with a painted panel to enhance high-quality image and to differentiate from conventional scooters. The frame is colored glossy black, which is the trend in automobile interior, to create a contrast with the polypropylene parts around it. The intention was to create a mature, refined design, rather than being bold.
(3) The above-mentioned frame visually separates the meter and the indicators inside and the information LCD outside. The differentiated depths create a three-dimensional feel like an instrument panel of automobile.
(4) The information LCD provides features such as a clock convenient for commuting to work, and a fuel gauge.
(5) Decorative parts with gloss black finish, as used in the meter, are also applied to the handlebar cover, etc., to enhance the high-quality image around the instrument panel.
(6) Accessory parts such as meter frames and handlebar covers painted in colors matching body colors are made available for users seeking an even bolder look (Fig. 25).
(7) Presuming installation of an after-market part such as a smartphone holder, the handlebar cover was designed to be compact to accommodate such parts while also maintaining its good appearance (Fig. 26).

8.3.6. CVT case cover and air cleaner case cover

In the styling design of a motorcycle except for scooters, the appearance of engine plays a key role to create a high performance image. In a scooter, however, the engine is covered with body panels and virtually invisible. One of the goals of this model was realization of a style that evokes the image of superb dynamic performance. Thus, the model targeted to produce the high engine potential image by design considerations of the CVT case cover containing the power transmission system, instead of the appearance of the engine itself. To achieve this, an image of the swing arm on a sporty motorcycle was created with the CVT case cover by laying glossy painted parts on a background of textured semi-glossy Polypropylene parts. Additionally, a mechanical and solid image was adapted to the air cleaner case cover to give the impression of a high power engine. The design of air cleaner case cover also helps to prevent entry of dirt and water from the air intake opening.



Fig. 23 Glove compartment



Fig. 24 Instrument panel



Fig. 25 Example of furnished accessory parts



Fig. 26 Example of smart phone installation

By designing functional parts to the details as per the function and styling concept, the image of entire vehicle is unified, contributing to enhancement of high-quality image (Fig. 27).

8.4. Colors

A total of five color variations are offered (color variations vary slightly by country of sales) (Fig. 28). Scooters sold in Europe are predominantly in the black-and-white range to accommodate various types of cloths in day-to-day commuting. Accordingly, four of the five types are in generally chicly colorless shades such as black and gun metallic.



Fig. 27 Covering of CVT case and covering of air cleaner case



Fig. 28 Color variations

The remaining one type is of a characteristic coloring, intentionally done so to match the sensibility and fashion of the French people. With a combination of matte white and matte blue, the color scheme radiates a strong aura of presence, adds color to user's life, and produces a sporty yet mature allure. Although the combination of white and blue is high in contrast, the matte finish for both colors subdues the design to be not too loud. Thus realized is the color scheme which is unique yet not unusual.

9. Reactions in Market

The Forza125 was introduced at Paris Motor Show in October, 2014, and its sales began in April 2015.

Though the data was from a short period of time including those at the time of release, the sales volume recorded No.1 in the 125 cc scooter category in the cumulative unit sales volume from January through July, 2015, in France (Fig. 29). Accordingly, Honda's share in the 125 cc scooter category in France grew remarkably (Fig. 30). The Forza125

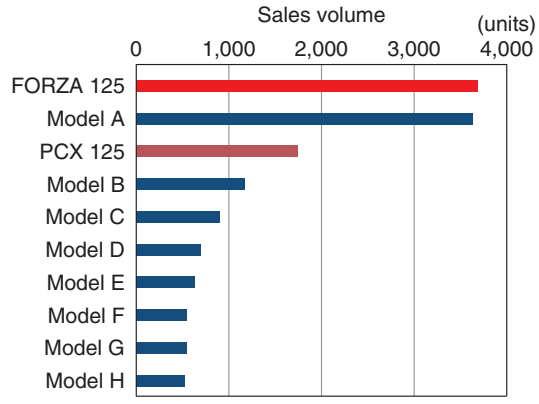


Fig. 29 Top ten models in accumulated sales units of 110 to 125 cc class scooters in France (January to July, 2015) (from Honda internal material)

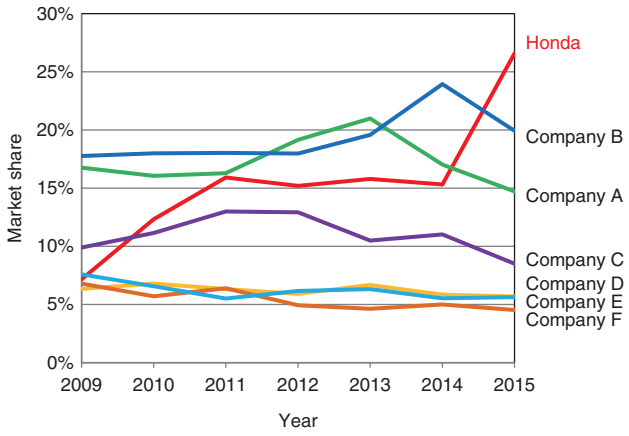


Fig. 30 Transitions of shares among manufactures for 110 to 125 cc class scooters in France (until October, 2015) (from Honda internal material)

received extremely good reviews from the interviewed users and journalists. The styling design in particular received especially high remarks and contributed significantly to the popularity of the model.

With respect to the color scheme, despite the scooter being used predominantly for commuting, the matte white/matte blue combination comprised 25% of all colors. That is the second highest of all five colors (Fig. 31). This fact proves that our intention in the Forza125 color scheme matched the sensibility of the French.

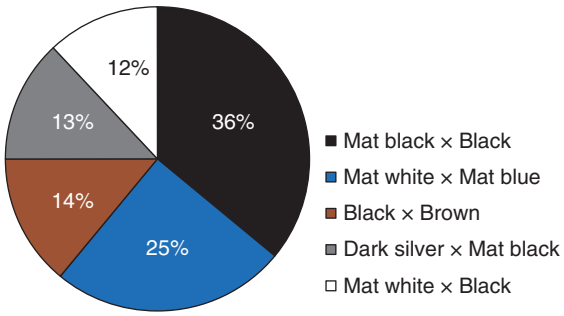


Fig. 31 Constituent proportions of vehicle body color variations for the Forza125 in sales

10. Conclusion

After clarification of customer needs by market research, the development of the Forza125 targeted the creation of an entirely new GT scooter.

Taking into account how the scooters were being used, “New Stylish Sport” was chosen as the key word of product development. Goals were set to satisfy performance demands in highway use as well as in city use at a high level. The aim of the styling design was not only at the attractiveness such as intelligence and allure, but also at creation of the image of highly dynamic performance. To achieve the goal, a style incorporating the functions such as realizing maximum wind protection was thoroughly pursued.

As a result, the Forza125 has been well received in the market, which we see as a proof that our styling intentions were correct.

That said, the real value of a product is not truly revealed until after a long period of use. We will therefore continue to listen to customer voices, look at the product from customer viewpoints, and improve it so that the Forza125 will be continue to be accepted by customers as a true standard model.

References:

(1) http://world.honda.com/Global-125cc-engine/

■ Author ■



Taro NISHIMOTO

Styling Design of New Tact, 50 cc Standard Scooter

Mamoru OTSUBO*

ABSTRACT

The development of a new scooter to be recognized as a next standard model has been required for the market of 50 cc scooter category in Japan, which is already in the status of its maturity, to respond to the requests from existing users providing features attractive enough as an entry model as well. Through the results from our market survey, it was found that flexibility in design to provide usability enhancements was considered to be more important than that for having features or uniqueness of a product. That is, the neutrally featured model, which is suitable to be the best partner for every individual user, was requested. Accordingly, the key word of the exterior design was defined as "relieved feeling" aiming at a creation of styling design based on logical consequences from the functions and usability, keeping away from embellishments. The model name was inherited from the first generation Tact, which was the first 50 cc scooter from Honda, because the goal the development for the first Tact was identical with that for our developing model. Because of that naming, it attracted the interests of many media people and made it easy to straightforwardly introduce the vehicle design concept to dealers and customers. Through this development, including coloring options selectable to fit a user's preference and belongings, a scooter that pleasantly supports their lives with conveniences acting as a good partner was successfully established.

1. Introduction

The 50 cc scooter category grew in the motor-equipped bicycle market under Japan's unique vehicle classification and licensing regulations. Due to the easy license acquisition, simple operation and low price, it is positioned as an entry category of motorcycles. Even now, there are steady demands and a variety of models being introduced in the 50 cc scooter market from various brands, catering to various customer needs. With the shift in the core user demographic from the younger generations to those in and over their 40s[(1)], explosive sales of a specific model as was seen in the 1980s and 1990s are rarely seen these days (Fig. 1).

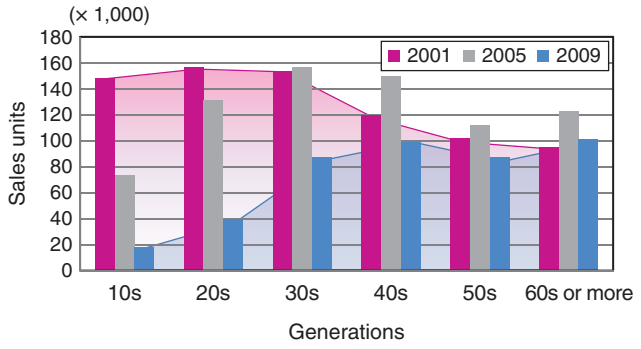


Fig. 1 Generation transitions of motorcycle buyers in Japan

Nevertheless, due to the above-mentioned convenience of 50 cc scooters, there are still a considerable number of users who require and fondly use these products. We also consider that it is indispensable for the future motorcycle market to appeal their convenience to young people.

With the background mentioned above, the decision was made to develop a new standard scooter that is attractive as an entry model that also fulfills needs of existing users.

2. Market Survey

2.1. How Scooters are Used in Large Metropolitan Areas

In the case of this model, due to its positioning as a standard scooter, the product has to appeal to various customers. Therefore, we could not set conditions such as appealing to narrow-target users. We first conducted studies on actual 50 cc scooter users at dealers in heavily populated metropolitan areas, which allowed us to acquire information on Honda's current standard scooters, Today (Fig. 2) and Dio (Fig. 3).

With Today, it was confirmed that many of its users focus on its price. This was more or less predicted as Today is the most inexpensive product of Honda. We were also able to gather information on the appeal of Today's styling design, which significantly contributed to this project.

Although Today is a low-cost model, "cheap" image had to be avoided. Thus, it was developed to exude a

* Motorcycle R&D Center

fashionable image to establish its own identity by applying features such as a cover-less handlebar, an independent headlight and meter design. However, the recent survey clarified that the intended styling design was not necessarily widely accepted. While there are young people who view the style as fashionable, there also are elderly people who like the conventional design having the handlebar covered with plastic parts. Similar voices were heard from a number of dealers.

With Dio, we were able to obtain many comments from repeat users, who are equally important targets as new customers are. They were asked to provide comments with the assumption of having to choose a 50 cc scooter from Honda products. At the time of the survey, high-price models with distinctive styling, such as Giorno (Fig. 4) and Zoomer (Fig. 5), were also available. However, when a so-to-speak ordinary model is pursued they said that the only option was Today or Dio. Moreover, some commented that for the above-mentioned elderly users the only option was Dio with a body construction and a design around the handlebar similar to the previous models.

For more in-depth analysis of user mind, researches were also conducted on users in regional cities with high-volume scooter sales.

2.2. How Scooters are Used in Regional Cities

It has been confirmed by directly observing the market that the 50 cc scooters are used in a wider variety of ways and more closely tied to their day-to-day activities in regional cities than in the metropolitan areas.

In large cities, public transportation system is extensive and many convenient means of transportation are available. Meanwhile in some regional cities, availability of public transportation is limited. This is why 50 cc scooters are deeply rooted as one of the life lines that support day-to-day activities of the people.

A large number of public and private parking lots are provided around the railway stations, which are important hubs for transportation. In the rush-hours, scooter users flow into those parking lots one after another. They ride their scooters wearing business suits or school uniforms, with neatly organized belongings placed on the floorboards at their feet or in the utility space underneath the seats.

We saw many scooters in a parking lot of a collage. That



Fig. 2 Exterior view of the Today



Fig. 4 Exterior view of the Giorno



Fig. 3 Exterior view of the Dio



Fig. 5 Exterior view of the Zoomer

collage is located high on a hill and it was easily assumed that scooters are important means for the students. Many of the scooters there were old models. That implies those were mostly the ones handed down by their senior students from generation to generation. We also could observe that some of the vehicles were uniquely changed or attached with articles showing personally accented appearances.

At a parking lot in a vocational school, we recognized that most of the scooters parked there were of the models with fashion-oriented exterior designs, such as the Giorno. Perhaps reflecting the current trend, many of them were of a similar body color.

During busy shopping hours at a supermarket, we saw quite a few units of Today and Dio in the parking lot. Many of them were equipped with a basket in both the front and rear, or having an empty cardboard box on the floor board to increase carrying capabilities, completely irrelevant to the styling of scooter (Fig. 6). The users would fill these spaces with purchased goods to take home.

From those survey results, it was understood that the flexibility that encompasses a variety of demands for enhanced usability is the key factor for developing a scooter to be the next generation standard. It was considered more important than having a fashionable exterior design or exhibiting sporty features. Following technology advancements, it is unquestionable necessity to incorporate the enhancement of basic performances in our development. However, what we confirmed was that they are seeking a moderately featured scooter suited to own it as the best partner for their mobility needs.



Fig. 6 User using the Dio equipped with both of front and rear baskets for delivery

3. Concept

3.1. User Expectations and Development Goals

From the results of the market survey as described above, we clarified user expectations for a 50 cc standard scooter. For example, newness or an expression of difference is sometimes perceived as unsettling by some elderly users. Also, housewives using a scooter mainly for shopping seek carrying capabilities regardless of the style of the scooter. In other words, how much that specific vehicle fulfills the requirements of their particular use is crucially counted as one of the important criteria for choosing their scooters.

As this particular vehicle was developed to be a next standard scooter, it was understood that the vehicle should have been meeting various requirements from wider range of users. To realize that, it was necessary to enhance the measures to cope with the requested factors from existing users to be a standard scooter, and make it attractive to the new customers as well. At the same time, it is also important that the vehicle is also able to win a favor from the people who do not have any positive affection towards abrupt changes in vehicle features. To create a product that can be included in customers' favorable purchasing options, it was required to consider, in objective and flexible manner, the attractive common features that can touch their minds.

3.2. Selection of Key Word

From the user expectations mentioned in the preceding paragraph, we chose "relieved feeling" as the key word of product development. This phrase sounds nothing about throbbing excitement. Nevertheless, the phrase reminds us of a considerate thought of caring while standing close to the people's lives, comprehensively enclosing all the functions and appearances of a product.

3.3. Concept

A vehicle called standard scooter is destined to be used as a means of transportation. It bears a responsibility as one of the necessary means for individual users' daily lives. In order to respond various needs from a variety of customers, the concept to be pursued in this development is to allow every user to use the vehicle with relieved feeling.

It is a matter of course to progressively apply benefits from technology advancements in the development. However it must not be in a way of compelling them to accept pre-designed values in the product. It is not what this model is intended to.

4. Selection of Base Model

For the platform of this model, the same platform applied to the 50 cc scooter Dunk[(2)], which is already on the market, was employed (Fig. 7). This platform was developed afresh including the engine and all of the frame body structures to create a brand-new platform dedicated to the applications for 50 cc scooters, envisioning the enhancement of fundamental performances and usability. By using this platform, it was made possible to keep the cost increase minimum while receiving the benefit of providing relieved feeling to customers with having the latest technologies equipped to the vehicle.



Fig. 7 Body frame configuration and exterior view of the Dunk

5. Styling

Descriptions on the features of the vehicle exterior that contribute to provide users with relieved feelings are described below.

The first critical point in designing was to determine the perceptual body dimensions including seat height. These dimensions reflect the relieved feelings they can have when they are riding the vehicle relating to, for example, maneuverability or ease of handling.

The next crucial point is whether or not the functions are adequately equipped to the intended use. These functions include allocations of storage spaces for individual requirements. Through these functions, users can feel relieved feeling in terms of their satisfaction in usability.

Another important design point is the exterior design that exhibits sturdy outlook of enduring a long term vehicle usage. It is not allowed to design a structure giving any impression that makes the customers feel the vehicle look easy to be broken, even though the developing vehicle is a scooter for a lower price range. That is, it should also be absolutely kept in mind to consider the customers' relieved feeling they have when they are in the process of purchasing.

Those factors mentioned above were required to be expressed in the styling design in a way by which it is perceived as an atmosphere producing relieved feeling.

5.1. Condition Setting

Prior to the individual examinations, we predeterminatively set several requirements in the process of styling design that provides relieved feeling to the users. The prepared concept board is shown in Fig. 8 and Fig. 9.

The conditions set at that time are as follows:

(1) The vehicle should be compact enough for easy handling to be considerate of aged or female users who are of a part of the critical target user strata.
(2) The handlebar should be in a higher position for ease of pushing and pulling when parking, etc. (Fig. 10).
(3) Presuming use of the scooter by users of a variety of build, the floor board and the seat should be flat for flexible accommodation.
(4) The front cover should be as upright as possible to prevent the optional front basket from sticking out when installed (Fig. 11).
(5) The front fender should be of an easy to control, independent construction, so the rider can immediately see the direction the front wheel is turned to.



Fig. 8 Conceptual descriptions on specifications and equipment

(6) The overall styling and the shape of each part should be such that one sees simplicity and solidness to avoid a fragile image.

It was determined that these conditions would serve as basis for the creation of its styling.

5.2. Design Method

The styling design was conducted keeping in mind the following key points.



Fig. 9 Conceptual descriptions on styling



Fig. 10 Styling sketches of front and rear quarter view for new standard scooter concept

(1) To keep the overall size compact, the rear end should be of a short-tail type in which the space is minimized between parts including the lighting instrument.

Firstly the clearance was minimized between the external body parts and the inner parts such as the frame body. Especially in the tail light located at the rear end, which significantly affects the impression of overall size, the concentric, multi-step reflector is applied to achieve compactness (Fig. 12).

(2) The overall proportion should be such that the rear end is slightly raised from the horizontal base line to provide a moderately swift impression.

To create a "just right" image that is not too aggressive or dull, the upper line at the end of body is set almost horizontally and the lower line slightly rising toward the end. An accented line in the middle of body side that runs between the above-mentioned lines makes the styling agile and dynamic (Fig. 13).

(3) To create a high-quality and tough image, the external body parts should be basically of a simple yet shapely

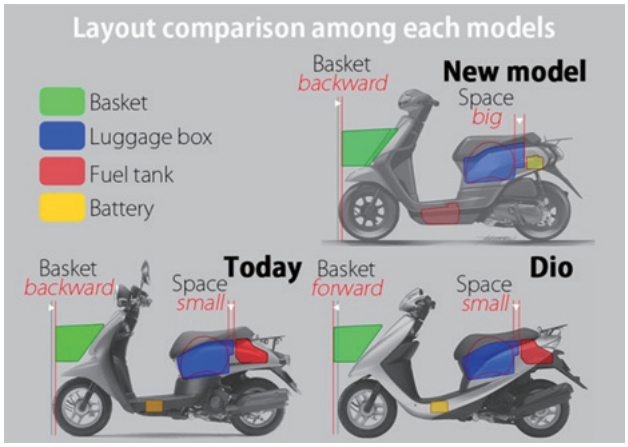


Fig. 11 Comparison of utility space arrangement of developed model with those of the Today and the Dio



Fig. 12 Exterior views of rear end of body including combination lamp assembly representing a short tail

surface composition.

To simplify surface contour, it was decided to use fairly large outer body parts. It should however be noted that the draft angle (one of the preset conditions for demolding) tends to become critical in a largish body part. Thus, creative measures were taken such as gradually changing the roundness on the edge lines to satisfy the draft angle requirements, to create a simple yet shapely surface. To reinforce the "tough" image, each accented line is emphasized, and the end fold made thicker. By the effect of the accented line of the end fold, the simple surface enclosed by the accented line becomes compact and dynamic in form (Fig. 14).

(4) With regards to scratching on painted surfaces, colored plastic parts should be used where they are more likely to have contacts in situations such as parking or loading luggage.

From the standpoint of user-friendliness in day-to-day use, the above-mentioned consideration is a significant benefit. Colored plastic parts, which are more scratch-resistant, are applied to the leg shield and the floor board that are prone to contacts when parking, and to the rear body where a contact is unavoidable when loading luggage on the rear carrier or when accessing the helmet box. Moreover, the colored plastic parts are shaped in such a manner that they protrude further than the painted parts to protect painted surfaces from scratches (Fig. 15).

(5) To create a high-quality feel of its appearance when seen from front, a multi-reflector headlight in which the right and left turn signal lights are integrated should be applied.

Regarding the configuration around the handlebar, the model applies a handle bar covered with plastic parts, which is a common design for 50 cc scooters, and a multi-reflector headlight integrated with turn signal lights. As there are virtually no cut lines in the lens of a multi-reflector headlight, the design of the reflector can play a key role in creating a high-quality image; however, due to reasons such as regulation compliance and retention of practical luminance, the level of freedom with its design is relatively limited. With this model, a coherent and dynamic styling was achieved by emphasizing the accented line that run from the lower end of the headlight to the upper end of right and left turn signal lights. With this, we were able to create a lighting instrument with a high quality feel while satisfying the functional requirements (Fig. 16).

(6) To make the speedometer easy to read at a glance, highly legible letters should be laid out in an easy-to-read manner while paying attention to the color placements.

Considering the targeted elderly users, large letters are used where the layout permits for quick transmission of information. With respect to the overall color scheme, the number of colors is reduced to simplify the appearance of the meter (Fig. 17).

(7) To express sportiness in the wheel areas, a wheel that symbolized a spoked wheel should be applied.

The wheel of the first-generation Tact has been used in various Honda scooter models for nearly 30 years



Fig. 13 Exterior design scheme of the Tact



Fig. 14 Intensified expressions of rigidity applied to exterior part



Fig. 15 Arrangement of colored parts on the Tact

and has been regarded as a highly functional, universal design. A decision was made to renew the wheel design at this occasion of a new standard scooter development. Thus developed is the functional and simple wheel that symbolizes a spoked wheel that is applicable to scooters of various styles (Fig. 18).

With these methods employed, a styling design that culminated from the requirements of function and user-friendliness, rather than decorative, was achieved. We believe that we created a model that can become an indispensable partner in day-to-day activities for the users and that the users can feel good about using it.



Fig. 16 Design concept for headlight and accented lines surrounding turn signal lights



Fig. 17 Simplified speedometer design for good visibility



Fig. 18 Steel wheel with spoke like radial pattern

6. Naming

The product name Tact was originally of a model launched in 1980 and the originator of Honda 50 cc scooters (Fig. 19). Its production continued for 22 years until 2002, spanning seven generations.

As mentioned earlier, this project is of a development of a new standard scooter model that is neither Today nor Dio, and not merely renewing an existing model. Thus, no name was assigned to it at the beginning of its development. As the styling design progressed, some began saying “This is Tact, isn’t it?” and the name “Tact” naturally started to appear in the idea sketches.

Given such development of events, we reviewed the press release statement of the first-generation Tact[3]. Seen in that text were phrases such as rich, quality feel; compact body; easy-to-use devices; and clean-cut styling that matches a wide variety of fashion. Although the historical background and the way the idea is expressed are different, the targeted product concept of the first-generation Tact was applicable to the new development almost entirely.

After this, the product name Tact, which used to be synonymous to Honda’s 50 cc standard scooters, became regularly used among the product development team members. No objections were raised, and it was later decided to use it as its formal name.

As mentioned above, Tact was not the originally intended name; rather, it came naturally afterwards because what the new model was aimed at coincided with that of the first-generation Tact. The naming had a big impact and drew attention from the media, and the model concept was conveyed straightforwardly to users and the dealers. We came to believe that there was no other name that better suited the model.



Fig. 19 Exterior view of the Tact of the first generation in 1980

7. Colors

Color is the finishing touch for a product to appeal the charm to users. When considering what color scheme suited the concept of this model, we reached the conclusion that the individual user who would ride it for day-to-day activities should be at the center of attention, not the scooter.

Based on this, a total of six colors were selected (for the initially released model line up at January, 2015) while keeping in mind that the product should complement user's lifestyle (Fig. 20).

(1) Candy noble red: A red with a high-quality feel that is deep yet pronounced highlights
(2) Pearl jasmine white: A neutral and gentle white with the glossiness of a pearl
(3) Poseidon black metallic: A black with blue metal flakes that evokes the deep sea
(4) Delicate blue metallic: A light blue with a bright tone with a balanced intensity
(5) Force silver metallic: A very bright, high-quality silver without being too shiny
(6) Mahogany brown metallic: A brown with a good balance of slight reddishness and subtle brightness



Fig. 20 Color variations of the Tact

None of these color tones tries to draw attention to itself. A neutral color palette was selected based on the colors' ability to complement the user, regardless of the user's outfit, location or situation. A variety of colors are offered so that the user can choose one that suits his or her preference or belongings. All six colors have a metallic feel that create beautiful contrasts of highlight and shadow to elegantly accentuate the simple yet dynamic surfaces.

8. Conclusion

A new 50 cc standard scooter was developed. It was named Tact, since its concept overlapped with that of the first-generation Tact. A desirable styling design was achieved by focusing on users and pursuing user-friendliness.

The design was intended to make its functions visible to users: easy to mount or dismount, easy to handle when parking, the body is compact yet strongly built, and the riding position is highly flexible to accommodate various body sizes. With this, the concept of this model is well conveyed to evoke "relieved feeling" from users. The role that the styling design played in this model was not merely a creation of its external shape, but a medium to comprehensively inform the customer of the outstanding characteristics of the product called Tact. We hope that it will be utilized by many users as their good partner to provide comfortable support in making life more convenient.

References

(1) http://www.jama-english.jp/release/release/2012/120404-4.html
(2) Mitsukawa, M., Hirayama, S., Otsubo, M., Tateishi, Y.: Development of New 50 cc Scooter Dunk, Honda R&D Technical Review, Vol. 26, No. 2, p. 53-64
(3) http://www.honda.co.jp/news/1980/2800903.html

■ Author ■



Mamoru OTSUBO

Development of RC213V-S

Hiroshi UNUKI* Ryuji TSUCHIYA* Hodaka MUKOUHARA*
Naoki MURASAWA* Satoru OKOSHI*

ABSTRACT

The RC213V-S was developed aiming at a creation of a motorcycle, which can be legally driven on a public road, based on the MotoGP racing machine RC213V while succeeding its mechanisms and detailed specifications. To comply with regulations and to apply necessary equipment needed for practical use, some of the parts manufacturing processes were changed. However, the basic configurations and exterior styling design were maintained within a limited range of changes, minimizing its weight increase to achieve the dry weight of 170 kg. Consequently, it was made possible to have ordinary riders enjoy the attractive feature of maneuvering feeling that is so called "excellence of maneuverability," which is a crucial element needed for RC213V to win the races.

1. Introduction

The RC213V, a MotoGP racing machine (Fig. 1), started to participate in MotoGP races in 2012, and won the triple crown of the rider's title, the constructor's title and the team title in consecutive two race seasons of 2013 and 2014. One of the most important features of this machine, which is dedicatedly developed for winning races, was "excellence of maneuverability." That is to say, the RC213V can be recognized as the easiest racing machine to maneuver in the world. The developed motorcycle of the RC213V-S (Fig. 2) is vehicle legally drivable on public roads while inherited most of the mechanisms and the detailed specifications of the RC213V. The objective of the development was to share the fascination of "excellence of maneuverability" with ordinary riders. In other words, the RC213V-S is not for applying the technologies that Honda has gained through races to ordinary production motorcycles, which Honda has sometimes done so far, but for making an unprecedented challenge to have a machine developed for MotoGP legally driven on a public road.

In this paper, the concept of the development, the applied engine technologies and the vehicle control technologies are introduced.



Fig. 1 RC213V



Fig. 2 RC213V-S

* Motorcycle R&D Center

2. Development Concept

Having an engine that cranks out a maximum power more than 175 kW mounted in the motorcycle as light as approximately 160 kg, the RC213V has an overwhelming engine performance as well as having excellent handling characteristics to allow for use of the full performance. In the RC213V-S, which is a commercial motorcycle for use on public roads, the main target of development is set to have the rider enjoy the maneuverability of high quality rather than the engine performance. The "fun to riding" attainable from the maneuverability can be experienced by ordinary riders regardless of speed even if he is unable to ride like a MotoGP racer. The development concept therefore is to fully reproduce the maneuverability while maintaining the racing machine package.

3. Overview

Figure 3 shows the position of the RC213V, the RC213V-S and the RCV1000R, which is a commercially-available racing machine based on the RC213V for races in the open category of MotoGP. Major specifications of the RC213V-S are shown in Table 1. The complete motorcycle packaging, basic specifications and the mechanism that constitutes basic configuration of the RC213V are maintained wherever possible in the RC213V-S. Just like the RC213V, the masses are thoroughly centralized and the friction in various moving parts is minimized to enhance maneuverability. The weight saving and high precision of component parts, which the overwhelming difference between a MotoGP machine and a commercial motorcycle

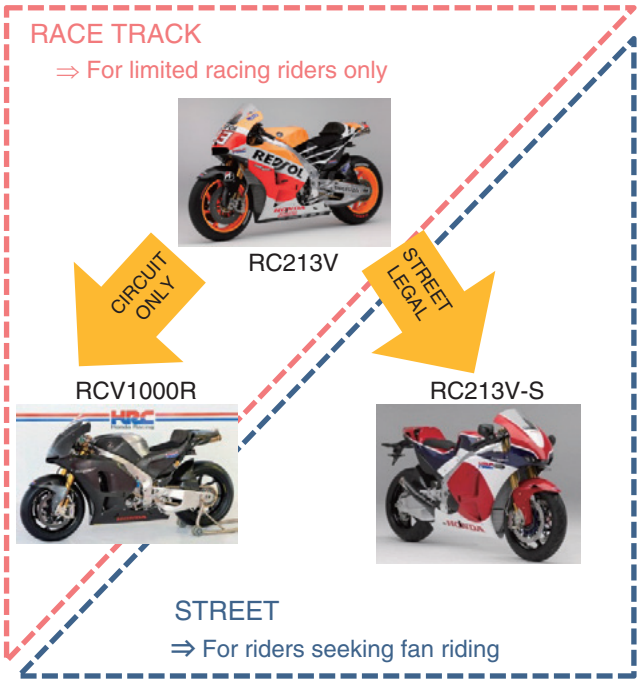


Fig. 3 Positioning of each model

Table 1 Specifications of RC213V-S

Engine type	Liquid-cooled 4-stroke 4-valve DOHC V-4
Fuel supply system	PGM-DSFI electronic fuel injection
Engine displacement (cm^3)	999
Frame type	Diamond
Dry weight (kg)	170
Kerb weight (kg)	188
Caster angle (deg)	24.6
Dimensions (L×W×H) (mm)	2110 × 770 × 1115
Ground clearance (mm)	115
Seat height (mm)	830
Trail (mm)	105
Wheelbase (mm)	1460

is attributable to, are also emulated. To ensure even higher quality, this motorcycle is produced by expert technicians having excellent skills. In the meantime, some modifications have been made to allow service in the general maintenance environment as well as for law compliance by addition of minimum necessary parts to make it street legal. The following are the modifications and additions from/to the RC213V.

(1) Presuming service in the general maintenance environment, the valve system has been modified from the pneumatic system to the coil spring type while maintaining the gear-train driven camshafts. The transmission has also been modified from the seamless type to the conventional dog clutch type. These modifications are common to the RCV1000R.

(2) To make the motorcycle street legal, the lighting instruments, rear view mirrors, speedometer, muffler with catalyst, license plate holder, horn, etc. are added without making big changes to the basic configuration and styling of the RC213V.

(3) To make the motorcycle practical for use on public roads, the Honda smart key system, starter motor, side stand, etc. are added as well as modifying the specifications of tire, brake disks, pads and the steering stopper angle.

3.1. Coloring

The RC213V-S is offered only in the traditional tricolor scheme, which is the corporate color of HRC (Honda Racing Corporation) inaugurated in 1982, as well as a typical color of Honda factory machines. The red represents passion of the persons committed to winning, the blue for the high technology based on theories, and the white symbolizing all customers fond of motor sports. A motif of Japanese flag is displayed on the sides of front fairing as a symbol of manufacturer's passion and challenging spirit of R&D members who play important part of precision manufacturing in Japan.

3.2. Packaging

In the packaging of the RC213V as a complete motorcycle, the masses are thoroughly centralized to enhance maneuverability. While setting the wheelbase longer than a general super-sport motorcycle to cope with the high power output, a priority of weight reduction is given to the wheels and suspension parts located far from motorcycle's center of gravity (CG). In addition to that, the fuel tank is located near motorcycle's CG to reduce inertia moment of vehicle body as a complete motorcycle and to minimize shift of CG from changes of fuel volume. The packaging as a complete motorcycle along with the basic specifications from the materials to the manufacturing methods of frame components of the RC213V is maintained in the RC213V-S. Considering use on public roads, the battery capacity is increased and electrical components such as the lighting instruments are added to the RC213V. Regarding these modifications and addition, the parts are laid near the CG of complete motorcycle to prevent increase of inertia moment of the complete motorcycle to achieve desired maneuverability.

In the meantime, the sport kit, which is exclusively for use in a closed course such as a race track, has also been developed. By removing the lights and other equipment for street use and installing the kit parts, the body inertia moment becomes the same level as the RC213V, allowing emulation of the riding experience in the speeds closer to the world of the RC213V.

3.3. Frame Body

In the RC213V, each and all frame body component parts are ground-fit by specialists, and then welded together using Tungsten Inert Gas (TIG) welder. Consequently, a high precision and welding quality are maintained despite the need of large number of welding. In the RC213V-S at this occasion, the materials and the manufacturing methods employed in the RC213V are also maintained wherever possible.

Moreover, the machining bolts made of titanium alloy are employed for tightening of frame body parts of the RC213V-S just like in the RC213V to reduce weight. When assembling, the molybdenum grease is applied to the threads to obtain consistent axial force, and all bolts are hand-tightened to the specified torque which is different from that of an ordinary steel bolt.

3.4. Swingarm

The swingarm of the RC213V is that of an under-brace type to cope with the shape of fuel tank aimed at reduction of inertial moment of the motorcycle, and the torsional stiffness and the lateral stiffness are properly balanced to achieve necessary maneuverability. The swingarm is composed of the press-molded aluminum arm, the end piece and cross body which are entirely machined from an aluminum billet. The parts are welded together by skilled expert technicians using a TIG welder to ensure maneuverability while reducing weight. The same configuration and manufacturing method of the RC213V are maintained in the RC213V-S wherever possible.

4. Engine

4.1. Overview and Basic Specifications of Engine

The engine of RC213V is designed with an aim at mass centralization, weight saving and compactness to enhance maneuverability of the complete motorcycle. The engine of the RC213V-S succeeded to the basic design concepts of the original engine of the RC213V. In addition, specifications and production methods for mass production were implemented even though expected production volume was quite limited. Despite the application of those methods, the engine kept the size that fits in the frame of the original RC213V as well.

Compared to the same 90-degree V type four-cylinder (V4) engine of the mass-production motorcycle VFR800, the weight is less by 10 kg, the length between the crankshaft and the output shaft is shorter by 51.5 mm, and the engine width is less by 40 mm. The engine sizes of the RC213V and the VFR800F are compared in Fig. 4.

The external view of the RC213V-S engine is shown in Fig. 5, and the transparent view in Fig. 6. The engine specifications are given in Table 2.

This paper mainly concerns the technical features that contribute to the lightness and compactness of the RC213V-S engine while permitting service in general maintenance environment.

4.2. Crankcase

When designing the crankcase with integrated cylinder blocks, a breather chamber having an adequate volume is incorporated in the area between two banks to separate oil

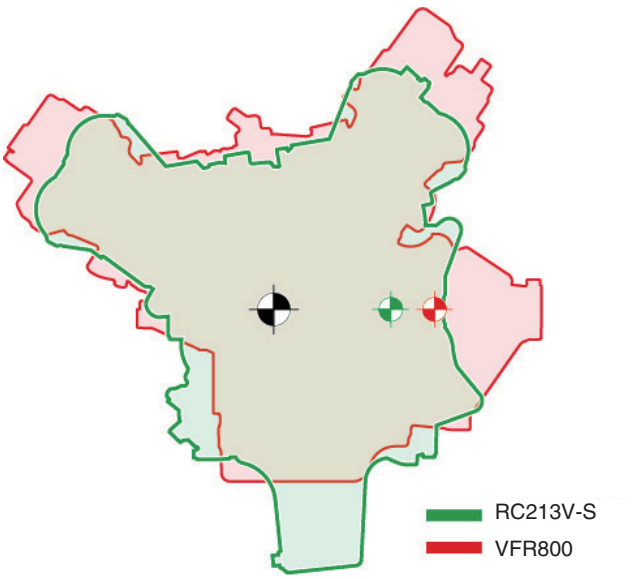


Fig. 4 Comparison of engine sizes

from the blow-by gas to achieve a breather performance necessary for use on public roads. As the breather chamber is that of a construction having a complex labyrinth, the crankcase is made of sand-cast aluminum that permits casting of a hollow product. The cylinder block is that of a closed deck type from which a high stiffness is attainable around the cylinder bores to cope with a high power output. In this method, cast-out holes remain on the deck surface due to the core print for securing of the sand core for the water jacket. Such a cast-out hole causes a loss of stiffness of the deck surface. Accordingly, aluminum plugs are pressed into holes at the time of machining except the ones for coolant passage as shown by Fig. 7 to prevent lowering of stiffness of the deck surface. The Ni-SiC compound plating is applied on the cylinder bore to reduce friction from sliding of the piston while enhancing seizure resistance.

Table 2 Specifications of engine

Engine type		Liquid cooled 4-stroke 90° V transverse 4 cylinder
Engine displacement (cm^3)		999
Bore × Stroke (mm)		81.0 × 48.5
Combustion chamber Shape		Pentroof
Compression ratio		13.0
Valve train		DOHC 4 valve cam gear train
Valve Dia. (mm) × Number / Cyl.	Intake	32.5 × 4
	Exhaust	28.5 × 4
Max. power (kW/rpm)		117/11000
Max. torque (Nm/rpm)		102/10750
Clutch type		Dry multi-plate type
Transmission		6 speed constant mesh



Fig. 5 External view of engine

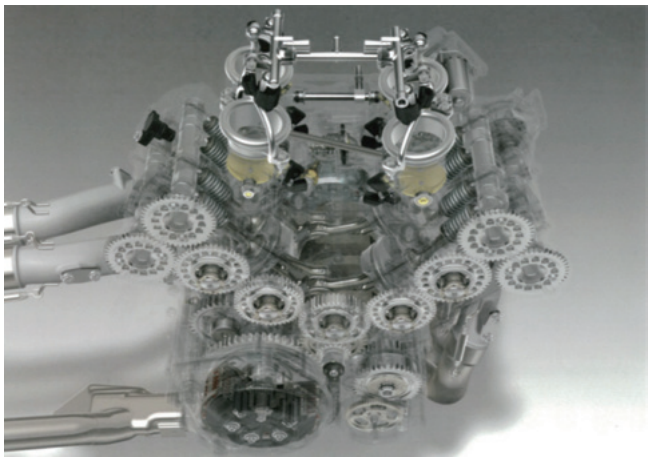


Fig. 6 Transparent view of engine

The same semi-dry sump construction as in the 2002 year-model MotoGP machine RC211V is employed in the crankcase as shown by Fig. 8 to reduce pumping loss. It is of such a construction in that the crankcase is of a dry sump type using the transmission housing as an oil tank[(1)]. The reed valves are incorporated in the pump case of the

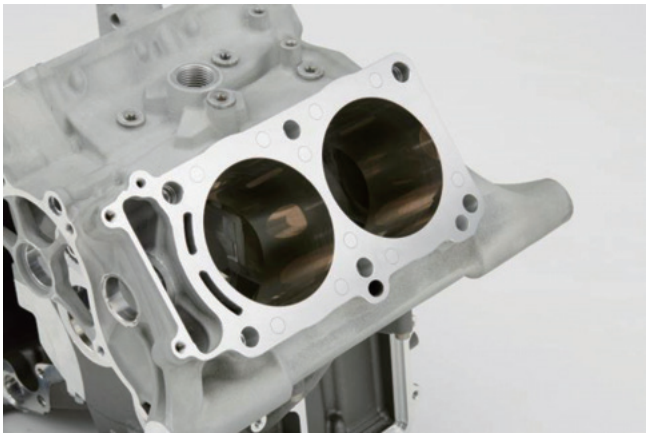


Fig. 7 Closed deck type cylinder block

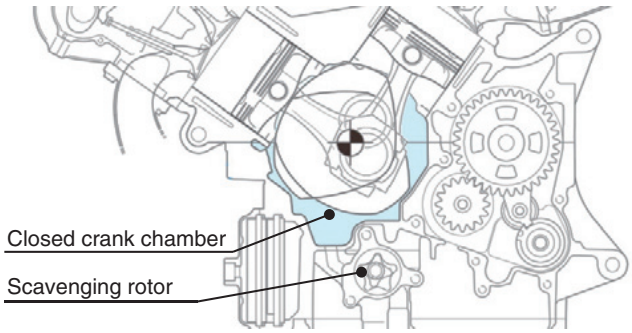


Fig. 8 Structure of closed crank chamber

scavenging pump that has a rotor per two cylinders to ensure its function. This construction permits reduction of pressure in the crankcase and efficient extraction of oil from the crankcase (Fig. 9).

A comparison of total friction loss with the commercial in-line four-cylinder (L4) engine of the same displacement is shown in Fig. 10. The friction loss of the RC213V-S engine is less than that of the L4 engine by 25% at 12000 rpm. The reduced friction loss is considered attributable to the sealed crankcase construction and the latter-mentioned gear-train driven camshafts.

4.3. Reciprocating and Rotating Parts

The crankshaft is made of high-cleanliness steel with vacuum degassing process having a high fatigue resistance. To avoid interference of the counter weight with the piston at the bottom dead center, the center of machining of the outer circumference of counter weight is offset toward the crank pin from the center of journal. When compared to the case without offset, the offset design permits reduction of length of connecting rod, which allows reduction of cylinder head height. Separately prepared weights made of a heavy metal (specific gravity: 18.1 g/cm^3) are pressed into the counter weights. This construction is aimed at retention of appropriate inertia moment, which is necessary to ensure throttle linearity and traction characteristics, while achieving compactness. The appearance of crankshaft is shown in Fig. 11.

The connecting rod is made of the titanium alloy Ti-64A. As shown in Fig. 12, the cross section is of an X shape made by hot forging to attain a high torsional stiffness. Compared to the conventional titanium alloy connecting rod of the VFR750R, the weight is less by 6.8%.

The piston is made of the high strength aluminum alloy A2618-T6 which has a high strength at high temperatures. As shown in Fig. 13, the connection of right and left piston pin bosses with a bridge permits reduction of weight and increase of stiffness.



Fig. 9 External view of oil pump assembly

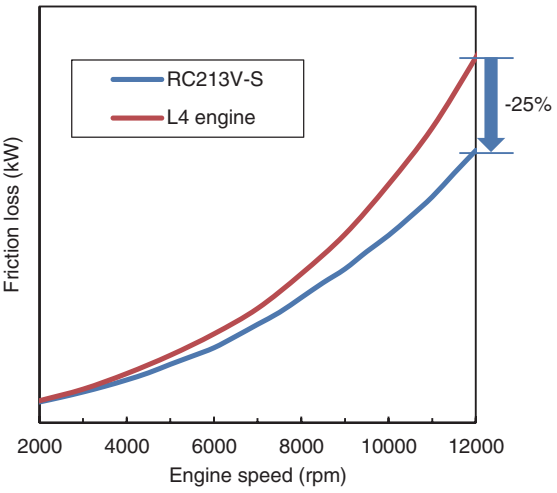


Fig. 10 Effect of friction reduction

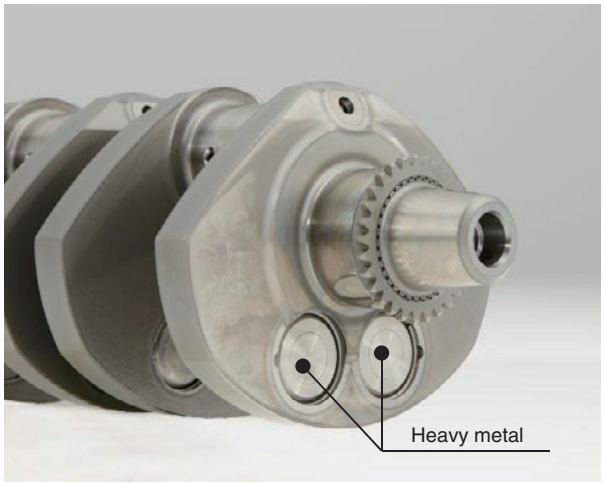


Fig. 11 Crank shaft

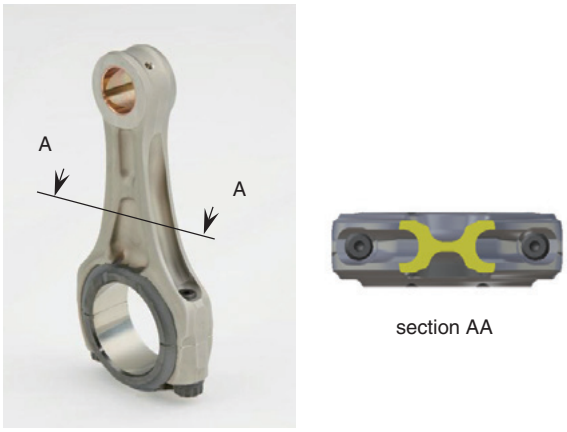


Fig. 12 Connecting rod with X-shaped cross-section

4.4. Camshaft Drive System

The gear train is employed in the camshaft drive system for accurate valve actuation at high revolutions and reduction of friction in the cam drive system. The gear train is shown in Fig. 14.

The gear train, which is composed of a total of 10 gears in the front and rear bank, has a backlash adjuster using an eccentric shaft as shown in Fig. 15 in the second, third and fourth idle gear shafts. The inside of the eccentric shaft is splined. The idle gear rests on the off-centered outer circumference of the eccentric shaft, allowing backlash adjustment by turning the eccentric shaft. After adjusting backlash, the eccentric shaft is locked from turning by tightening the fixing nut. Then, the axial bolt is tightened to lock the eccentric shaft, which locates the idle gear in the axial direction. This construction allows proper adjustment of gear backlash to control gear noises such as rattle or whine as well as preventing resonating vibrations in the cam drive system. For fine adjustment of valve timing, such a construction is employed in the cam gear/camshaft retaining system that allows selection of a set of retainer bolt holes from the seven sets of holes having a slightly varying orientation referenced from the center of gear tooth.

In the engine assembly process, the backlash and the valve timing are adjusted unit by unit.

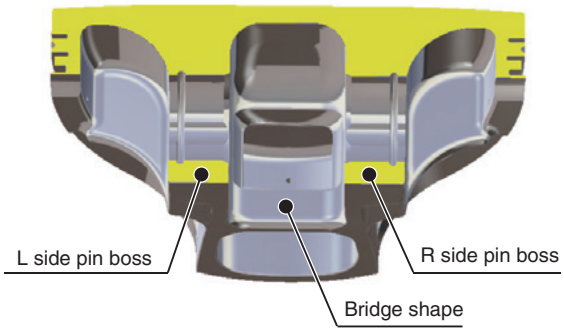


Fig. 13 Piston cross-section

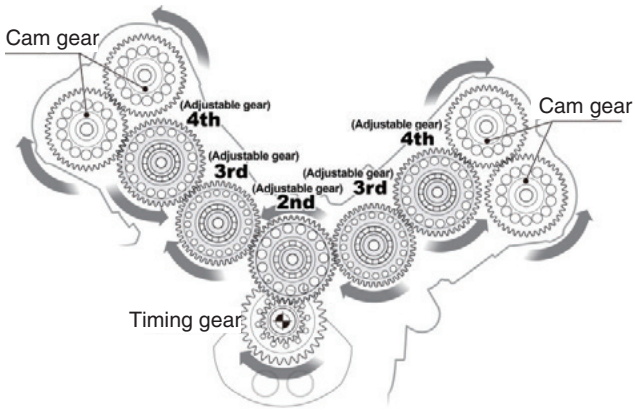


Fig. 14 Gear-driven camshaft

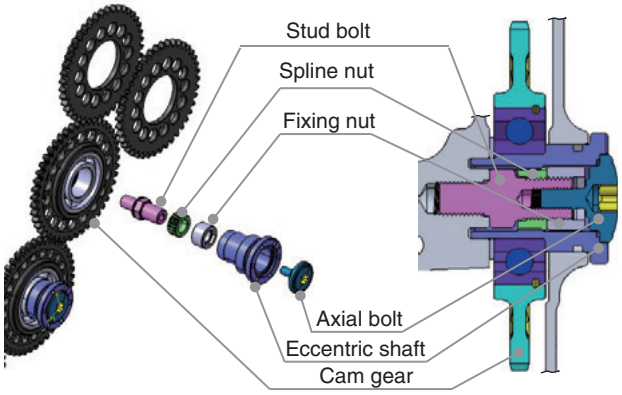


Fig. 15 Backlash adjustment mechanism

4.5. Oil Feed System

The oil passages to feed oil to the crankshaft are shown in Fig. 16. The oil is fed from right and left ends of crankshaft to the big ends of connecting rods though the crankshaft. Independently from that, the oil is fed to the crank journals via the passages in the cylinder block. The passages are created independently to feed optimum amount of oil to each system. The oil is also fed to the piston from the piston jet located in the exhaust side exclusively for each cylinder. The piston jet shown in Fig. 17 has four outlet holes having various directions to allow efficient lubrication and cooling.

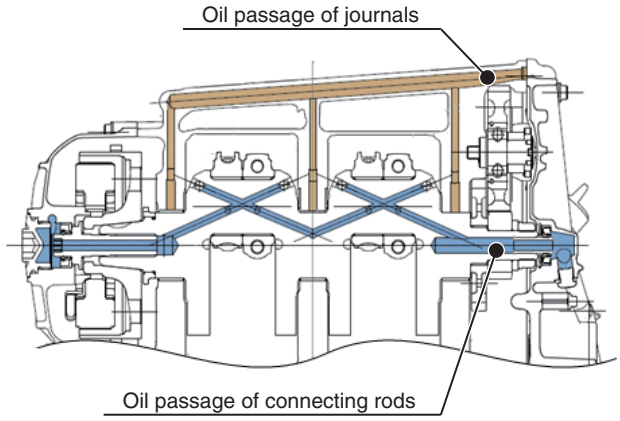


Fig. 16 Oil supply for crankshaft

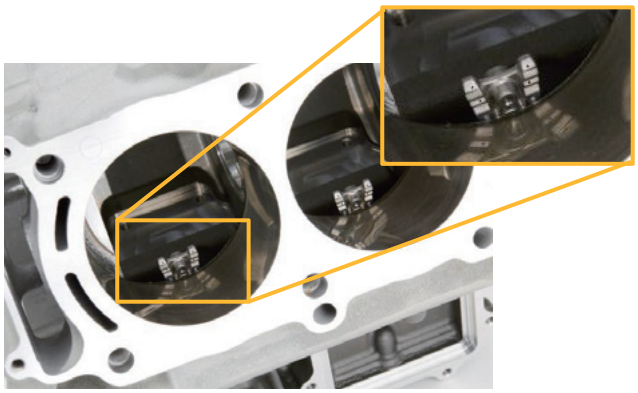


Fig. 17 Piston oil jet

4.6. Clutch

To reduce operating effort of clutch lever and to control excessive torque in the reverse direction, the dry clutch having an assist-slipper system is employed. The clutch facing is made of the heat-resistant and wear-resistant sintered material. The structure of clutch is shown in Fig. 18. The clutch center, which is a solid piece in a conventional design, is split to the center A and the center B. The sub springs are incorporated between the center A and B. The spring load acts in such a manner that lifts the pressure plate via the center B. Accordingly, when the clutch lever is pulled, the force from the sub-springs is added to the clutch lifting load which pushes the pressure plate, thus reducing lever effort. The assist cams and the slipper cams are also incorporated between the center A and B, and the both clutch center are engaged via either type of cams.

How the assist-slipper system functions is explained in Fig. 19. When acceleration, the center B is pulled in toward the center A by the thrust force from the assist cam, allowing only the main clutch spring load to act on the pressure plate. Accordingly, the normal torque transmission capacity is obtainable from the clutch. When deceleration, the thrust force from slipper cams acts in the direction that lifts the clutch center B and the adjacent pressure plate. The force from the main spring acting on the pressure plate decreases, causing the clutch capacity to lower. Thus an excessive torque transmission in the reverse direction occurring at the time of a quick down shift is moderated by the slipping of clutch. This helps to reduce rear wheel hopping and rear tire slippage.

To allow push starting of the engine, the plunger system (Fig. 20) is employed to control travel of the clutch center by the thrust force of slipper cam. The plunger is installed in the clutch center B in such a manner that allows travel in the radial direction. When the engine is not running, the clutch center B is locked by the plungers while contacting with the clutch center A to maintain the normal clutch capacity, which prevents clutch slippage to allow push starting. As soon as the engine starts running, the centrifugal force moves the plungers toward the outer circumference to allow the clutch center B to travel to the axial direction.

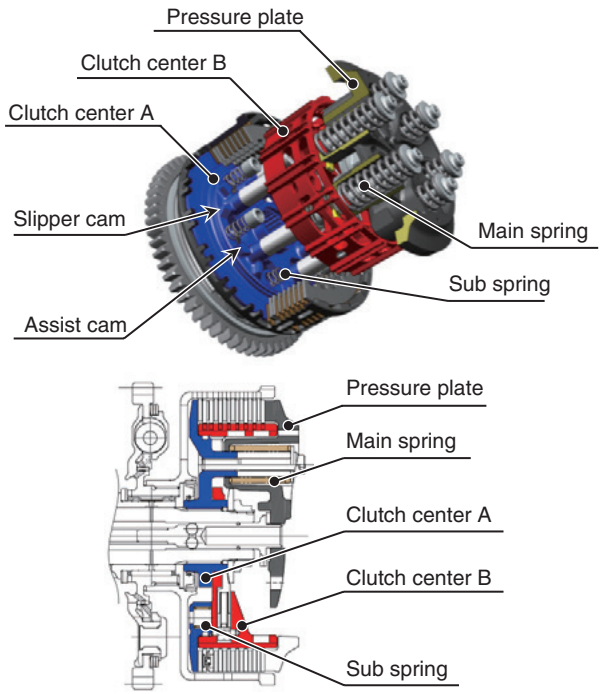


Fig. 18 Structure of assist-slipper clutch

4.7. Intake System

All the intake air passages in the cylinder head and in the throttle body are machined to obtain precision of port shape for steady flow of intake air. The length of intake manifold is maintained same as that of the RC213V by the use of insulators having only a face-sealing function instead of conventional plug-in type insulators for connection of the throttle body to the cylinder head. For connection, the rubber-mount construction is employed to reduce vibrations in the entire throttle body. Two injectors are incorporated in each cylinder to supply optimum amount of fuel across the broad engine speed and throttle opening ranges. One of the two injectors is located after the throttle valve to allow

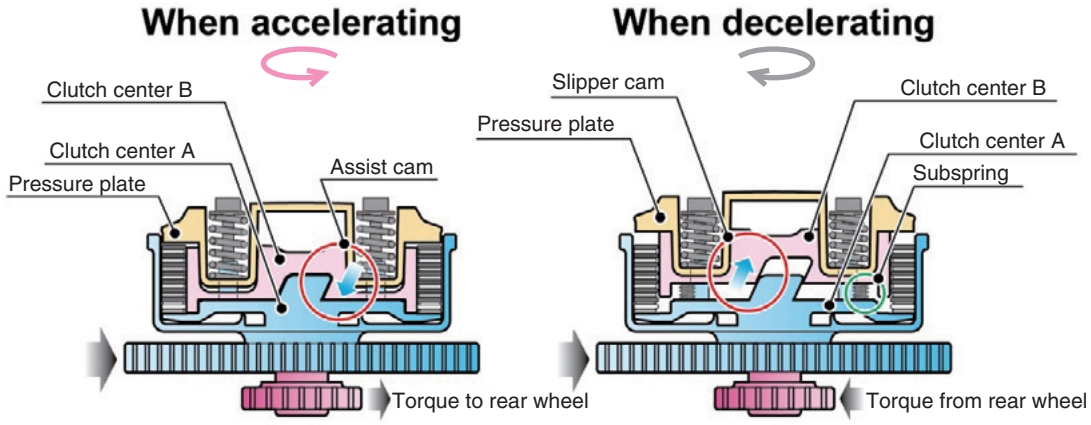


Fig. 19 Operational diagram of assist-slipper clutch

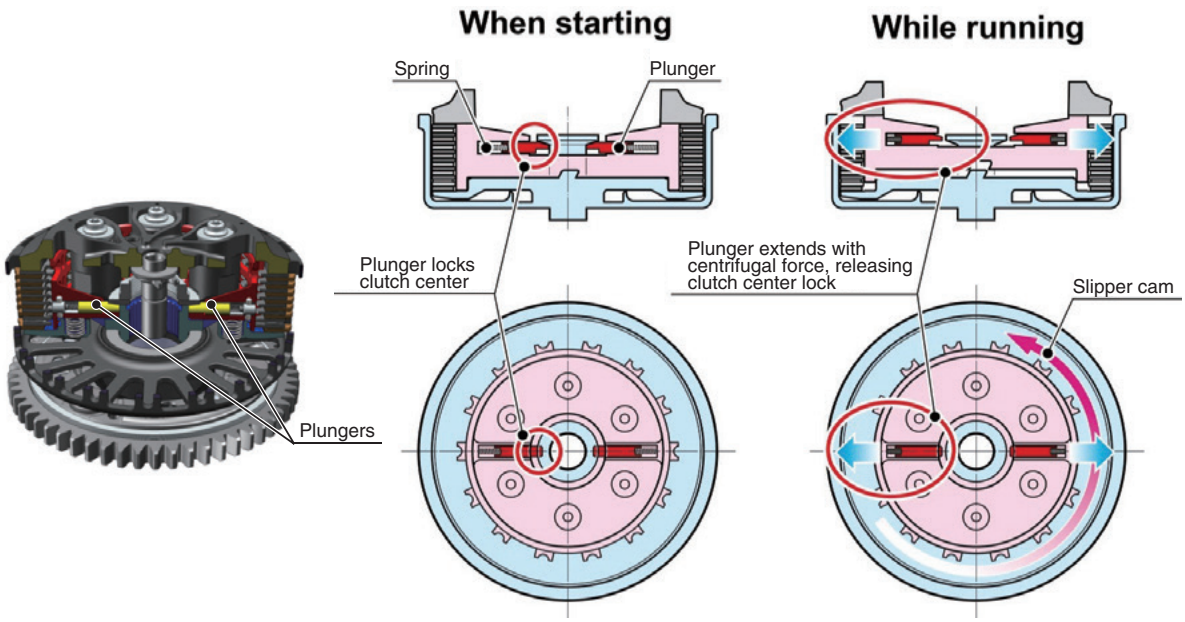


Fig. 20 Slipper cancellation mechanism for push-start

spraying of fuel on the back of intake valve faces. Another one is located above the bellmouth. Optimum injection volume and injection timing are selected for each injector. The configuration of intake system is shown in Fig. 21.

4.8. Exhaust System

There are the following issues in the exhaust system of a V4 engine.

- Front bank exhaust pipes interfere with radiator cooling fan
- Rear bank exhaust pipes interfere with rear shock and frame member

To cope with these issues, the separate color, in which the cross section gradually changes from an oval at the start of exhaust port to a true circle, is incorporated. By the employment of oval shape at the position directly under the exhaust port, the above-mentioned interference is avoided. The separate exhaust color is made of cast stainless steel SCS13 by lost-wax casting.

To make the motorcycle street legal, an expansion chamber having a volume larger than the RC213V is required to comply with the noise regulation. However, if the expansion chamber is laid outside of the cowling, an increase of air drag and/or lowering of maneuverability due to an increase of inertia moment will result. To cope with this issue, the uniquely-shaped, independent expansion chambers are employed for the front and rear cylinders. The one for the front cylinders is laid in the lower right side of motorcycle, and the one for the rear cylinders inside of the tail cowl to keep the expansion chambers within the cowl. The configuration of exhaust system is shown in Fig. 22.

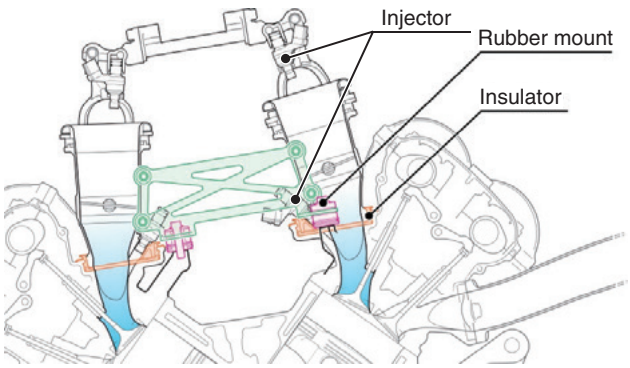


Fig. 21 Configuration of intake system

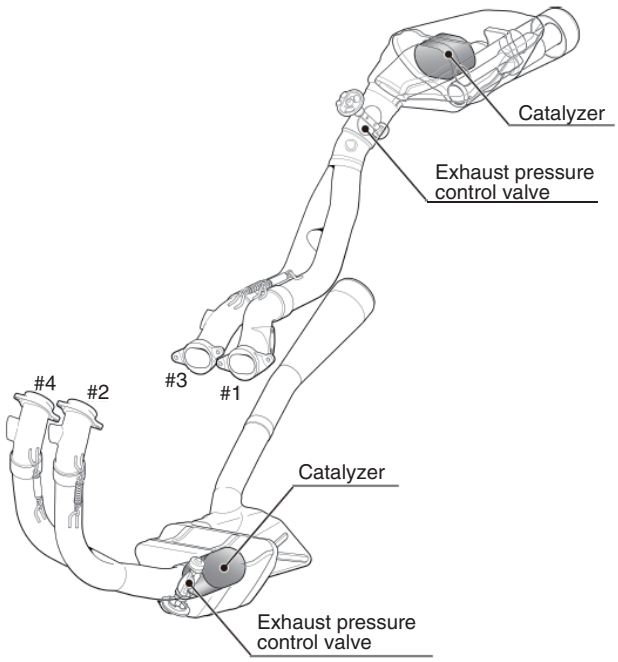


Fig. 22 Configuration of exhaust system

The variable exhaust valve, which controls pressure in the exhaust pipe, is incorporated after the exhaust pipe collector both in the front bank and the rear bank. The catalyst is located at the entrance of expansion chamber. With the above-mentioned layout employed, the same level of appearance as the RC213V has been maintained.

5. Control System

5.1. Overview of Control System

To make the RC213V "excellence of maneuverability," which is a key to winning, various control systems are incorporated for engine power management and control of motorcycle behavior. The machine characteristics can be fine-tuned to adjust to the track conditions by altering various control parameters. Moreover, a number of combinations of such parameters can be set into various riding modes. The rider rides the machine while shifting the mode depending on changes of road surface conditions and tire grip during the race. Such a mode shifting unique in racing machines is also incorporated in the RC213V-S so that the rider can experience the "excellence of maneuverability" characteristics of the RC213V even on public roads. The technical features are introduced hereafter.

5.1.1. Control system configuration

The configuration of electronic control system of the RC213V-S is shown in Fig. 23. The throttle by wire (TBW) system is incorporated in the RC213V-S to realize an electronic control derived from the RC213V. The Inertial Measurement Unit (IMU) is also incorporated to accurately detect dynamic conditions of motorcycle. The Accelerator Position Sensor (APS) is that of a grip-position type which uses no throttle cable from the standpoint of weight reduction and space saving. The Engine Control Unit (ECU)

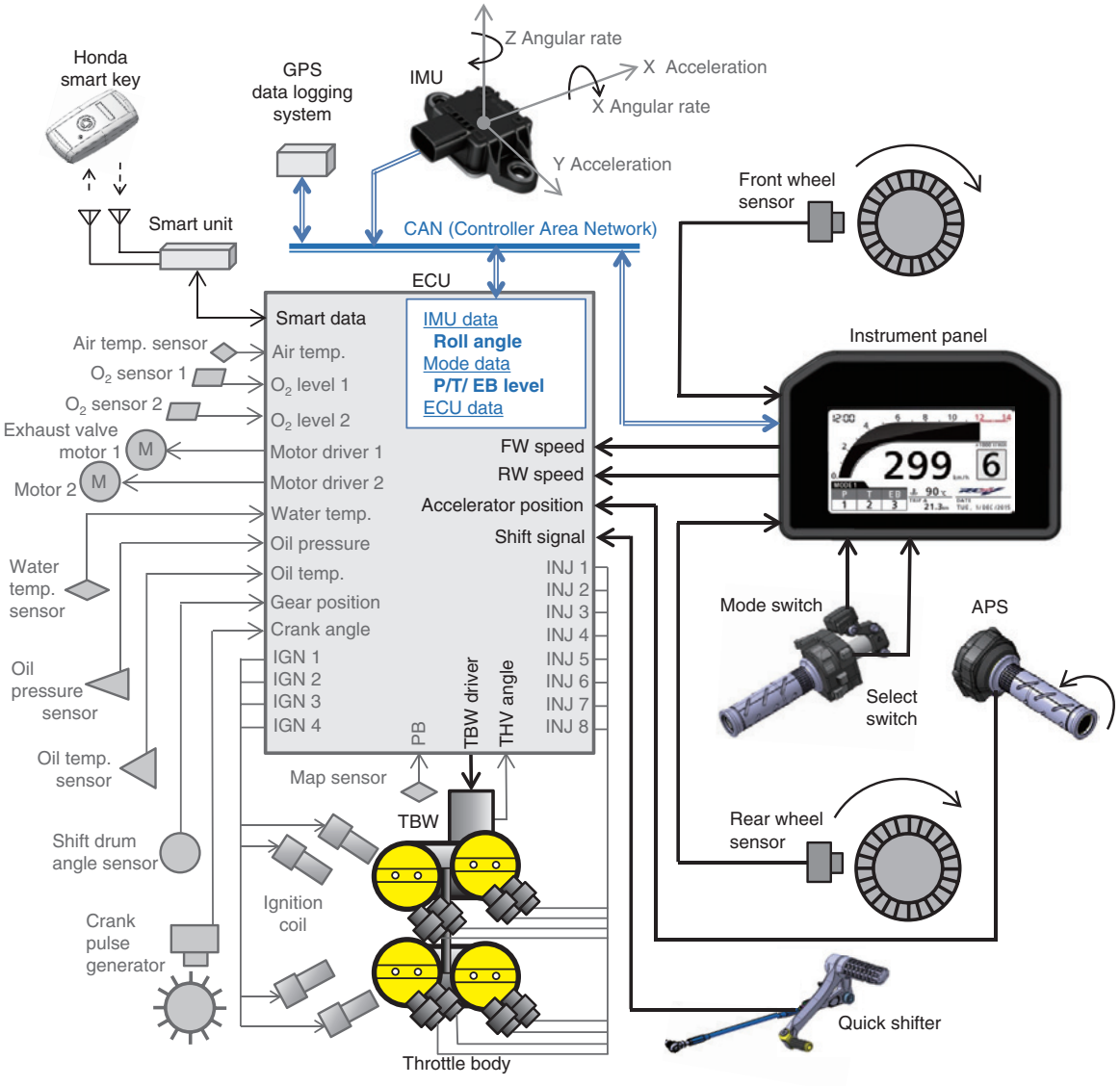


Fig. 23 Electronic control system

is newly developed from the standpoint of user-friendliness and environmental protection requirements necessary for a commercial motorcycle. Various sensors necessary for various types of control are also selected from the same standpoint.

5.1.2. Riding mode

The three systems, i.e., the power selector, the selectable torque controller, and the selectable engine brake that regulate power transmission response against rider's throttle operation are incorporated in the RC213V-S (Table 3). The system permits the rider to independently select power output characteristics from three levels (P level: 1 through 3), torque characteristics from 10 levels (T level: 0 through 9), and engine brake from 4 levels (EB level: 1 through 4). In addition to that, five riding modes in which these three parameters are preset are provided. The mode 1 is for the best surface condition with minimum intervention by the control system to take full advantage of powerful and direct engine characteristics. In the modes 2, 3, 4, and 5, the level of intervention by the control system increases in the order of number. The rider can choose any mode from 1 through 5 when riding by pressing the mode switch on the left handlebar. Moreover, the rider can freely set each parameter in each mode. This permits the rider to ride the machine to his preference in a variety of riding situation.

Table 3 Default values of riding mode

Riding mode	Engine power (P)	Torque control (T)	Engine brake (EB)
Mode 1	1	2	3
Mode 2	2	2	3
Mode 3	2	5	3
Mode 4	2	8	2
Mode 5	3	8	1
Selectable range	1 - 3	0 - 9 0: off	1 - 4

5.1.3. Power selector (P)

Image pictures of output characteristics of the power selector are shown in Fig. 24. The power selector permits selection of engine power output characteristics against throttle opening from three levels. This system achieves various levels of output characteristics by setting Throttle Valve (THV) opening characteristics against APS opening for each level. The THV opening characteristics against the APS at each power level are shown in Fig. 25.

Level 1: Allows peak power at any of the six gear positions

Level 2: Restricts engine power output by a maximum of 12% from the level 1 when APS opening is 10% or more

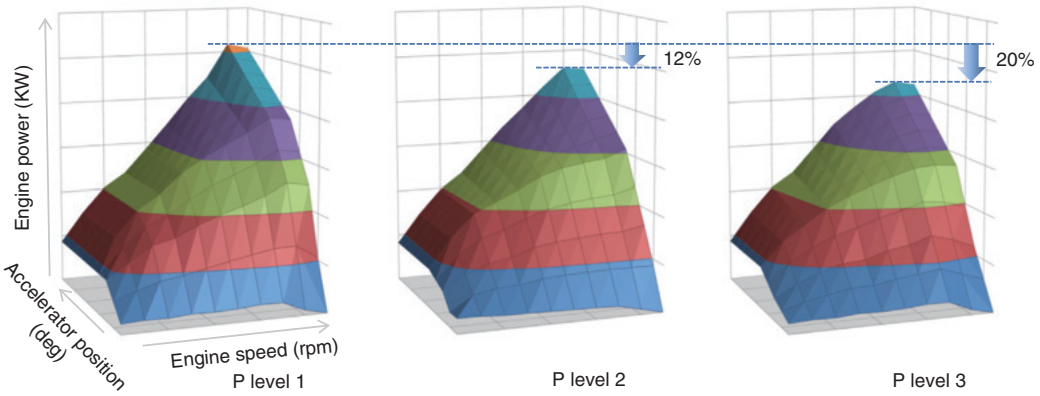


Fig. 24 Change of engine output characteristic by power selector

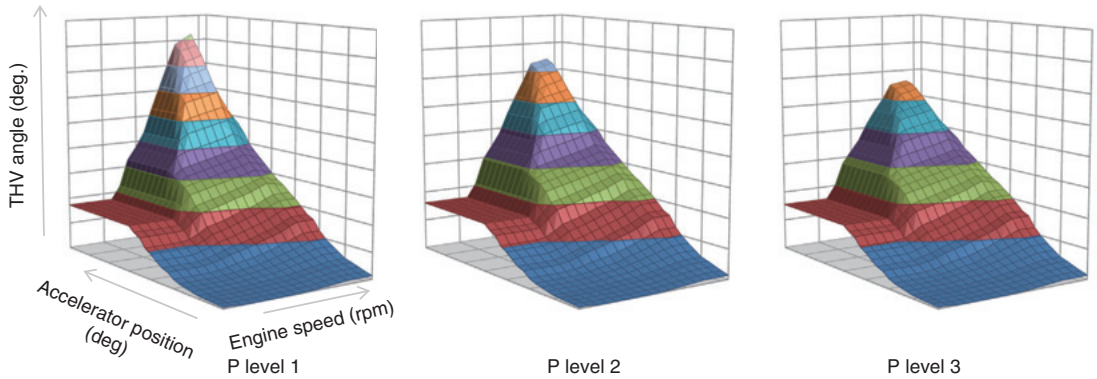


Fig. 25 Relationship between APS output and THV angle in each P level

Level 3: Restricts engine power output by a maximum of 20% in the same manner

5.1.4. Selectable torque controller

If the throttle is opened excessively when accelerating at a corner exit, the rear tire may slip causing a loss of traction and stability, which affects lap time and makes a win or loss difference. The selectable torque controller is a system that makes the motorcycle easy to ride by reducing such rear tire slippage at acceleration to maintain stability. The speed of each wheel is detected by the wheel speed sensor incorporated in the front and rear wheels. The ECU calculates rear wheel slip ratio from the wheel speeds. The ECU calculates roll angle of the motorcycle on the basis of the angular velocity and acceleration detected by the IMU, which is located in the front cowl. The ECU determines a target slip ratio from the roll angle and the APS output, and controls driving force by regulating throttle valve opening so as to converge to the target slip ratio. Thus, even if the rider opens the throttle widely, an adequate driving force as per rider's acceleration demand can be provided while controlling rear tire slippage. This system permits selection from 10 levels of torque controller intervention including OFF depending on rider's preference.

5.1.5. Selectable engine brake

The selectable engine brake is a system that permits selection of engine brake characteristics from four levels when APS is fully closed. When APS is fully closed, the throttle valve opening is regulated at a prescribed level by TBW in accordance with the engine speed. The engine brake is hardest in Level 1, and weakens as the number increases. The control map of selectable engine brake is shown in Fig. 26.

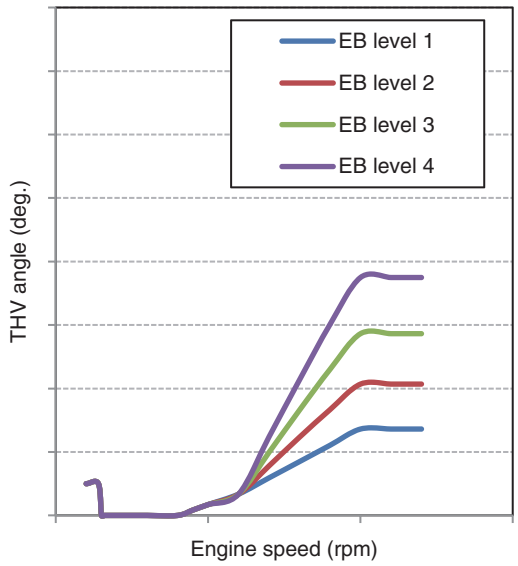


Fig. 26 Engine brake (EB) control map

5.1.6. Quick shifter

The quick shifter is employed in the RC213V-S just like in the RC213V. The quick shifter is a device that allows the rider to shift up only by a shift pedal operation without closing throttle or pulling clutch lever. When a shift up operation is detected on shift pedal, the ECU controls fuel injection volume and ignition timing. That makes possible to shift up in quick and ensured manner. The shifting operation is detected by a sensor incorporated in the shift rod. While a piezoelectric sensor is employed in the RC213V to achieve a direct feel for a racing machine, a switch is applied to the RC213V-S from the standpoint of easy maintenance.

6. Electrical Systems

6.1. Meter Display

In the RC213V, the dot-matrix, multi-function meter, which can provide necessary information only for racing upon rider's request, is employed. Meanwhile in the RC213V-S, the full-color TFT liquid crystal display (LCD) meter is employed for the first time in Honda motorcycles to allow display of abundance of information taking into account the use on public roads. The visibility in various environmental conditions is enhanced by the backlight having a maximum luminance of 1000 cd/m^2 and automatically adjusting luminance depending on the ambient brightness. Presuming that the rider switches LCD display depending on the situation, two display formats, i.e., the street format that displays speed in the middle, and the circuit format that indicates lap time in the middle, are incorporated. The displays of riding mode and the level of each control parameter, i.e., power (P), torque (T) and engine brake (EB) are gathered together and laid in the lower left part of screen for easy recognition when running. In addition to the lap time measurement by tapping the switch on the handlebar, the lap time can be measured and displayed automatically by the attached GPS data logging system, and recorded in the USB memory. The lap time can be retrieved and shown on the meter display after driving. After downloading recorded data to a computer from the USB memory, data of each lap including various vehicle information such as the throttle opening, engine speed etc. can be inspected using the custom application. Other functions derived from the RC213V include the mechanic format and the shift up indicator. The mechanic format permits data display when stopping by a switch operation, allowing monitoring of conditions such as the water temperature, oil temperature, oil pressure, etc. when the rider or mechanic inspects the machine or warms up the engine. The shift-up indicator is a device that notifies the rider of proper shift-up timing so that the rider can efficiently accelerate the machine. To make the indicator recognizable even when the rider is staring ahead, high-luminance LEDs are lined up horizontally in the upper part of meter. The shift-up point can be set at any engine speed

between 4000 rpm and 14000 rpm with an increment of 200 rpm. When the engine speed reaches the preset level during acceleration, the indicator turns from glowing to blinking to urge shift up. External view of the instrument panel and the display formats are shown in Fig. 27.

6.2. Honda Smart Key

The Honda smart key system for electronic identification between the vehicle and the key is employed in the RC213V-S (Fig. 28). This system allows the user to turn on ignition without using a conventional mechanical key. As a key cylinder is eliminated from the upper triple clamp, the same cockpit view as the RC213V is realized. Also, as the rider can start the engine just by a press of the start button, a series of operations to start riding has become smooth.

It should however be noted that the steering lock and the fuel filler lock are still by a mechanical key for weight reduction purposes. The mechanical keys for steering lock and fuel filler lock are stored in the Honda smart key for user convenience.



Fig. 27 Instrument panel and display formats

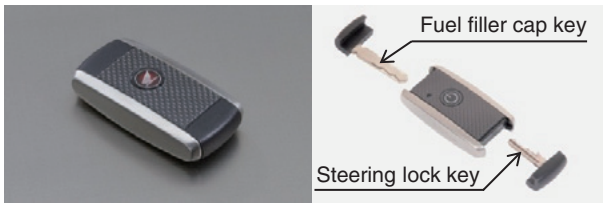


Fig. 28 Honda smart key

7. Conclusion

The RC213V-S fully reproduces the “fun to ride” characteristics attainable from the complete package and the handling of the MotoGP racing machine RC213V. Accordingly, it is now possible for an ordinary rider to experience its benefits on public roads regardless of the speed. Various technical innovations acquired through the development of this motorcycle can be applied to future motorcycles in due orders, thereby offering motorcycles having new features to the market.

References

(1) Kadomasu, H.: Presentation of RC211V Equipped with 4-stroke Engine, Honda R&D Technical Review, Vol. 15, No. 2, p. 17-24

■ Author ■


Hiroshi UNUKI


Ryuji TSUCHIYA


Hodaka MUKOUHARA


Naoki MURASAWA


Satoru OKOSHI

New In-Line 4-Cylinder Gasoline Direct Injection Turbocharged Downsizing Engine

Koji NAKANO* Yusuke WADA*
Mitsutaka JONO* Shigeru NARIHIRO*

ABSTRACT

Two new models of in-line four-cylinder VTEC turbo engine have been developed as part of the cluster of new-generation power train technologies known as EARTH DREAMS TECHNOLOGY, which achieves a high-level balance between driving performance and fuel consumption. Both VTEC engines use high-tumble ports, valve timing control (dual VTC) of both intake and exhaust camshafts, multi-hole direct side injectors, and high-response turbochargers with attached electric waste gate actuator. With these technologies in common, the new engines successfully yield maximum thermal efficiency and power through cooperative control and turbocharging conditions based on combustion technology that uses high-tumble flow. The 1.5 L engine puts out the same 110 kW of maximum power as the 2.0 L naturally aspirated engine while increasing low- and medium-speed torque by a maximum of 30%. A vehicle with this engine installed achieved fuel consumption of 17 km/L in JC08 mode, which puts it at the top of the minivan class, and a 75% reduction relative to the level required by Japanese 2005 regulations for exhaust emissions. As a high-powered sport engine, the 2.0 L model achieves maximum output of 228 kW and maximum torque of 400 Nm. A vehicle with this engine installed achieved CO_2 emissions of 170 g/km in European fuel economy mode and Euro 6b compliance.

1. Introduction

Target values for fuel economy regulations have been set to be met in developed countries in North America, Europe, and elsewhere from 2020 to 2025, and in developing countries by 2015. As a technology that achieves a balance between compliance with those fuel economy regulations and product competitiveness, the downsizing turbocharged engine is being developed by OEM manufacturers in Europe, in particular, and is being marketed in Europe, the United States, and China. Honda has also issued press releases announcing global marketing of VTEC TURBO variations that are part of the cluster of new-generation power train technologies known as EARTH DREAMS TECHNOLOGY, which achieve a balance of driving performance and fuel consumption. The VTEC turbo engine provides greater torque, and it can achieve dynamic performance matched to the vehicle class even with a smaller displacement than naturally aspirated (NA) engines. The reduction of engine friction also makes it possible to increase fuel economy.

This VTEC turbo engine is scheduled for global marketing, to include the Europe market, and it is positioned as a world strategy engine intended to contribute to heightened fuel economy and increased product competitiveness. Figure 1 shows the EARTH DREAMS TECHNOLOGY line-up and the positioning of the two types of developed engine described herein.

This paper will introduce the applications of these technologies and the performance they achieve.



Fig. 1 EARTH DREAMS TECHNOLOGY

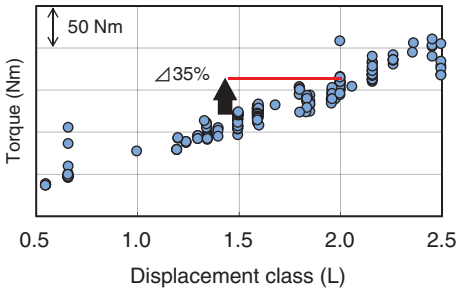
* Automobile R&D Center

2. Development Aims

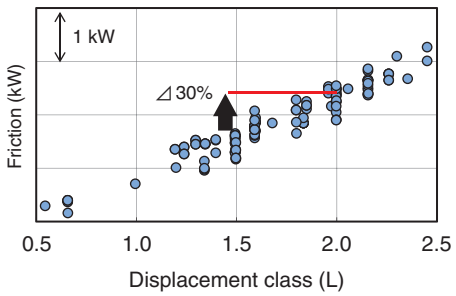
The main aim of the downsizing turbocharged engine is to heighten fuel economy[1), 2)]. Reducing displacement and actively using the high-load range at low engine speeds can lower the proportion of torque required for driving that is engine friction, thereby heightening fuel economy. The tendency of torque in the range of actual use as it differs with different engine displacements is shown in Fig. 2(a) and the tendency of friction at normal engine speeds is likewise shown in Fig. 2(b). On the one hand, these tendencies suggest that when engine displacement is changed from 2.0 L to 1.5 L, friction can be expected to decrease by approximately 30%, and fuel economy to increase. On the other hand, an increase of approximately 35% or more in torque will be required in order to maintain the same level of practical performance. That is why the engine is combined with a highly efficient turbocharger that yields effective turbocharged pressure in the low engine speed range to produce that part of the power accounted for by the reduced displacement.

In order to be competitive on the downsizing turbocharger market where European OEM manufacturers have gone first, development was carried out with the aim of achieving the top category in its class by balancing fuel economy, power, emissions (EM), and cost.

The newly developed 1.5 L downsizing turbocharged engine was intended to replace 1.8 L to 2.0 L displacement class NA engines. A compact turbocharger that delivers good response with peak torque from low engine speeds was selected, and the aim of development was defined as simultaneously achieving acceleration performance for ease of handling on city streets and top level power performance in its class together with low fuel consumption and low emissions.



(a) 2000 rpm wide open throttle engine



(b) 1500 rpm friction (partial)

Fig. 2 Improved fuel efficiency by downsizing turbo

The development objectives for the 1.5 L downsizing turbocharged engine were:

(1) A balance of high power and high torque at low engine speeds
(2) Low fuel consumption and low emissions at the top level in its class

The newly developed 2.0 L downsizing turbocharged engine, as a high-powered sport engine, was equipped with a large turbocharger. The aim of development was defined as achieving a balance between the world's highest speed for a front-engine, front-drive vehicle, based on lap times on the Nürburgring circuit, and excellent environmental performance.

The development objective for the 2.0 L downsizing turbocharged engine was to achieve a balance between the top class of per-liter power in the world and environmental performance.

3. Main Engine Specifications

The 1.5 L and 2.0 L VTEC turbo engines were made with the same bore pitch and other main specifications, and with the same block structure as the updated NA engine[3)]. At the same time, the specifications were configured with the optimal combustion concept for turbocharged engines as the basis.

In a turbocharged engine, the rise in temperature of the compressed air-fuel mixture makes knocking more likely to occur, and even if the ignition timing is retarded for that reason because of the rapid combustion, it becomes important to obtain stable combustion. Therefore a high-tumble port was adopted to generate stronger tumble motion inside the cylinder and heighten the turbulent kinetic energy, and the piston crown was shaped so that the high tumble flow could be maintained until close to compression top dead center. The main combustion system was also configured with a multi-hole direct injector to form a homogeneous air-fuel mixture while limiting its adhesion to the surfaces of the piston and sleeve wall and with dual-VTC for optimal control of the scavenging effect and the amount of internal exhaust gas recirculation (EGR). Combining this with a high-response turbocharger achieved higher thermal efficiency and higher output.

The engines were matched to the requirements of the vehicles in which they are installed, and in the case of the 1.5 L type, the emphasis was placed on ease of handling on city streets and economy, and priority was therefore given to high low-speed torque and low fuel consumption. The 2.0 L turbocharged engine to be installed in the CIVIC TYPE R was configured with specifications to achieve maximum power performance

Table 1 Engine specifications

Engine type	1.5 L		2.0 L	
	Developed	BASE	Developed	BASE
Cylinder configuration	In-line 4-cylinder	In-line 4-cylinder	In-line 4-cylinder	In-line 4-cylinder
Bore x Stroke (mm)	73 × 89.4	73 × 89.4	86 × 85.9	86 × 86
Displacement (cm^3)	1496	1496	1996	1998
Aspiration	Turbocharged	Natural	Turbocharged	Natural
Turbin/Compressor diameter (mm)	37/46	no	47/58	
Crank journal diameter (mm)	46	46	55	55
Compression ratio	10.6	11.5	9.8	11.0
Valve train	DOHC In-Ex VTC	DOHCi-VTEC In VTC	DOHC In-Ex VTC	DOHC VTEC In-Ex VTC
Number of valves	4 per cylinder	4 per cylinder	4 per cylinder	4 per cylinder
Valve diameter (mm) Intake/exhaust	28/23	29/25	35/29	35/30
Engine oil	0W-20	0W-20	0W-20	5W-30
Fuel injection type	DI	DI	DI	PI
Fuel	RON91	RON91	RON95	RON95
Maximum Power (kW/rpm)	130/5500	97/6600	228/6500	148/7800
Maximum Torque (Nm/rpm)	230/1600-5000	155/4600	400/2500-4000	193/5600
Maximum thermal efficiency (%)	38.0	34.8	36.6	*

while maintaining a high level of environmental performance as a high-powered sport engine. Table 1 shows the main specifications of the engines.

The 1.5 L type runs on regular gasoline but has a compression ratio of 10.6, and achieves a high level of environmental performance with maximum thermal efficiency of 38% together with maximum torque of 203 Nm from 1600 rpm for low-speed characteristics that are favorable for usability on city streets. The 2.0 L type was equipped with a larger turbocharger in order to realize the top class of per-liter power in the world with maximum power of 228 kW, while at the same time achieving a balance with high-level environmental performance with maximum thermal efficiency of 36.6%.

Figure 3 shows comparisons of each engine with the base NA engine in terms of power performance. The 1.5 L type was a replacement for the 2.0 L NA engine, but it has the same maximum power of 110 kW while yielding low and medium-speed torque that is a maximum of 30% higher. In the case of the 2.0 L turbocharged engine, the base NA engine for the CIVIC TYPE R is a 2.0 L engine, so heightened performance was achieved in all areas with power 50% higher at maximum and torque 100% higher.

The substance of the technology adopted in order to achieve the balance of power performance and environmental performance described to this point will be described below.

4. Achieved Technology

4.1. Rapid Combustion Technology

In order to suppress knocking and enable high-load operation with a direct injection turbocharged engine, as well as to take steps to promote the evaporation of direct injected fuel and to make the air-fuel mixture homogeneous, and also to satisfy particulate matter (PM) regulations, it is important to strengthen the tumble motion inside the pipe. Ordinarily, tumble flow is strengthened by narrowing down the area of the intake port to increase the flow velocity inside the intake port, but this lowers the flow coefficient. Since the engine is also required to output power at high engine speeds, this requires enhancing the flow coefficient while maintaining the high-tumble flow. This optimization was carried out using CFD.

Figure 4 shows the differences in intake port and piston shape between the naturally aspirated and turbocharged 1.5 L engines.

The intake port lies closer to the horizontal than the angle of the port in the NA engine to realize an intake flow that follows the pentroof shape. The edge of the port at the bottom side (A in Fig. 4) is raised more toward the perpendicular, and this suppresses the opposing tumble flow inward from the opposite direction, limiting the lowering of the flow coefficient while realizing a high tumble ratio. Steps were then taken for rapid combustion by adopting a piston top with a shape that smoothly reverses the main tumble flow in the piston direction that occurs during the intake stroke and maintains the tumble flow until close to compression top dead center. Figure 5 shows the flow pattern in the cylinder at an engine speed of 1500 rpm and wide-open throttle as sought using CFD (VECTIS Ver. 3.12 from Ricardo). Figure 6 shows a comparison of the tumble ratio and turbulent kinetic energy.

A powerful flow in the direction of the piston was observed to form during the first half of the intake stroke (crank angle of 100 deg). This flow is reversed by the shallow-dish shape of the piston crown, forming a tumble flow. Tumble vortices observed during the compression stroke (crank angle of 270 deg) are flattened down into

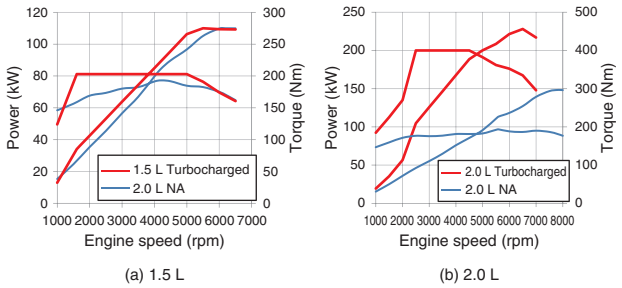


Fig. 3 Comparison of performance curve

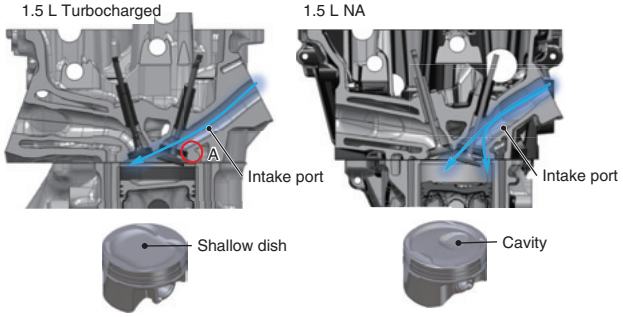


Fig. 4 Comparison of intake port and piston shape

the pentroof, are held there from 60 deg to 0 deg before top dead center, are converted into turbulent kinetic energy (turbulence), and promote flame propagation combustion. The turbulent kinetic energy near compression top dead center has approximately twice the value of the corresponding energy in an NA engine.

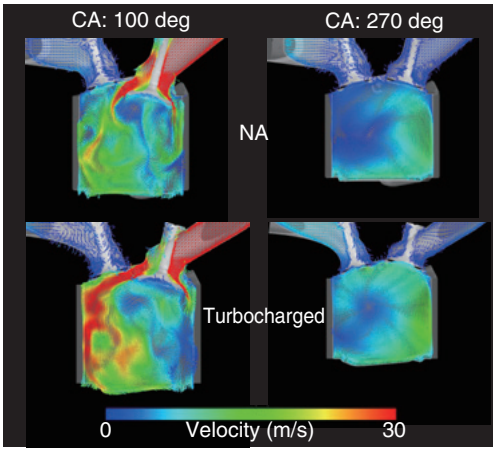


Fig. 5 In-cylinder flow pattern (1500 rpm motoring)

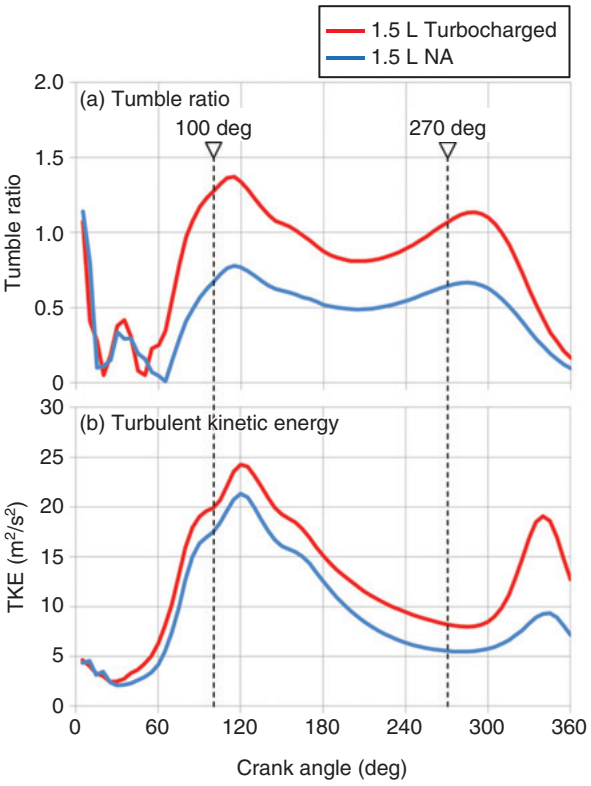


Fig. 6 In-cylinder flow pattern (1500 rpm motoring)

Table 2 Turbocharger specifications

		1.5 L	2.0 L
Turbocharger supplier		Mitsubishi	Mitsubishi
Turbine	Scrawl	Mono	Mono
	Wheel Diameter/Vane	ϕ37/11	ϕ47/11
	Permissible speed	245000 rpm	195000 rpm
	Housing material	A3K (austenitic cast steel)	A3K (austenitic cast steel)
Compressor	Wheel Diameter/Vane	ϕ46/6+6	ϕ58/6+6
	Permissible speed	241000 rpm	191000 rpm
Waste gate	Actuator	Electronic	Electronic
	Valve diameter	ϕ28	ϕ35

4.2. Turbocharger Technology

Single-scroll-type turbochargers were adopted and their optimal specifications were chosen according to their performance targets.

A cylinder head with integrated exhaust port was adopted for highly efficient cooling of exhaust gases together with a turbine housing made of cast stainless steel for high heat resistance. The aim was to raise high-load fuel economy by expanding the range in which driving in stoichiometric mode is possible. This established specifications capable of withstanding exhaust gases at temperatures up to 950°C without relying on enriching the air-fuel ratio to lower the exhaust gas temperature, even when the exhaust gases are at high temperatures. A newly developed electric waste gate actuator (E-W/G ACT.) was adopted as a means for heightening fuel economy under low-load conditions.

Table 2 shows the turbocharger specifications for each engine, and Fig. 7 shows an external view of the turbocharger. The 1.5 L type was configured as a compact turbocharger that emphasizes high torque and response from low engine speeds. For the 2.0 L type, a size was chosen to provide flow volume that satisfies the requirement for 228 kW power output. The compressor

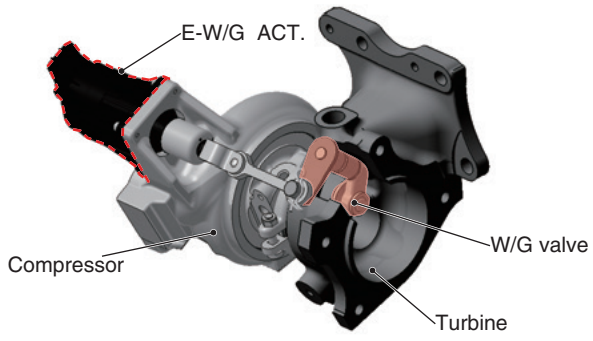


Fig. 7 Turbocharger assembly

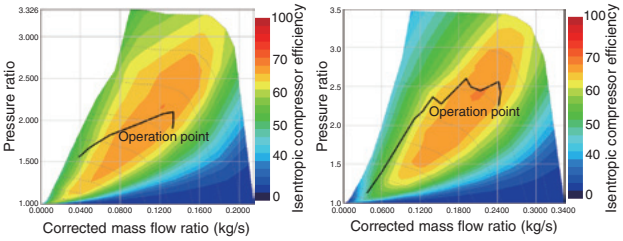
map for the 1.5 L engine is shown in Fig. 8(a) and for the 2.0 L engine in Fig. 8(b). The compressors were adopted each with its own broad flow volume range characteristics, allowing for an extra margin in the surge limit and speed limit with regard to operation points.

Figure 9 shows the E-W/G ACT. The E-W/G ACT. has a screw lead system in the thrust transmission unit of the waste gate valve (W/G valve) to provide greater retention by means of friction. Consequently, it is capable of retention with a smaller holding current even when the exhaust pressure is high.

The adoption of an E-W/G ACT. made it possible to set up and control the optimal turbocharged pressure by making use of the degree of freedom in opening and closing the W/G valve [Fig. 10(a)]. In the NA range, the W/G valve is set wide open to limit the difference between the pressure in the exhaust manifold and the pressure after the turbine. The reduction in the exhaust pumping loss yielded greater fuel economy. Cooperative control of the intake throttle and W/G valve aperture also generated torque according to the vehicle demand, and when it is excessive, the intake throttle aperture and W/G valve aperture are controlled according to the target turbocharged pressure, enhancing response [Fig. 10(b)].

With the former, positive-pressure W/G valve, the valve could not be opened unless the intake pressure (PBA) matched or exceeded the W/G valve set pressure. Consequently, the valve could not be opened in the NA high engine speed range, where the PBA is close to atmospheric pressure. The turbocharger was therefore made to do unproductive work, causing exhaust pressure to rise and increasing the pumping loss. Here, the adoption of an E-W/G ACT. avoids this issue (Fig. 11).

Figure 12 shows the rate of decrease in brake specific fuel consumption (BSFC) due to adoption of



(a) 1.5-L compressor efficiency map (b) 2.0-L compressor efficiency map

Fig. 8 Compressor efficiency map

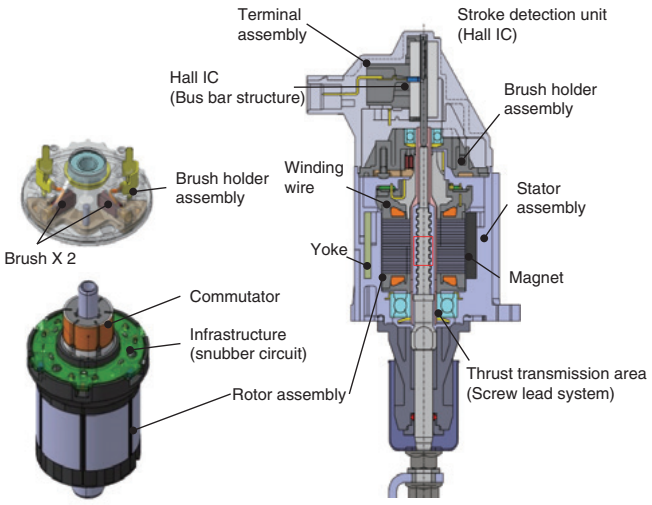
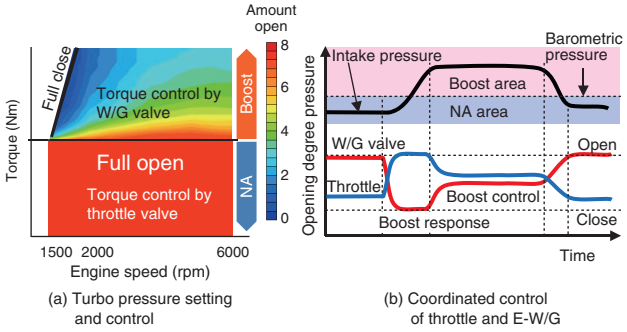


Fig. 9 E-W/G ACT.



(a) Turbo pressure setting and control (b) Coordinated control of throttle and E-W/G

Fig. 10 Coordinated control

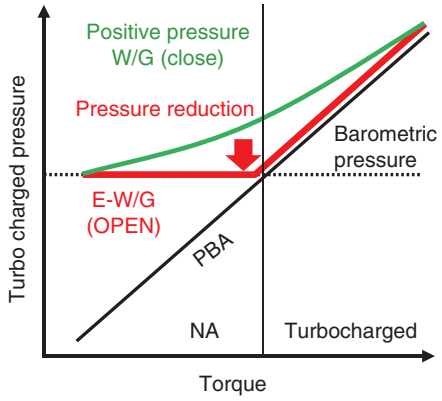


Fig. 11 Comparison of W/G valve specification

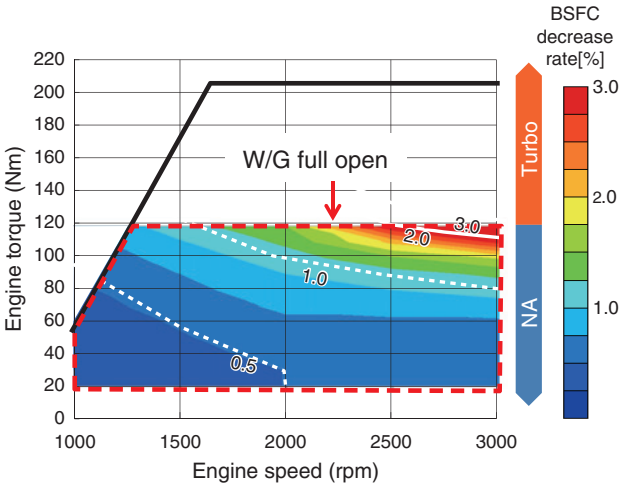


Fig. 12 BSFC decrease map

the E-W/G ACT. In the NA range, the positive impact on BSFC becomes greater on the higher engine speed side, where the exhaust flow increases, reaching a maximum of 3.0%.

4.3. Dual VTC Technology

Dual VTC was adopted for the 1.5 L type while the 2.0 L type additionally adopted VTEC on the exhaust side. Figure 13 shows some typical operating regions, and the following describes the use of valve timing control in these regions.

4.3.1. Low engine speed, high-load range

The region shown as (1) in Fig. 13 contributes greatly to response when a vehicle starts moving from a stop, and it requires greater low-speed torque. It is effective in that case to take advantage of the scavenging effect that uses the unique turbocharger condition in which the intake pressure is higher than the exhaust pressure. When the intake and exhaust valve overlaps are set larger under conditions where intake pressure is relatively high, the residual gas in the cylinder is scavenged to the exhaust system, and this can raise charging efficiency and suppress knocking (area (a) in Fig. 14).

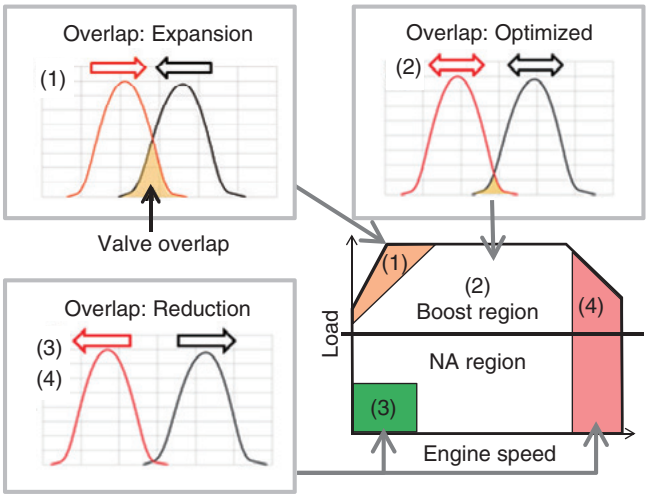


Fig. 13 Dual-VTC strategy

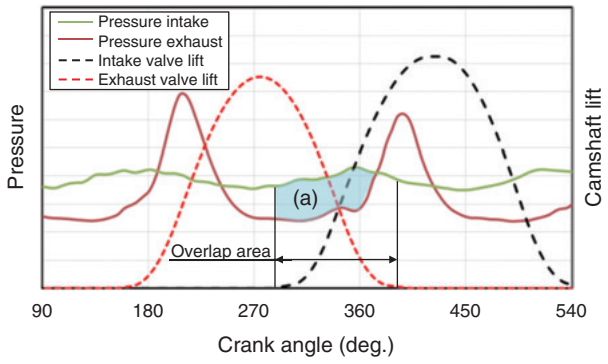


Fig. 14 Intake, exhaust pressure and scavenging area

At the same time, the increased gas flow due to scavenging can increase the turbine speed, yielding a 30% increase in torque at 1500 rpm relative to the 2.0 L NA engine.

Figure 15 shows a comparison of the pressure diagrams for the 2.0 L NA base engine and the 1.5 L turbocharged engine under full load at 1500 rpm. The decrease in stroke volume caused by downsizing is compensated for by the turbocharged pressure, so that high pressure is generated in a small stroke volume. The ignition timing is retarded in order to avoid the knocking due to increased pressure from turbocharging, but the rapid combustion produces a higher rate of heat release, which enables a higher indicated mean effective pressure (IMEP).

4.3.2. Medium engine speed range

In the medium to high engine speed range shown in graph (2) in Fig. 13, gradually reducing the overlap limits the increase in residual gas that accompanies increased exhaust pressure. When driving under acceleration, immediately controlling the electric waste gate valve to close completely makes it possible to raise the turbocharged pressure effectively.

4.3.3. Low vehicle speed and low engine speed range and high power range

In the low vehicle speed and low engine speed range shown in graph (3) in Fig. 13, the overlaps are reduced in order to heighten combustion stability by reducing the internal EGR amount as well as to lower exhaust resistance in the high-speed range at (4) and heighten knocking resistance.

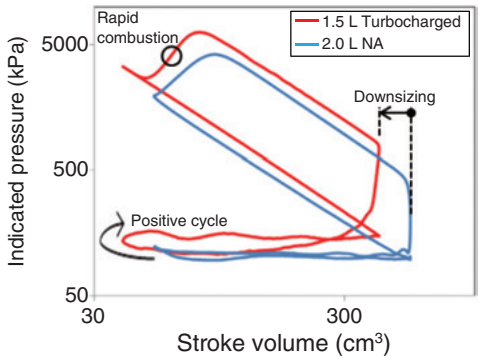


Fig. 15 Comparison of P-V diagram (1500 rpm WOT)

5. Fuel Consumption and Emissions

5.1. Fuel Consumption

Figure 16 shows the separate fuel consumption characteristics of each engine. The 1.5 L engine achieves the lowest BSFC of 220 g/kWh, and the 2.0 L engine achieves the lowest BSFC of 230 g/kWh. Comparison

with the separate fuel consumption characteristics of the 2.0 L NA engine, shown for reference at (b) in the figure, indicates not only that both the 1.5 L and 2.0 L engines have more favorable maximum efficiency point values, but that they have a broader range of higher efficiency.

The downsizing turbocharged engine can make active use of low engine speed and high-load operation. Therefore it is important to reduce fuel consumption in this range. Taking the 1.5 L engine as an example, Fig. 17 shows the breakdown of BSFC reduction under full load at 1500 rpm compared to the 2.0 L NA engine. In the case of the NA engine, the air-fuel ratio is set richer in order to increase power at wide-open throttle, and this avoids knocking. The downsizing turbocharged engine, on the other hand, increases its knocking resistance by means of rapid combustion and the scavenging effect, and therefore it can be operated stoichiometrically. Stoichiometric operation contributes 75% of the BSFC reduction effects, which is larger than cooling loss and pumping loss at 24% and friction reduction at 1%. Control of the internal EGR amount by dual VTC and stable combustion by means of a high-tumble flow also reduce pumping loss and yield lower fuel consumption across a wide load range up to the medium-load range. A 2015 model STEPWGN with this engine installed achieved fuel consumption of 17 km/L in JC08 mode, which puts it at the top of the minivan class. By means of similar technology, a vehicle with the 2.0 L engine installed achieved CO_2 emissions of 170 g/km in European fuel economy mode.

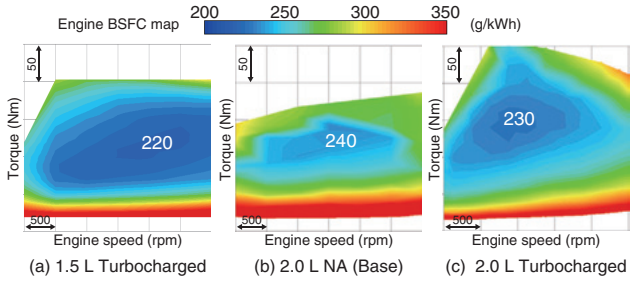


Fig. 16 Comparison of BSFC maps

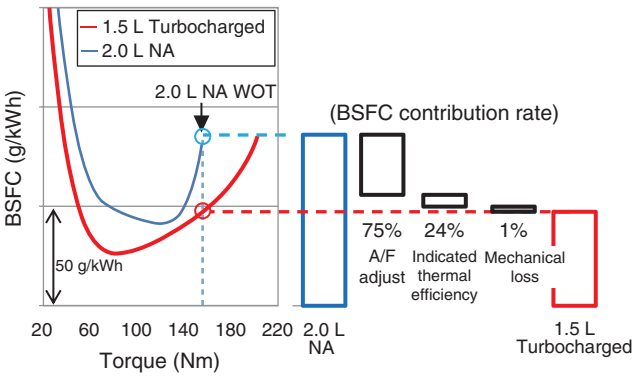
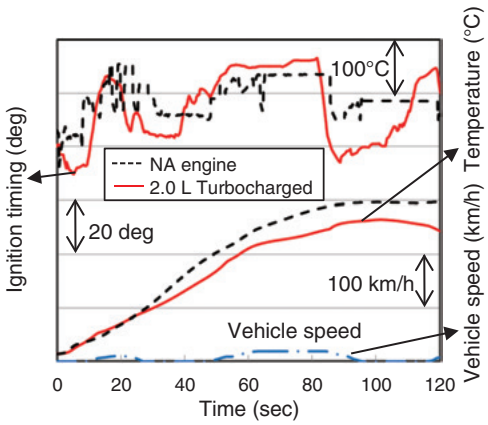


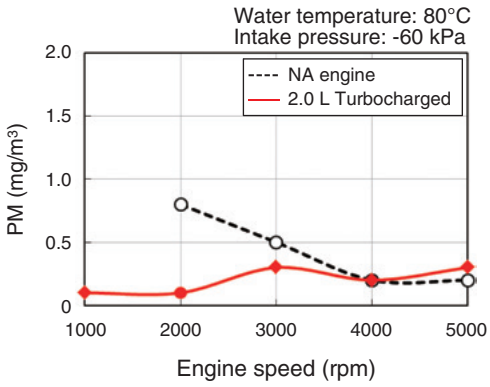
Fig. 17 Breakdown of BSFC reduction (1500 rpm WOT)

5.2. Low Emissions

In catalyst warm-up mode in a turbocharged engine, the increased heat mass due to the turbocharger becomes an issue. By contrast, the higher combustion stability gained by the use of a high-tumble port makes it possible to enlarge the valve overlap to introduce hot internal EGR into the combustion chamber, and this yields promotion of fuel evaporation. The ignition timing can also be retarded by comparison with the NA engine, making it possible to achieve a rise in catalyst temperature sufficient for application of Euro 6b [Fig. 18(a)]. With regard to soot emission performance after the engine is completely warmed up, the high-tumble flow and fuel injection pressure of 20 MPa together with optimal injection timing also successfully reduce the adhesion of fuel in the cylinder. Figure 18(b) shows measurement data for the 2.0 L engine. This engine achieved Euro 6b compliance by soot emission performance equal to or better than a mass-production direct injection NA engine. Using similar technology, the 1.5 L engine achieved a 75% reduction relative to the level required by Japanese 2005 regulations for exhaust emissions.



(a) Catalytic activity temperature comparison



(b) PM comparison

Fig. 18 Emission measurement data

6. Conclusion

A turbocharged downsizing engine employing a wide-range turbocharger with electric waste gate actuator, dual VTC, multi-hole direct side injector, and high-tumble port producing high-tumble flow was developed and obtained the following results.

(1) The 1.5 L engine raised low and medium-speed torque by a maximum of 30% relative to the 2.0 L NA engine while maintaining maximum power of 110 kW. A vehicle with this engine installed achieved fuel consumption of 17 km/L in JC08 mode, which puts it at the top of the minivan class, and a 75% reduction relative to the level required by Japanese 2005 regulations for exhaust emissions.

(2) As a high-powered sport engine, the 2.0 L engine achieved maximum output of 228 kW and maximum torque of 400 Nm. A vehicle with this engine installed achieved CO_2 emissions of 170 g/km in European fuel economy mode and Euro 6b compliance.

References

(1) Petitjean, D., Bernardini, L., Middlemass, C., Shahed, S. M.: Advanced Gasoline Engine Turbocharging Technology for Fuel economy Improvements, SAE Technical Paper, 2004-01-0988, (2004)

(2) Shahed, S. M., Bauer, K.: Parametric Studies of the Impact of Turbocharging on Gasoline Engine Downsizing, SAE Technical Paper, 2009-01-1472, (2009)

(3) Suzuki, M., Hayakawa, S., Ishihaya, Y., Shindo, T.: Development of the New L4 Gasoline Engine for Compact Cars, JSAE Annual Congress Proceedings, No. 91-14, p.9-12, (2014)

■ Author ■


Koji NAKANO


Yusuke WADA


Mitsutaka JONO


Shigeru NARIHIRO

6-Speed Manual Transmission for Honda S660

Masaaki IWASAKI* Takuya HOSOKAWA* Dohta YAMAMOTO*

ABSTRACT

A six-speed manual transmission has been newly developed for use in the new model S660 two-seater open-top sports car.

The new transmission was developed as a compact six-speed manual that nevertheless can support up to 104 Nm of maximum input torque.

In order to take advantage of the engine characteristics, the gear ratios for the first five speeds were configured with close ratios. The sixth gear was configured with a cruise ratio to enhance the quietness of the cabin when cruising at high speeds.

The shift was configured with a short stroke to enable the quick handling of a sports car, and the load displacement characteristics during gear shift operation were optimized. This produced a smooth, moderate gear change feeling when shifting gears.

The noise caused by rotational speed fluctuation of the crankshaft, which is characteristic of three-cylinder engines, was reduced through the adoption of a no-backlash gear and friction washer.

1. Introduction

Manual transmissions for Honda's K-cars (mini-vehicles) include a five-speed manual transmission (K-car 5MT) that is teamed with a 0.66-L naturally aspirated engine (maximum torque of 59 Nm).

The S660, by contrast, is equipped with a 0.66-L boost engine, requiring a new manual transmission with the strength and endurance to support a maximum torque of 104 Nm.

In developing this new transmission, it was decided to make it a six-speed manual transmission (new model 6MT), the first such for a K-car, in order to make advantageous use of the engine's power and torque. Development of this new model 6MT also sought to realize a light, sporty gear change feeling. This paper will introduce technological features of the new model 6MT.

2. Development Goals

The S660 development concepts include the joy of driving and the joy of handling. In order for the transmission to realize these concepts, the following goals were specified in development of the new model 6MT.

(1) Compact 6MT that can support an engine with maximum torque of 104 Nm
(2) Gear ratios for six speeds configured to achieve a balance between performance on winding roads and quiet in the cabin when cruising at high speed
(3) A smooth gear change feeling with a sense of agility and moderation when changing gears
(4) Limit the noise and vibration (NV) of a three-cylinder engine

3. Basic Construction and Gear Ratio Settings

Table 1 shows the main specifications. Figure 1 shows a cross-section view of the transmission, and Fig. 2 shows a perspective view.

The gear train is a parallel dual-shaft configuration with one counter shaft for the input shaft. Reverse gear was made a selectable sliding configuration. In order to enhance transmission efficiency, splashing-type lubrication was adopted. In order to limit the influence of rotational speed fluctuation in the three-cylinder engine, a no-backlash gear (NB gear) was adopted for the first- and second-gear counter gears.

The input shaft and output shaft were positioned vertically one above the other in order to fit the new model 6MT into the limited space of the engine compartment.

Use of this vertical arrangement introduced the possibility that splashing-type lubrication might prove inadequate for both input and counter shafts since they are farther from the oil surface at the bottom of the transmission. Addressing this by increasing the volume of oil would not only increase the weight, it would also increase oil stirring resistance and therefore reduce

* Automobile R&D Center

Table 1 Specifications of developed 6MT

Transmission type		6-speed Manual	5-speed Manual
Torque capacity [Nm]		104	59
Dimension overall length [mm]		340	319
Shaft axis distance [mm]	Input-Counter	65	60
	Counter-Final	112	110
Oil amount [L]		1.4	1.3

transmission efficiency. The issue was resolved by placing an oil separator plate between the transmission case and the clutch case to make a two-level oil surface structure by which the transmission case wall forms an oil reservoir below the counter shaft (Fig. 2).

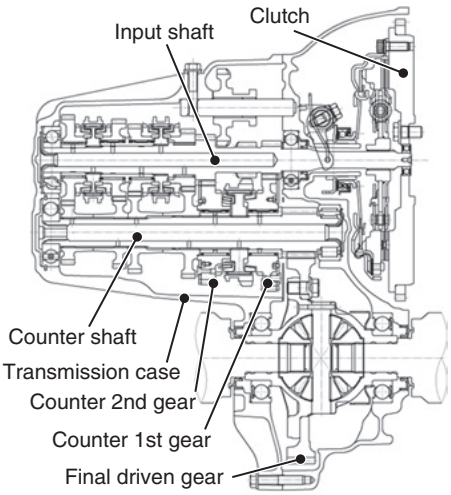


Fig. 1 Cross-section view of developed 6MT

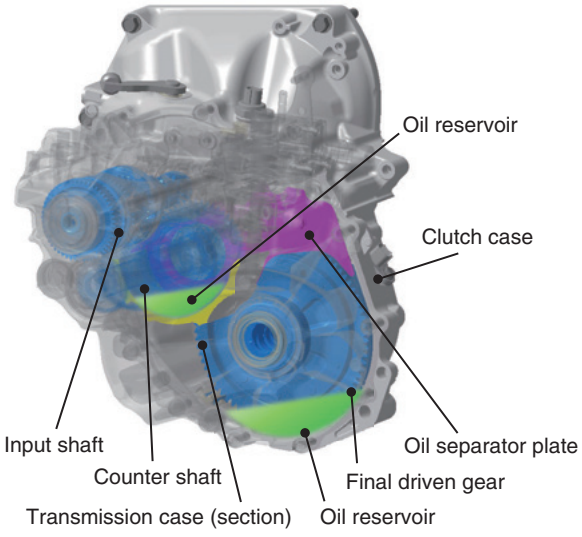


Fig. 2 Perspective view of developed 6MT

The structure was arranged so that oil splashed up by the final driven gear would also collect under the counter shaft. The reservoir of oil there would be splashed up by the counter shaft gear to lubricate the gear stages. With this arrangement, the increase in oil relative to the K-car 5MT was held down to just 0.1 L, and the required overall lubrication was secured without degrading the transmission efficiency.

The gear ratios were configured so that first through fifth are close-ratio gears that enable effective use of the engine's high torque range. Second gear, in particular, was configured to reach 75 km/h in the 7,700 rpm red zone. This allows it to cover the range from 30 to 60 km/h, which is the normal operating range for driving on winding roads. The sixth gear is set so that the engine speed when driving at 100 km/h will be the same 3,200 rpm as found with Honda's FIT RS 6MT. This enhances cabin quietness when cruising at high speeds. Figure 3 shows the driving force curve.

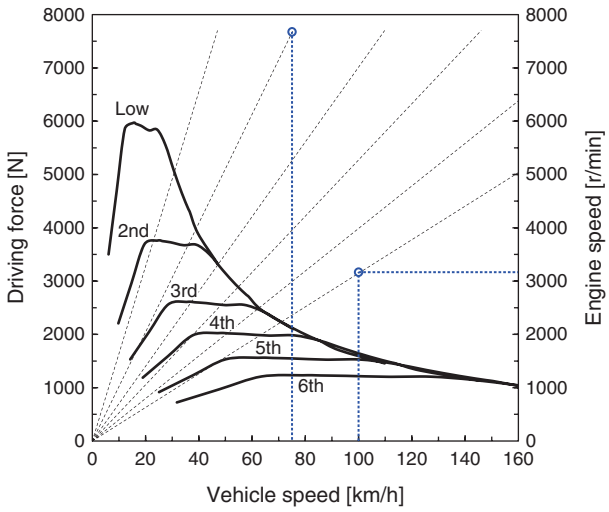


Fig. 3 Driving force curve

4. Increasing Capacity and Compactness

4.1. Increasing Capacity

In order to assure the strength and endurance to support high torque of 104 Nm while also achieving lighter weight and compactness, distances between the shafts were optimized. Higher torque can be supported by increasing the size of bearings or gears, or by switching to a stronger material. Dealing with this without changing the material requires increasing the distance between the input and counter shafts. Steps were taken to limit the increase in weight due to the increased distance between shafts. Bearing size was chosen according to strength and endurance requirements, and synchronizer size

was selected to achieve an appropriate shift load with a short shift stroke. The distance between shafts was set accordingly.

4.2. Increasing Compactness

In order to increase the transmission to six speeds while assuring its mountability in the vehicle, the total length of the transmission needs to be limited. A design for strength[1] was implemented, taking misalignment into account, in order to optimize the gear tooth width, and the synchronizer sleeve stroke was shortened[2]. Third through sixth gears were also combined into a compact module to assure the contact ratio while reducing the gear width by 5 mm. Optimization of the NB gear configuration also achieved a combined reduction of 0.8 mm in the first and second gears. These measures achieved support for high torque and the increase to six speeds while limiting the increase in total transmission length to just 21 mm relative to the K-car 5MT.

5. Gear Change Feeling

The joy of handling was realized in the S660 by development of a gear change feeling centered on three sensations: agility, moderation and smoothness.

5.1. Agile Feeling

A short stroke configuration was adopted in order to enable the agile sports car handling that would realize a light, agile feeling when changing gears. The shift stroke, shorter than in the previously marketed BEAT, was made 37 mm, which is on a par with the S2000 and NSX. The select stroke was made 22 mm to balance with the shift stroke and to allow for the compact packaging (Fig. 4).

Gear shift operation with a short shift stroke involves an increased synchronization load. Measures were taken to reduce this load by employing a double-cone synchronizer for the second gear and carbon synchronizer for the third gear.

Synchronizer selection was made according to synchronization load when shifting down, which is a criterion for judging the light, agile feeling[3]. This will be explained using the selection of synchronizer for second gear as an example. Figure 5 is a chart showing the relationship between the shift stroke when shifting down from third to second and the synchronization load during gear shift operation.

5.2. Moderate Feeling

The load characteristic during gear shift operation is determined by the resultant of forces generated in three parts inside the transmission, namely the shift arm detent, the shift fork detent and the synchronizer spring (Fig. 6).

Figure 7 shows the load displacement characteristics of each part together with their total load displacement characteristics. The moderate feeling cannot be obtained when the load peak during gear shift operation (part A in Fig. 7) has a double peak or when the load rise and fall slopes are too gradual. With the new model 6MT, the load peaks of the three load generating elements (part B in Fig. 7) are combined to result in a single peak where the load rapidly rises and then falls. This realizes a naturally moderate gear change feeling.

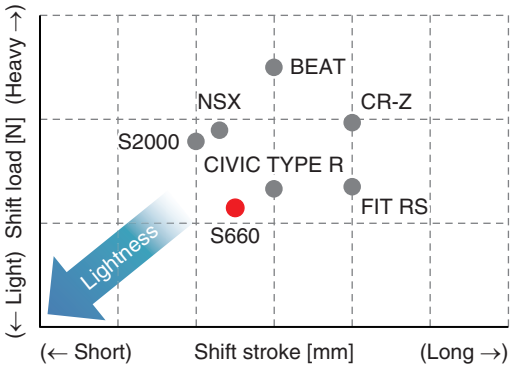


Fig. 5 Shift performance chart (Shift down from 3rd to 2nd)

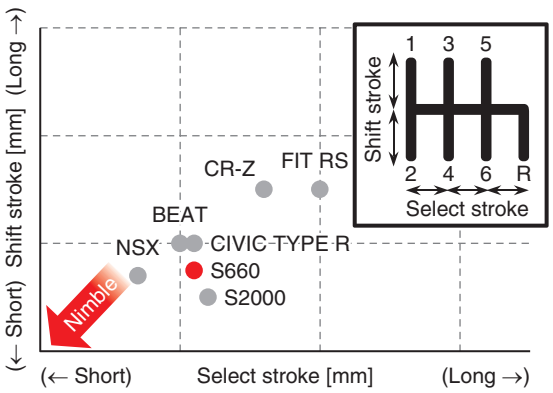


Fig. 4 Shift and select stroke

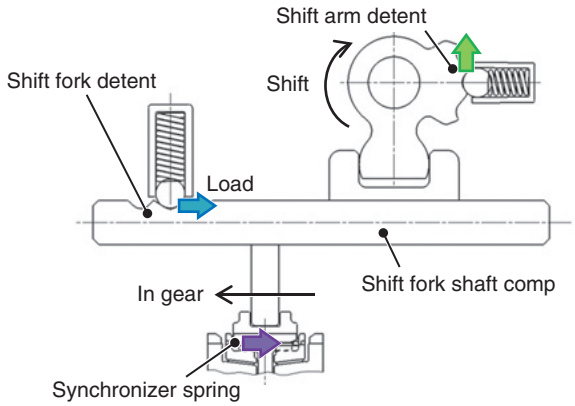


Fig. 6 Gear shift mechanism

5.3. Smooth Feeling

In order to obtain a smooth gear change feeling, the load characteristic that satisfies the moderate feeling in the previous section is modulated while at the same time performing modulation to increase the swallow feel[(1)], which refers to the feeling during gear shift operation that the shift is being sucked into position in the latter part of the operation. This swallow feel was also realized to an appropriate extent by aligning the load peaks (part C in Fig. 7).

Achieving a smooth gear change feeling also requires limiting the occurrence of a double-bump. A double-bump is a phenomenon felt as bumpiness during synchronization when the gear dog and sleeve are repelled by the drivetrain torsional reaction force[(1), (2), (4)] (Fig. 8). In the new model 6MT, the double-bump load generation was reduced by the shape[(3)] of the smaller-diameter part of the synchronizer sleeve and by adoption of a preceding sleeve tooth[(1)].

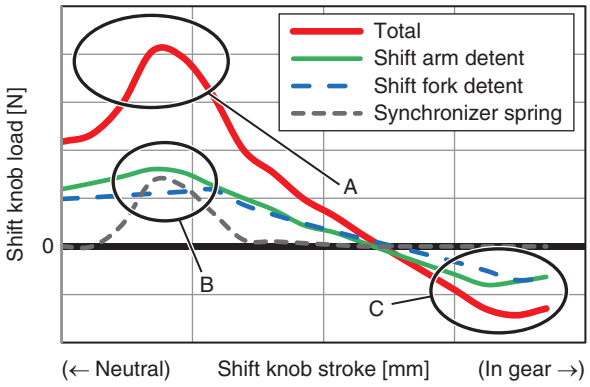


Fig. 7 Characteristics of shift load

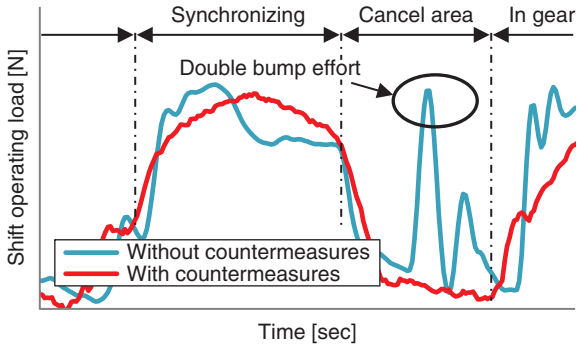


Fig. 8 Gear shifting time chart

6. Limiting Three-Cylinder Engine NV

In-line three-cylinder engines generally have higher cylinder pressure in a single cylinder than in-line four-cylinder engines with the same displacement, and therefore experience greater combustion torque fluctuations. In addition, the S660 has a boost engine with increased power at lower engine speeds. This means that combustion torque fluctuations are greater in the low-speed range, and engine rotational speed fluctuations rise to a greater level than in naturally aspirated engines with the same displacement. As a result, the rotational speed fluctuations transmitted to the transmission are also greater. The new model 6MT adopts an NB gear and friction washer to limit NV when idling and when driving.

6.1. NB Gear

As a measure to counter the rattling noise caused by rotational speed fluctuations when idling, an NB gear structure like that in the K-car 5MT was adopted for the first and second gear counter gears, which are idle gears located above the counter shaft.

An NB gear eliminates backlash in order to limit noise caused by gear teeth rattling due to rotational speed fluctuations. Just as in the K-car 5MT, a spring is used to press the NB gear against the deceleration tooth surface of the corresponding gear in a structure that eliminates backlash. This measure limits rattling noise without causing any unnecessary increase in clutch inertia.

6.2. Friction Washer

The rotational speed fluctuations that are transmitted to the transmission because of combustion torque fluctuations are transmitted to the synchronizer hub, the synchronizer mechanism that follows the input shaft. The hub and the synchronizer ring collide inside the hub slots to produce a continuous metallic jangling noise. The rotational speed fluctuation increases in particular when the vehicle starts moving from a stop and when accelerating from low speeds, and this is transmitted to the cabin interior together with power plant vibrations. In the K-car 5MT, the synchronizer mechanism located on the input shaft has increased noise sources at three locations, for gears three to five, and the new model 6MT has an additional synchronizer mechanism due to the increased number of gear stages. This has increased the noise level.

In order to limit this jangling noise, a friction washer was placed between the synchronizer ring and the hub. This functions as a buffer that directly suppresses the source of noise, thereby achieving a reduction in cabin noise.

As shown in Fig. 9, the friction washer is a circular plate structure. It has 12 inside projections that slide circumferentially, functioning as a spring against the bosses inside the hub, and also has six outside projections that control the degree of freedom of the slots in the synchronizer ring.

The operation of the friction washer is shown in Fig. 10. In operating regions where combustion torque fluctuations are smaller, the friction washer, together with the synchronizer ring, is caused by centrifugal force to be positioned up against the edge of the slot in the hub. When

the combustion torque fluctuations increase, the rotational speed fluctuations of the input shaft also increase, causing the hub and synchronizer ring to collide inside the slots. When this happens, the inside projections that have a spring effect will generate torque from friction with the hub while the outside projections impede collision between the synchronizer ring and the slots, reducing the noise produced.

The friction torque value was set with upper and lower limit values according to the range of the interference fit. The upper torque limit value comes into play when, after synchronization by the synchronizer ring, the ring locks to a gear, so the inside projections of the friction washer need to move forcibly outward to that extent in a circumferential direction. The value is therefore set after determining the threshold at which it will not interfere with the synchronization function or the gear change feeling.

The lower limit takes into account the fact that wear of the areas that contact the inside projections due to deterioration of durability can lead to diminished torque. The deterioration of durability was therefore considered in setting the threshold value.

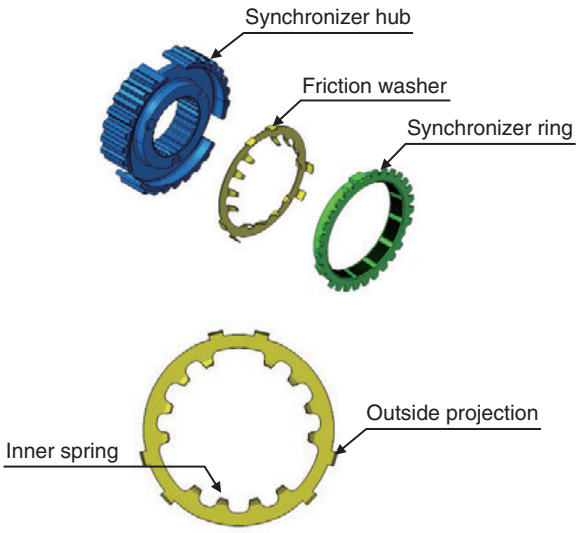


Fig. 9 Structure and function of washer

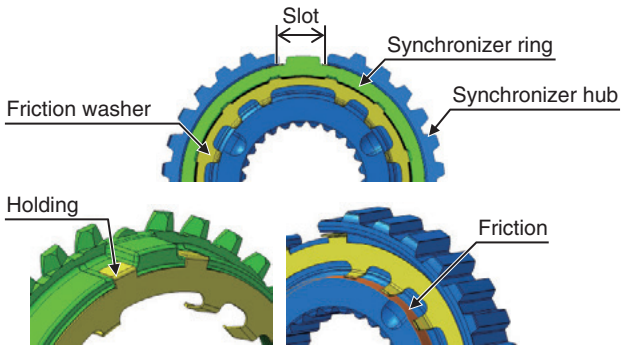


Fig. 10 Operating principle of friction washer

Figure 11 shows the effect of the friction washer. The graph shows transmission case vibration levels when the engine is accelerated from idling speed in second gear to 5,000 rpm at wide-open throttle. The difference between the level with friction washers in all the synchronizer mechanisms above the input shaft (third through sixth gears) and that without having washers in any clearly shows that effects were obtained across a wide frequency range. The new model 6MT adopted friction washers for third through sixth gears, yielding satisfactory performance in NV, which had been an issue.

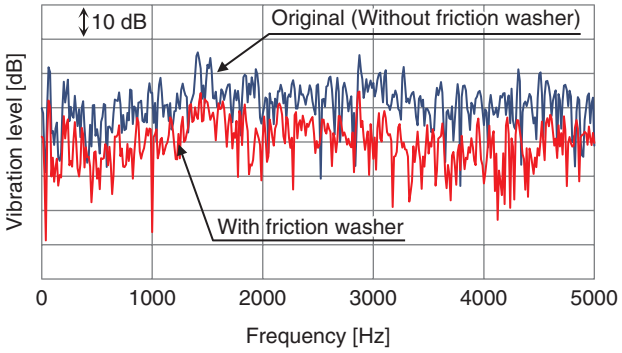


Fig. 11 Vibration level of transmission case

7. Conclusion

The new model 6MT has the following features:

(1) A 6MT was achieved that supports a maximum torque capacity of 104 Nm while remaining compact enough to enable mounting in the vehicle.
(2) The gear ratios set with the increase to six speeds achieve a balance between winding road driving and cabin quietness when cruising at high speeds.
(3) Adoption of a short stroke and optimization of the load characteristics during gear shift operation achieved a smooth gear change feeling that provides a sense of agility and moderation.
(4) Adoption of NB gears and friction washers reduced the noise and vibration of the three-cylinder engine.

References

(1) Yokoyama, T., Kuzuhara, K., Haginiwa, M., Takahashi, T., Nakamura, A.: Development of New Manual Transmission for Middle-Torque Engine, Honda R&D Technical Review, Vol. 24, No. 2, p. 54-61
(2) Matsuda, K., Manita, M., Yokomizo, K., Iwasaki, T., Haginiwa, M.: Development of Lightweight and Compact 6-speed Manual Transmission, Honda R&D Technical Review, Vol. 18, No. 1, p. 28-33

(3) Kitajima, K., Okada, Y., Hirano, K., Mitani, S., Udou, H.: Development of a High-revolution 6-Speed Manual Transmission for the HONDA S2000, HONDA R&D Technical Review, Vol. 11, No. 1, p. 39-44
(4) Murai, A., Okazaki, K., Okuno, K.: Sporty Shifting Feel of the HONDA S2000, HONDA R&D Technical Review, Vol. 11, No. 2, p. 73-78

■ Author ■


Masaaki IWASAKI


Takuya HOSOKAWA


Dohta YAMAMOTO

Accurate Capacity Estimation and Forecast of Li-ion Battery for BEV Using Telematics

Koichiro TAKEMASA* Takuya MIYASHITA* Kenji AKAMATSU**
Satoshi HADA*** Masao JOKO***

ABSTRACT

A battery traceability system that uses telematics technology was developed in order to acquire timely battery data from all FIT EVs that have been leased in the United States since 2012. The main purpose of this system is to track lithium-ion battery usage and capacity.

It has become possible to estimate battery capacity with greater accuracy than on-board Electronic Control Units by loading the time-series battery data collected from all the vehicles onto Honda servers, and applying an algorithm created to isolate the data of high accuracy from the totality of battery capacity estimation data. As a result, it was confirmed that battery capacity degradation remains within 3% in 97% of the FIT EV. It was also confirmed that FIT EV battery usage has a low frequency of remaining in the accelerated capacity degradation zone. In addition, it has been forecast by applying this data to the capacity forecast model for user patterns of usage that capacity degradation will be within 5% over the next several years.

1. Introduction

Lithium-ion battery (LIB) capacity diminishes according to battery usage and number of years of use. This has an impact on the product appeal of LIB-equipped battery electric vehicles (BEV) in terms of their driving range and other such factors. It is important, therefore, to track LIB capacity degradation in an accurate and timely manner for BEV performance evaluation when assessing trade-ins, for pricing used vehicles for sale, and so on.

Leasing of the FIT EV began in the United States in 2012. The leases were set up with a three-year lease period to start, with determination as to whether the lease period could be extended depending on a judgment based partly on the extent of LIB capacity degradation after a certain period of time. In order to extend the lease period, it would be necessary to confirm that the LIB was in a good state of health and that it had not been used in an idiosyncratic way when the LIB performance was evaluated. It would also need to be confirmed that the LIB could be expected to remain in a good state of health during the extended lease period.

With hybrid electric vehicles (HEV), the usage and state of performance of the on-board LIB previously was collected by means of the Honda Diagnostic System (HDS).

Under this method, usage data picked up by on-board sensors and estimated LIB capacity data from the on-board Electronic Control Unit (ECU) were stored in the ECU. That stored data was then collected by the HDS at Honda dealers during vehicle inspections and other such occasions that occur at irregular intervals. The collected data was transmitted to Honda servers, where it has been analyzed and utilized.

However, there were three issues with the method of collecting data by means of HDS for judging extension of the lease period. The opportunities to collect data are limited to when vehicle inspections and other such occasions occur, so that data cannot be analyzed and utilized in a timely and comprehensive manner. The on-board ECU on an HEV is used to estimate LIB capacity primarily for the purpose of fault determination. Consequently, it does not have the accuracy of capacity estimation needed to evaluate the influence on driving range, which is crucial for the BEV in a way it is not for vehicles that do not depend exclusively on batteries for power. Moreover, future capacity forecast requires the accumulation of vast amounts of data on usage and high-load computation of future capacity based on that usage. Given the allowed mounting space and cost constraints on the on-board ECU, however, dealing with the above issues was challenging. In order to resolve these

* Automobile R&D Center
** TIC Co., Ltd.
*** IBM Japan, Ltd.

issues and collect data without imposing any burden on the user, it was decided to make use of telematics technology, which Honda is already deploying as a service.

2. Development Goals

It was determined that a new system to collect, store, and analyze BEV LIB data would be needed in order to resolve the issues in the previous chapter. The following three points were taken as the main goals:

(1) To be able to collect, analyze, and utilize usage and changes in LIB capacity in all vehicles in a timely manner without additional burden on users;
(2) To be able to make a more accurate estimation of LIB capacity than the ECU estimated value; and
(3) To be able to forecast future changes in LIB capacity in accordance with individual vehicle usage.

3. Flow of LIB Data Utilization

The quantity of LIB-related time series data that is collected while a FIT EV is traveling and while it is charging is enormous. There was concern that, when analyzing an enormous amount of data, the intended analysis results could not be efficiently obtained if collection and analysis of the data was begun before the issues and the flow for resolution of issues had been defined. In building the data collection system, therefore, the aim was to clearly define the issues and create an LIB data utilization flow (Fig. 1) intended to efficiently collect, analyze, and utilize LIB-related data.

In order to collect data on approximately 1,000 FIT EV without any burden on users or dealers, a battery traceability system was developed to make use of the telematics system[1] already being deployed for service in the United States.

Data collection involves gathering time series data on every FIT EV in the United States in a timely fashion after the users' consent has been obtained. Raw data on the vehicle and LIB while traveling and while charging is transmitted as time-series binary data by means of the on-board telecommunications unit (Telematics Control Unit: TCU) and the mobile telephone network. The transmitted data is accumulated on Honda servers. The accumulated data is intermittently converted to text data and summarized as per single drive and per single charge data sets. This allows a comprehensive grasp of usage for all the vehicles. Data relating to highly accurate estimation of LIB capacity, analysis of usage, and capacity forecast is extracted from the summarized data and a model for analyzing it is created. As the person performing analysis inputs the data to the model, the model is modified and made more accurate in the process. Capacity estimation and capacity forecast are high-load computation processes, and these are implemented on the server side with the aim of achieving estimation of capacity and forecast of changes with a greater accuracy than the ECU. The capacity forecasting makes use of the LIB Capacity Forecast Model[2] that was created in parallel with the FIT EV development.

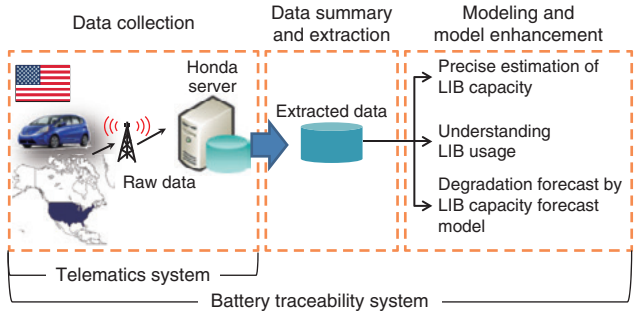


Fig. 1 LIB data utilization flow

4. Highly Accurate Capacity Estimation

4.1. On-Board ECU Capacity Estimation Method

LIB capacity is sought from the integration of current (ΔAh) divided by the displacement (ΔSOC) in the LIB charging rate (State Of Charge: SOC) during the same period by linear regression (Fig. 2) using the sequential least square method[3]. This is shown in Eq. (1).

$$Capacity = \frac{\Delta Ah}{\Delta SOC} \quad (1)$$

When this is done by the on-board ECU, ΔAh is calculated by integrating the electrical current values from on-board electrical current sensors.

On the other hand, SOC is a physical quantity that cannot be observed directly by on-board sensors. Therefore it has to be estimated, and there are two general methods for doing this. In the first method, the open circuit voltage (OCV) at the LIB terminals is first estimated. Then the SOC-OCV curve (the SOC-OCV relationship unique to the LIB) is used to convert OCV to SOC. This is the OCV

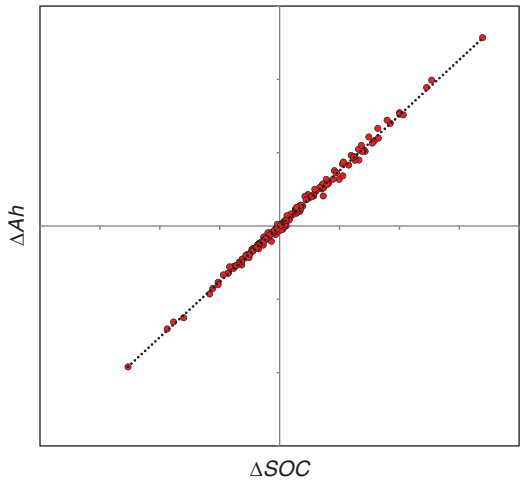


Fig. 2 Recursive least square method for capacity estimation

estimation method (Fig. 3).

The second method uses the integration of current and LIB capacity to estimate the SOC change from when the vehicle initially started traveling. This is the current integration method.

4.2. Capacity Estimation Error of the On-Board ECU

With the OCV estimation method, an OCV estimation error occurs when the battery is loaded, because OCV cannot be directly observed in this condition. When OCV is converted to SOC, therefore, the OCV estimation error influences the SOC estimation error (Fig. 4).

On the other hand, the current integration method involves a measurement error of several percentage points in on-board current sensors. That error therefore becomes cumulative with the passage of time, and the SOC estimation error grows larger.

Whichever of the above two methods is used, the estimated SOC will contain an error, and therefore error will also occur in the LIB capacity estimation. Figure 5 shows the change over time in LIB capacity estimation by the on-board ECU as a percentage of the LIB capacity true value, which is 100%. During approximately 4,000 seconds of travel, ECU estimation capacity has an error of about ±10% relative to the capacity true value. This capacity estimation error presents an issue in that it means LIB capacity degradation cannot be tracked with high accuracy by the on-board ECU.

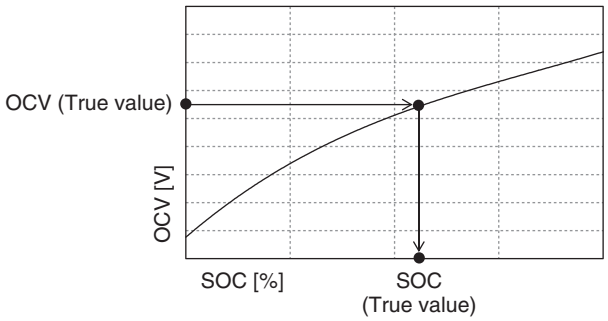


Fig. 3 Conversion of OCV to SOC

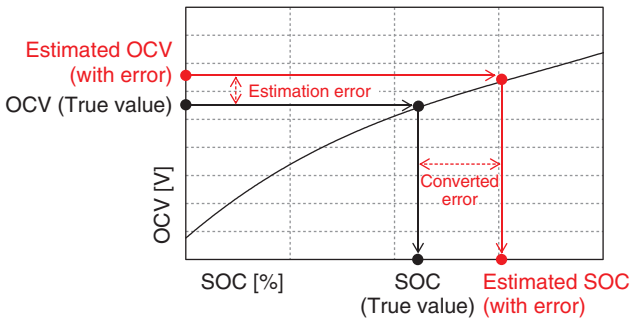


Fig. 4 Conversion of estimated OCV with error to SOC with error

4.3. Highly Accurate Method of Capacity Estimation Using Servers

In order to deal with the error with respect to capacity true value, the possibility of building a model to use the enormous quantity of time-series data accumulated on the servers to calculate capacity with a high degree of accuracy was examined.

In setting a target for capacity estimation accuracy, it was assumed that a 10% decrease in driving range would affect driver usability. Considering this assumption and taking into account that LIB capacity would diminish, the target tolerance was set at ±6% or less.

When creating the model, the notion was conceived that just the data for travel where capacity estimation error is smaller (where estimation accuracy is greater), or where data is for charging conditions only, could be extracted from all travel and charging data. Therefore, various travel and charging conditions were examined in order to extract those conditions with greater estimation accuracy. As a result, it was found that greater estimation accuracy could be obtained under the following two conditions.

The first condition was that where ΔSOC is larger (travel distance is longer), the capacity estimation accuracy becomes greater. Figure 6 shows ΔSOC on the horizontal axis and the capacity estimated by the ECU on the vertical axis. As

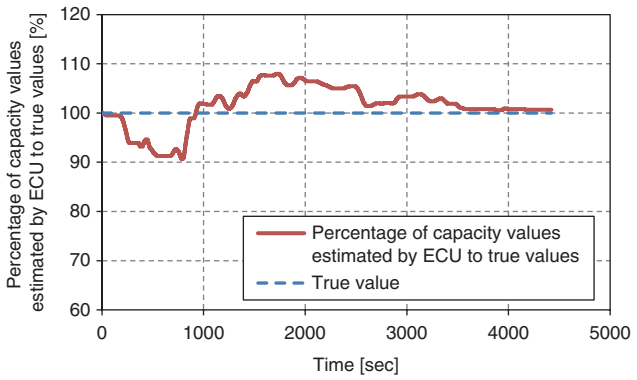


Fig. 5 Variation in capacity values estimated by ECU

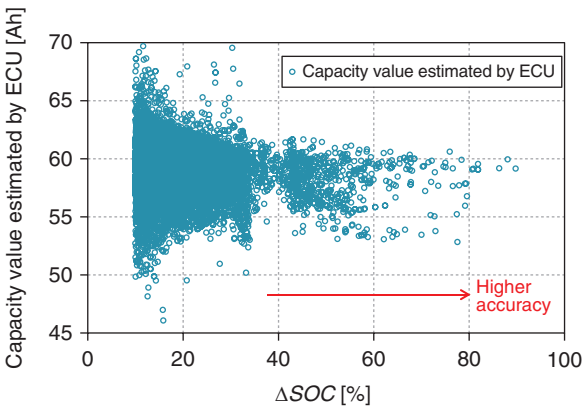


Fig. 6 Used range of SOC and variation in capacity estimation

the ΔSOC becomes larger, the true value of capacity tends to converge on 60 Ah.

The second condition was that when an adequate rest period is included after travel or charging, such that when capacity estimation also includes the rest period, the estimation accuracy becomes greater. The reason for this, as shown in Fig. 7, is that capacity estimation accuracy is greater when an SOC figure obtained from an OCV that has become stable after adequate rest is used rather than an SOC figure calculated by the ECU when travel has ended. Consequently, capacity was calculated using a period that includes rest, by selecting from the collected time-series data those items of travel or charging data linked with extended rest data.

When data meeting the above two conditions was extracted from the total quantity of data collected, it was confirmed that, as envisioned, the extracted sample provided greater estimation accuracy. A new issue then emerged, however, because it was found that the greater the estimation accuracy became, the smaller the number of vehicles became that could be used for capacity estimation (Fig. 8).

This is because, as a matter of user patterns of usage, there is a lower frequency of long-distance travel (travel with a larger ΔSOC). In order to achieve the target error tolerance of ±6%, data for ΔSOC 30% and greater has to be extracted. In this case, however, the vehicle coverage (the percentage of vehicles that can be calculated with a target error tolerance within ±6%) ends up dropping to 78%, with the result that 22% of vehicles could not have their capacity estimated with great accuracy.

4.4. Increasing Vehicle Coverage

The approach conceived to resolve the issue of reduced vehicle coverage was to connect individual travel data items to create a new travel pattern with larger ΔSOC. The multiplicity of travel ΔAh and ΔSOC values that could be connected to satisfy the rest time condition for data extraction were connected to form single data sets. These data sets were then used for capacity estimation (Fig. 9).

Performing capacity estimation in this way by connecting travel history data make it possible to achieve a balance between greater estimation accuracy and increased vehicle coverage. Connecting travel history data with ΔSOC of 20% or greater can achieve accuracy within the target error tolerance together with vehicle coverage of 97% or greater (Fig. 10).

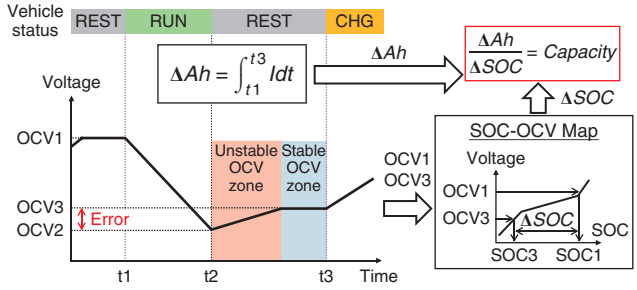


Fig. 7 Method for capacity estimation with battery traceability data

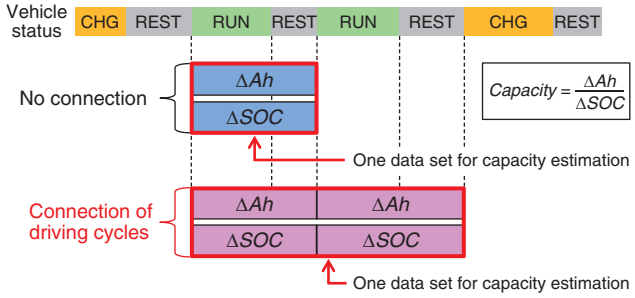


Fig. 9 Connection of driving cycles for precise capacity estimation

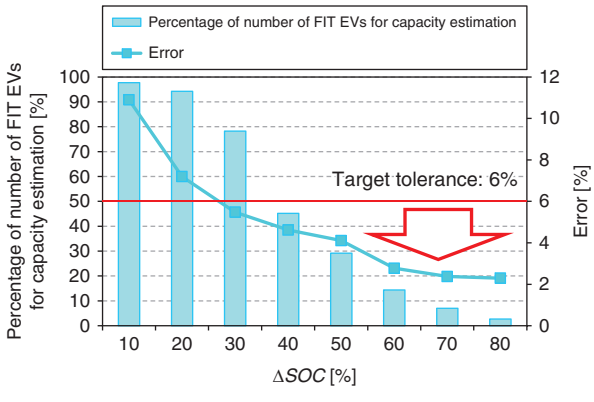


Fig. 8 Number of EVs with accurate capacity estimation and estimation error to used ranges of SOC

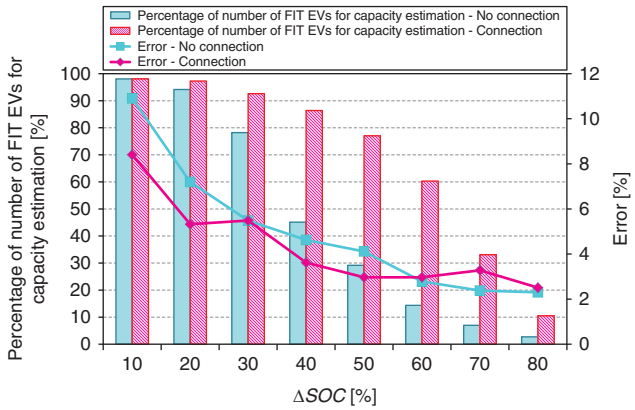


Fig. 10 Enhancement of vehicle coverage and estimation error

4.5. Results of Capacity Estimation

Figure 11 is a graph with LIB capacity of 805 FIT EV units for the United States market estimated using this capacity estimation method at 10,000 km travel intervals. The capacity estimation error margin and frequency are shown in a box plot graph. The areas with darker color indicate greater sample density, and lighter color indicates lower sample density. In order to verify the accuracy of this capacity estimation method, the LIB packs were removed from four FIT EV units that include the above durability tested vehicles, and their LIB capacity was measured using the LIB charge and discharge test system with highly accurate electrical current sensors. The actually measured capacity values were located along the interpolation line and extrapolation line for median capacity value calculated by this capacity estimation method. It was found that the accuracy of this capacity estimation method and the LIB capacity degradation do not diverge by more than 3%.

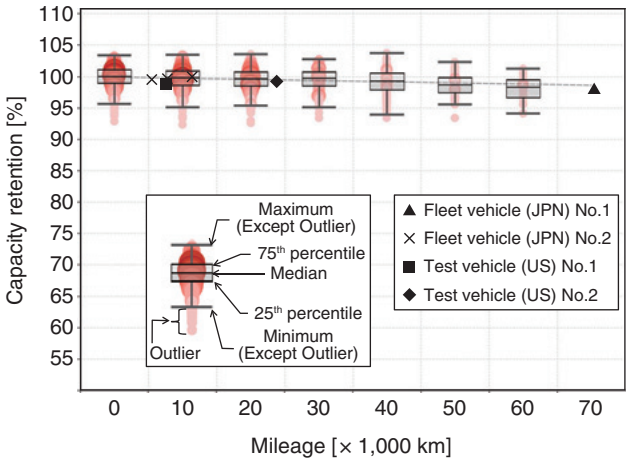


Fig. 11 Estimated FIT EV capacity

5. Changes in LIB Capacity

5.1. Capacity Degradation Acceleration Conditions

The factors that accelerate LIB capacity degradation are generally said to include LIB temperature, charge and discharge current values, and usable SOC (voltage) width[4].

The LIB for the FIT EV was subjected to cycle durability testing with the above factors varied. This bench testing confirmed the extent of acceleration of capacity degradation under the various conditions.

Figure 12 shows the results for examination of the influence of temperature by fixing the current during charge and discharge at 20 A and the width of SOC from 100% to 0% while the LIB temperature is varied at the four levels of 25°C, 35°C, 45°C, and 55°C. It was found that the capacity degradation is accelerated at higher LIB temperatures, with conspicuous capacity degradation observed at 55°C and above, in particular.

Figure 13 shows the results for examination of the influence of SOC width during charge and discharge on capacity degradation by fixing the current during charge and discharge at 20 A, the LIB temperature at 35°C, and SOC at the start of discharge at 100% while only the SOC at the end of discharge is varied at the four levels of 0%, 40%, 70%, and 85%. Conspicuous capacity degradation was observed when SOC at the end of discharge was 0%.

Figure 14 shows the results for examination of the influence of current on capacity degradation by fixing the LIB temperature at 35°C and the width of SOC from 100% to 0% during charge and discharge while varying the current

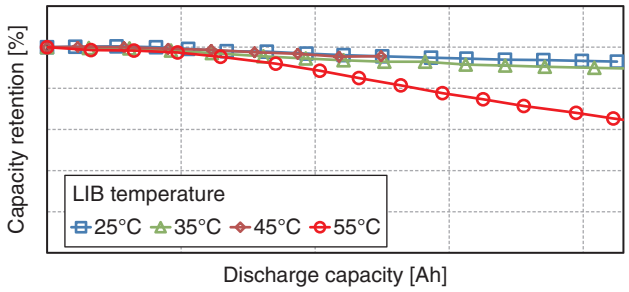


Fig. 12 Durability test with LIB temperature as parameter

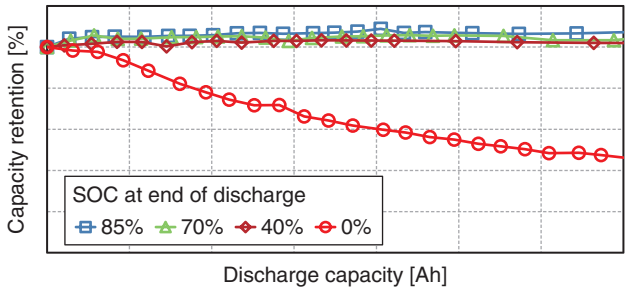


Fig. 13 Durability test with width of SOC window as parameter

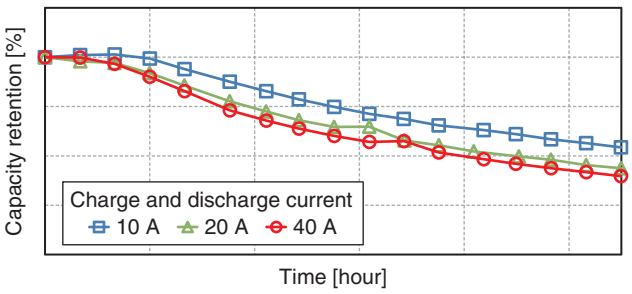


Fig. 14 Durability test with current as degradation parameter

at the three levels of 10 A, 20 A, and 40 A. It was found that increasing the current caused acceleration of capacity degradation by a very slight amount, but it was confirmed that no conspicuous tendency, as seen with temperature and width of SOC, was to be observed.

As explained above, the result of durability testing conducted under various conditions was that the extent of capacity degradation could be grasped quantitatively in terms of the three factors of temperature, SOC at the end of discharge, and current.

Given an environment of use by the user, when the frequency of entry into the accelerated capacity degradation zone of these factors was higher, LIB capacity degradation was anticipated to advance more conspicuously.

5.2. Influence on LIB from Usage Analysis

In each of the accelerated capacity degradation zones confirmed in the previous section, the frequency of LIB use was studied using the data from 580 vehicles with a record of driving for one year or more from the start of leasing.

As shown in Fig. 15, confirmation of the maximum LIB temperature frequency during traveling and charging showed that the frequency in the accelerated capacity degradation zone of 55°C or higher was virtually zero.

Confirmation of the frequency distribution (resolution 5%) of SOC at start of charge shows that SOC from 55% to 60% is the most frequent value. The frequency of remaining in the accelerated capacity degradation zone (SOC 0% to 5%) was the lowest of all zones at less than 3.8% (Fig. 16).

Figure 17 confirms the frequency of current during travel and charging. The peak near zero represents the supply of electric power for system operation. If this is removed, the graph more or less has the shape of normal distribution. On the regeneration side (in the negative zone), it does not remain in the accelerated capacity degradation zone, and on the discharge side, there is a higher frequency of remaining than on the regeneration side, but no conspicuous difference in frequency was observed.

The frequency of remaining in the zone was 3.8% only in the accelerated capacity degradation zone for width of SOC, and the frequency of remaining in other accelerated capacity degradation zones was nearly zero. Considering that the frequency of remaining in these three accelerated capacity degradation zones was generally low, the influence of usage by users on the acceleration of LIB capacity degradation could be said to be slight. The usage analysis results confirm that the FIT EV experiences little reduction in LIB capacity.

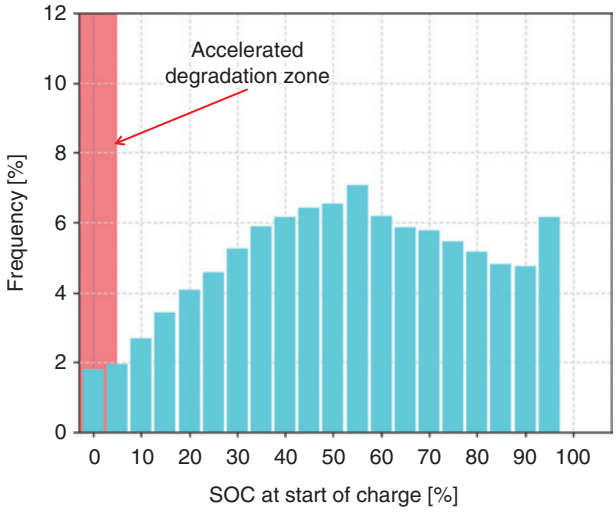


Fig. 16 Frequency distribution of SOC at start of charge

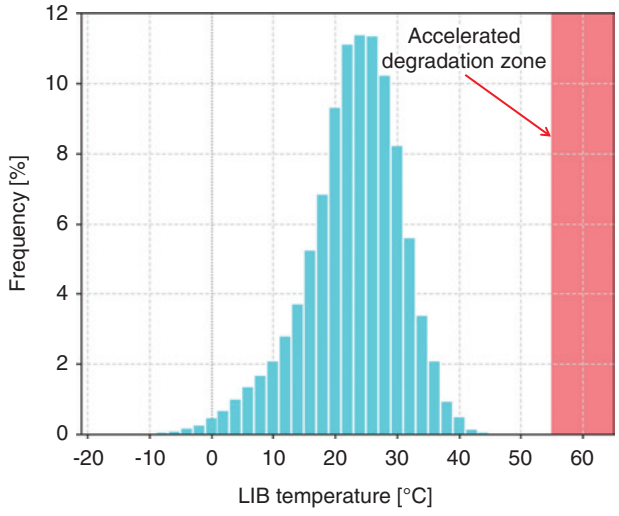


Fig. 15 Frequency distribution of battery temperatures

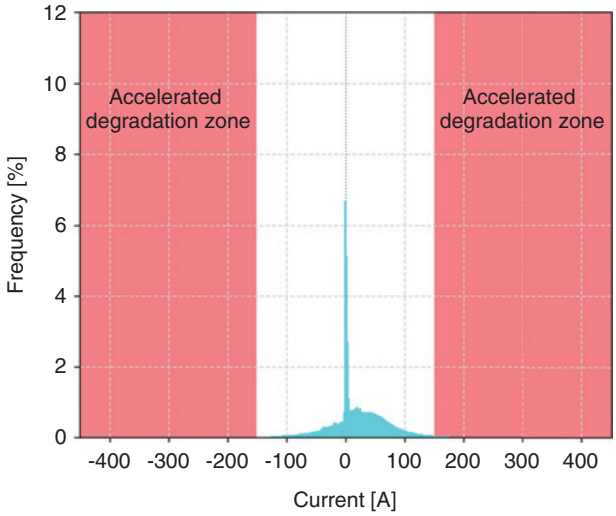


Fig. 17 Frequency distribution of battery current

5.3. Capacity Forecast

It was reasoned that future LIB capacity forecasting is important when judging whether to extend a lease period. Therefore, the LIB usage data for the most recent year from 682 vehicles was plugged into the LIB Capacity Forecast Model[(2)] vehicle by vehicle, and the capacity was tentatively forecast for the case of the same usage being repeated again in the future. The result was a forecast that even if the lease period were to be extended, LIB capacity degradation would remain at or under 5% during the lease period (Fig. 18).

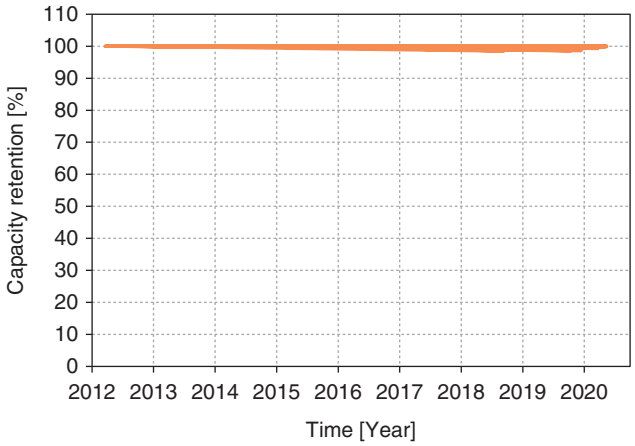


Fig. 18 Forecasted capacity degradation

6. Conclusion

A battery traceability system based on telematics technology was created and yielded the following results.

(1) A highly accurate capacity estimation method was established that satisfies the requirements of a target accuracy tolerance within ±6% and vehicle coverage of 97% or greater. This method confirmed that LIB capacity degradation in the FIT EV remains within 3%.
(2) It was confirmed that LIB usage in the FIT EV has a low frequency of remaining in the accelerated capacity degradation zone.
(3) When usage by users was plugged into the capacity forecast model and capacity was forecast, capacity degradation was forecast to remain within 5% during the period of the lease that is to be extended.

There were requests from users for extension of the lease period, and since the good state of health of the LIB was verified as described above, the American Honda Motor Co., Inc. announced on March 23, 2015 that it would extend FIT EV leases by two years.

References

(1) Takemasha, K., Uchida, T., Tsurutani, T., Tominaga, Y., Satoh, K.: Development of Battery Traceability System for EV, Honda R&D Technical Review, Vol. 25 No. 1, p. 36-41
(2) Tominaga, Y., Kawamura, M., Takemasa, K.: Creation of a Model of Battery Capacity Degradation Reflecting Battery Internal States, the 54th Battery Symposium in Japan, p. 101, (2013)
(3) Maruno, N., Komoda, S., Nishida, Y.: Battery Control Technology of Li-ion Battery System for HEV, Honda R&D Technical Review, Vol. 24 No. 1, p. 76-81
(4) Ichimura, M.: A Study of Life Characteristics of Small Lithium-Ion Batteries, NTT Building Technology Institute 2005, p. 1-7, (2005)

■ Author ■


Koichiro TAKEMASA


Takuya MIYASHITA


Kenji AKAMATSU


Satoshi HADA


Masao JOKO

Development of Vehicle System Supporting Vehicle-Grid Integration

Hakaru SADANO* Yutaka MARUYAMA* Satoru SHINZAKI**
Hiroyuki KANAZAWA* Jun KUDO* Takeshi FUJINO*

ABSTRACT

With the aim of achieving a balance between contribution to society and benefit to users, Honda has fabricated a plug-in electric vehicle that can help to stabilize electric power supply and demand by performing charge-discharge in collaboration with the power grid and obtaining a user benefit as compensation for that collaboration. The Accord Plug-In for the U.S. market was used as the base vehicle. It was equipped with an on-board bi-directional AC-DC converter unit that is capable of interconnection with the power grid and a digital communication unit that is capable of bi-directional communication between charge-discharge facilities and the vehicle. It was also equipped with a control application that has new power supply control functionality added to a base of charge control. This vehicle was used to participate in the frequency regulation market by means of the eV2G Project, a demonstration of Vehicle-Grid Integration technology conducted in the state of Delaware in the United States. The developed technology was demonstrated and the value to users was quantified. The results of the demonstration indicated that users able to participate in Vehicle-Grid Integration at home and at work for 18 hours per day can expect to receive an income of 3,000 dollars or more over a three-year period.

1. Background

The COP 3 conference held in 2007 with the participation of 187 or more countries adopted the Framework Convention on Climate Change (the Global Warming Convention) with the aim of reducing CO_2 as a way of addressing the increasing advance of global warming. This conference set targets and timetables for reduction of greenhouse gas (GHG) emissions, and each country is taking measures to reduce its GHG emissions.

The zero emissions vehicle (ZEV) regulations administered by the California Air Resources Board (CARB) in the state of California in the United States appear likely to bring increasing sales of plug-in electric vehicles (PEV) in that state. The California Public Utilities Commission (CPUC) estimates that 3.5 million PEV will be in use in 2022, and the installed battery capacity will rise to 30 GW[(1)].

Statistically speaking, private-use automobiles are considered to spend 96% of their lifetime parked. While the vehicle is parked, it is thought that the PEV battery can be connected to the power grid as a distributed power resource so that the electric power system can use it as a power buffer, thereby contributing to stabilization of the power supply. However, only the experimental use of PEV batteries has been described, and envisioned actual-use scenarios have not been verified with vehicles. In the present usage environment, the distributed power resources are large batteries dedicated to that purpose or emergency power generation facilities at corporations, hospitals, and so on.

The function that connects a PEV and the electric power system is referred to as Vehicle-Grid Integration (VGI). This is a function that makes use of the battery installed in the PEV as a distributed power resource. Not only will VGI be capable of contributing to the reduction of GHG emissions by expanding the use of renewable energy resources, but it may also be able to provide PEV users with a financial reward for that use. The CPUC has made proposals for measures to build the social infrastructure for putting VGI into practical use[(1)].

In putting VGI into practical use, however, there are issues that must first be resolved. These include the reduction in battery durability due to VGI use, assurance of the electrical reliability and safety of charging and discharging electric power, and the balance achieved between functionality as a vehicle and as a participant in VGI[(2), (3)]. It is important that these issues not be left just to automobile manufacturers, but that they be addressed in cooperation with a large number of stakeholders. In moving

* Automobile R&D Center
** AMERICAN HONDA MOTOR CO., INC.

toward realization of the VGI concept, it is necessary for the public and private sectors, as well as for industry and academia, to work together on measures for establishing a system that can realize VGI[4].

This paper will describe the development and verification of a vehicle system that supports VGI. The focus is on the state of California in the US, where active measures are being taken to introduce renewable energy resources and realize the VGI concept.

2. Electric Power Markets in the United States

The state of California passed the Global Warming Solutions Act of 2006, and has set a target for reduction of GHG emissions in California by 80% of the 1990 level by the year 2050. Another measure toward that target is the Renewable Portfolio Standard (RPS) of the California Energy Commission (CEC), the state's energy policy and planning agency. The CEC calls for the proportion of electric power generated in the state by renewable resources to be raised to 33% by the year 2020.

However, weather significantly impacts the amount of power generated and the times when power can be generated by solar power and wind power generation, which are typical of renewable energy resources that do not emit GHG. This means that the balance between demand and supply cannot readily be stabilized, making these unsuitable as baseload power sources. Another factor is that imbalances in electric power demand and supply can lead to deterioration of electric power quality, such as fluctuations in the frequency, distortion of AC voltage waveforms, and so on. Further deterioration of power quality increases the risk of large-scale power outages.

The power grid in the state of California is managed by an organization called an independent system operator (ISO) in order to stabilize the supply-demand balance of electric power. The California ISO constantly monitors the balance of demand and supply on the power grid and also forecasts demand. Based on the electric power demand forecast, the ISO works to stabilize the balance of electric power supply and demand by issuing power generation commands to electricity producers, establishing a wholesale power market for the procurement of electric power, and other such means.

2.1. Electric Power Market Transactions and Arrangements

The electric power market in California is operated by the ISO, and participated in by electric power companies, power transmission companies, power distribution companies, and other controlling entities.

The ISO uses the power demand forecasts as a basis for procuring electric power on the market a maximum of three years in advance. The power station operation plans are reformulated at set intervals with greater accuracy each time, and they are finalized on the day before operation. When an operation plan is finalized, further operational reserve capacity transactions, called the day-ahead electric power market, take place to prepare against unforeseen power station outages and so on. On, operational reserve capacity is procured by bidding based on operation plans.

Table 1 Examples of wholesale power markets

Ancillary service market	Frequency regulation market
	Primary reserve force market
	Secondary reserve force market
Energy market	Day-ahead electric power market
	Real time market
Transmission rights market	
Capacity market	

Enterprises known as aggregators that combine and control distributed power resources bid on these electric power transactions. The system is arranged so that the aggregator placing the lowest price on the power wins the successful bid right. Aggregators receive revenue from their successful bid price and at the same time take on the responsibility for providing operational reserve capacity according to commands from the ISO. On the operation day, the ISO adjusts its commands according to the supply capacity secured in this way while maintaining the balance between supply and demand.

For this paper, the frequency regulation market shown in Table 1 has been selected as the market for VGI verification. The reason is that this market can make use of the PEV battery characteristics that enable output and input of high levels of power in a short period of time. Frequency regulation starts within 10 minutes after a command from the ISO, after which it has to be able to output and input electric power according to the command signals that are updated every four seconds. Meanwhile, there is a stable balance of output and input electric power within a specified time, and since fluctuations in the battery SOC are small, it is thought that the impact on battery deterioration will also be small.

Figure 1 shows the relationships among the stakeholders involved in the present research.

The structure of VGI is equivalent to that of the current frequency regulation market, with the exception of the distributed power resources being replaced by the VGI-capable vehicles. The roles of other stakeholders are equivalent both in the current market and in the VGI. The ISO issues commands to the aggregator to provide the electric power procured on the market according to the balance of supply and demand on the power grid. The aggregator transmits supply and demand control signals to vehicles participating in VGI. Depending on the supply and demand commands they receive, the vehicles either receive power or transmit power. In this way, the electric power on the power grid is adjusted, and in this arrangement, the vehicle users receive compensation for their participation.

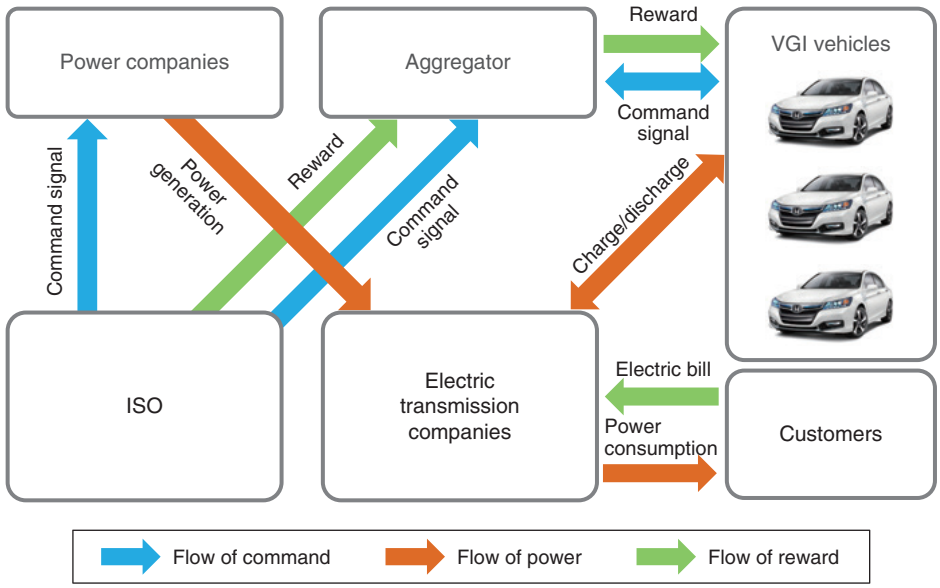


Fig. 1 Structure of VGI

3. Development Goals

Users who purchase a PEV that supports VGI can earn income by participating in the wholesale power market through an aggregator. Meanwhile, VGI uses the vehicle's battery, which means that, for constructing the system, it will be necessary to understand characteristics of battery deterioration caused by use of VGI, to establish charge-discharge control for the purpose of achieving a balance between vehicle usability and VGI, to assure the robustness of vehicle control functions with respect to the quality of electric power on the grid, and to assure responsiveness and controllability with respect to charge-discharge commands.

Controls and hardware to address these issues were created. The validity of their specifications was verified using demonstration vehicles.

4. Configuration of Vehicle Systems

4.1. System Concept

The conventional PEV has only the functionality to recharge from the power grid. A PEV that supports VGI, on the other hand, has a bi-directional power transfer function for sending and receiving electric power between the power grid and the vehicle battery, bi-directional communication function for exchanging control information with the aggregator that is needed for the output and input of electric power, and functions for controlling the vehicle components, including discharging power.

The concept for this research was defined as adding VGI functionality while maintaining the functionality, performance, or quality of the base PEV. In order to achieve such a system with minimum changes to existing systems in the vehicle, the authors aimed at integrating only the bi-directional power conversion capability and the bi-directional communication functionality, and building a control system that can maximize the value obtainable by VGI without diminishing the intrinsic value of the vehicle.

4.2. System Configuration

Figure 2 shows an example of electrical and communication links established with the grid for implementing VGI. When an ordinary residence is taken as the example, a distribution board for receiving and distributing electric power and a unit known as an electric vehicle power system (EVPS) that controls charging and discharging are integrated between the vehicle and the power grid. The EVPS not only handles the transmission of electric power and circuit switching, it also has the functionality for converting charge-discharge control signals sent and received by the aggregator over Internet connection using TCP/IP into a power line communication (PLC) signal in the HomePlug Green PHY (HPGP) physical layer for communication between the EVPS and the vehicle as defined in SAE J2931[5]. An SAE J1772[6] connector is used to connect the VGI-capable vehicle with the EVPS, allowing the vehicle to transfer electric power and communicate with the aggregator.

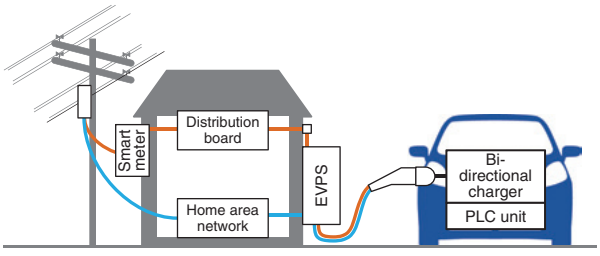


Fig. 2 VGI connection system

The hardware that is built into the vehicle is based on the conventional PEV system with the system connecting to the outside of the vehicle, as described above (Fig. 3). The connector that transfers power is also used for communicating with outside the vehicle. In place of the on-board uni-directional converter unit (the on-board charger: OBC) that converts AC power from the grid into DC power to charge the on-board battery, the vehicle is equipped with an on-board bi-directional converter that also functions to convert DC power to AC power; this enables VGI connections not just at home, but also at destinations away from home. PLC communication by the HPGP system, which is capable of high-speed, bi-directional communication of high-volume data defined by SAE J2931, was adopted for communication between the vehicle and the EVPS, and a dedicated PLC unit was put in place. PLC communication is superposed on the control pilot line (CPL), which is a signal for charge control, so a dedicated connection is not needed.

4.3. VGI Control

4.3.1. Battery control

In order to create more value in the frequency regulation market described above, a VGI-capable vehicle is required to be connected with the power grid over a longer period of time and implementing VGI with higher output. However, at the same time, this can cause insufficient charge time, chronic low SOC, and accelerated battery deterioration. VGI constitutes a technology that uses PEV batteries while the vehicles are parked. Maximizing the benefit obtained through VGI and responding to user demand for driving are requirements of battery control systems.

In this research, the following three points were taken into consideration in setting the target SOC during VGI operation.
(1) Maximize the benefits that can be obtained through VGI

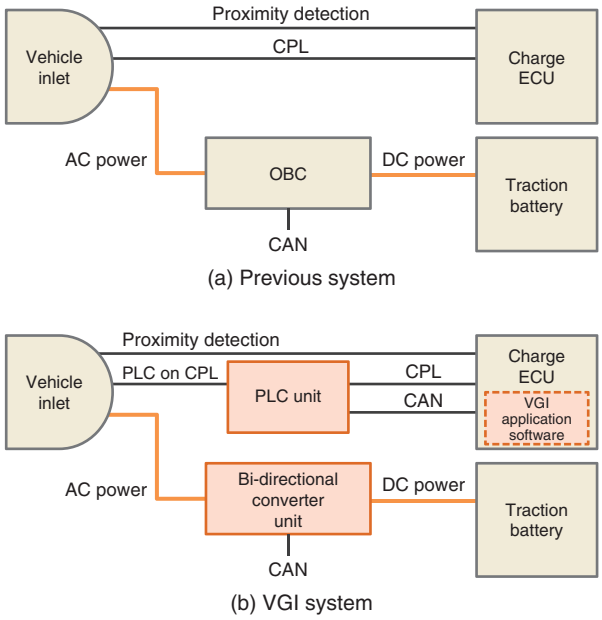


Fig. 3 Comparison of charging system

Table 2 Battery deterioration simulation with VGI operation

VGI use case	Simulation condition
Area	LA, California
SOC	90%
Peak power	±4 kW
Effective power	2.4 kW
Operating time	8:00 p.m. - 6:00 a.m. 10 hr/day (36500 hr)
Simulation period	10 yrs, 100,000 miles

Table 3 Result of battery deterioration ratio with VGI working

Battery pack capacity	Capacity retention		Deterioration ratio
	Without V2G	With V2G (Used for 10 yrs)	
20 kWh	78%	75.9%	-2.1%

(2) Assure the EV driving range required by the user
(3) Limit the impact of VGI on battery deterioration

In general, the deterioration of lithium-ion batteries tends to be advanced by high temperatures and a high SOC. While VGI is active, batteries tend toward a lower SOC than when they are fully charged, and so it is thought that no increase in the rate of deterioration would occur. However, in a scenario of a continuing power transfer by VGI operation when the SOC remains at 80% or greater, which is in the vicinity of a full charge, the battery temperature may be held higher than the ambient temperature due to the heat generated by the charge-discharge power, which could lead to additional deterioration. In order to identify the increase of the rate of battery deterioration, a simulation of battery deterioration that integrated a battery-equivalent circuit with a thermal simulation of cooling was carried out to predict how battery deterioration would be affected during VGI use (Tables 2 and 3). The simulation envisioned VGI use in the possible usage environment of the vehicle, so in addition to temperature and other such environmental factors and the input and output of electric power for driving, the simulation also incorporated data on VGI power input and output obtained from the frequency regulation market. The result showed about 1.5°C higher battery temperature rise, averaged over the vehicle life, given the assumption that VGI would be implemented for 10 hours per day while the vehicle is parked. For a PEV with a 20-kWh battery installed, this was estimated to cause 2% deterioration over a 10-year period.

4.3.2. Charge-discharge control

The charge-discharge is controlled according to the battery condition in order to achieve battery control described above.

In the case of VGI intended for participation in the frequency regulation market, the aggregator controls electric power by issuing charge-discharge commands to multiple

vehicles that are connected to the power grid.

As explained above, the frequency regulation market as it is administered at present utilizes fixed power generation facilities and stationary batteries. Consequently, they are always connected to the power grid and the available electric power is ensured. VGI, on the other hand, utilizes batteries that are installed in vehicles and that are therefore not always connected to the power grid. Furthermore, even when they are connected to the power grid, the battery temperature may rise high in the extreme heat of summer or fall low in the bitter cold of winter, and the amount of available power can also be expected to vary from vehicle to vehicle.

Under these circumstances, the aggregator will be unable to calculate the regulating power, and frequency regulation will fail to be implemented. The system was therefore set up to have the vehicle transmit its own power limit value to the aggregator, so that it could receive a charge-discharge command value in accordance with its battery state. This enables the aggregator to monitor the capabilities of individual vehicles' charging and discharging so that the power can be distributed appropriately. This also made it possible to create a control system that would not adversely impact battery deterioration.

When the various conditions of temperature, SOC, and so on do not allow the vehicle to charge or discharge, so that it cannot respond to aggregator demands, the system stops the vehicle's charge-discharge activity and goes into a standby state.

Figure 4 shows the typical content of communication that is required between the vehicle and aggregator in order to implement these various forms of control.

In order to implement VGI without losing any of the performance of the base vehicle, the control is designed to set a lower limit for battery SOC so that the minimum guaranteed driving range is ensured. Steps are also taken so that the vehicle will be at full charge at the time set on the charging timer by the user. The estimated time to a full charge is calculated and the time to finish VGI discharge is determined. The control is set up so that it subsequently only performs charging (Fig. 5).

4.4. Bi-directional Converter Unit for Installation in VGI-Capable Vehicle

4.4.1. Circuit configuration

In addition to the OBC function of converting AC power from the power grid into DC power to charge the on-board battery, the bi-directional converter unit for VGI-capable vehicles needs to have the capability to convert DC power from the on-board battery into AC power and discharge it onto the power grid. One method for providing these two functionalities on-board would be to install a DC-AC inverter unit exclusively for discharging power in addition to the OBC. Another method would be to install a bi-directional converter unit that has circuits capable of converting AC and DC power in both directions. For this research, a bi-directional converter system was selected in order to minimize increases in the size and weight of the unit as well as the increase in cost, for the purpose of limiting both the curtailment of vehicle interior space and the impact on fuel economy on the road. The bi-directional converter unit was fabricated by changing the rectifier circuit component and the power factor correction (PFC) circuit component that are parts of the OBC into an AC-DC conversion circuit[7].

The design target figures for the bi-directional converter

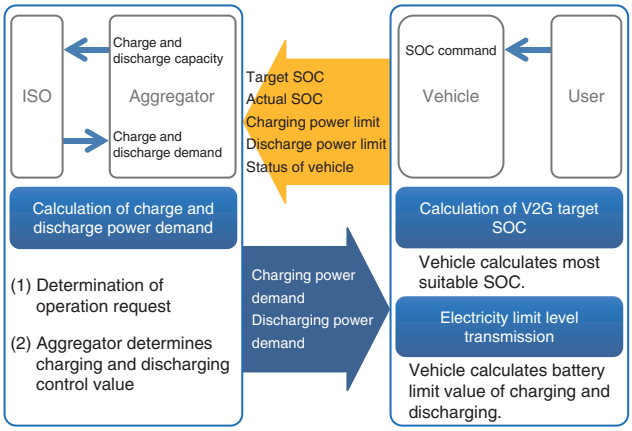


Fig. 4 Communication between aggregator and vehicle

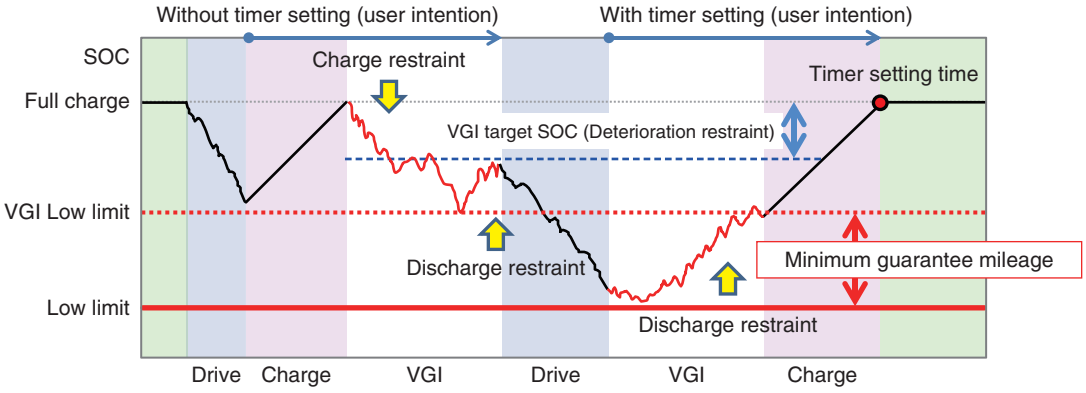


Fig. 5 VGI control for customer

Table 4 Design target of bi-directional converter

Item		Design target	Note
Volume		≦ 10 L	Equal to or less than 2013 model
Efficiency	Charge	≦ 90.6% (240 VAC)	Equal to or more than 2013 model
	Discharge	≧ 87%	More than power conditioner for facilities

unit are shown in Table 4. The conversion efficiency during charging was made equal to or better than that of the base model, thus ensuring charging performance. For minimizing impact on space utility in a vehicle, the target volume for the unit's circuit component was defined as a volume of 10 liters.

Figure 6 shows the circuit configurations of a uni-directional converter and the bi-directional converter fabricated in this research. The AC-DC converter component has a rectifier circuit function (AC-DC conversion) and a power factor correction function, in addition to which there is a function for converting the DC power of the vehicle's traction battery to AC for the power grid. In conjunction with making the transferred power bi-directional, the secondary side (battery side) of the DC-DC converter was also changed from a diode rectifier circuit to a semiconductor switching element, enabling the circuit to convert power in both directions.

4.4.2. Applicable standards

The only function of the OBC was to receive electric power from the grid. Therefore, in the case of North American specifications, for example, communications between inside and outside the vehicle as well as the compatibility and safety of connectors and other such items,

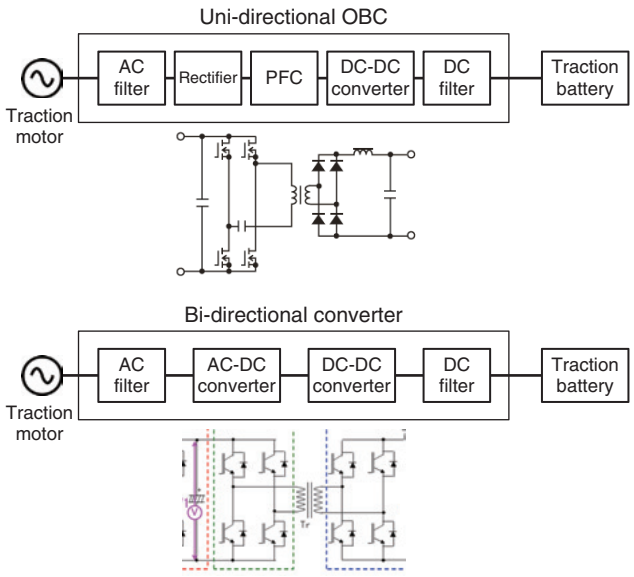


Fig. 6 Comparison between uni-directional and bi-directional converters

Table 5 Standards related to VGI

	charge		VGI	
OBC	AC charging	SAE J1772	discharge power quality	NEC 702
	compatibility for grid	SAE J2894	leak intercept	NEC 705
		IEC 61851		
Grid connection	—		grid parallel off	IEEE 1547
			grid follow	
			grid protection	
			anti islanding operation	
			automatic recovery	

were ensured by complying with the relevant SAE and IEC standards. In the case of a bi-directional converter, however, it has functions for both charging and discharging power to the grid. It was necessary, therefore, for the design to comply with standards relating to safety functions, such as the function of suspending electric power discharging when the system detects a power outage on the grid, and standards relating to maintaining the electric power quality, such as shaping the power supply waveform and applying harmonics. The standards required for compliance are shown in Table 5.

Since this research applies to North America, the design was made to comply with IEEE 1547[8].

4.4.3. Robust control against the electric power quality on the grid

The electric power quality on the grid is known to vary with the method of generation, environmental conditions, load conditions, and other such factors. Through monitoring the power quality on the grid over a long period of time, the results revealed that substandard voltage waveform was observed (Fig. 7). When this kind of voltage waveform from the grid is used to control the unit, the control specifications have to allow for sufficient robustness. The impact of the substandard voltage waveform on the unit was therefore verified in both hardware and control aspects, and the impact was addressed by enhancing the abnormal waveform detection performance of the unit and increasing the reliability of its protective operation.

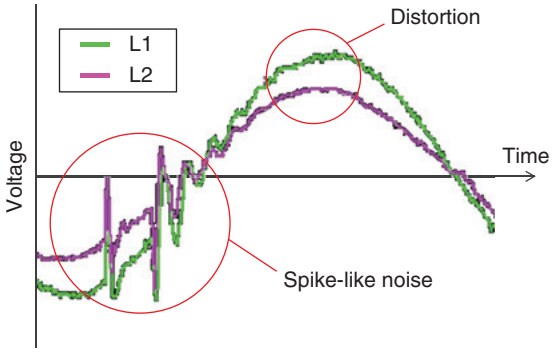


Fig. 7 Example of grid power quality

5. Demonstration Results

Honda participated in the eV2G Project, a demonstration of the VGI concept held at the University of Delaware in the United States, for the purpose of verifying the robustness and quantifying the value of the basic technology created in this research. (See Fig. 8.) This demonstration is being administered by a consortium that includes America's largest ISO (PJM Interconnection), an electricity generating company (NRG Energy), and a VGI aggregator (the University of Delaware). This project is engaged in demonstrating the compatibility of VGI on the frequency regulation market operated by PJM Interconnection.

An Accord Plug-In for the U.S. market was used as the base vehicle in the demonstration. The demonstration vehicle was equipped with an on-board bi-directional AC-DC converter unit (output of ±2 kW) capable of interconnection with the power grid in compliance with IEEE 1547, and a vehicle smart link (VSL) unit for digital communication between the vehicle and the equipment provided by the University of Delaware. The VSL unit replaces the PLC with a control area network (CAN), which is similarly superposed on the CPL. The control application is based on charge control with production specifications to which a discharge control function, a function for fault detection during discharge, and a fail-safe function were newly added.

Verification was conducted over the 12-month period from November 2013 to November 2014. It involved confirmation of VGI controllability, SOC adequacy, and other aspects of system compatibility, verification of the validity of converter unit settings for interconnection with the power grid, and quantification of user benefits.

Data on grid connection times, grid power quality, and vehicle electric power input and output was acquired in the demonstration. The operations of the various vehicle components and failure detection data were analyzed, and the market compatibility of basic VGI technology as well as the quantification of user benefits were also evaluated.

5.1. Ensuring Robust Control with Respect to Grid Power Quality

As a result of long-term monitoring of the grid power quality, it was found that voltage waveforms occasionally fall significantly short of the values specified in the standard. The on-board bi-directional AC-DC converter was robustly operated until the end of the demonstration.



Fig. 8 VGI capable Accord participating in eV2G project

Table 6 SOC control responsiveness

Item	Expectation	Experimental data
SOC band	±10%	+4.1% -3.5%
Average output	±0.5 kW	+0.55 kW -0.46 kW
Peak output	±2.0 kW	+1.9 kW -1.5 kW

5.2. Response and Control with Respect to Input-Output Command

The aggregator receives figures for the lower SOC limit usable in VGI from each vehicle. It uses those figures to forecast and manage the electric power input and output for the group of VGI vehicles as a whole, as well as to determine values for charge-discharge command for each vehicle. As shown in Table 6 and Fig. 9, these functions combined with the SOC management control in the vehicle were confirmed to provide control that was capable of complying with the lower limit SOC values. It was also confirmed that electric power input and output by the vehicle successfully followed the charge-discharge commands received (Fig. 10).

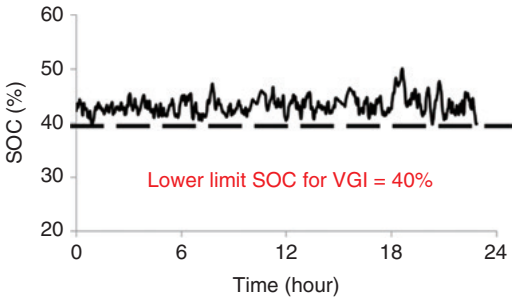


Fig. 9 SOC control performance

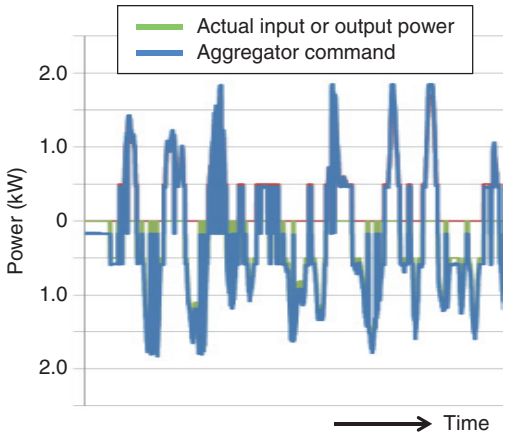


Fig. 10 Transient response performance of VGI system

Table 7 Incentive obtained through VGI

Connected time (hr/day)	Estimated value based on (Q1, 2013 – Q2, 2014) ($)	Average ($/month)	Estimated value in 3 years ($)
18	1,733	91	3,276
12	1,065	56	2,016

5.3. Quantification of Income to Users

Data on connected times acquired from participation in the frequency regulation market during the demonstration together with unit prices for electric power from actual transactions on the market were used to calculate the income to users. The results are shown in Table 7. In the case of users that participate in VGI for 12 hours at home and six hours at work, for a total of 18 hours per day, it was found that they would receive an income averaging US$91 per month, or $3,000 over a three-year period. Even users whose VGI participation amounted to 12 hours per day would receive $2,000. This confirmed that sufficient benefit would be gained.

6. Conclusion

(1) The basic technology was created, with VGI vehicle hardware and control specifications, for establishing electrical connections between vehicles and the power grid, and for accurately performing charge and discharge operations according to aggregator commands. The hardware and control specifications for an on-board bi-directional AC-DC converter with the robustness and ability to operate in concert with an unstable electric power grid were confirmed. The ability to follow demand for input and output of electric power and the potential for compatibility with battery SOC control were also confirmed.

(2) Deterioration of the vehicle battery due to utilization of VGI was verified by a simulation based on input-output demand waveforms from the aggregator that were acquired during the demonstration. With the scenario of a PEV with a 20-kWh battery installed and charge-discharge output of ±4 kW, it was estimated that deterioration would be advanced by about 2% over a 10-year period.

(3) As a result of participation in the demonstration and actual operation of a frequency regulation market, it was found that users participating in VGI at home and at work for 18 hours per day could be expected to earn an income of $3,000 or more from operation over a three-year period.

References

(1) Langton, A., Crisostomo, N.: Vehicle-Grid Integration, California Public Utilities Commission, R. 13-11-007, (2014)

(2) Kempton, W., Udo, V., Huber, K., Komara, K., Letendre, S., Baker, S., Brunner, D., Pearre, N.: A Test of Vehicle-to-Grid (V2G) for Energy Storage and Frequency Regulation in the PJM System, Results from an Industry-University Research Partnership, p. 32, (2008)

(3) Hasuike, H., Shintani, T.: Economical Evaluation and Challenges for Realization of Vehicle to Grid, JSAE Annual Congress (Spring) Proceedings, No. 27-14, p. 21-24, (2014) (In Japanese)

(4) Shinzaki, S., Sadano, H., Maruyama, Y., Kempton, W.: Deployment of Vehicle-to-Grid Technology and Related Issues, SAE Technical Paper, 2015-01-0306, (2015)

(5) SAE J2931: 2011, Digital Communications for Plug-in Electric Vehicles

(6) SAE J1772: 2012, Electric Vehicle and Plug in Hybrid Electric Vehicle Conductive Charge Coupler

(7) Izumi, T., Hirota, M., Hatanaka, K., Isoyama, Y., Sano, K., Takayama, K.: Bidirectional Charging Unit for Vehicle-to-X Power Flow, SEI technical review, No. 185, p. 34-37, (2014) (In Japanese)

(8) IEEE 1547: 2013, Standard for Interconnecting Distributed Resources with Electric Power Systems

■ Author ■


Hakaru SADANO


Yutaka MARUYAMA


Satoru SHINZAKI


Hiroyuki KANAZAWA


Jun KUDO


Takeshi FUJINO

Nonlinear Finite Element Method Solver for Design of Automotive Cable Layout

Takuya SHUDO*

ABSTRACT

A new nonlinear finite element method solver has been developed for use in a simulation tool for the design of automotive cable layouts. The solver uses a hybrid method combining static implicit and static explicit methods. The use of this method has made it possible to complete calculations for models for which calculations did not converge on a solution using conventional iterative methods. A method of modeling the stiffness of the clamp-end of a cable was also developed in order to increase the accuracy of analyses. The formulation of modeling templates for different types of clamp has made it possible for designers to conduct accurate cable layout designs in short periods using simple operations. The developed hybrid method and library are in use as cable analysis tools in Honda research and development centers in Japan and overseas.

1. Introduction

Automobiles employ a large number of cables, including brake hoses, heater hoses, and parking wires. Figure 1 shows an example of a brake hose. The hose undergoes considerable bending and twisting in order to wind it into the gaps between surrounding parts. Automotive suspensions have an up-down stroke, and the steering system is also in the vicinity of the brake hose. From its initial layout, in addition to twisting, the brake hose is given a large bend in order to respond to the movement of the suspension. Because the movement of these cables follow the movements of surrounding parts and the cables undergo oscillation, it is necessary to employ layouts in which there is no interference between the cables and the surrounding parts.

Because during the initial stage of development it is highly possible that the positions or shapes of surrounding parts may be changed, it is necessary to conduct repeated studies of the cable layout during the layout design process at this stage in order to respond to these changes. Cable layout design has therefore conventionally employed simulations in order to make it possible to study layouts in a short period of time.

Figure 2 shows an overview of an in-house cable layout design tool. The designer sets the shape of the cable in the tool, and indicates the material and the types and positions of the clamps employed. The tool automatically generates a model using the nonlinear finite element method ("nonlinear FEM" below) employing beam elements. The tool displays the results calculated by the solver, making it possible for the designer to study factors including deformation of the cable shape and the section force on the beam elements.

In the conventional cable layout design tool, nonlinear equations are solved using an implicit method via an iterative procedure, based on an FEM model taking geometrical nonlinearity and material nonlinearity[1] into consideration. For pure bending as the dominant deformation, it has been possible to predict the nature of deformation in actual cables even when they undergo considerable bending. However, when the cables are bent while undergoing a high level of twisting, the failure of the iterative calculations to converge on a solution results in the procedure being suspended without a conclusion, and it is not possible to study the

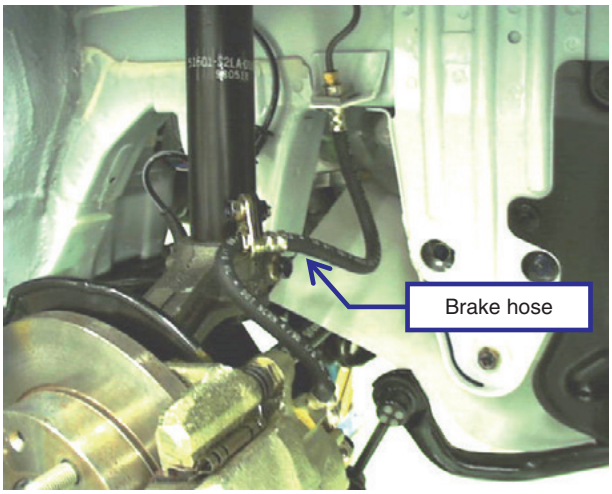


Fig. 1 Brake hose

* Automobile R&D Center

cable layout. It is thought that in the domain in which the iterative calculations do not converge on a solution, the state of deformation undergoes large changes in response to miniscule external input, making it unstable as a physical system. This phenomenon could be calculated using an explicit method, but in order to realize numerical stability, it would be necessary to set low load increments, resulting in a considerable increase in calculation time. It would be desirable to accurately solve nonlinear phenomena of this type in a short period. Up to the present, the cable layout design tool has employed commercial solvers, but none have been satisfactory from the perspective of accurately outputting solutions for the phenomenon of twisting of a cable as it is bent within a short period.

In addition to convergence on solutions, the calculations have also presented issues of accuracy. Figure 3 shows a situation in which a clamp and a hose are connected, and there is local bending of the hose in the area of the connection. Because the conventional cable layout design tool is not able to generate a physical model of this phenomenon, its analytic and predictive accuracy has been inadequate, resulting in issues in terms of the accurate design of cable layouts. It was therefore necessary to newly develop a method of modeling the phenomenon of local bending of the cable, and thus increase accuracy against the conventional method.

Incorporating the stiffness of the clamp in the model would necessitate specialist knowledge of FEM modeling methods and solvers, making it challenging for designers to create the necessary FEM models in a short period. Automation would therefore be desirable in order to help enable the design of cable layouts in a short period.

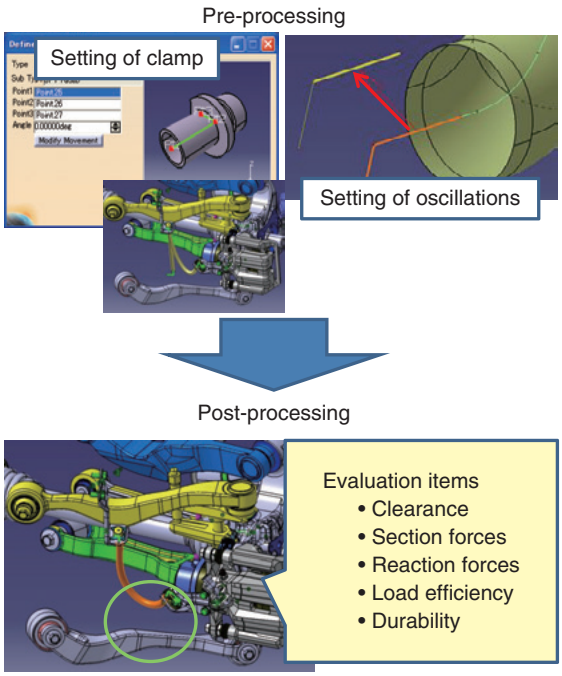


Fig. 2 In-house tool for cable layout design

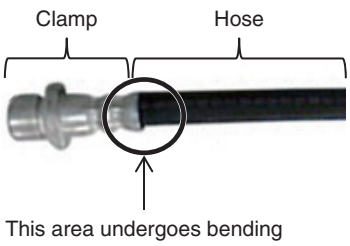


Fig. 3 Connection between clamp and hose

2. Development Aims

The following four main aims were set for the research discussed in this paper:

(1) Accurate calculation of solutions while maintaining ability of calculations to converge;
(2) Calculation speed equivalent to that of the conventional method;
(3) Calculations incorporating the stiffness of the connection with the clamp; and
(4) Equivalent level of simplicity of operation as conventional method even when designers possess no specialized knowledge in relation to solvers.

The developed solver and method of modeling the stiffness of the connection with the clamp will be discussed below.

3. Hybrid Solution

3.1. Concept

Conventionally, static implicit methods[2] have been the main methods applied to the solution of nonlinear equations that numerically model static nonlinear phenomena. Static implicit methods commence from the predicted value of the solution for the equilibrium of forces at the time a specific load is applied, and seek the solution by correcting the predicted value using iterative methods such as the Newton-Raphson method. During the repeated iterations, geometrical nonlinearity and material nonlinearity are considered[3, 4]. This method is able to accurately determine physical quantities at the time a set load is applied, and because it is a completely stable time integration method, it is also possible to use large load increments[3, 4]. The method is also able to complete calculations in a shorter period than other methods, assuming that there is no issue in terms of convergence on a solution.

However, there are occasions on which iterative calculations do not converge on a solution due to nonlinearity. An example is presented below. Figure 4(a) shows a conceptual diagram of buckling, during which the solution curve features inflection points. Because the gradient of the tangent line changes rapidly in the vicinity of these inflection points, it is challenging to determine solutions to nonlinear equations using an iterative method.

Figure 4(b) shows a conceptual diagram of the bifurcation of a solution. Because the solution for the nonlinear equation is non-unique, the solution bifurcates. For example, Points a and b in Fig. 4(b) are both on the solution curve, but while the input loads differ, they each have the same displacement. Real-world examples include cases in which a hose that has been routed settles into different states of deformation with the application of a miniscule load, and cases in which the solution mode varies rapidly, for example a thin-plate snap-through.

As this indicates, when seeking numerical solutions for strongly nonlinear phenomena, there are cases in which, when using static implicit methods, the calculations will not converge on a solution, and it will not be possible to continue the calculations. A method by means of which calculations could be conducted stably up to their conclusion was therefore desirable. Static explicit methods[5], in which solutions were successively determined while seeking equilibrium, irrespective of iterations, represented methods of this type.

Static explicit methods are methods that do not repeat iterations, but determine the value of increments, such as increases in the strain in elements or the degree of rotation of nodal points, within an allowable range. These methods make it possible to stably complete the calculation process and determine a solution, but because it is not possible to use large load increments in order to help ensure numerical stability, calculation time increases against implicit methods. Given this, it was necessary to find a means of minimizing the amount of use of static explicit methods within the entire calculation process.

A hybrid solution method was therefore proposed. Combining the advantages of the implicit and explicit methods, this hybrid method would use an implicit method in the domain within which an implicit method could generate a solution, and use an explicit method in the domain within which an implicit method could not generate a solution.

Figure 5 shows a flow chart of this hybrid method. First, solutions are sought using a static implicit method. Following this, if it is judged that the phenomenon displays strong nonlinearity and it will not be possible to find a solution using an iterative method (Condition A), the method switches to a static explicit method and continues to seek a solution. The method continues to seek a solution using a static explicit method, but if it is judged that the nonlinearity of the phenomenon has become weak and it is possible to once again seek a solution using an implicit method (Condition B), the static implicit method is returned to, and the method continues to seek a solution. This alternation continues until the calculation is concluded.

3.2. Switching from Static Implicit Method to Static Explicit Method

When it is judged that the calculation will not converge on a solution when a static implicit method is used (Condition A), the method switches to a static explicit method. The method of switching is as follows: First, when the calculation does not converge on a solution after a predetermined number of iterations, the time increments (load increments) are reduced (this is termed “cutback”), and the predetermined number of iterations is again conducted in order to have the calculations converge on a value. When cutback is repeated and the operation is performed for the set number of times without convergence on a value, it is judged that a solution cannot be found using a static implicit method, and the tool switches to a static explicit method.

3.3. Switching from Static Explicit Method to Static Implicit Method

It would be possible to continue using the static explicit method until the calculations reach their conclusion, but when it is possible to employ the static implicit method (Condition B), the tool switches to this method in order

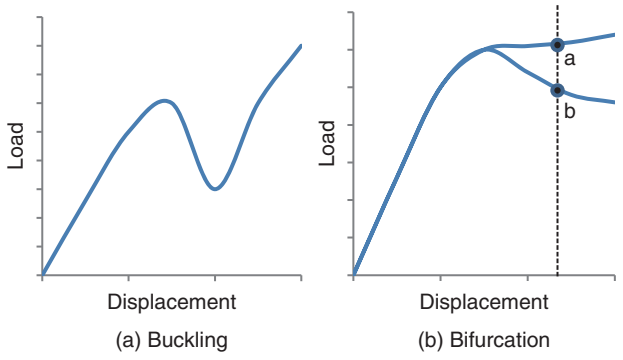


Fig. 4 Typical nonlinear phenomena

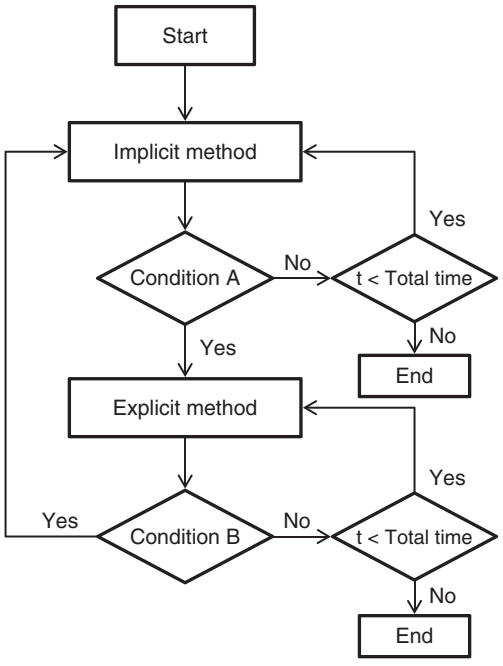


Fig. 5 Flowchart of hybrid method

to reduce calculation time. It was necessary to attempt to ensure that, having switched to the static implicit method in such a case, the tool did not immediately switch back to the static explicit method when the iterative method failed to produce a convergence in the calculations. It was therefore essential to avoid areas of strong nonlinearity, for example when buckling occurs, when switching from the static explicit to the static implicit methods.

It is known that when using a static explicit method, residual error generally increases when nonlinearity increases[5]. The developed tool therefore switches to the static implicit method when residual error is lower than a specific value.

The following two characteristics can be ascribed to buckling and the bifurcation of solutions as standard examples of the failure to achieve convergence on a solution[3), (6)]:

(1) At the point of buckling, the determinant of the stiffness matrix is zero; and
(2) At the point of bifurcation, the eigenvector and the load vector of the stiffness matrix are orthogonal.

Based on the above, a rule for judgment of switching dependent on the determinant and the eigenvector of the stiffness matrix and residual error was proposed. Because determining the eigenvalue and eigenvector of the stiffness matrix each time would increase calculation time, the tool judges whether or not it is possible to calculate these values from the residual error. In addition, even when the eigenvalue is being calculated, calculation time is reduced by applying the Sturm-Liouville theorem[7] in order to achieve a result using the minimum calculations.

The use of this method minimizes the use of static explicit methods while also controlling the decline in accuracy and the increase in calculation time.

The combination of static implicit and static explicit methods in a hybrid method as described above realized a method making it possible to accurately produce a solution even when calculations do not converge on a solution using static implicit methods.

3.4. Comparison with Conventional Solver

In order to verify the usefulness of the developed method, calculations were conducted for a model for which calculations did not converge on a solution when the conventional solver was used, using a static implicit method, a static explicit method, and the hybrid method, and time to completion of the calculations and time increments were compared. Table 1 shows the results. When the static implicit method was used, the calculations were stopped without convergence on a solution. When the static explicit method was used, the calculations were completed, but because it was necessary to reduce the total numbers of time increments, the number of time increments increased, and calculation time also increased. The calculations were also completed when the hybrid method was used, but there was also a considerable reduction in calculation time against the use of the explicit method in isolation. Table 2 shows a comparison of results for calculation time for the conventional solver and the developed solver using a model for which the conventional solver was able to converge on a solution. The results show similar calculation times for the two methods. The results discussed above demonstrated the advantage offered by the developed method.

Table 1 Comparison of three solver algorithms

	Elapsed time	Increments
Static implicit	No convergence	No convergence
Static explicit	38 min	47283
Hybrid	6 min	487

Table 2 Comparison of solver speed

	Elapsed time	Increments
Static implicit	13 sec	124
Hybrid	15 sec	132

4. Study of Method of Modeling Clamp Stiffness

As indicated in Chapter 1, because bending stiffness in the connection between a clamp and the cable is low in the case of some cables, local bending deformation occurs at the connection. However, because this stiffness has not been considered in conventional models, it has not been possible to express local bending in the calculations.

A modeling method that enabled the cable to rotate relative to the clamp was therefore formulated, and a corresponding solver function was developed. Figure 6 shows a schematic diagram of the model. A joint (“universal joint” below) giving the cable freedom of relative rotation around two axes (two axial directions are both orthogonal to cable axial direction) is defined at a nodal point at the end of a clamp and a nodal point on the cable in the same position[8]. This biaxial rotation is defined as a rotational spring. A stopper is also defined in the direction of rotation in order to regulate the angle of relative rotation[9]. A contact model was substituted in the stopper in order to function as a contact constraint[10] when the angle of rotation exceeded the threshold value.

Figure 7 shows the deformation occurring when the left end of the cable is fixed and the other end is oscillated to

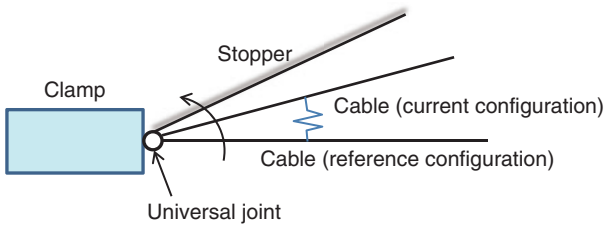


Fig. 6 Schematic image of stiffness of end of clamp

bend the cable. The incorporation of the bending stiffness of the clamp in the model has made it possible to realize values approaching actual values in the entire displacement direction of the cable.

In addition, the use of a one-dimensional model for the entire additional section has controlled the increase in the degree of freedom of the model. This means that it is possible to design cable layouts with sufficient accuracy with minimal increase in calculation time and using a simple modeling procedure.

However, the proposed modeling method involved the addition of a number of finite elements against the conventional model, and the imparting of stiffness values in response to the type of clamp employed. These operations necessitated detailed knowledge of solver use and FEM modeling tools, making it challenging for designers to conduct analyses in short periods. Modeling templates for simulations were therefore created in order to reduce the burden of modeling operations, making it possible to formulate models via simple operations using the specialized cable layout design tool. As Fig. 8 shows, when the designer selects the clamp type following the setting of coordinates for three points on the end of the cable in the specialized layout design tool (shown as red dots), the bending stiffness of the clamp, based on material characteristics, is reflected in the model in the tool, and the universal joint and contact conditions are set automatically. The use of this tool has made it possible for designers to conduct cable layout design more accurately than was previously the case.

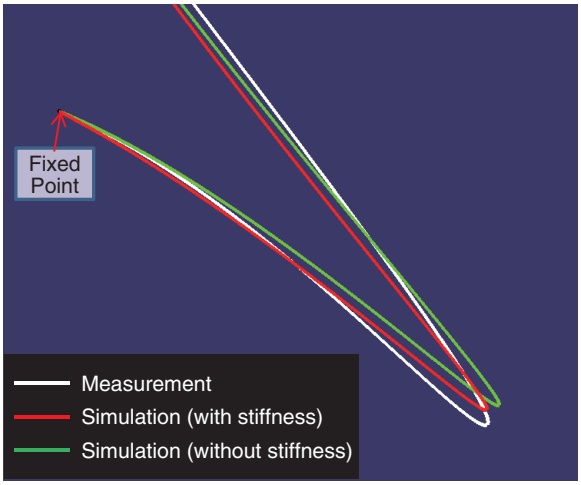


Fig. 7 Contribution of bending stiffness of clamp to cable deformation

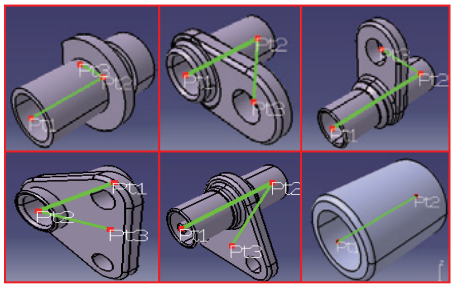


Fig. 8 Library of clamps

5. Verification

5.1. Comparison for Up-down Stroke

Simulation results were compared with measurement results for the deformation of a brake hose fitted in a vehicle positioned on a plane surface. The comparison focused on the minimum distance from surrounding parts with which there would be potential interference as calculated by the developed solver. Figure 9 shows the simulation results, and Fig. 10 shows measurement results. The distance between the hose and brackets and calipers in the same position, parts with which there might be interference, was compared. The areas compared are areas in which the radius of curvature of the cable is at its lowest, making prediction challenging, but the maximum difference

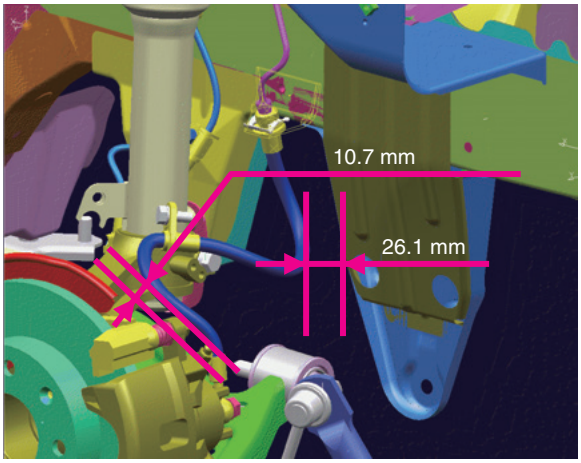


Fig. 9 Simulation result

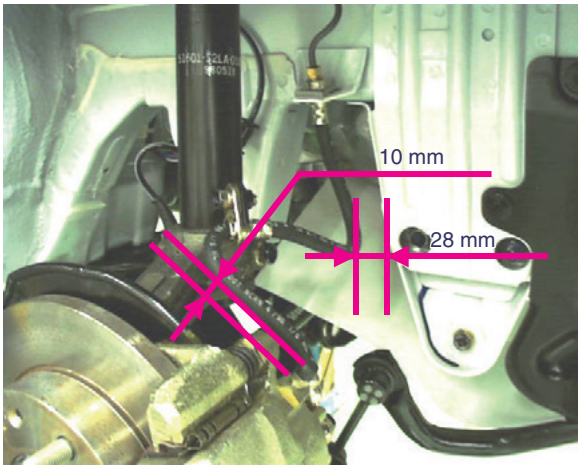


Fig. 10 Measurement result

between simulation and measurement results is around 7%, indicating that the developed method achieves sufficient accuracy for cable layout design.

5.2. Comparison with Combined Stroke and Steering Input

Figure 11 shows an example of simultaneous up-down suspension stroke and steering input. This figure compares the deformation of the brake hose following oscillation when the up-down tire stroke is ±60 mm and the steering wheel is turned a maximum of 30 deg for each stroke position. The solid line shows simulation results, and the broken line shows measurement results. The simulation is able to approximately reproduce measured values for the stroke in isolation and the stroke in combination with steering input. These results demonstrate that the developed method achieves sufficient accuracy for the design of layouts even in cases in which the brake hose undergoes a high degree of twisting as it is bent as a result of stroke and steering input.

The results of these verification tests indicated that when used by designers for the design of cable layouts, the developed method would display no issues of accuracy even when local bending occurred at clamps, and would be able to generate accurate solutions even for models for which calculations did not converge on a solution using the conventional method. The solver and library function discussed in this paper are in use as cable layout design tools in research and development centers in Japan and overseas.

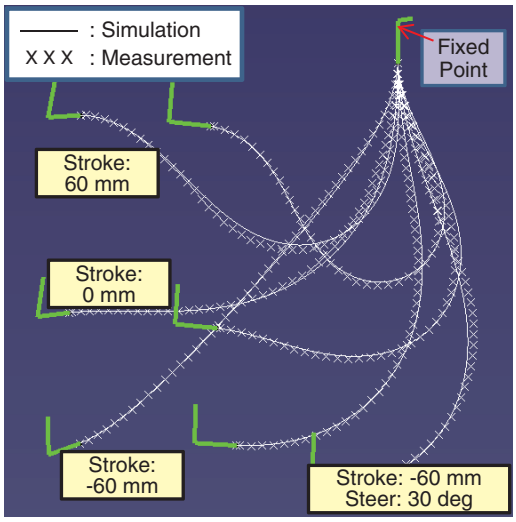


Fig. 11 Comparison of measurement and simulation results

6. Conclusion

A development was conducted in order to make it possible to accurately design automotive cable layouts in a short period.

(1) A hybrid method switching between static implicit and static explicit methods was proposed as a method of maintaining the ability of calculations to converge on solutions, and developed as an original tool.
(2) The developed method displayed similar calculation times to the conventional method even for models for which calculations converged on a solution using the conventional method.
(3) A modeling method able to incorporate the bending stiffness of connections between cables and clamps was developed, increasing analytic accuracy.
(4) The ability to select the necessary clamps from a library and the automatic generation of models within the tool has made it possible for designers to conduct analyses using simple operations, helping to enable cable layout design to be conducted in a short period.

References

(1) Bathe, K. J.: Finite Element Procedures, (2007)
(2) Belytschko, T., Liu, W., Moran, B.: Nonlinear Finite Elements for Continua And Structures: 676p., (2000)
(3) Chrisfield, M. A.: Nonlinear Finite Element Analysis of Solids and Structures, Vol. 2, Wiley, (1997)
(4) Noguchi, H., Hisada, T.: Integrated FEM Formulation for Total/Updated-Lagrangian Method in Geometrically Nonlinear Problems, JSME, Series A, Vol. 38, No. 1, p23-29, (1995)
(5) Takayuki Hama: Simulation of Tube Hydroforming by Static Explicit Finite Element Method, Doctoral Thesis, Waseda University, (2004)
(6) Yoshihiro Tomita: Numerical Elasoplastic Analysis, Yokendo, 227p., (1990)
(7) Masatake Mori: Numerical Analysis, Kyoritsu Publishing, 291p., (2002)
(8) Abaqus Theory Manual, V6. 10, (2010)
(9) Hughes, T. R. J.: The Finite Element Method, Linear Static and Dynamic Finite Element Analysis, 260p., (2000)
(10) Wriggers, P.: Computational Contact Mechanics, Springer, 518p., (2006)

■ Author ■



Takuya SHUDO

Introduction of Heat Exchanger Production Technique for Stirling Engine Using Additive Manufacturing

Masahiko ASANUMA* Tsuneo ENDO* Hitoshi SAKAI**

ABSTRACT

A prototype case with thin internal fins was created in the development of a Stirling engine with performance that exceeds that of conventional compact Stirling engines. Radial grooves are cut into the pistons located inside the case in order to avoid these fins, and high accuracy is called for to help prevent contact between the pistons and fins during operation.

Since conventional manufacturing processes are unable to satisfy these specifications, precise manufacturing was realized for the first time through additive manufacturing, that is to say, the use of a 3D printer for metal materials. However, there are also many locations where the needed specifications cannot be satisfied simply by existing additive manufacturing technology, so various manufacturing process know-how was needed.

Selection of the blade used to laminate the powder, use of reinforcing rings that are removed after molding, machining of small holes to remove powder remaining inside the structure before heat treatment, and other techniques were obtained as know-how. In addition, it was found that given sufficiently short length, molding can be performed even with a plate thickness of 0.5 mm.

1. Introduction

A prototype case that has thin radial fins inside the cylinder to increase heat transfer performance was created in the development of a compact, lightweight and high-performance Stirling engine with a target power-to-weight ratio of 1 kW per 10 kg. Fine radial grooves are cut in the pistons located inside the case in order to avoid these fins, and high shape accuracy is called for to help prevent contact during operation while at the same time minimizing the clearance with the fins. In addition, to reduce both the number of parts and the weight, a multifunctional structure is used that integrates the heat exchanger parts on the high- and low-temperature sides where the working gas circulates and the cooling water channels. The heat exchanger also uses a fine shape with millimeter-size gaps in a complex arrangement to reduce the heat exchanger size while still maintaining high performance. Since conventional manufacturing processes are unable to accommodate these specifications, this manufacturing was realized for the first time through additive manufacturing (AM), that is to say, the use of a 3D printer for metal materials.

Lamination-based 3D molding technology continues to make remarkable advances, but the main trend is typically to take shapes created with existing manufacturing processes such as casting or machining and instead use a lamination manufacturing process without modifying the shape.[(1)-(3)]

This study first investigated the characteristics of the lamination manufacturing process, and then performed design to obtain the optimum performance using shapes able to be created only by 3D technology. However, when an attempt was made to actually manufacture these shapes, many locations were found where the needed specifications could not be accommodated simply by existing AM technology. For this reason, various manufacturing process know-how was called for.

Examples of this know-how include the use of shapes consisting entirely of thin elements with minimal variation in thickness to help prevent a reduction in shape accuracy due to thermal contraction, and reducing deformation during lamination by modifying the shape of the supports removed by machining or other processing after molding. This paper introduces specific examples of manufacturing know-how obtained as a result of trial and error.

* Automobile R&D Center

** NTT DATA ENGINEERING SYSTEMS Corporation

2. Heat Exchanger Case for Stirling Engine

2.1. Structural Features

The developed Stirling engine is called a β-type. A power piston (PP, Fig. 1) that produces power and a displacer piston (DP, Fig. 2) that moves the working gas alternately between the high- and low-temperature ends are arranged coaxially, and these pistons perform reciprocating motion with a phase difference. In addition, the DP configuration has a regenerator in the middle and pistons on both the upper and lower sides. Both the PP and DP have a bore diameter of 58 mm and a stroke of 23 mm.

Normal Stirling engines have fins that promote external heat exchange located on only the outside of the cylinder. In contrast, a characteristic of the developed Stirling engine is that radial fins are also provided inside the cylinder to promote heat exchange with the working gas at the inner wall surface. Fine radial grooves are cut into the pistons located inside the case to avoid these fins, and high shape accuracy is called for to help prevent contact during operation while at the same time minimizing the clearance with the fins.

The overall case consists of two parts: a high-temperature upper case with sheet metal fins brazed to the outside (Fig. 3) and a low-temperature lower case (Fig. 4). The upper case contains radial fins and a heat exchanger located around its inner circumference that heats the working gas as the gas moves. The lower case also contains radial fins and a heat exchanger located around its inner circumference that cools the working gas as the gas moves, and these are surrounded by a water jacket through which cooling water flows (Fig. 5). These parts are all integrated to form a multi-functional compound case. In addition, the heat exchanger uses a fine shape with millimeter-size gaps in a complex arrangement to reduce the heat exchanger size while still maintaining the performance.

Since conventional manufacturing processes are unable to accommodate these specifications, this manufacturing was realized for the first time by AM, that is to say, the use of a 3D printer for metal materials.

2.2. Needed Accuracy

In order to reduce weight, the pressure-resistant vessel that holds the high-pressure gas is only 1 mm thick, and a machining margin of 0.2 mm is removed by finish machining. In addition, the radial fin thickness is 0.5 mm and the radial grooves cut into the pistons to avoid the fins have a width of 0.9 mm to 1.2 mm, so the groove clearance is just 0.2 mm to 0.35 mm. Therefore, strict accuracy is called for with respect to the circularity of the cylindrical case and the straightness and thickness of the fins.

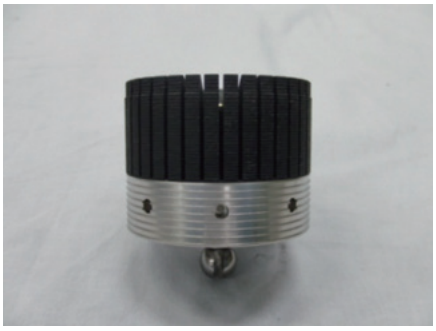


Fig. 1 Power piston



Fig. 2 Displacer piston

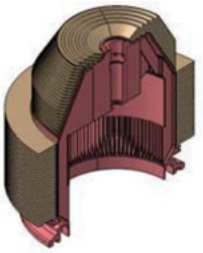


Fig. 3 Upper case

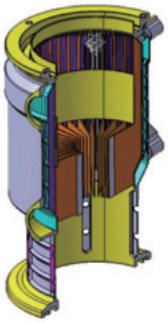


Fig. 4 Lower case

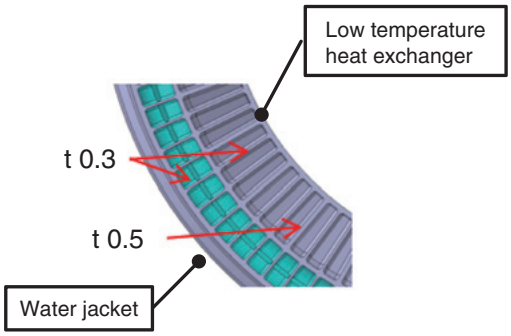


Fig. 5 Water jacket and heat exchanger of lower case

3. AM Device

3.1. AM Device

An EOSINT M270 was used for molding. Table 1 lists the device specifications. Heat-resistant alloy powder was used as the material. Figure 6 shows a photograph of the device exterior and controller screen. Molding is performed while flowing an inert gas (N_2) into the small chamber inside the device where laser irradiation is performed in order to reduce oxidation.

3.2. Prototype Model

Two sets each for a total of four upper and lower cases were manufactured simultaneously as prototype models. In addition, cutout test pieces for material verification to check the inside of those cases were also molded at the same time. The lamination molding time excluding the previously prepared base plate was 140 hours. Figure 7 shows the molding model.



Fig. 6 Additive manufacturing device

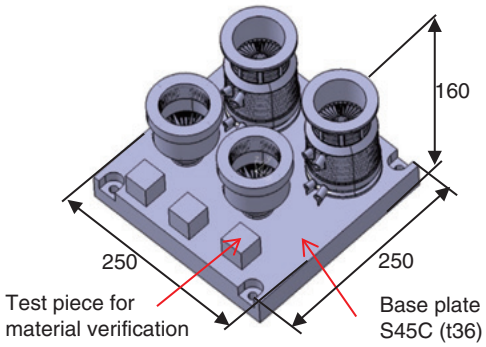


Fig. 7 Molding model

Table 1 Molding conditions

Device name	EOSINT 270
Powder materials	Co-Cr-Mo
Powder grain size [μm]	30 - 40
Laser output [W]	200
Spot diameter [mm]	0.1 (minimum)
Scan speed [mm/s]	800 (maximum)
Laminating thickness [μm]	40
Blade	Carbon brush
Building size [mm]	250X250X215

The product was molded by repeatedly using a plate called a blade to lay a thin layer of powder material at a constant thickness while applying a load and then melting the areas to be molded with a laser to laminate from the bottom up in 40-μm increments. Figure 8 shows photographs of the molding process.

4. Prototype Manufacture

The prototype was an unprecedented shape for Honda as well as the specialized manufacturer, so trial manufacture and modification were repeated three times before finally realizing a finished product.

4.1. Radial Fin Reinforcing Ring and Carbon Brush

Maintaining the molding accuracy of thin radial fins with a plate thickness of 0.5 mm was anticipated to be challenging even before prototype manufacture. Therefore, a reinforcing ring that is removed in a subsequent process was added with the goal of increasing the strength to reduce deformation during molding (Fig. 9).

As a result, the radial fins did not deform and sufficient accuracy was secured, but the fin shape deformed in the area where the fins intersect the micro heat exchanger partitioning blade (Fig. 10). This is assumed to occur



(a) Preparation for recoating of material powder (b) Recoating of material powder (c) Laser irradiation

Fig. 8 Molding process

because the powder is laid while pressing strongly with a metallic or ceramic blade to increase the powder density as much as possible. Therefore, a carbon brush was used like a broom to address this issue (Fig. 11).

When a carbon brush is used with thick parts, the issue of uneven powder density arises and there is the concern of a drop in relative density. However, it was found that a drop in density is not an issue when used with a thin shape such as a fin. This was confirmed in the material inspection described hereafter.

4.2. Reinforcing Ring for Long Vertical Fins around Lower Case Periphery

Use of a carbon brush refined the radial fins, but next undulation occurred in the low-temperature fin-type heat exchanger around the periphery of the lower case (Fig. 12).

Therefore, like the radial fins of the upper case, a thin reinforcing ring covering the exposed parts of the fins was added as a countermeasure with the assumption of removal by subsequent machining. A new prototype with this reinforcing was manufactured, and it was found that there was no undulation after reinforcing ring removal (Fig. 13).

The upper case has similar vertical fins around the periphery inside the case, but it was found that undulation did not occur over short distances of approximately 2 cm or less, such as areas hidden by the upper case and the radial fins (Fig. 14).

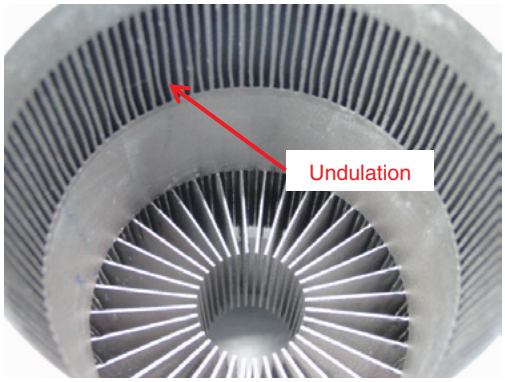


Fig. 12 Vertical fins (0.5 mm thickness) with undulation

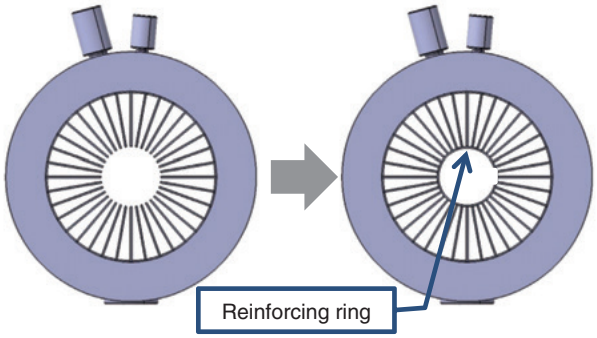


Fig. 9 Reinforcing ring

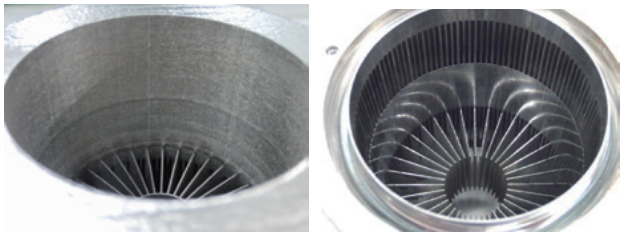


Fig. 13 Reinforcing ring before machining (left) and after machining (right)

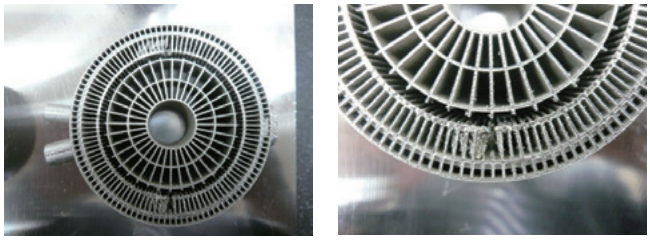


Fig. 10 Fin damage

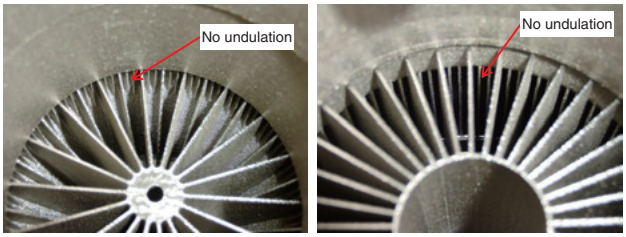


Fig. 14 Short vertical fins without undulation



Fig. 11 Conventional metal and ceramic blades and carbon blade

4.3. Holes for Removal of Residual Material

As a result of attaching a reinforcing ring as an undulation countermeasure for the low-temperature fin-type heat exchanger around the periphery of the lower case, powder remaining inside the case congealed in the heat treatment stage and became a challenge to remove (Fig. 15). The reason for this is thought to be that diffusion bonding occurred when the temperature was raised to 1050°C by heat treatment after molding.

It was found that when a fine structure has small gaps with a deep shape and no through outlet, such as those formed by attaching reinforcing rings in this manner, the sedimented material powder congeals due to diffusion bonding during heat treatment after molding. Therefore, it is important to consider ways to remove this powder in advance (Fig. 16).

As a countermeasure, small holes were opened in the reinforcing rings for powder removal, and the sedimented powder was removed before heat treatment. Small holes were opened in the three supports that are removed by machining after molding (Figs. 17 to 19).



Fig. 15 Congealed powder remaining after machining work to remove reinforcing ring

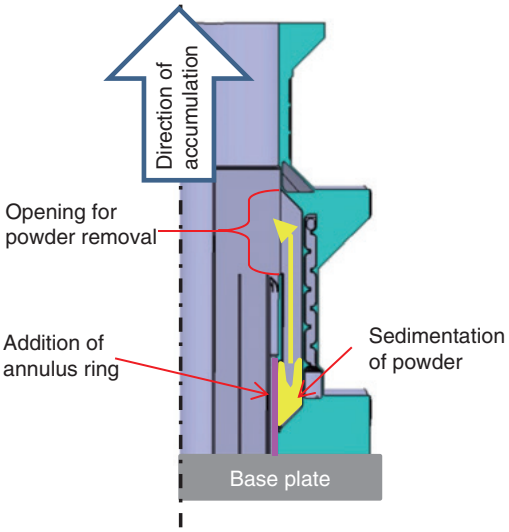


Fig. 16 Section of lower case

4.4. When Adjacent Part Thickness Differs such as Bosses

In the area around the boss where thin and thick parts are adjacent, molding resulted in a screw hole center offset of 1 mm or more. The reason for this is thought to be

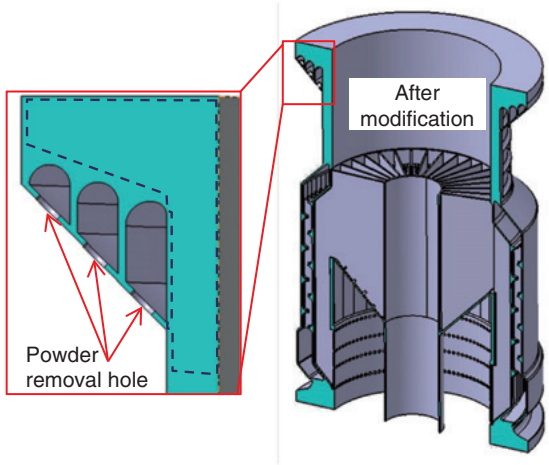


Fig. 17 Powder removal hole-1

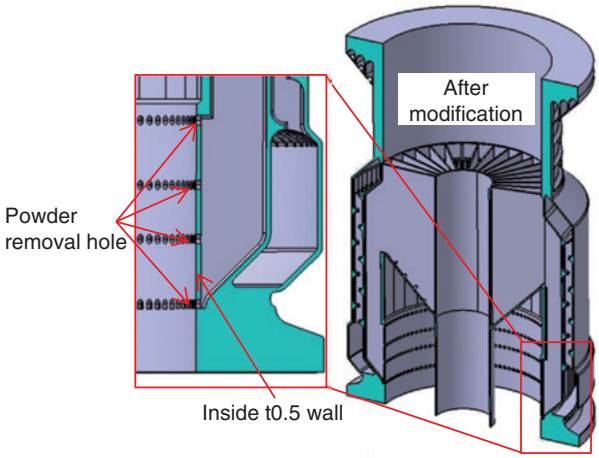


Fig. 18 Powder removal hole-2

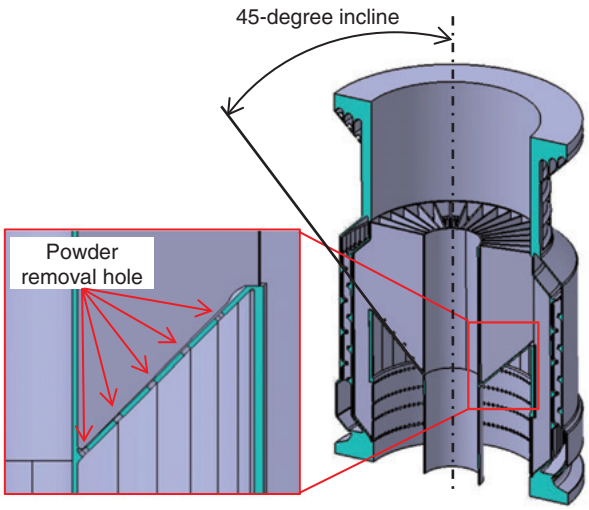


Fig. 19 Powder removal hole-3

deformation due to thermal contraction.

In cases like this it is important to modify the design so that all parts are as close to the same thickness as possible, such as by using a constricted shape at the base of the boss and opening a pilot hole beforehand (Fig. 20).

4.5. Brazed Parts and Finish Machining

The heat exchanger fins on the outside of the upper case consist of sheet metal pressed parts brazed to the case. This is because it is necessary to use a shape consisting of stacked upward facing conical shapes with an angle smaller than 45° and parallel disks, so it was determined that lamination-based molding could not be used. However, the combination of metal lamination and brazing technology enabled fabrication (Fig. 21).

Electric discharge was initially attempted as the finish machining method to remove the reinforcing ring (sleeve inner diameter), but sufficient surface roughness could not be secured, so this was changed to grinding using a grindstone.

Grooves for mounting the neodymium magnets used to float the piston and other shapes were also machined in the lower case (Fig. 22).

5. Inspection

5.1. Confirmation of Powder Removal by X-ray Inspection

The SMX-225CT-SV3 Micro-focus X-ray CT System (tube voltage: 225 kV) made by Shimadzu Corporation was used as the inspection device. Sectional inspection measured multiple cross-sections where powder easily remains. Figures 23 and 24 show the inspection device and the sectional inspection locations.

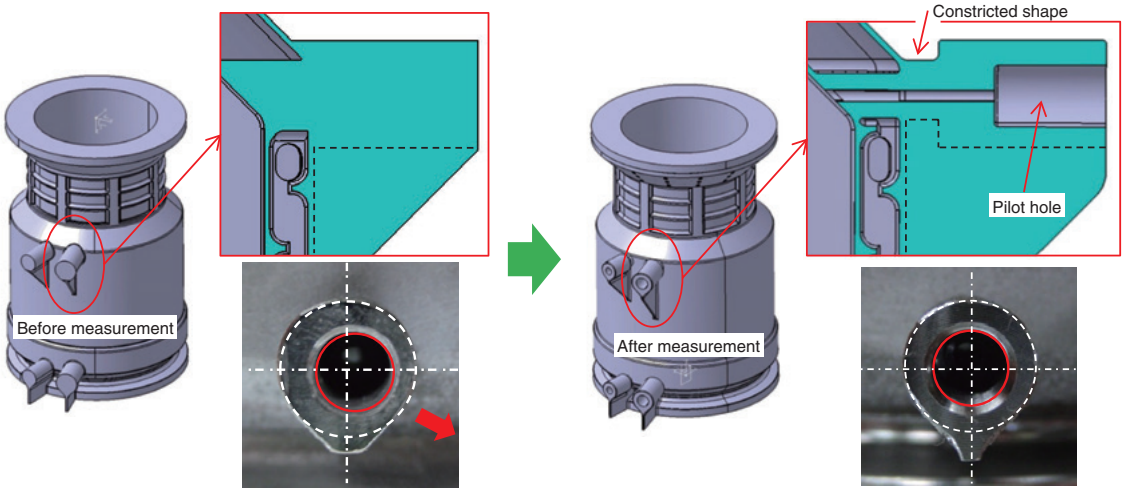


Fig. 20 Modification of boss shape



Fig. 21 Upper case

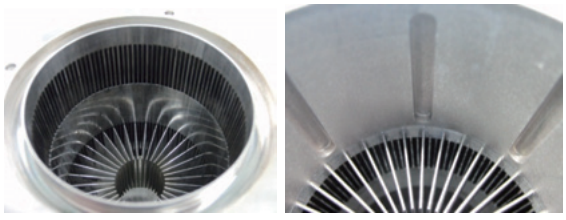


Fig. 22 Lower case



Fig. 23 Shimazu Micro-focus X-ray CT System (SMX-225CT-SV3)

X-ray imaging enabled to confirm that the powder had been removed from all locations as a result of opening small holes in the reinforcing rings (Figs. 25 and 26).

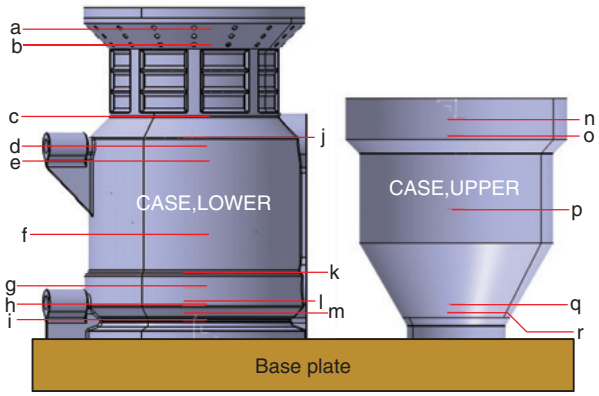


Fig. 24 X-ray measurement sections a - r

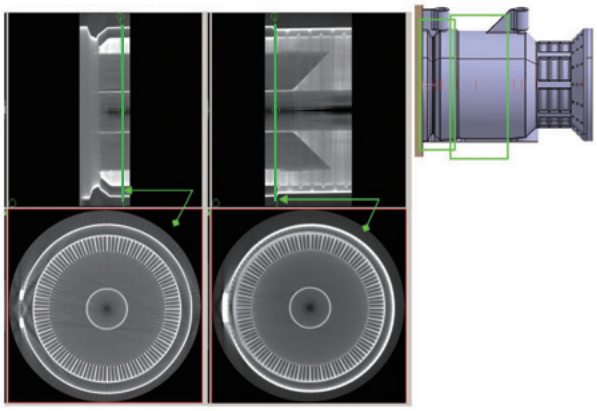


Fig. 25 Lower case sections (radial fins)

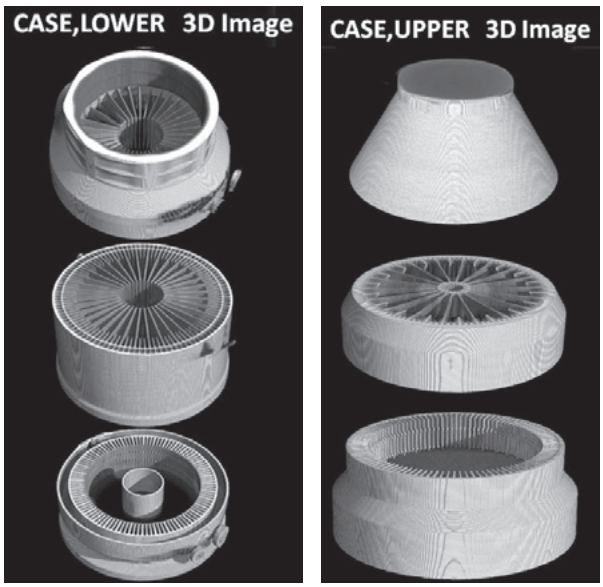


Fig. 26 Lower and upper case sections

5.2. Dimensional Inspection

High diameter accuracy and cylindricity are needed to realize a fine clearance between the case inner diameter and the pistons. Machining cannot be performed after molding in the cylinder area at the base of the fins (Fig. 27), so 3D measurement was performed during the initial molding to measure the deviation from the design value and perform calibration. As shown in Fig. 28, the product was molded with an inner radius approximately 0.2 mm smaller than the design value due to thermal contraction. In addition, the radius variation was 0.17 mm (max.), so taking into account thermal contraction provided prospects for achieving the needed tolerance of 0.2 mm.

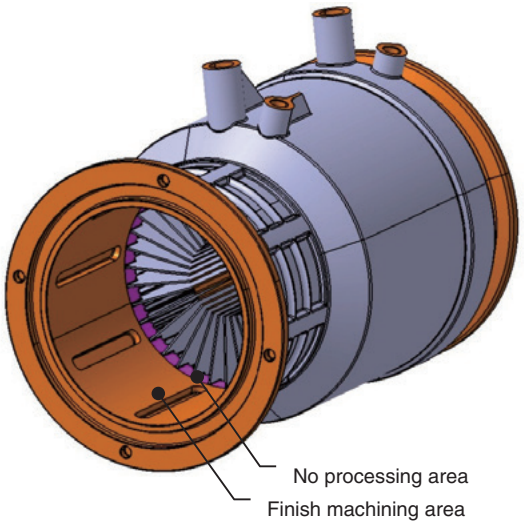


Fig. 27 Area where finish machining cannot be performed

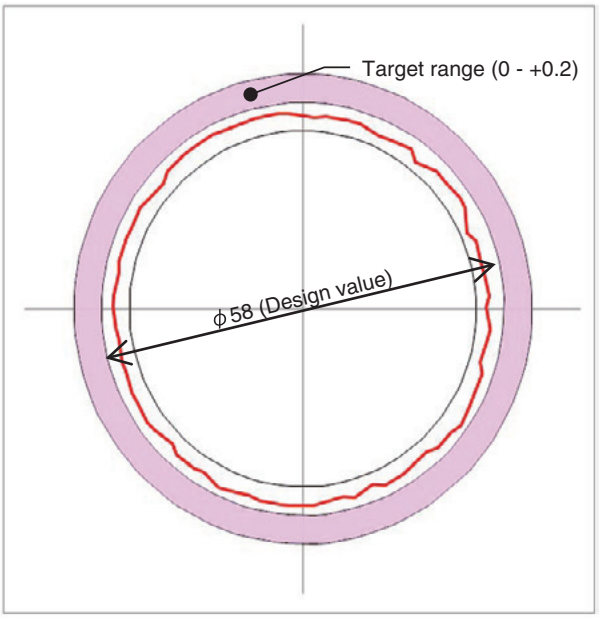


Fig. 28 Examination for dimension calibration

Table 2 Density of test pieces

Test piece	Volume [cm^3]	Mass [g]	Density [g/cm^3]
1	8.10	67.75	8.36
2	8.25	69.00	8.36
3	8.37	69.70	8.33
Average	-	-	8.35

Ultimately, the needed tolerance was secured using a diameter setting value of 58.4 mm, which is a slight increase in consideration of contraction.

5.3. Material Characteristics Inspection

It was confirmed that use of a carbon brush did not result in material imperfections.

5.3.1. Verification of density

Measurement by the water suspension (displacement) method using a digital densitometer confirmed that the density was the same level as the material data (8.3 g/cm^3) (Table 2).

5.3.2. Verification of hardness

The hardness was measured using a Rockwell hardness tester. The hardness tester used a 120° diamond cone with a tip radius of 0.2 mm, and applied a load of 150 kgf.

Figure 29 shows the results of measuring the test pieces with a hardness tester. The X/Y axis indicates the planar direction and the Z axis indicates the lamination direction. The hardness in the planar direction tended to be somewhat lower than the material data (35 to 45 HRC), but was determined to be a level that does not pose issues for practical use.

5.3.3. Inspection of internal quality by optical microscope

Structural inspection of the surface layer and the interior (10 mm to 20 mm) did not find any detrimental imperfections.

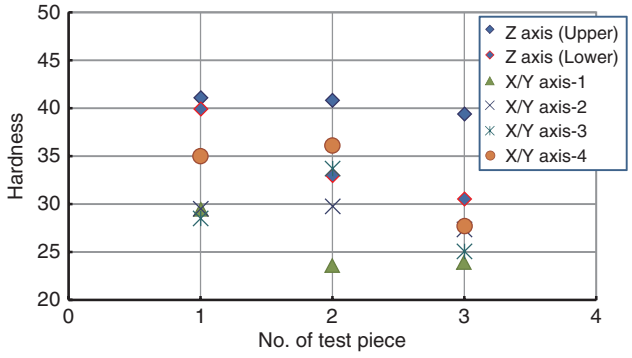


Fig. 29 Comparison of test piece hardness (HRC)

6. Summary of Design Method

6.1. Constraints

AM is a lamination molding method that stacks powder materials from the bottom up, one layer at a time. Therefore, shapes that hang down from above are supported from below by structures called supports that need to be removed after molding. In addition, even when stacking from the bottom up, there is the constraint that stacking cannot be performed at an angle of less than 45°.

Furthermore, when used for typical structures, AM is said to be unsuitable for thin plates with a thickness of 1 mm or less as deformation increases in these cases, although this also depends on the powder grain size. In fact, when structures with a fine construction such as those described in this paper are molded without any countermeasures, deformation sometimes occurs in thin locations.

6.2. Design Know-how

Changing the blade that lays the powder to a carbon brush reduces the pressing load and helps to prevent shape deformation even when molding thin plates.

Long and thin fins with a plate thickness of 0.5 mm can be molded without deformation by attaching reinforcing rings that are removed after molding. Short fins such as the heat exchanger fins with a length of 2 cm or less do not deform even when the plate thickness is 0.5 mm. Likewise, the fins inside the water jacket also have a fine structure with a plate thickness of 0.3 mm, but molding could be performed without issue over short lengths of several millimeters.

When the addition of reinforcing members creates pockets with no through outlet, it is necessary to create small holes to remove the powder remaining inside before heat treatment.

When thin plate shapes are adjacent to thick parts such as a boss or flange, deformation can be effectively reduced by opening a screw pilot hole in the boss beforehand or otherwise reducing the variation in thickness.

In locations where lamination molding cannot be used, such as the conical fins around the outside of the upper case, parts created using different forming processes (e.g., sheet metal pressed parts) can also be attached by brazing or the like.

In locations where machining cannot be performed and high material dimension accuracy after lamination is called for, the amount of dimensional change due to thermal contraction should be measured beforehand and calibration performed.

7. Conclusion

The latest AM technology was used to manufacture a prototype case with built-in heat exchanger for a Stirling engine that has high molding accuracy and a precise and complex shape. During the course of this process, it was

found that various modifications are needed in addition to conventional know-how.

These included the use of a carbon brush to effectively reduce the pressing force of the blade in the manufacturing device; modification of the support shapes that are removed by machining after molding to help prevent deformation during lamination molding; and opening holes to completely remove residual powder before heat treatment.

It was demonstrated that by introducing this new know-how from the design stage, products with precise and complex shapes that cannot easily be imitated by other manufacturing processes can be manufactured by metal lamination.

References

(1) Niino, T., Anzai, M.: Trend of Lamination Model Technology - Selective Laser Sintering (SLS) Method as the Main Subject, SOKEIZAI, Vol.48, No.7, p.1-5, (2007)
(2) Sakai, T.: New Production Method “Additive Manufacturing (AM)” Its Use and Vital Point, SOKEIZAI, Vol.54, No.2, p.47-53, (2013)
(3) Kikawa, K.: Application of Metal Additive Manufacturing in Automotive Industry, Japan Society of Mechanical Engineers annual conference, No.15-1, (2015)

Author


Masahiko ASANUMA


Tsuneo ENDO


Hitoshi SAKAI

Stir-casting Process and Mechanical Properties of Forged Mg-Zn-Y Alloys for Piston

Yuichi IENAGA*

ABSTRACT

Research has been conducted on a high-strength, heat-resistant extruded and forged magnesium alloy able to be formed into large-diameter ingots, with a view towards application in pistons for internal combustion engines, parts in which weight savings are sought. The addition of Zr to an $Mg_{96}Zn_2Y_2$ (at.%) alloy with a long-period stacking ordered structure phase refined the crystal grains. In addition, the use of a new casting method in which the ingot case is rotated and the molten metal is agitated helped to prevent segregation and the coarsening of the crystal grains, in order to make it possible to form large ingots (diameter: 335 mm; height: 850 mm) for extrusion displaying fine and uniform microstructures. Following formation of extruded pieces of 100 mm in diameter at an extrusion ratio of 10, dummy piston shapes were forged, and the mechanical properties of the material were measured before and after forging. From room temperature to 573 K, the developed alloy displayed tensile and fatigue strength in excess of commercial aluminum alloys. The alloy displayed a 0.2% yield strength of 209 MPa at 523 K following forging, approximately twice that of the high-strength aluminum alloy A4032-T6 that is used as a piston material. The addition of a high specific gravity element had minimal effect on the alloy's density, and reduced its weight to approximately 70% that of aluminum alloys. Given the above, the developed Mg-Zn-Y forged alloy can be considered to be an extremely promising material in terms of realizing fuel efficiency and performance increases through the achievement of weight reductions in automobile, motorcycle and power product pistons.

1. Introduction

Magnesium alloys are the lightest metal materials in practical use, and are expected to contribute to addressing environmental issues, for example through the realization of increased fuel efficiency in automobiles, motorcycles, and power products. It is known that the strength of Mg-Zn-Y alloys, which have a long-period stacking ordered structure (LPSO) phase, increases significantly even at high temperatures when they are subjected to extrusion processing and their microstructure is refined[(1), (2)]. However, these materials have not been reported as possessing good mechanical properties for the large-diameter extruded materials used in pistons, nor has a casting process for the large ingots used to manufacture pistons been reported. This is because in large ingots the low speed of solidification and uneven temperature distribution can produce coarsening of the crystal grains and solidification segregation, with the result that a homogeneous material cannot be obtained. As a result, it has not been possible to obtain adequate mechanical properties (tensile characteristics and fatigue strength) in tests conducted on small test pieces. The research discussed in this paper therefore sought to develop a heat-resistant magnesium alloy for casting possessing higher strength than conventional heat-resistant aluminum alloys, and developed an alloy composition for large ingots, a casting method, and extrusion and forging conditions.

2. Research Method applied to Forged Alloy

Subjecting Mg-Zn-Y alloys to plastic working processes such as extrusion gives the materials strength characteristics exceeding those of heat-resistant aluminum. In addition to compound strengthening when the material is cast, this effect is due to work hardening during extrusion, texturing and refinement of the crystal grains, and kink band strengthening[(3), (4)]. However, when ingots of this material are increased in size to help enable its practical use, the coarsening and non-uniform dispersion of the as-cast microstructure (the LPSO phase) and other compound phases mean that using conventional methods, the target strength and ductility cannot be realized. The present research was therefore advanced with a focus on three processes – casting, extrusion, and forging.

At the commencement of the project, casting experiments were conducted with a focus on the refinement

* Power Products R&D Center

of the crystal grains and the realization of a uniform microstructure, two of the factors in strengthening the material discussed above. Compared to metals such as iron or aluminum, the contribution of refinement of the crystal grains to increased strength is high in the case of magnesium[5]. In the research under discussion, the crystal grains were refined through the addition of Zr, which has a high melting point and could be expected to form the point of origin for the formation of crystal nuclei[6]. In addition, nucleus formation was promoted by rotating the ingot case and agitating the melt inside the case. In the standard casting process, the ingot solidifies from the wall of the mold inwards, with the center of the ingot the last section to solidify. This results in the segregation of concentrated eutectic components in the center of the ingot. Rotation and agitation controls solidification commencing from the mold wall until the center of the ingot is at solidification temperature. Because this would mean that solidification would commence close to solidification temperature and be completed in a short period of time, it was expected that this method would significantly reduce solidification segmentation.

Next, ingots for extrusion were produced with varying compositions and under varying conditions. The basic characteristics of the developed alloy were studied and compared with existing magnesium alloys and aluminum alloys.

Finally, the material was forged into dummy piston shapes and evaluated. It was verified that forging temperature influenced the occurrence of forging defects and tensile characteristics. The material displayed a higher level of performance than heat-resistant aluminum alloy in unit endurance tests.

3. Test Method

An $Mg_{96}Zn_2Y_2$ alloy and an $Mg_{95.8}Zn_2Y_2Zr_{0.2}$ alloy were employed as test materials for the study. Table 1 shows representative values for the materials determined through analysis of their chemical composition. For melting and casting, a turntable was positioned in a vacuum melting furnace, as shown in Fig. 1. The alloys were melted in an iron crucible in an Ar gas environment using high-frequency melting equipment. 200 kg of each of the alloys were poured into ingot cases of 1,200 mm in height, with internal diameters of 335 mm. The ingot cases were rotated to produce agitation as the melt was poured. Conditions that would effectively agitate the melt without causing excessive disturbance were determined from water models. The ingot cases were rotated at 30 rpm, reversing every 35 sec, until the melt solidified. For the purpose of comparison, ingots were also cast without agitation. The ingots were peeled to 305 mm in diameter, and extruded at diameters of 100 mm at a temperature of 623 K. Finally, the extruded alloys were sliced and forged into dummy piston shapes after pressing in a 1,000-ton hydraulic press at material temperatures of 598-783 K for 30 min. In order to evaluate the ingots, vertical cross-sections were taken, and inductively coupled plasma emission spectrometry (ICPES) and optical microscopy (OM) were employed to analyse chemical composition and observe as-cast microstructures. Phases formed following casting and extrusion were identified using x-ray diffraction (XRD) and energy-dispersive x-ray spectrometry (EDS), and microstructures were observed using scanning electron microscopy (SEM).

Table 1 Chemical composition of Mg-alloys used in this study (at. %)

	Zn	Y	Zr	Mg
$Mg_{96}Zn_2Y_2$	1.96	2.10	-	Bal.
$Mg_{95.8}Zn_2Y_2Zr_{0.2}$	1.93	1.85	0.27	Bal.

Mechanical properties were evaluated in tensile tests, tension and compression fatigue tests, and creep tests. Tensile tests employed micro test pieces of 3 mm in diameter in parallel sections, and with 15 mm between reference points. A strain rate of 5×10^{-4}/s and temperatures of 298-573 K were used in tensile tests. Fatigue tests were conducted using micro test pieces of 3 mm in diameter in parallel sections, and with 8 mm between reference points. The stress ratio was R=-1, at sine wave frequencies of 20-40 Hz, with a maximum number of repetitions of 10^7 and a test temperature of 473 K. Creep tests used micro test pieces of 3.65 mm in diameter in parallel sections, with 28 mm between reference points, and were conducted at a temperature of 573 K and a pressure of 50 MPa. The laser flash method specified by JIS R 1611 was used to measure thermal conductivity, and the thermomechanical analysis method specified by JIS R 1618 was used to measure the coefficient of thermal expansion. The ultrasonic method specified by JIS Z 2280 was used to measure Young's modulus, and Archimedes' principle, as specified by JIS Z

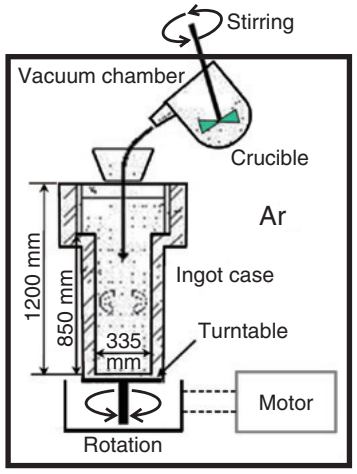


Fig. 1 Method of ingot casting in vacuum melting furnace using turntable

8807, was used to measure density. Values for the alloys were compared with values for existing materials.

4. Test Results and Discussion

4.1. Analysis of Stir-cast Ingots

4.1.1. Distribution of chemical composition

The results of analysis of the chemical composition of the ingots following casting showed that in the ingots cast using a conventional method, with no agitation, Zn and Y had become concentrated at 270 mm from the bottom of the ingot and above, and exceeded 2.25 at.%, higher than the 2.00 at.% allowable limit. The Zr added in order to refine the crystal grains was concentrated at a height of 140 mm, and exceeded 0.60 at.%. Zn and Y are constituent elements of the crystalline phase, and it was considered that they concentrated in the sections of the ingot that were the last to crystallize. Because Zr has a high melting point, a low solid solubility limit, and a high specific gravity at 6.52, it is considered that gravity segregation affected the unmelted Zr. By contrast, the stir-cast alloys were within the 10% acceptable limit for target chemical composition, including distribution in the radial direction.

4.1.2. As-cast microstructure

Figure 2 shows changes in the as-cast microstructures of the $Mg_{96}Zn_2Y_2$ and $Mg_{95.8}Zn_2Y_2Zr_{0.2}$ alloy ingots in the height direction of the central axis, and includes differences between stir-cast and conventionally cast ingots. The conventionally cast $Mg_{96}Zn_2Y_2$ alloy ingot [Fig. 2(a)] displays increased crystal grain diameter (2 mm and above) in the region above a height of 530 mm. By contrast, in the stir-cast $Mg_{96}Zn_2Y_2$ alloy ingot [Fig. 2(b)], the crystal grain diameter is uniform in all regions in the direction of height. This indicates that the crystal grains coarsened in the areas of the ingot produced by conventional casting that were the last to solidify, because the ingot solidified slowly from the bottom and walls of the ingot case towards the top or the center, while in the stir-cast ingot, solidification did not commence until the center of the ingot reached solidification temperature, and actual solidification time was short, controlling coarsening and segregation. Similarly, in the conventionally cast $Mg_{95.8}Zn_2Y_2Zr_{0.2}$ alloy ingot [Fig. 2(c)], crystal grains are fine at a height of 10 mm above the bottom of the ingot case but become progressively coarser towards the top. By contrast, in the stir-cast $Mg_{95.8}Zn_2Y_2Zr_{0.2}$ alloy ingot [Fig. 2(d)], crystal grains are fine at approximately 0.1 mm in all regions in the direction of height and a homogeneous as-cast microstructure has been achieved. Because the crystal grains in the case of the stir-cast ingots were noticeably finer than was the case for other as-cast microstructures, it was judged that stir-casting contributed significantly to promoting the formation of crystal nuclei.

The results discussed above demonstrated that the new stir-casting method had realized initial goals set for controlling the coarsening of the crystal grains and the segregation of the chemical composition of the alloy when the ingots were increased in size. Together with the addition of Zr, the new casting method refined the alloy crystal grains and realized a homogeneous microstructure.

4.2. Analysis of Extruded Material

4.2.1. Microstructure

Figures 3 and 4 show XRD patterns and photographs of the microstructures of the $Mg_{95.8}Zn_2Y_2Zr_{0.2}$ alloy ingot before and after extrusion. This alloy is made up of α-Mg, $Mg_{12}ZnY$ (LPSO) and $Mg_3Zn_3Y_2$ phases, and there is no change in the constituent phases following extrusion. However, there are differences in the form of each phase. Before extrusion, the LPSO phase is insular, as shown in Fig. 4(a). Following extrusion, the LPSO phase becomes extended in the direction of extrusion [Fig. 4(c)]. In the case of the $Mg_3Zn_3Y_2$ phase, before extrusion the phase displays a coarse reticulated structure [Fig. 4(b)], while following extrusion it transforms into a sub-micron fine crystal grain structure, as shown in Fig. 4(d).

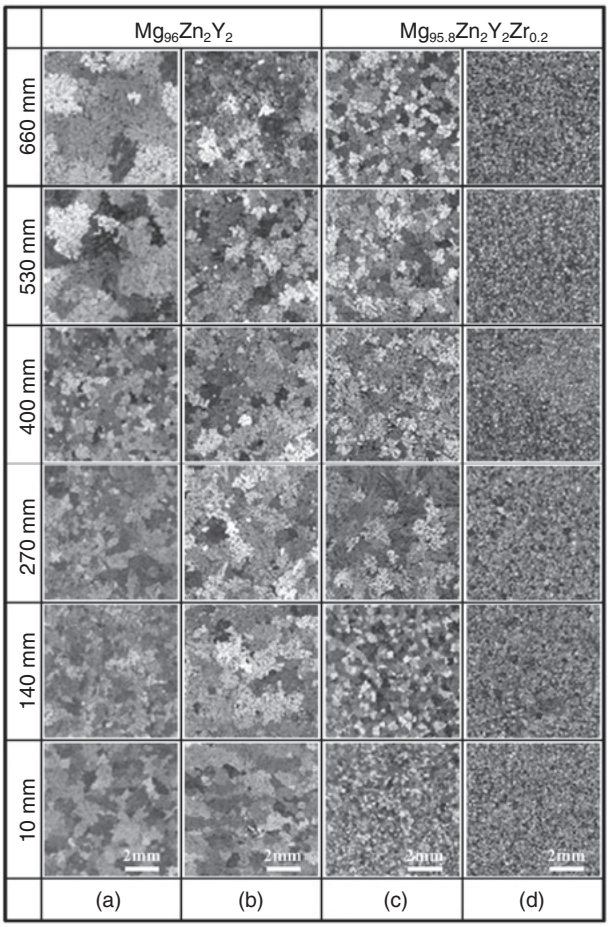


Fig. 2 Optical microscope images at various distances from base of ingot: (a) Conventional casting; (b) Stir-casting; (c) Conventional casting with Zr; and (d) Stir-casting with Zr

4.2.2. Mechanical properties

Figure 5 shows the test temperature dependence of 0.2% yield strength ($\sigma_{0.2}$) in the $Mg_{96}Zn_2Y_2$ and $Mg_{95.8}Zn_2Y_2Zr_{0.2}$ alloys from room temperature to 573 K, including lab data for small test pieces of 9 mm in diameter. 0.2% yield strength for the commercially available heat-resistant magnesium alloys WE54-T6 and RZ5-T5 and the aluminum alloy A4032-T6 is also shown for the sake of comparison. The developed alloys not only display greater yield strength than the commercially available heat-resistant magnesium alloys, but their yield strength also exceeds that of A4032-T6. It is noteworthy that at 523 K, the 0.2% yield strength of the developed alloys is approximately twice that of A4032-T6 at 208 MPa or higher, and almost three times higher at 573 K. In addition, by contrast with A4032-T6, which displays a significant decline in strength at 473 K and above, no sudden decline in the strength of the Mg-Zn-Y alloys was observed up to 523 K. The Mg-Zn-Y alloys display increasing strength in proportion to the refinement of their crystal grains, but this strength increase reverses at 573 K. Figure 6 shows differences in surfaces of the $Mg_{95.8}Zn_2Y_2Zr_{0.2}$ alloys fractured at 298 K and 573 K in order to elucidate this phenomenon of reversal of strength increase. Figure 6(a) shows a ductile fracture producing fine dimples, while Fig. 6(b) shows a grain boundary fracture producing large voids corresponding to the diameters of crystal grains, as indicated by the arrows in the figure[7]. Based on the fact that dimples can be observed in fracture surfaces up to 473 K, it was conjectured that between 523 and 573 K, there is a change in the fracture morphology, and alloys with large-diameter crystal grains

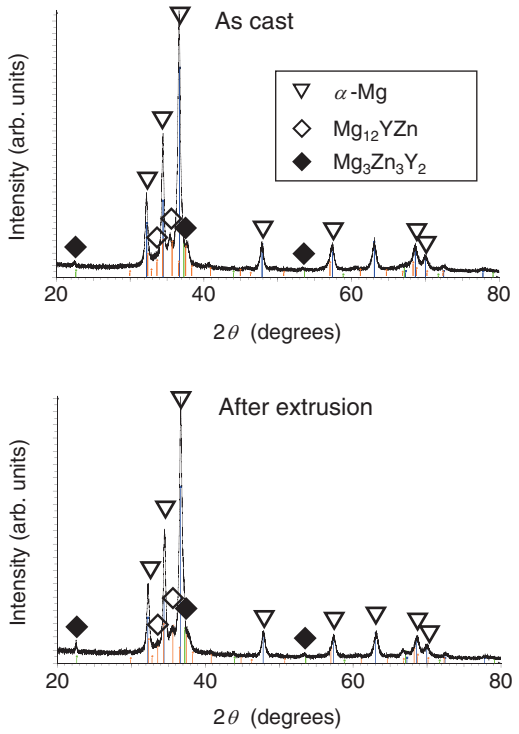


Fig. 3 XRD patterns of $Mg_{95.8}Zn_2Y_2Zr_{0.2}$ alloy before and after extrusion

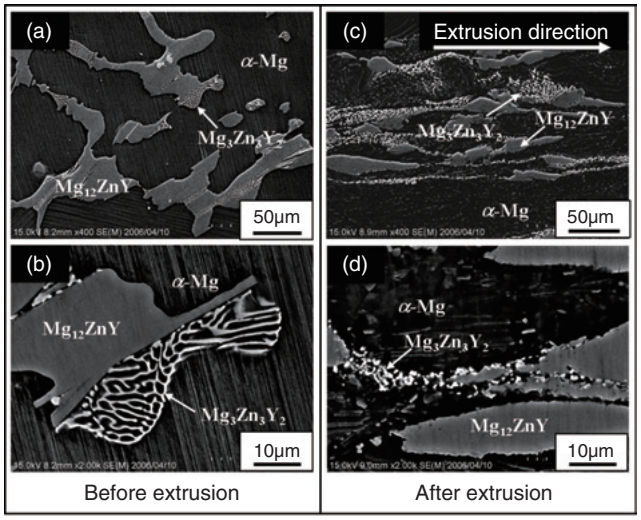


Fig. 4 Microstructures before ((a) and (b)) and after ((c) and (d)) extrusion; (a) and (c) shown at low magnification and (b) and (d) at high magnification

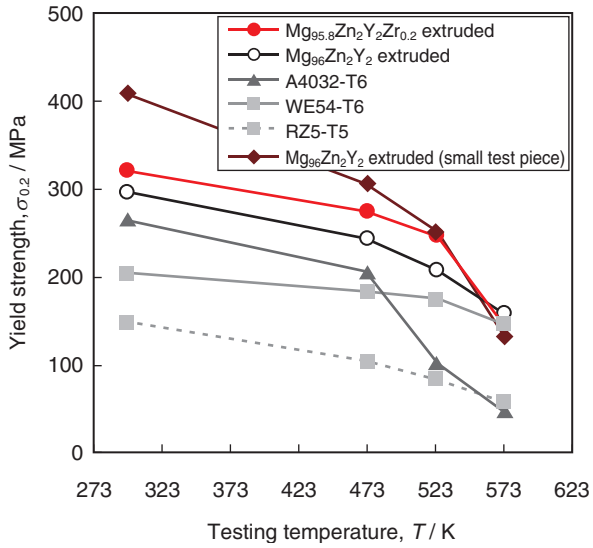


Fig. 5 Yield strength of Mg-Zn-Y alloys compared to A4032, WE54 and RZ5 alloys

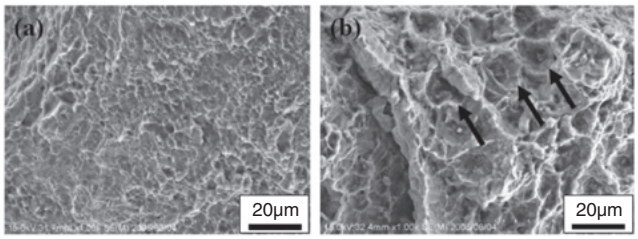


Fig. 6 Fractured surfaces of specimen $Mg_{95.8}Zn_2Y_2Zr_{0.2}$ alloys at (a) 298 K and (b) 573 K after extrusion

displaying resistance to grain boundary fracture increase in strength.

Next, the fatigue strength characteristic of the $Mg_{95.8}Zn_2Y_2Zr_{0.2}$ alloy at 473 K was compared with A4032-T6. The results are shown in Fig. 7. The arrows in the figure show test pieces remaining unfractured even after 10^7 repetitions. In other words, by contrast with aluminum alloys that do not display clear fatigue limits like A4032-T6, the $Mg_{95.8}Zn_2Y_2Zr_{0.2}$ alloy shows a fatigue limit at 100 MPa, as indicated by the bent line[8]. In addition to exceeding the 85 MPa limit for A4032-T6 at 10^7 repetitions, it was conjectured that an even more significant difference would be obtained at 10^8 repetitions, a figure that is essential in modern parts design.

Modern high-power engines use oil jets and other cooling mechanisms to reduce the temperature of the apices of the pistons, but these cooling methods have limits. In cases in which it is necessary to realize temperature resistance at the 573 K level, it is necessary to increase both fatigue strength and creep strength in reducing the weight of the pistons[9]. Figure 8 shows the creep properties of A4032-T6 and the $Mg_{95.8}Zn_2Y_2Zr_{0.2}$ alloy at 573 K under a 50 MPa load. The $Mg_{95.8}Zn_2Y_2Zr_{0.2}$ alloy displays greater creep strength than A4032-T6. It has been reported that the creep strength of the alloy is increased at high temperatures because compound phases such as the LPSO phase (a crystallized grain boundary phase) control grain boundary slip, and stacking faults strengthen the α-Mg matrix[10].

As this demonstrates, even when fashioned into large extruded materials of a size suited to practical use, the high-temperature properties of the $Mg_{95.8}Zn_2Y_2Zr_{0.2}$ alloy surpass those of high-strength forged aluminum alloys, as exemplified by A4032.

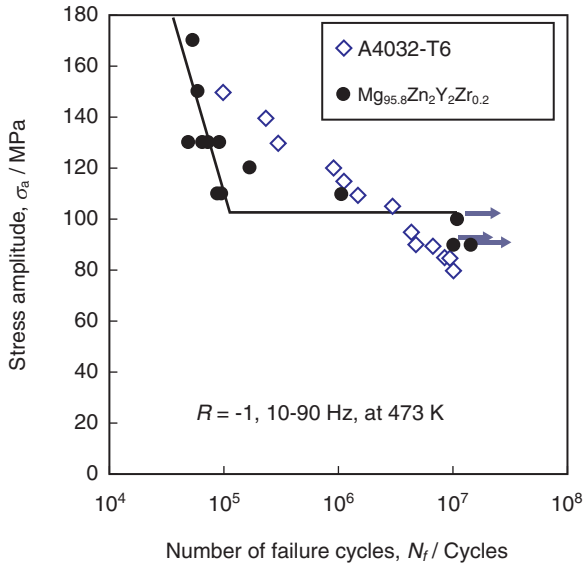


Fig. 7 S-N curves of A4032-T6 and stir-casting $Mg_{95.8}Zn_2Y_2Zr_{0.2}$ alloys after extrusion

4.3. Analysis of Forged Material

4.3.1. Forging temperature and forging defects

Figure 9 shows photographs of sections cut from the $Mg_{95.8}Zn_2Y_2Zr_{0.2}$ alloy and subjected to dye penetrant tests following forging into dummy piston shapes (Fig. 9(b) shows a crack occurring at 773 K). Table 2 shows the relationship between forging temperature and forging defects. At 613 K and below, cracking occurs and there are unfilled sections. From 623 to 748 K, there are regions with no forging defects. Cracking occurs again at the higher

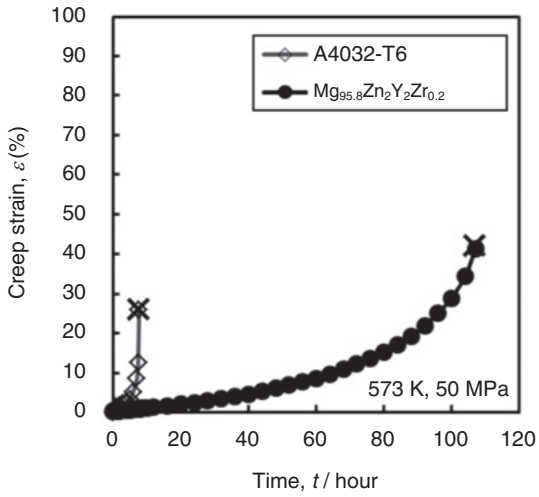


Fig. 8 Creep properties of A4032-T6 and stir-casting $Mg_{95.8}Zn_2Y_2Zr_{0.2}$ alloys after extrusion

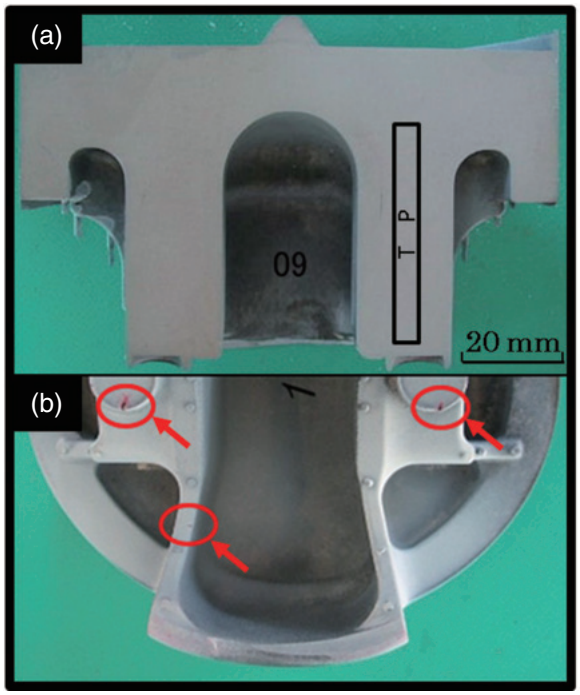


Fig. 9 Forged pistons after penetrant inspection: (a) Location for cutting of tensile specimen; (b) Cracked piston after forging at 773 K

Table 2 Relationship between forging temperature and forging defects

Forging temperature (K)	Forging defect	
	Crack	Unfilled
598	existence	existence
613	existence	existence
623	none	none
648	none	none
673	none	none
698	none	none
723	none	none
748	none	none
773	existence	none

temperature of 773 K. Defects in the low-temperature range are believed to be due to the fact that there is insufficient plastic flow at these temperatures. Because the cracks occurring in the high-temperature range follow the grain boundaries, it was conjectured that the components with low melting points that had crystallized at the grain boundaries had melted again due to the forging temperature.

4.3.2. Tensile properties

Figure 9(a) shows an image of a cross-section of the developed alloy following forging into a dummy piston shape and the position at which a tensile test piece was taken (the boss section). Figures 10(a) and (b) respectively show the tensile properties of the material at 298 K and 523 K (σ_B: Tensile strength; $\sigma_{0.2}$: 0.2% yield strength; δ: Elongation). At 209 MPa, the yield strength of the alloy at 523 K is almost twice that of the extruded A4032-T6 shown in Fig. 5. Forging has reduced the yield strength of the $Mg_{95.8}Zn_2Y_2Zr_{0.2}$ alloy by almost 20% against the alloy following extrusion, as shown in Fig. 5. The horizontal axes of the graphs show the holding temperature of the material prior to forging. As the holding temperature increases, strength declines further. The cause of this phenomenon will be discussed through a consideration of the alloy microstructure.

4.3.3. Microstructure

Figure 11 shows the microstructure of the boss sections of $Mg_{95.8}Zn_2Y_2Zr_{0.2}$ alloy dummy pistons of different pre-forging holding temperatures following forging. The forging direction was vertical, and the microstructures are elongated in the same direction. In the 648 K sample shown in Fig. 11(a), only a vertical microstructure possessing anisotropy can be observed. A fine, recrystallized microstructure has begun to form in the 698 K sample shown in Fig. 11(b), as shown by the arrows in the figure. In the 748 K sample, the α-Mg matrix is entirely filled by recrystallized grains, and the recrystallized grains have become coarser. It was conjectured that because basal slip is generated at a lower level of stress than other slip systems in the hexagonal crystals characterizing the developed alloy, a decline in the basal texture in the tensile direction due to recrystallization would produce a decline in 0.2% yield strength. Figure 12 shows the results of a study of the relationship between forging temperature and the degree of texture. The degree of texture of vertical cross-sections in the direction of forging was analyzed using XRD, and the value obtained by dividing the peak strength of the prismatic planes of the hexagonal crystals by the peak strength of the basal planes was multiplied by 100. The degree of orientation of the basal plane declines with increase in the holding temperature prior to forging, corresponding to the tendency of 0.2% yield strength to decline, as shown in Fig. 10(a).

These results indicated that forging at the low temperature of 623 K, at which forging defects and recrystallization did not occur, made it possible to realize a yield strength approximately twice that of A4032 forged aluminum alloy (209 MPa at 523 K).

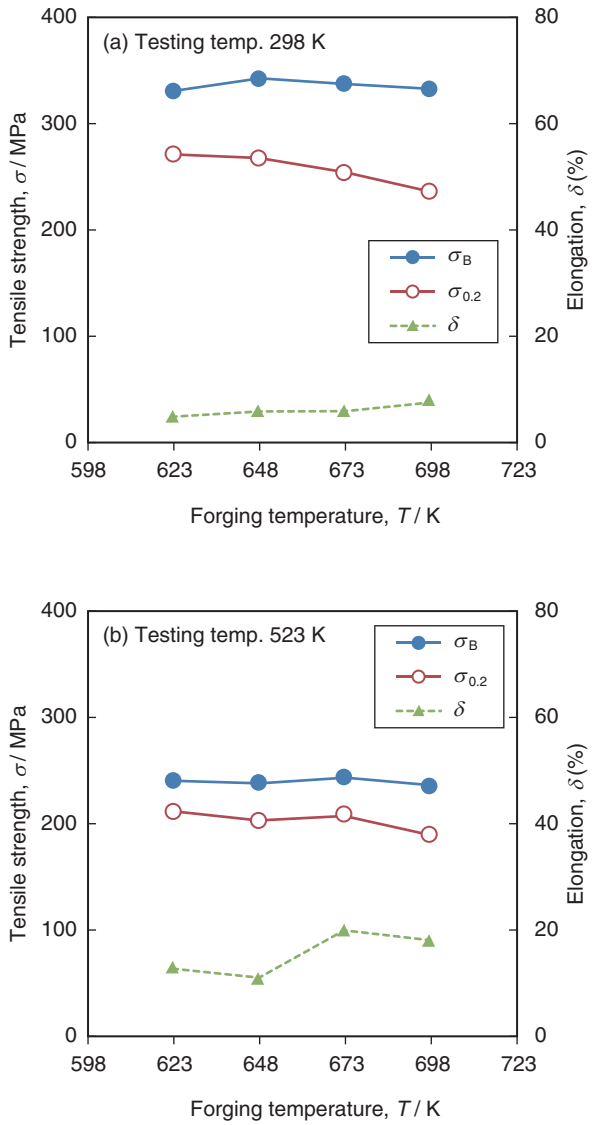


Fig. 10 Tensile properties after forging: (a) 298 K and (b) 523 K

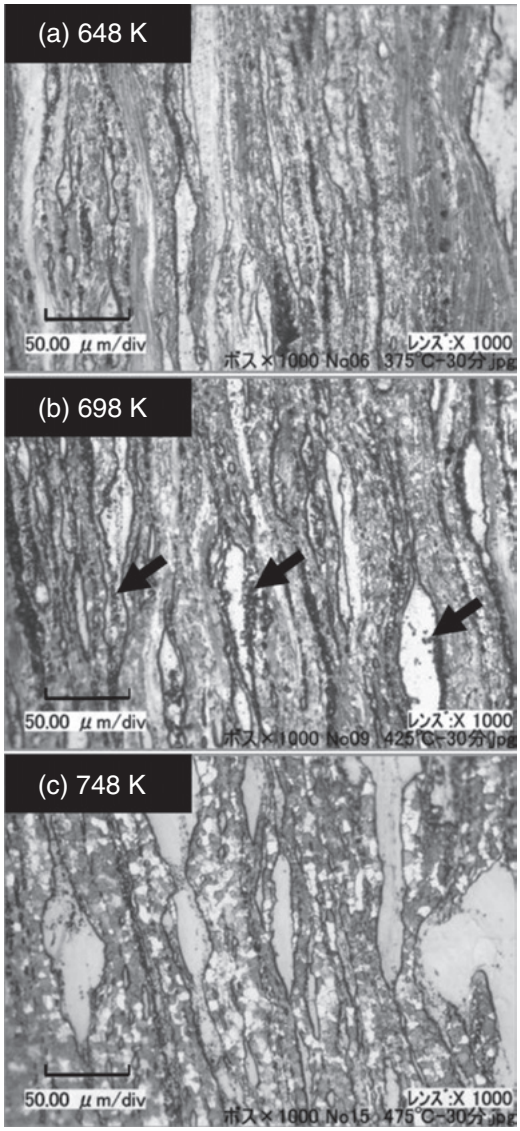


Fig. 11 Microstructure of forged $Mg_{95.8}Zn_2Y_2Zr_{0.2}$ alloys: (a) 648 K, (b) 698 K and (c) 748 K

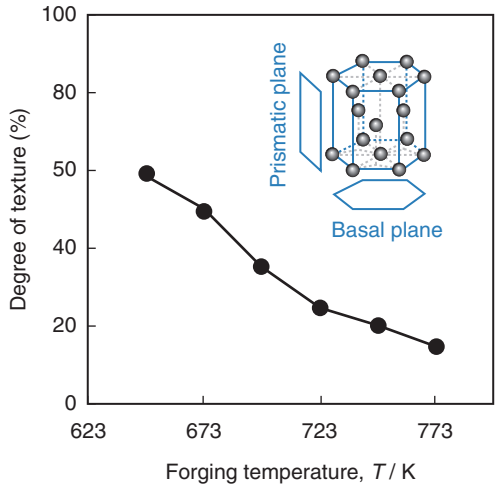


Fig. 12 Relationship of degree of texture and testing temperature after forging

4.3.4. Physical properties and other characteristics

Thermal dimensional stability, an essential property for the $Mg_{95.8}Zn_2Y_2Zr_{0.2}$ alloy as a high-temperature material, was studied. Figure 13 shows a comparison of the rate of dimensional change in the alloy after 100 hr at 503 K with A4032-T6. Compared to A4032-T6 at 33 - 34×10^{-3}%, the alloy displays an extremely low rate of dimensional change at 5 - 13×10^{-3}%. By contrast with the precipitation-hardened microstructure of A4032-T6, the alloy's constituent phases ($Mg_{12}ZnY$ (LPSO) and $Mg_3Zn_3Y_2$) are stable, and do not display volumetric expansion as a result of aging.

Table 3 shows various characteristics of the $Mg_{95.8}Zn_2Y_2Zr_{0.2}$ alloy. Results for the commercial aluminum alloys A4032 and AC8A and the commercial magnesium alloys AZ91 and WE54 are also shown for the sake of comparison. Taking the use of the materials in high-temperature environments as pistons and other automotive parts into consideration, thermal conductivity is an issue from the perspective of cooling performance. The developed alloy displays significantly higher thermal conductivity than the commercial magnesium alloys, and realizes a comparatively good characteristic in this area. The material's coefficient of thermal expansion and Young's modulus are of a similar level to the commercial magnesium alloys, and lower than those of the commercial aluminum alloys. The developed alloy displays a low density like the commercial magnesium alloys, and is approximately 70% that of the aluminum alloys, meaning that it can be expected to contribute to the reduction of the weight of parts in automotive and other engines.

In addition, unit fatigue tests of pistons manufactured from forged Mg-Zn-Y alloys in oil at 523 K demonstrated that the pistons realized approximately 1.5X the strength of A4032 pistons (10^7 repetitions).

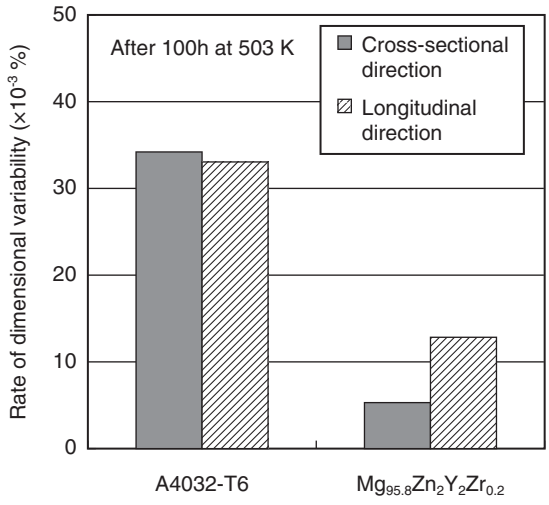


Fig. 13 High-temperature dimensional stability of A4032-T6 and stir-casting $Mg_{95.8}Zn_2Y_2Zr_{0.2}$ alloys after extrusion

Table 3 Characteristics of stir-casting $Mg_{95.8}Zn_2Y_2Zr_{0.2}$ alloy compared to commercial aluminum and magnesium alloys

Alloy	Thermal conductivity (W/(m·K))		Coefficient of thermal expansion at 298-573 K (1/K)	Young's modulus (GPa)	Density (kg/m^3)
	at 473 K	at 298 K			
$Mg_{95.8}Zn_2Y_2Zr_{0.2}$	89.8	72.4	25.4×10^{-6}	46.9	1920
A4032-T6	141	-	21.5×10^{-6}	73	2690
AC8A-T6 (JIS)	128	125	21.4×10^{-6}	78	2720
AZ91D	-	51	27.2×10^{-6}	45	1830
WE54-T6	-	52	24.6×10^{-6}	44	1850

5. Conclusion

In an effort to reduce the weight of structural automotive parts through the use of a high-strength heat-resistant magnesium forged alloy, the solidification microstructures of Mg-Zn-Y alloys were controlled, and the microstructures and properties of the alloys were examined. The research produced the following findings.

(1) A new casting method in which the ingot case is rotated and the molten metal inside the case is agitated was developed. In addition to promoting the formation of crystal nuclei, this stir-casting method controls the solidification of the molten metal from the walls of the ingot case inwards until the solidification temperature was reached. This has helped to prevent the usual segregation and coarsening of the crystal grains, and made it possible to realize a fine and uniform microstructure in a large ingot for extrusion, measuring 335 mm in diameter and 850 mm in height.

(2) A plastically worked (extruded) Mg-Zn-Y alloy formed from ingots displaying this fine and uniform microstructure realized tensile, fatigue and creep characteristics exceeding those of commercial heat-resistant magnesium alloys and aluminum alloys at a wide range of temperatures, from room temperature to 573 K. With regard to physical properties, the alloy displayed 70% lower specific gravity than aluminum alloys. Thermal conductivity can represent an issue, and the performance of the alloy significantly exceeded the commercial magnesium alloys in this respect, reaching levels close to those of commercial aluminum alloys.

(3) Forging the alloy at the low temperature of 623 K, at which forging defects and recrystallization do not occur, made it possible to realize a yield strength at 209 MPa and a fatigue strength respectively approximately twice and 1.5 times those of A4032 forged aluminum alloy used in pistons in 523 K high-temperature conditions.

Mg-Zn-Y alloys possess good high-temperature characteristics, and can be considered promising forging materials in the attempt to reduce the weight of heat-resistant parts. They possess a 30% lower specific gravity than aluminum alloys, and thin-wall design exploiting their high yield strength and fatigue strength can be expected to realize weight savings of over 30%.

References

(1) Yoshimoto, S., Yamasaki, M., Kawamura, Y.: Microstructure and Mechanical Properties of Extruded Mg-Zn-Y Alloys with 14H Long Period Ordered Structure, Mater. Trans., Vol.47, p.959-965, (2006)

(2) Zhu, Y. M., Morton, A. J., Nie, J. F.: The 18R and 14H long-period stacking ordered structures in Mg-Y-Zn alloys, Acta Mater., Vol.58, p.2936-2947, (2010)

(3) Shao, X. H., Yang, Z. Q., Ma, X. L.: Strengthening and toughening mechanisms in Mg-Zn-Y alloy with a long period stacking ordered structure, Acta Mater., Vol.58, p.4760-4771, (2010)

(4) Yamasaki, M., Hashimoto, K., Hagihara, K., Kawamura, Y.: Effect of multimodal microstructure evolution on mechanical properties of Mg-Zn-Y extruded alloy, Acta Mater., Vol.59, p.3646-3658, (2011)

(5) Mabuchi, M. and Higashi, K.: Strengthening mechanisms of Mg-Si alloys, Acta Mater., Vol.44, p.4611-4618, (1996)

(6) Tamura, Y., Kono, N., Motegi, T., Sato, E.: Grain refining of pure magnesium by adding Mg-Zr master alloy, J. JILM 47, p. 679-684, (1997)

(7) Marya, M., Hector, L.G., Verma, R., Tong, W.: Microstructural effects of AZ31 magnesium alloy on its tensile deformation and failure behaviors, Mat. Sci. Eng., A418/1-2, p.341-356, (2006)

(8) Ando, S., Toda, K., Tsushida, M., Kitahara, H., Tonda, H., and Kawamura, Y.: Fatigue Properties of Mg-Zn-Y Alloys with Long Period Ordered Structure, J. Japan Inst. Metals, Vol. 71, No. 9, p. 699-703, (2007)

(9) Fujii, H., Oka, T., Yoneyama, M., Deguchi, T., Murakami, H.: Development of Lightweight Forged Piston Material by Controlling Needle-type Intermetallic Compound Size Using Carbon Mold Continuous Casting Method, HONDA R&D Technical Review, Vol. 20 No. 2, p. 132-140

(10) Shibata, A., Suzuki, M., Maruyama, K.: Effects of Eutectic Compounds Formed along Grain Boundaries in Thixomolded Alloy $Mg_{96}Zn_2Y_2$ on Creep Deformation, Mater. Trans., Vol.50, p.1426-1432, (2009)

■ Author ■



Yuichi IENAGA

Prediction of Fracture of Cylinder Block Main Bearing by Fretting Fatigue and Development of Verification Method

Yoshimichi ISHIHARA* Takeru HAMAKAWA* Kenji SATOH*
Takeyuki YAMASAKI* Chao SHI* Hisashi HASHIMOTO*
Hiroaki HANEDA* Shinichi TAKAHASHI*

ABSTRACT

A method of prediction of the occurrence of fretting fatigue fracture of the main bearing in the cylinder block development process and a method of verification of the results of predictions have been developed.

Because fretting fatigue strength differs from material fatigue strength when fretting does not occur, a fatigue limit diagram when fretting occurs was obtained using material test pieces, and criteria for the evaluation of stress generated in an actual engine were determined. A method of measurement of stress amplitude and relative slip using a unit test apparatus was developed, making it possible to predict fretting fatigue fracture before the stage of tests using actual engines. The development of a method of conversion of strain values determined using the unit test apparatus into figures for relative slip made it possible to formulate a method of evaluation of relative slip in an actual engine.

1. Introduction

With growing environmental awareness worldwide, demand on the automotive industry to reduce the weight of engine parts in order to boost fuel efficiency is increasing. The use of a configuration that makes the bearing cap in the main bearing supporting the crankshaft independent is available as a means of reducing the weight of the cylinder block, one of the parts making up the engine[(1)]. However, connection rigidity is lower in a configuration with an independent bearing cap than with a ladder configuration, and micro-slip occurs in the bearing cap mating faces, which can result in fractures due to fretting fatigue[(2)].

Fretting fatigue fractures are known to occur as a result of the development and propagation of fatigue cracks due to the destruction of surface oxide films and the presence of abrasion powder adhering to surfaces[(3)]. Stress measurements of the mating faces of the main bearing conducted in actual engines during cylinder block strength evaluations show that the stress generated when fatigue fractures occur due to fretting is lower than the fatigue strength of materials when fretting does not occur. Because of this, it is challenging to predict fretting fractures, and it has been necessary to verify specifications in endurance tests using actual engines. This accounts for a significant amount of time during the cylinder block development process.

Fault tree analysis (FTA) was employed to break down the phenomenon of fretting fatigue fracture based on its mechanism of occurrence, and showed that the two major causes of fatigue fracture are stress amplitude and relative slip[(3)].

The research discussed in this paper studied the fatigue strength of materials in relation to these two major causes, obtaining fatigue limit diagrams when fretting occurs, and developed a method of investigation that can be applied to actual engines. In addition, a test method employing a unit test apparatus was devised, and a method of prediction of fretting fatigue at a stage prior to actual engine tests was developed.

2. Development Goals

The development set out to establish a method of prediction of fretting fatigue fractures using a cylinder block unit test apparatus. In addition, it aimed to develop a method of investigation of fretting fatigue fracture using actual engines.

By means of achieving these goals, the research sought to reduce the man-hours focused on fretting fatigue in the cylinder block development process.

* Automobile R&D Center

3. Materials Tests

3.1. Aim of Tests and Test Method

Fretting fatigue tests were conducted in accordance with the fretting fatigue test method specified by the Japan Society of Mechanical Engineers (JSME)[3]. The aim of the tests was to establish criteria for evaluation of stress amplitude and relative slip, the two major factors in fretting fatigue fractures, by determining the correlation between these factors and material fatigue strength in tests in which slip and a load were simultaneously applied to test pieces.

The test method is shown in Fig. 1. Using this method, fretting was reproduced by pressing a contact pad (FC250) onto a test piece (ADC12). Surface pressure was imparted to the contact area by tightening a bolt, and calculated from the value of strain in a ring-shaped fixing jig. The relative slip between the test piece and the contact pad was directly measured by affixing high-temperature clip gauges to each with stays. There is no reference to the use of clip gauges to measure relative slip in the JSME fretting fatigue test method; the method was devised specifically for the tests under discussion. The test piece was machined from vacuum diecast material, and the contact pad was machined from material cut from cylinder block bearings. Figure 2 shows the shapes of the test piece and the contact pad. In order to vary the magnitude of relative slip, contact pads of 10, 15, and 30 mm in width (shown as L in Fig. 2) were prepared. Table 1 shows the test conditions. Fatigue tests were conducted in a constant-temperature oven at 150ºC. Push-pull fatigue was applied at a test speed of 15 Hz. The maximum number of repetitions was 10^7. Fatigue lifetime in relation to relative slip was calculated from the relationship between stress amplitude and fatigue lifetime (S-N curves) obtained for each test condition. Tests were considered completed when the test piece fractured, and the number of repetitions at this time was evaluated.

3.2. Test Results

Figure 3 shows the results of measurements of fatigue strength in relation to relative slip at 10^7 repetitions. There is a correlation between relative slip and fatigue strength. At a relative slip of 15 μm, fatigue strength declines by approximately 25%.

These tests clarified values to serve as criteria for the evaluation of stress when fretting occurs, and made it possible to define a fretting fatigue limit diagram.

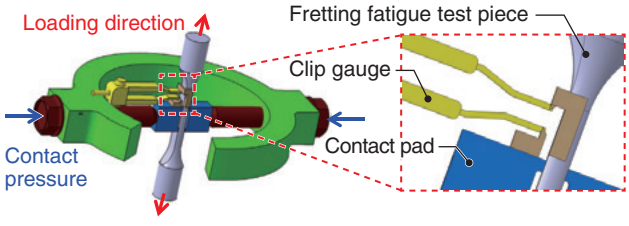


Fig. 1 Fretting fatigue test method

Table 1 Test conditions

Test machine	SERVO PULSER
Test temperature, atmosphere	150°C, air
Test speed	15 Hz
Contact pressure	50, 100, 150 MPa
Number of cycles	Max 10^7

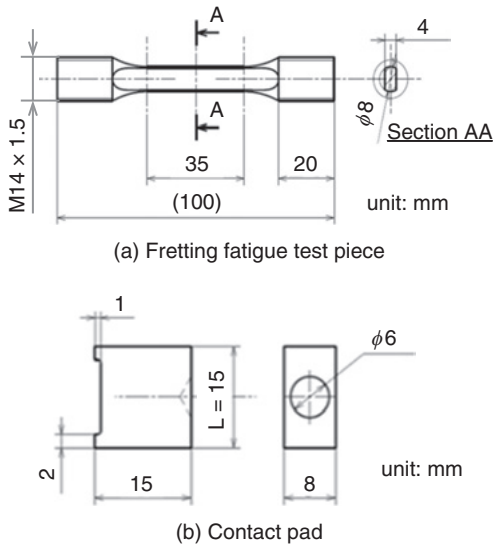


Fig. 2 Fretting fatigue test pieces

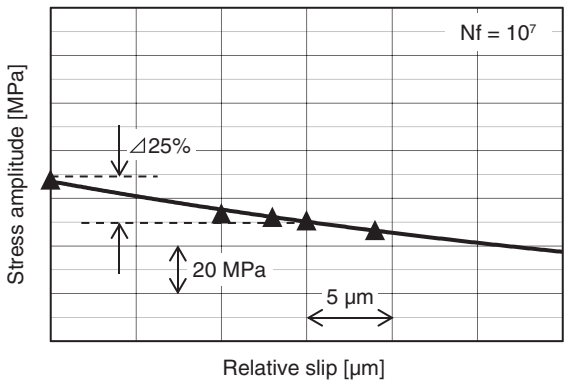


Fig. 3 Relationship between stress and relative slip measurement

4. Cylinder Block Unit Tests

4.1. Aim of Tests and Test Method

Sections of actual cylinder blocks were cut out, and a cylinder block unit test apparatus was produced (Fig. 4).

Using this test apparatus, the main bearing of the unit cylinder block was shaken to produce fretting, and stress

amplitude and relative slip were measured. The aim of the test was to make it possible to predict fretting fatigue fracture without using a complete engine by plotting the measurement results on the fretting fatigue limit diagram obtained from unit tests using test pieces.

The test apparatus shook the crankshaft on two orthogonal axes. Independent control of the amplitude and phase of the shakers on each axis made it possible to set load conditions as desired.

The cylinder block was cut to make it possible to impart loads to the central bearing section in isolation. The central bearing section has the highest force amplitude of the main bearing of an inline 4-cylinder (L4) engine, and is a site at which fretting fatigue occurs.

Strain gauges were affixed to the surfaces of the cylinder block and the main bearing at regular intervals in opposing pairs in order to measure stress amplitude and relative slip. Strain was measured in a direction parallel to the mating faces of the cylinder block and main bearing, and the strain gauges were affixed in positions as close as possible to the mating faces (Fig. 5).

Stress amplitude and relative slip were calculated from the strain measurement results. In order to calculate relative slip, the difference between cylinder block and main bearing strain was found, and the difference in strain at each measurement point was integrated. The resulting value was considered to represent relative slip. Figure 6 shows the calculation method. Equation (1) was used in the calculations.

$$S_{strain} = \sum (\varepsilon Ai - \varepsilon Bi) \times L \quad (1)$$

In order to evaluate the measured stress amplitude and relative slip using the fatigue limit diagrams determined in fretting fatigue tests, it was necessary to establish a correlation between the relative slip measured by the strain gauges and the values measured by the clip gauges used in the fretting fatigue tests. In order to do so, clip gauges were attached to the cylinder block and the main bearings, and measurements were taken using these gauges at the same time as the strain gauges (Fig. 7). The determination of the correlation between relative slip measured by the strain gauges and relative slip measured by the clip gauges made it possible to use strain gauges to measure relative slip in unit tests and in actual engines, in which clip gauges cannot be used.

The coefficient of correlation between relative slip calculated from strain gauge results and that calculated from

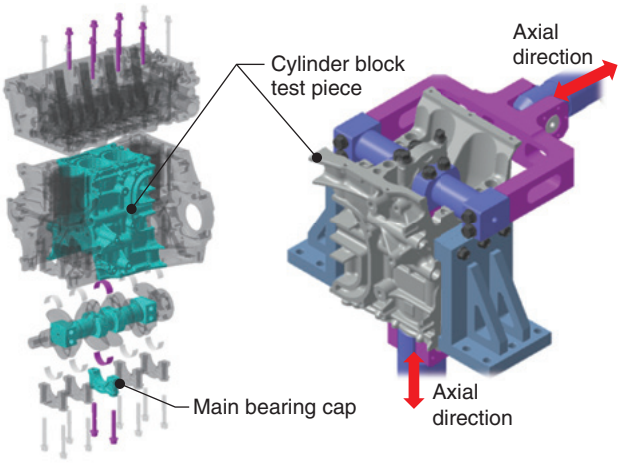


Fig. 4 Test equipment

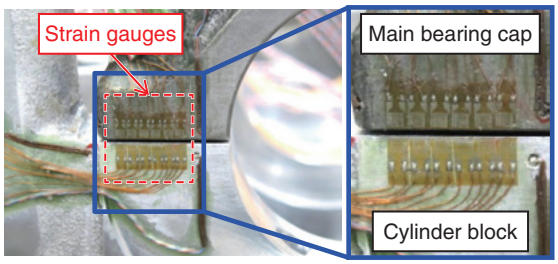


Fig. 5 Cylinder block and main bearing with strain gauges

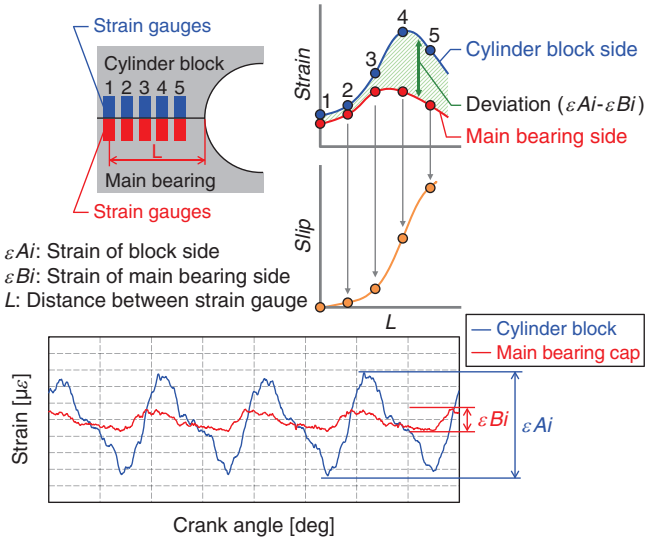


Fig. 6 Method of calculation of slip

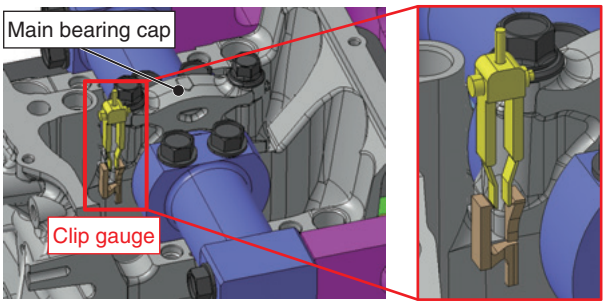


Fig. 7 Test equipment with clip gauge

Table 2 Test conditions

Force amplitude	15 kN
Frequency	100 Hz
Phase difference	90 deg
Bolt axial force	Base: 11% reduction
Stiffness	Base: Width 5% reduction

clip gauge results, termed K, was determined. Figure 8 shows results for the coefficient of correlation.

Finally, the following equation was employed for the calculation of relative slip using strain gauge results:

$$S_{clip} = \sum (\varepsilon Ai - \varepsilon Bi) \times L \times K \quad (2)$$

4.2. Test Conditions and Test Results

The test conditions are shown in Table 2. The force amplitude was imparted on two axes (horizontal and vertical directions) with a 90º phase difference. It was possible to reproduce a load configuration similar to that occurring in an L4 engine by generating a synthetic load from the loads on each axis (Fig. 9). The maximum load was 15 kN, corresponding to the maximum load in an actual engine.

For the tests, the crankshaft force amplitude and frequency were held constant, and the values of the main bearing bolt axial force and the main bearing stiffness (mating face width), parameters that fretting stress displays sensitivity to, were varied.

In addition, tests based on quality engineering have clarified the contribution of the surface forms of the cylinder block and main bearing mating faces to fretting fatigue fracture[4), 5)]. The surface properties of the test pieces were therefore measured prior to the tests. A stylus roughness tester was employed in the measurements. Surface data based on measurement point group information was obtained using a sensing-pin device that measures roughness in the lateral direction combined with a longitudinal feeder. Measurement scans of cross-sectional shape were conducted 140 times, and the differences in height of the surfaces were numericized. Figure 10 shows results for measurements of the surface shape of the main bearing. Tests were conducted using cylinder blocks produced with the aim of achieving differences in surface height within 10 µm. The incorporation of numericized surface shape data in simulations of fretting fatigue fracture will help to increase the predictive accuracy of the simulations.

Figure 11 shows results for measurements of stress amplitude and relative slip. Results for stress amplitude and relative slip for the base specifications were lower than values on the fretting fatigue limit diagram obtained from unit tests

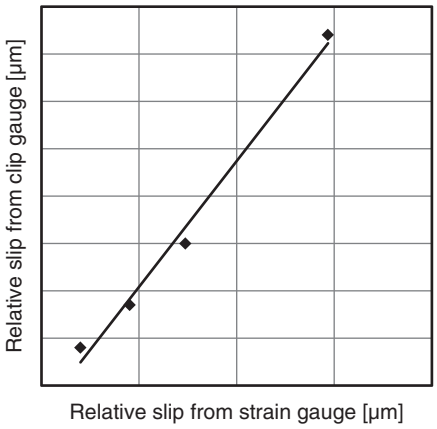
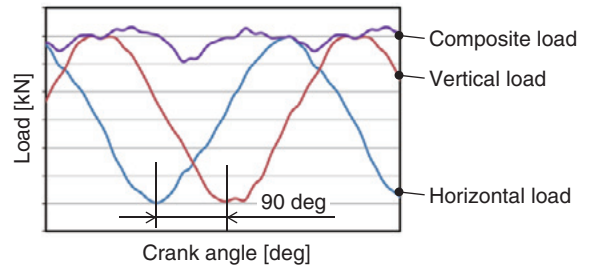


Fig. 8 Relationship between strain gauge and clip gauge



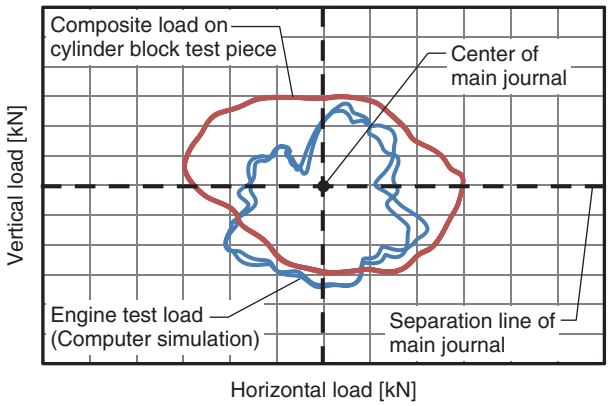


Fig. 9 Cylinder block test piece test loads

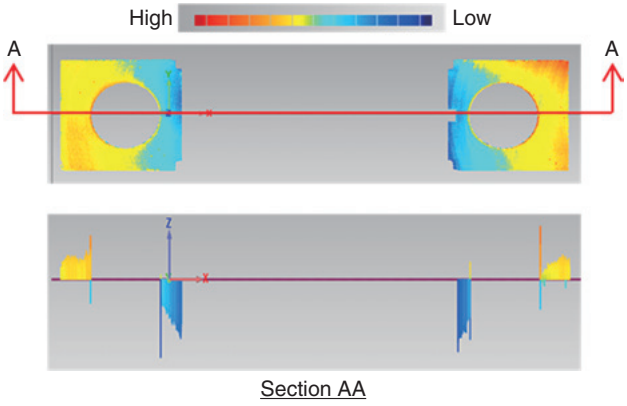


Fig. 10 Surface property from measurements

on material test pieces, and fractures did not occur even in endurance tests involving continuous vibration. Results for stress amplitude and relative slip for a specification in which the bolt axial force and the block stiffness were reduced were higher than values on the fretting fatigue limit diagram, and fractures occurred in endurance tests involving continuous vibration. The facts that the bearing mating face turned black and the fracture originated in the mating face were considered to indicate that fretting wear was a factor in the development of the fracture[3]. Figure 12 shows the results of inspection of the surface affected by the fretting fracture.

Based on these results, it was possible to verify a correlation between the relationship between stress amplitude and relative slip obtained using the developed test method and the fretting fatigue limit diagram and the occurrence or non-occurrence of fretting fatigue fracture. This is believed to indicate that it is possible to predict fretting fatigue fracture without using an actual engine, by means of the developed test apparatus that models an engine.

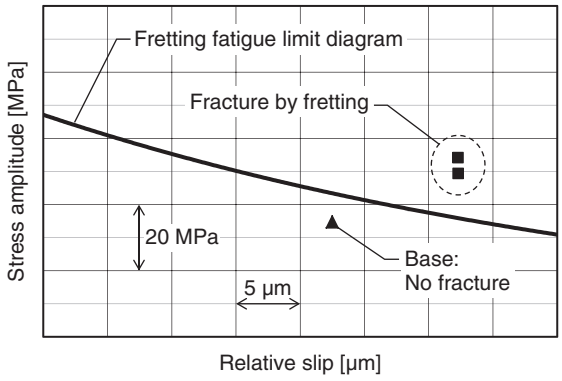


Fig. 11 Results of stress and relative slip measurements

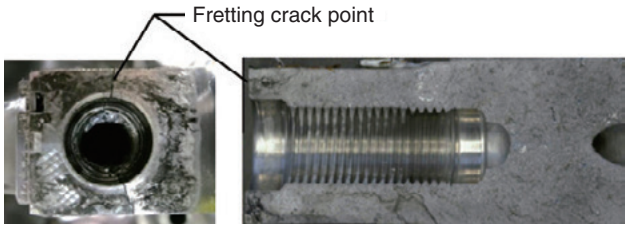


Fig. 12 Results of material inspection after cylinder block test

5. Establishment of Method for Verification in Actual Engine

5.1. Verification Test Conditions

In order to verify that tests using an actual engine would produce the same results as cylinder block unit tests, endurance tests were conducted on an actual engine, and stress amplitude and relative slip were measured using the method employed in unit tests. Because clip gauges could not be fitted in an actual engine, measurements were conducted using strain gauges.

Table 3 Test conditions

	Test 1	Test 2
Engine type	1.5 L Engine	Same as left
Oil temp	80°C	Same as left
Water temp	80°C	Same as left
Engine speed	6800 r/min	Same as left
Endurance test time	100 hr	26 hr
Bolt axial force	Base	11% reduction
Force amplitude on crankshaft	Base	56% increase

Tests were conducted using two patterns in which the main bearing bolt axial force and the force amplitude on the crankshaft (factors that stress amplitude displays sensitivity to) were varied[5].

Table 3 shows the engine test conditions.

5.2. Results of Verification Tests

Figure 13 shows the results of stress amplitude and relative slip measurements. The results for stress amplitude and relative slip in Test 1 were lower than the values shown in the fretting fatigue limit diagram, and fracture did not occur even after 100 hours of endurance testing at 6800 rpm. The results for stress amplitude and relative slip in Test 2 were higher than the values shown in the fretting fatigue limit diagram, and fracture occurred after 26 hours of fatigue testing at 6800 rpm. Fracture occurred between 1×10^6 and 1×10^7 repetitions in the results for measurement of stress amplitude and relative slip, according with the results of predictions. The state of the bearing mating face following the endurance tests and the

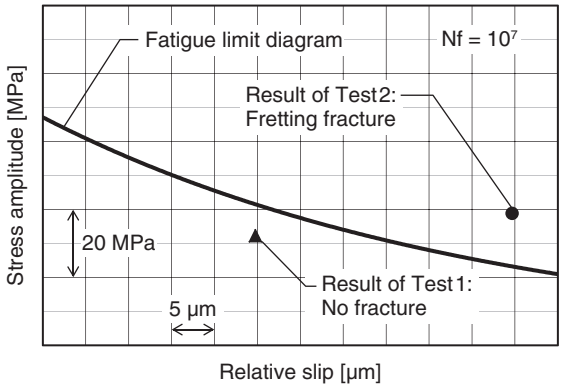


Fig. 13 Results of stress and relative slip measurements

origin point of the fracture were the same as the results of unit tests, and it was therefore considered that a fretting fatigue fracture had occurred. Figure 14 shows the results of inspection of the fracture face.

The results obtained using the developed test method displayed the same tendency as the results of cylinder block unit tests, demonstrating its validity as a method of evaluating fretting fatigue fracture in actual engines using strain gauges.

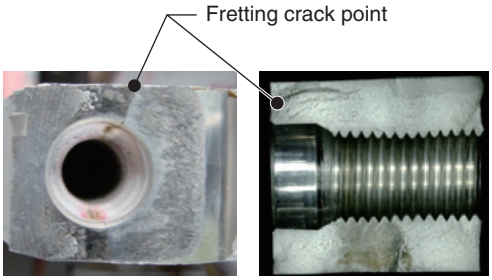


Fig. 14 Results of material inspection after actual engine test

6. Conclusion

The research discussed in this paper developed a method of prediction of fretting fatigue fracture in the cylinder block development process prior to the implementation of endurance tests and a method of verification of prediction results, producing the outcomes discussed below. The results of this research will make it possible to reduce the number of endurance tests performed on actual engines in order to study fretting fatigue fracture, and thus reduce the number of man-hours involved in the development process.

(1) Unit tests of material test pieces showed that fatigue strength declined by approximately 25% at a relative slip of 15 μm when fretting occurred, and made it possible to define a fretting fatigue limit diagram.
(2) The development of a method of evaluation of fretting fatigue fracture in unit tests using test pieces cut from actual cylinder blocks has enabled prediction of fretting fatigue fracture prior to endurance tests using actual engines.
(3) The development of a method for the evaluation of fretting fatigue fracture in actual engines using strain gauges has made possible simple verification of results in a short time period.

References

(1) Suzuki, M., Hayakawa, S., Ishihara, Y., Shindo, T.: Development of the New L4 Gasoline Engine for Compact Cars, JSAE Annual Congress Proceedings, No. 91-14, p. 9-12, (2014) (in Japanese)
(2) Cha, S., Chang, H., Lee, K., Cho, S., Hwang, D.: A Development of the Fretting Fatigue Analysis Techniques for Engine Aluminum Block, SAE Int. J. Mater. Manuf. 4(1), p. 7, (2011)
(3) Japan Society of Mechanical Engineers: JSME S015 Fretting fatigue test method (revised version), 90 p, (2009) (in Japanese)
(4) Taguchi, G.: Robust Design for Functional Assessment - Methods for Efficient Development, Japanese Standards Association, 351 p, (2000) (in Japanese)
(5) Takeru, H., Sato, K., Yamasaki, T., Shi, C., Hashimoto, H., Haneda, H., Takahashi, S., Ishihara, Y.: Development of the Fretting Fatigue Prediction of a Main Bearing, JSAE Annual Congress Proceedings, No. 46-15A, p. 1107-1112, (2015) (in Japanese)

■ Author ■


Yoshimichi ISHIHARA


Takeru HAMAKAWA


Kenji SATOH


Takeyuki YAMASAKI


Chao SHI


Hisashi HASHIMOTO


Hiroaki HANEDA


Shinichi TAKAHASHI

Honda R&D Co., Ltd.
Honda R&D Technical Review Editorial Committee

Motorcycle R&D Center
Automobile R&D Center
Power Products R&D Center
Aircraft Engine R&D Center
Fundamental Technology Research Center

Editorial Afterword

In the past several years, reports have been published concerning the realization of substantial increases in the efficiency of electric and gasoline vehicle systems, in addition to advances in fuel cell vehicles. We have also witnessed considerable technological evolution in the areas of automation and intelligent operation. Research and development in the field of mobility technology can be considered to be entering an era of technological revolution.

Despite this tide of technological revolution, the basic approach to the development of individual technologies has not changed. That is to say, there has been no change in our "spiral-up" methodology, which involves the steady repetition of a cycle of prediction based on theory and simulations, testing to verify our hypotheses, analysis of results and comparison with our predictions, and reflection of new findings. The reality of the process is that the results we obtain are frequently not the results that we expected.

As is always the case, while each of the authors in this edition of Honda R&D Technical Review has undoubtedly experienced repeated failures in the course of their research and development of the technologies they discuss, these do not appear in their papers. We hope that readers will take these papers and technological introductions as the essence of this process, and will consider them with an understanding of the process of persistent and steady modification using the latest prediction, testing, and analysis techniques and the great personal effort involved in the production of results of considerable scientific and technological value.

Ultimately, reading this edition makes me aware of the importance of the steady development of individual technologies based on the consistent exercise of creativity and ingenuity, like those reported on here, in the creation of groundbreaking products.

Toshio Tokune

©2016 Honda Motor Co., Ltd. (All rights reserved)

ISSN 1881-6223

Published by:
Honda Motor Co., Ltd.
2-1-1, Minami-Aoyama, Minato-ku,
Tokyo 107-8556, Japan

Edited by:
Honda R&D Co., Ltd.
Honda R&D Technical Review Editorial Committee

Printed:
Mar. 1, 2016


CLARITY
FUEL CELL